Sebastian Schmitt

Experimental and Numerical Investigations of Two-Phase Flow with Non-Isothermal Boundary Conditions under Microgravity Conditions

---

Cuvillier Verlag Göttingen
Internationaler wissenschaftlicher Fachverlag

Experimental and Numerical Investigations of Two-Phase Flow with Non-Isothermal Boundary Conditions under Microgravity Conditions

Experimental and Numerical Investigations of Two-Phase Flow with Non-Isothermal Boundary Conditions under Microgravity Conditions

Dem Fachbereich Produktionstechnik
der
UNIVERSITÄT BREMEN

zur Erlangung des Grades
Doktor-Ingenieur
vorgelegte

Dissertation

von
Dipl.-Ing. Sebastian Schmitt

Gutachter:
Prof. Dr.-Ing. M. E. Dreyer, ZARM, Universität Bremen, Bremen
Prof. Dr. E. Hopfinger, LEGI, Université Joseph Fourier, Grenoble

Tag der mündlichen Prüfung:
11. November 2016

Bibliografische Information der Deutschen Nationalbibliothek
Die Deutsche Nationalbibliothek verzeichnet diese Publikation in der Deutschen Nationalbibliografie; detaillierte bibliografische Daten sind im Internet über http://dnb.d-nb.de abrufbar.
1. Aufl. - Göttingen: Cuvillier, 2017
Zugl.: Bremen, Univ., Diss., 2016

Nonnenstieg 8, 37075 Göttingen
Telefon: 0551-54724-0
Telefax: 0551-54724-21
www.cuvillier.de

1. Auflage, 2017
Gedruckt auf umweltfreundlichem, säurefreiem Papier aus nachhaltiger Forstwirtschaft

ISBN 978-3-7369-9493-5
eISBN 978-3-7369-8493-6

Abstract

The purpose of the present work is to enhance the existing knowledge about cryogenic and storable liquids with a free surface and non-isothermal boundary conditions under varying accelerations. The motivation behind is the ongoing development of a cryogenic upper stages with restart capability. For a save operation the driving physical effects must be understood. There is the surface reorientation, also known as axial sloshing, occurring upon a gravity step reduction, such as engine cut-off. This reorientation process is furthermore influenced by the superheated tank wall. In the ballistic flight phase, when no body forces are present, a new stable free surface dominated by capillary forces establishes. This new interface configuration again is influenced by a temperature gradient along the tank wall. Evaporation and condensation occur simultaneously on several parts along the liquid-vapor interface. These phase change effects are the driving parameters for the overall tank pressure progression which must be controlled over the mission (up to several hours). The contact angle at the three phase contact line (solid-liquid-vapor) acts as a boundary condition for the free surface curvature. It is also influenced by the thermal condition of the wall. On the other hand, the advancing liquid layer cools down the wall. These effects result in a coupled system between fluid kinematic, heat and mass transfer over the free surface, heat conduction within the solid structure and heat transfer over the solid-fluid interface. For a better understanding, drop tower experiments at ZARM, University of Bremen, and suborbital flight experiments were conducted. These experiments were used to validate the commercial flow solvers Flow-3D and Fluent. Simulations of the experiments were performed to supplement the experimental findings and extend the gained data.

Two campaigns, with three drop tower experiments each, using liquid parahydrogen in a partly filled right circular tank were carried out to investigate axial sloshing. The thermal preparation of the experiments allowed to create defined wall temperature gradients, $0.00\,\mathrm{K\,mm^{-1}} \leq \Delta T/\Delta z \leq 0.92\,\mathrm{K\,mm^{-1}}$, and a stratified or homogenous liquid temperature distribution. Several sensors along the cylinder wall and in the vapor region monitored the temperature. The pressure inside the experiment was recorded and optical access was enabled by an endoscope.

Two-dimensional axisymmetric simulations of the drop tower experiments were conducted using Fluent. A mesh study with different cell sizes was carried out to eliminate the influence of the spatial discretization. Furthermore, one isothermal experiment ($\Delta T/\Delta z = 0.00\,\mathrm{K\ mm^{-1}}$) and one non-isothermal ($\Delta T/\Delta z = 0.05\,\mathrm{K\ mm^{-1}}$) experiment were simulated. To cover the range in between these two experiment, six simulations were conducted, whose temperature gradients were within $0.00\,\mathrm{K\ mm^{-1}} \leq \Delta T/\Delta z \leq 0.05\,\mathrm{K\ mm^{-1}}$.

A free surface in ballistic flight conditions was examined numerically using the suborbital flight experiment SOURCE-II conducted by the French-German research group COMPERE. The experiment was simulated utilizing Flow-3D and Fluent with two different grids each to take the mesh influence into account. Within the 140 s experimental time two filling periods and four pressurizations with relaxation phases had to be captured. The numerical simulations were necessary for a detailed understanding of the mass transfer over the free surface and how the temperature in the fluid and solid evolved.

The drop tower campaigns revealed a sensitive behavior of parahydrogen to the wall superheat. Besides two isothermal cases only one non-isothermal case could be established without nucleate boiling. The other three experiments experienced bubble formation throughout the reorientation process.

The first time regime, $t_{pu,Lc} \approx 13\,\mathrm{ms}$, after the gravity step reduction was too short to be captured by the camera. Simulations allowed to observe this time span and could verify the used scaling. A second time regime, which characterizes the reorientation process could be confirmed using experimental and numerical data. The velocity of the advancing liquid layer along the wall seemed not to be influenced by the wall superheat, whereas the oscillation frequency increased with the wall temperature gradient. Even though the experimental time was not long enough to allow the free surface to form a new stable shape, the final center point location could be estimated. The isothermal data is in good accordance with the theory. With an increasing wall superheat the center point deflection decreased. The numerical simulations indicated, that the wall superheat up to $0.05\,\mathrm{K\ mm^{-1}}$ was neutralized within the first 2 s. This was still enough to alter the oscillation frequency, whereas the damping showed no significant difference before a stable surface established after approximately 10 s.

Temperature data of the sensors was falsified by an additional heat input from the laser. This error could be corrected afterward. For the isothermal case almost no change of the wall temperature could be recorded throughout the experiment, which indicated a sufficient thermal insulation of the experiment. For non-isothermal experiments the wall temperature, which was measured on the outside of the cylinder, decreased with a certain delay once the wall was wetted. The preparation procedure caused an initial thermal stratification of the vapor region. Due to the downward moving center point of the free surface the stratified vapor was pulled with the free surface. This motion was captured by the temperature sensors located in the ullage. Even though only limited data was available to initialize the temperature field of the numerical simulations, the described temperature progression was predicted with good accuracy for the non-isothermal case.

The pressure evolution over the experimental time was mostly influenced by phase change effects. With increasing wall superheat a stronger pressure increase could be monitored. The available models in the Fluent version used, did not allow a correct pressure prediction, hence the experimental findings could not be verified by numerical means.

The SOURCE-II experiment was utilized to study a stable free surface in microgravity conditions. Flow-3D was able to predict the pressure progression within $-20\,\% \leq \Delta p_{M1} \leq 11\,\%$ and $-17\,\% \leq \Delta p_{M2} \leq 21\,\%$ for the finer and coarser mesh, respectively. Fluent had a pressure deviation within $-37\,\% \leq \Delta p_{MA} \leq 7\,\%$ for the finer mesh and $-25\,\% \leq \Delta p_{MB} \leq 15\,\%$ for the coarser mesh. Examination of the experimental data revealed, that the pressure progression was dependent on the phase change effects along the free surface. Flow-3D computations could confirm the experimental results and further showed, that a region close to the superheated wall with strong evaporation exists whereas the condensation dominates along the remaining free surfaces. Fluent did not confirm these effects. Here pressure was driven by thermal expansion and contraction of the vapor.

The static contact angle of the free surface was affected by the local wall superheat, the difference between wall and saturation temperature. Experimental data showed a dependence of the static contact angle on the local wall superheat according to the micro-region model. The numerical data differed from the experimental results underestimating the theoretical values of the micro-region model.

Zusammenfassung

Ziel dieser Arbeit ist, das bestehende Wissen über kryogene und lagerfähige Flüssigkeiten mit einer freien Oberfläche und nichtisothermen Randbedingungen unter veränderlichen Beschleunigungen zu erweitern. Die dahinterstehende Motivation ist die fortlaufende Entwicklung an kryogenen Oberstufen mit Fähigkeit zur Wiederzündung. Für einen sicheren Betrieb müssen die treibenden physikalischen Effekte verstanden werden. So tritt eine Oberflächenreorientierung aufgrund einer schlagartigen Verminderung der Gravitation, wie beim Ausschalten der Motoren, auf, welche auch unter axialem Schwappen bekannt ist. Dieser Reorientierungsprozess wird zudem von der überhitzten Tankwand beeinflusst. In der ballistischen Flugphase, wenn keine Körperkräfte vorhanden sind, bildet sich eine neue stabile freie Oberfläche aus, welche durch Kapillarkräfte dominiert ist. Diese neue Grenzflächenkonfiguration wird wiederum von einem Temperaturgradienten entlang der Tankwand beeinflusst. Verdampfung und Kondensation treten gleichsam an verschiedenen Stellen entlang der Flüssigkeits-Dampf Grenzfläche auf. Diese Phasenumwandlungseffekte sind die treibenden Parameter für den integralen Druckverlauf des Tanks, welcher über den Verlauf der Mission kontrolliert werden muss (bis zu einigen Stunden). Der Kontaktwinkel an der Dreiphasenkontaktlinie (Festkörper-Flüssigkeit-Dampf) wirkt als Randbedingung für die Krümmung der freien Oberfläche und ist ebenfalls vom thermalen Zustand der Wand abhängig. Andererseits kühlt der voranschreitende Flüssigkeitsfilm die Wand. Diese Effekte resultieren in einem gekoppelten System zwischen Kinematik des Fluides, Wärme- und Stofftransport über die freie Oberfläche, Wärmetransport innerhalb des Festkörpers und Wärmetransport über die Festkörper-Fluid Grenzfläche. Zum besseren Verständnis wurden Fallturmexperimente am ZARM, Universität Bremen, und Suborbitalexperimente durchgeführt. Simulationen dieser Experimente wurden ausgeführt um die experimentellen Erkenntnisse und die Datenmenge zu ergänzen.

Um das axiale Schwappen zu untersuchen, wurden zwei Kampagnen mit jeweils drei Fallturmexperimenten und flüssigem Parawasserstoff, in einem teilweise gefüllten zylindrischen Tank, durchgeführt. Die thermale Vorbereitung der Experimente ließ zu, definierte Wandtemperaturgradienten zwischen $0.00\,\mathrm{K\ mm^{-1}} \leq \Delta T/\Delta z \leq 0.92\,\mathrm{K\ mm^{-1}}$ und eine geschichtete oder

homogene Temperaturverteilung in der Flüssigkeit zu erzeugen. Sensoren entlang der Zylinderwand und in der Gasphase erfassten die Temperatur. Der Druck innerhalb des Experiments wurde aufgezeichnet und ein optischer Zugang durch ein Endoskop ermöglicht.

Zweidimensionale achsensymmetrische Simulationen der Fallturmexperimente wurden mit Fluent durchgeführt. Eine Netzstudie mit verschiedenen Zellgrößen wurde erstellt, um den Einfluss der räumlichen Diskretisierung zu eliminieren. Weiterhin wurde ein isothermes ($\Delta T/\Delta z = 0.00\,\mathrm{K\ mm^{-1}}$) und ein nicht isothermes ($\Delta T/\Delta z = 0.05\,\mathrm{K\ mm^{-1}}$) Experiment simuliert. Sechs weitere Simulationen mit Gradienten zwischen $0.00\,\mathrm{K\ mm^{-1}} \leq \Delta T/\Delta z \leq 0.05\,\mathrm{K\ mm^{-1}}$ wurden aufgesetzt, um den Bereich zwischen den vorher genannten Experimenten abzudecken.

Basierend auf dem SOURCE-II Suborbitalexperiment, durchgeführt von der französisch-deutschen Forschungsgruppe COMPERE, wurde die freie Oberfläche unter ballistischen Flugbedingungen numerisch untersucht. Das Experiment wurde mit Flow-3D und Fluent mit jeweils zwei Netzen, um den Netzeinfluss zu berücksichtigen, untersucht. Während der 140 s Experimentierzeit waren zwei Füllperioden und vier Bedrückungen mit Entspannungsphasen zu erfassen. Die numerischen Simulationen waren für ein detailliertes Verständnis des Stofftransports über die freie Oberfläche und den Temperaturverlauf in Fluid und Festkörper notwendig.

Die Fallturmkampagne zeigte ein sensibles Verhalten des Parawasserstoffs bezüglich der Wandüberhitzung. Neben zwei isothermen Fällen konnte nur ein nicht isothermer Fall ohne Blasensieden erstellt werden. Bei den anderen drei Experimenten war Blasensieden während der Reorientierung sichtbar.

Die erste Zeitskala $t_{pu,Lc} \approx 13\,\mathrm{ms}$ nach der sprunghaften Reduzierung der Schwerkraft war zu kurz, um von der Kamera erfasst zu werden. Die Simulationen erlaubten diesen Zeitbereich zu betrachten und konnten die verwendete Skalierung verifizieren. Ein zweiter Zeitbereich, welcher den Prozess der Reorientierung beschreibt, konnte durch experimentelle und numerische Daten bestätigt werden. Die Geschwindigkeit des voranschreitenden Flüssigkeitsfilms entlang der Wand scheint nicht durch die Wandüberhitzung beeinflusst worden zu sein, wohingegen die Schwingungsfrequenz mit dem Temperaturgradienten der Wand zunahm. Auch wenn die Experimentdauer nicht ausreichte, um der freien Oberfläche zu erlauben, eine neue stabile Form zu bilden, konnte die finale Position des Mittelpunkts prognostiziert werden. Die isothermen Daten stimmen mit der Theorie überein. Mit steigender Wandüberhitzung reduzierte sich die Auslenkung des Mittelpunkts. Die numerischen Simulationen legten nahe, dass die Wandüberhitzung bis zu $0.05\,\mathrm{K\ mm^{-1}}$ innerhalb der ersten 2 s neutralisiert wurde. Dies reichte noch aus, um die Schwingungsfrequenz zu verändern, wohingegen keine Veränderung der Dämpfung festgestellt werden konnte, bevor eine stabile Oberfläche nach ca. 10 s auftrat.

Temperaturdaten der Sensoren sind durch einen zusätzlichen Wärmeeintrag des Lasers verfälscht worden. Dieser Fehler konnte im Nachhinein korrigiert werden. Während des Experiments konnte für den isothermen Fall fast keine Änderung der Wandtemperatur festgestellt werden, was für eine gute Isolierung des Experiments spricht. Für die nichtisothermen Experimente fiel die Wandtemperatur, welche an der Außenseite gemessen wurde, nach der Benetzung mit einer gewissen Verzögerung ab. Die Vorbereitungsphase führte zu einer anfänglichen Temperaturschichtung im Gas. Wegen des sich abwärts bewegenden Mittelpunkts der freien Oberfläche, wurde der geschichtete Dampf mit der freien Oberfläche mitgezogen. Diese Bewegung wurde von den Temperatursensoren in der Dampfphase erfasst. Auch wenn die vorhandenen Daten zur Initialisierung des Temperaturfelds in der Simulation begrenzt waren, konnte der Temperaturverlauf für den nicht isothermen Fall zuverlässig vorhergesagt werden.

Der Druckverlauf über die Experimentierzeit war hauptsächlich von Effekten des Phasenwechsels beeinflusst. Mit steigendem Wandtemperaturgradienten konnten ein stärkerer Druckanstieg festgestellt werden. Die verfügbaren Modelle in Fluent haben keine korrekte Druckvorhersage ergeben, somit konnten die experimentellen Ergebnisse nicht mit numerischen Methoden verifiziert werden.

Um eine stabile Oberfläche in Mikrogravitation zu untersuchen wurde das SOURCE-II Experiment verwendet. Flow-3D konnte den Druckverlauf für das feine Netz innerhalb von $-20\,\% \leq \Delta p_{M1} \leq 11\,\%$, beziehungsweise innerhalb von $-17\,\% \leq \Delta p_{M2} \leq 21\,\%$ für das grobe Netz vorhersagen. Fluent zeigte eine Druckabweichung innerhalb von $-37\,\% \leq \Delta p_{MA} \leq 7\,\%$ für das feinere Netz und innerhalb von $-25\,\% \leq \Delta p_{MB} \leq 15\,\%$ für das gröbere Netz. Eine Überprüfung der experimentellen Daten zeigte, dass der Druckverlauf von Effekten des Phasenwechsels entlang der freien Oberfläche abhängig war. Flow-3D konnte die experimentellen Ergebnisse bestätigen und zeigte zudem, dass in der Nähe der überhitzen Wand eine Region mit starker Verdampfung existierte. Entlang der restlichen freien Oberfläche dominiert hingegen Kondensation. Fluent bestätigte diese Effekte nicht. In diesen Simulationen war der Druck von thermaler Expansion und Kontraktion bestimmt.

Der statische Randwinkel der freien Oberfläche wurde von der lokalen Wandüberhitzung, also der Differenz zwischen Wand- und Sättigungstemperatur, beeinflusst. Experimentelle Daten zeigten eine Abhängigkeit des statischen Randwinkels von der lokalen Wandüberhitzung in Übereinstimmung mit dem Mikrozonenmodell. Die numerischen Daten wichen von den experimentellen Ergebnissen ab, in dem sie die theoretischen Werte aus dem Mikrozonenmodell unterschätzten.

Preamble

The presented work evolved from my employment as a research associate in the Multiphase Flow Group at the Center of Applied Space Technology and Microgravity (ZARM) at the University of Bremen from 2012 to 2015. This was made possible by my supervisor Prof. Dr.-Ing. habil. Michael E. Dreyer. First of all, I would like to thank you for the guidance, fruitful discussions and, of course, your time. Secondly, my gratitude goes to Prof. Dr.-Ing. E. Hopfinger from LEGI at the Université Joseph Fourier in Grenoble for being the second reviewer for this thesis.

This work was funded by Airbus DS and the German Federal Ministry for Economic Affairs and Energy (BMWi) through the German Aerospace Center (DLR) with grand number 50 RL 1120. Hereby, I thank all people involved in this project. Special thanks go to Dr.-Ing. Philipp Behruzi and Dr.-Ing Martin Konopka from Astrium DS for the support and exchange of thoughts throughout our quarterly discussions and also the opportunity to spend three month on the Airbus' premises.

Furthermore, I thank my colleagues at ZARM for their support and great work ethic. The biggest gratitude goes to Peter Prengel and Frank Ciecior for the construction, instrumentation and operation of the LH2 drop tower experiment. Without their technical experience, ambitious work, comments and suggestions there would be no cryogenic experiment. Special thanks to André Pingel and Peter Friese for proof reading paper manuscripts and drafts of this thesis. I know how tedious it can be and greatly appreciate your help. Many thanks also to my (former) colleagues and friends Max Bronowicki, Peter Canfield, Holger Faust, Edith Frank, Diana Gaulke, Ertan Göklü, Rodion Groll, Yulia Grebenyuk, Ronald Mairose, Zelimir Marojevic, Yvonne Chen, Nikolai Kulev, Eckart Fuhrmann, Kai Burow, Helmut Behrens and Yongkang Chen for the good time I had at and after work. Stephanie Dackow, you deserve special thanks for taking care of all the non-science related support. You keep this whole operation up and running. All of you made my time at ZARM a wonderful and unforgettable experience. My student assistants Christian Etmann and Simon Schmidt were a great support. I appreciate your contribution. I also want to note and thank the IT department and especially Oliver Daroszewski for fixing any hard- or software issues and Uta Salle, Andrea Fischer and Sabine Vogelsang for administration.

Last but not least, my gratitude goes to my family who was patient enough to supported me throughout my high school years and gave me the independence to find my way at university. Without your back up I would not have come this far. The last and most important person I want to thank is my partner Elisabeth. You were my closest person through this time (and still are). Thank you for your support, time and understanding when I was over excited or grumpy. You had to experience first hand the emotional roller coaster ride such a project is. There is no other person than you I rather would have shared these once in a lifetime moments. Be prepared for further endeavors.

Sebastian Schmitt Berlin, February 2016

Contents

List of Symbols

Scalars are written in the regular form, such as Q. If not stated otherwise, the extensive form is in capital letters and the intensive form in lower case letters. Exceptions are made for the temperature T and the pressure p. Flows, like the mass flow $\dot{m}$, can be identified by a dot above the variable and fluxes with a hat, such as $\widehat{m}$. A vector is indicated by a bold symbol, thus $\boldsymbol{v}$, whereas a tensor can be identified by a bold symbol with one arrow, e.g. $\vec{\boldsymbol{\tau}}$.

Roman Letters

A	area	m^2
a	thermal diffusivity	$m^2\ s^{-1}$
a	acceleration	$m\ s^{-2}$
C	constant for envelope of the center point oscillation	m
C	constant for polynomial function	various
C	exponential factor for cell growth	–
c	specific heat capacity	$J\ kg^{-1}\ K^{-1}$, $J\ m^{-3}\ K^{-1}$
$\widetilde{c}$	Flow-3D: accommodation coefficient	–
D	outer diameter	m
D	damping ratio	–
d	inner diameter	m
E	energy	J
e	specific energy	$J\ kg^{-1}$
F	force	N
F	volume fraction for VOF model	–
f	face	–
f	frequency	s^{-1}
$\overline{f}$	Fluent: phase change frequency	s^{-1}
g	gravitational acceleration	$m\ s^{-2}$
H	height	m
h	height	m
h	specific enthalpy	$J\ kg^{-1}$, $J\ mol^{-1}$

Δh	specific heat of evaporation	J kg^{-1}, J mol^{-1}
$\vec{\boldsymbol{I}}$	unity tensor	–
$\vec{\boldsymbol{J}}$	Fluent: coefficient matrix for gradient computation	various
k	slope of a the endoscope's optical path	–
k	surface curvature	m^{-2}
L	(characteristic) length	m
l	area density	m^{-1}
M	molecular weight	kg mol^{-1}
m	counter	–
m	mass	kg
$\dot{m}$	mass flow rate	kg s^{-1}
$\widehat{m}$	mass flux	kg m^{-2} s^{-1}
$\overline{m}$	mass source	kg m^{-3} s^{-1}
N	number of cells	–
$\boldsymbol{N}$	dimensionless normal to interface	–
n	counter	–
n	refractive index	–
n	normal to interface	m
O	relative location of the endoscope	m
O	origin of the principal radius	m
P	power	W
p	pressure	Pa
Q	heat	J
$\dot{Q}$	heat flow	J s^{-1}
$\widehat{q}$	heat flux	J m^{-2} s^{-1}
R	radius	m
$\overline{R}$	universal gas constant	J mol^{-1} K^{-1}
$\Re$	specific gas constant	J kg^{-1} K^{-1}, J mol^{-1} K^{-1}
r	radial direction	m
S	volumetric source term	various
s	direction along the surface	m
T	periodical time	s
T	temperature	K
T_{vexp}	Flow-3D temperature coefficient to calculate T_{sat}	K^{-1}
t	tangential direction on interface	m
t	time	s
u	specific internal energy	J kg^{-1}, J m^{-3}

V	volume	m^3
$\dot{V}$	volume flow rate	$\mathrm{m}^3\ \mathrm{s}^{-1}$
$\boldsymbol{v}$	velocity	$\mathrm{m\ s}^{-1}$
$\overline{v}$	specific volume	$\mathrm{m}^3\ \mathrm{kg}^{-1}$
W	work	J
X	point on the free surface	m
x	x-direction	m
Y	Fluent: Right hand side of time advection equation	various
y	y-direction	m
z	z-direction	m, pixel

Greek Letters

α	heat transfer coefficient	$\mathrm{W\ m}^{-2}\ \mathrm{K}^{-1}$
Γ	diffusion coefficient	various
γ	contact angle	$^\circ$
Δ	difference	–
δ	damping coefficient	s^{-1}
ϵ	emissivity	–
Θ	temperature difference	K
θ	circumferential direction	$^\circ$
κ	heat capacity ratio	–
Λ	logarithmic decrement	–
λ	thermal conductivity	$\mathrm{W\ m}^{-1}\ \mathrm{K}^{-1}$
λ	wave length	m
μ	dynamic viscosity	Pa s
ν	kinematic viscosity	$\mathrm{m}^2\ \mathrm{s}^{-1}$
ρ	density	$\mathrm{kg\ m}^{-3}$
σ	surface tension	$\mathrm{N\ m}^{-1}$
σ_T	temperature coefficient for surface tension	$\mathrm{N\ m}^{-1}\ \mathrm{K}^{-1}$
$\overline{\sigma}$	Stefan-Boltzmann constant	$\mathrm{W\ m}^{-2}\ \mathrm{K}^{-4}$
$\tilde{\sigma}$	accommodation coefficient in the Hertz-Knudsen model	–
τ	stress	Pa
Φ	viscous dissipation function	$\mathrm{kg\ m}^{-1}\ \mathrm{s}^{-3}$
ϕ	arbitrary variable	various
ϕ	angle	$^\circ$
ω	circular frequency	s^{-1}

Subscripts

∞	far field
0	initial
1	final
1	first axis of the free surface
2	second axis of the free surface
$2/3R$	isothermal final wall point height
$A5$	experiment A5
a	ambient
$B6$	experiment B6
BH	bottom heater
b	back
bl	boundary layer
bs	borosilicate
bu	bubble
CV	control volume
CS	control surface
c	center
c	condensation
E	experiment
EC	experiment cylinder
e	evaporation
F	Flow-3D: open to fluid flow
FH	flange heater
f	front
f	face
GH	glass heater
g	bottom of glass cylinder
he	helium
i	Flow-3D: cell counter in r-direction
if	interface
ig	ideal gas
k	Flow-3D: cell counter in z-direction
Lc	capillary length
$M1$, $M2$	Flow-3D: used grids for SOURCE-II simulations

$M1 - M3$	Fluent: used grids for LH2 simulations
MA, MB	Fluent: used grids for SOURCE-II simulations
m	mean
max	maximum
min	minimum
n	normal
nb	neighboring cell
p	constant pressure
ph	parahydrogen
pu	scaling based on pressure, convection and acceleration forces
r	radial component
r	rupture point
ref	reference
rel	relative
res	resulting
S	simulation
s	static
sat	saturation
sub	subcooled
$source$	source
sup	superheated
sys	system
T	theoretical
t	tangential
v	constant volume
$v1 - v4$	sensor position in the vapor
w	wall
wa	wave
wif	sensor position at the wall at the interface
$wl1, wl2$	sensor position at the wall in the liquid phase
$wv1 - wv5$	sensor position at the wall in the vapor phase
x	x-component
y	y-component
z	z-component
$zw1$	final wall point location
θ	circumferential component

Superscripts

$*$	dimensionless
$'$	corrected value
$'$	Flow-3D: value change between two time steps
$''$	Flow-3D: intermediate
T	transposed
f	fluid
l	liquid
s	solid
t	time
Δt	time step
v	vapor

Dimensionless Variables and Numbers

If not stated otherwise, all dimensionless numbers use the material properties of the liquid phase.

Bi	Biot number	$\frac{\alpha L}{\lambda^s}$
Bo	Bond number	$\frac{\rho g L^2}{\sigma}$
Ca	Capillary number	$\frac{\mu v}{\sigma}$
CFL	Courant number	$\frac{v \Delta t}{\Delta x}$
Fo	Fourier number	$\frac{a^s t}{L^2}$
Ma	Mach number	$\frac{v}{(\kappa \Re T)^{1/2}}$
Mo	Morton number	$\left(\frac{g_0 \nu^4 \rho^3}{\sigma^3}\right)^{1/4}$
Oh	Ohnesorge number	$\left(\frac{\rho \nu^2}{\sigma R}\right)^{1/2}$
$\mathrm{Re_M}$	Reynolds-Marangoni number	$\frac{\lvert\sigma_T\rvert \Theta L}{\rho \nu^2}$
We	Weber number	$\frac{\rho L v^2}{\sigma}$
$\mathrm{We_M}$	Weber-Marangoni number	$\frac{\lvert\sigma_T\rvert \Theta}{\sigma}$

Δp^*	pressure rise for drop tower experiments	$\frac{p - p_0}{p_0}$
Δp^*	quality indicator SOURCE-II simulations	$\frac{p_S - p_E}{p_E}$
$\Delta p^*_{M1,M2}$	Flow-3D: quality indicator for SOURCE-II simulations	$\lvert p^*_{M1}\rvert - \lvert p^*_{M2}\rvert$
$\Delta p^*_{MA,MB}$	Fluent: quality indicator for SOURCE-II simulations	$\lvert p^*_{MA}\rvert - \lvert p^*_{MB}\rvert$
$\frac{\Delta T^*}{\Delta z^*}$	wall temperature gradient for LH2 experiment	$\frac{\Delta T}{\Delta z}\frac{R}{T_{sat}}$
t^*	reorientation contact line time	$\frac{t}{t_{pu}}$
t^*_{Lc}	initial contact line time	$\frac{t}{t_{pu,Lc}}$
v^*	reorientation contact line velocity	$\frac{v}{v_{pu}}$
v^*_{Lc}	initial contact line velocity	$\frac{v}{v_{pu,Lc}}$
z^*	surface position	$\frac{z}{R}$
ω^*	center point oscillation frequency	ωt_{pu}

Operators

∇	Nabla operator
∇^2	Laplace operator
$\frac{\partial}{\partial x}$	partial derivative
$\frac{\mathrm{D}}{\mathrm{D}t}$	total derivative

Abbreviations

2D	**2 D**imensional
3D	**3 D**imensional
BC	**B**oundary **C**ondition
CFD	**C**omputational **F**luid **D**ynamics
CMOS	**C**omplementary **M**etal-**O**xide-**S**emiconductors
COMPERE	**Comp**ortement des **E**rgols dans les **Re**servoir
CPU	**C**entral **P**rocessing **U**nit
CS	**C**ontrol **S**urface
CSF	**C**ontinuum **S**urface **F**orce
CV	**C**ontrol **V**olume
DLR	**D**eutsches Zentrum für **L**uft- und **R**aumfahrt[1]
FAVOR	**F**ractional **A**rea/**V**olume **O**bstacle **R**epresentation
GMRES	**G**eneralized **M**inimum **Res**idual
LH2	**L**iquid **H**ydrogen
LOX	**L**iquid **OX**ygen
PRESTO!	**PRE**ssure **ST**aggering **O**ption
SOURCE	**Sou**nding **R**ocket **C**ompere **E**xperiment
SLS	**S**pace **L**aunch **S**ystem
STS	**S**pace **T**ransportation **S**ystem
TOI	**T**ime span **O**f **I**nterest
ULPM	**U**pper **L**iquid **P**ropulsion **M**odule
VOF	**V**olume **O**f **F**luid
ZARM	**Z**entrum für **A**ngewandte **R**aumfahrttechnologie und **M**icrogravitation[2]

---

[1] German Aerospace Center

[2] Center of Applied Space Technology and Microgravity

Chapter 1

Introduction

1.1 Background

Currently, access to space requires a chemical propulsion system, that delivers the necessary thrust. This is realized by either solid or chemical propulsion (or a combination of both). The combination of liquid hydrogen (LH_2) as fuel with liquid oxygen (LOX) as oxidizer provides with 390 s the highest specific impulse[1] which results in a low propellant mass [27]. This combination has a long flight heritage on the first stage of Saturn V, Space Transportation System (STS) Shuttle [70] and Ariane 5, for example. For future concepts, such as the Space Launch System (SLS) [78] and the Ariane 6 Upper Liquid Propulsion Module (shown in Fig. 1.1), this efficient system requires further advancement.

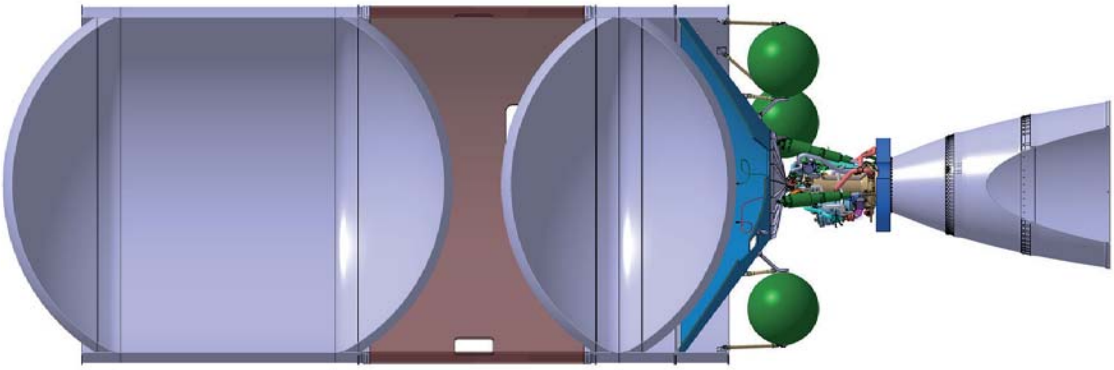

Figure 1.1: Preliminary Airbus DS A6 Upper Liquid Propulsion Module (ULPM), Courtesy of Airbus DS.

Cryogenic fluid management with varying accelerations becomes more important since new launcher concepts require a restartable cryogenic upper stage using liquid hydrogen/oxygen

---

[1] at $p = 7 \times 10^6\,\mathrm{Pa}$

for propulsion. A comprehensive understanding of the complex system of cryogenic fluids with a free surface within a closed tank with superheated walls is crucial to guarantee save operation. The accelerated phase ends with engine cutoff and the partially filled tanks enter the ballistic flight phase. At this instant of time hydrostatic forces caused by the acceleration vanish and the liquid-vapor interface changes from a flat surface to a shape with constant curvature. Throughout the reorientation process the free surface undergoes a damped axial sloshing motion.

Before the second engine burn a coasting phase may exist where the partially filled tank is exposed to weightlessness. Due to external heat loads (radiation, thermal conduction within the rocket structure) a thermal gradient builds up along the tank hull. Heat flux from the wall causes evaporation in the vicinity of the three phase contact line. The subcooled bulk outside the wall region leads to condensation along the free surface. These two mechanisms affect the pressure progression within the closed container. The shape of the free surface and its contact line have a major impact on the systems behavior.

1.2 Motivation

The here presented work addresses two main problems occurring in upper stage spacecraft propellant tanks.

First, the response of cryogenic fluids to a sudden change in gravity causes a reorientation of the liquid-vapor interface, also known as axial sloshing. This motion is influenced by thermal gradients along the tank wall. So far, no detailed study of this free surface motion of cryogenic parahydrogen with isothermal and non-isothermal boundary conditions has been conducted.

Second, phase change over the free surface has a major influence on the pressure progression in a tank, whereas the driving mechanisms strongly depend on the acceleration level. The integral influence of a present heat source in a normal gravity environment has been previously investigated by all means, but little information is available on the single mechanisms especially in weightlessness.

Obtained results from the executed work for this thesis help understanding how the free surface orientation is affected by external heat sources and how these heat fluxes influence phase change effects within the tank. Investigations were performed using numerical and experimental methods to supplement and validate the respective findings.

1.3 Outline

This thesis is divided into nine chapters. Following the background and motivation for this work, given in the introduction (Ch. 1), the theoretical background is introduced in Ch. 2. In this part the equations to solve basic and multiphase flow problems are specified together with the occurring physical phenomena, such as heat transfer and phase change. The used numerical tools are introduced and the characteristics of cryogenic liquids are briefly explained. An overview of the current state of the research regarding the experimental and numerical study of free surface reorientation, phase change effects and partially filled tanks with external heat loads under varying gravity conditions is given in Ch. 3.

In Ch. 4 all necessary equations and their boundary conditions, which are necessary to discuss single species, two phase flow problems with phase change, wall adhesion and conjugated heat transfer, are introduced. The set of equations is given for an infinitesimal small control volume in Cartesian and cylindrical coordinates addressing a compressible and an incompressible phase. The numerical implementation of the previously discussed set of equations within the used flow solvers is explained jointly with the solver theory in Ch. 5.

Chapter 6 describes the drop tower experiments and the setup of the numerical simulations. The experiment investigates a free surface in a party filled right circular cylinder upon a gravity step reduction. Along the tank wall, a well-defined temperature gradient could be imposed to investigate the influence of a superheated wall on the free surface reorientation. Two-dimensional (2D), axisymmetric simulations using the commercial flow solver Fluent v.15.0 were conducted to supplement the experimental findings. The simulations based on the suborbital flight experiment (SOURCE-II on MASER 12) are illustrated in Ch. 7. The purpose of this experiment was to investigate a single-species, two-phase fluid with a free surface and a superheated wall within 360 s of microgravity. This experiment was used to validate the numerical codes Flow-3D v.11.0.2 and Fluent v.15.0. Furthermore, the simulations provide substantial data to understand the driving mechanisms of the system. Main objectives were the pressure progression throughout several filling, pressurization and relaxation phases and the three phase contact line in presence of a superheated wall.

The results from the experiments and simulations introduced in the Chs. 6 and 7 are presented and discussed in Ch. 8. This chapter consists of two parts. First the topics concerning the free surface reorientation are addressed. In the second part the results from the numerical simulations of the SOURCE-II experiment are compared with the experimental data.

The final chapter (Ch. 9) firstly summarizes the results obtained from the experiments and simulations. In a second part, suggestions are made how to improve the experimental and numerical procedures and how to continue with research in this field.

Chapter 2

Theoretical Background

This chapter provides the theoretical background necessary for the understanding of this work. At first, the basic equations are introduced to describe fluid flow. In the following section, these equations are extended such, that they allow to enter a second phase. The third part lists methods of heat transfer in a given phase and between immiscible phases, followed by models to describe mass transfer between two phases of the same species. The last two sections give an overview of cryogenic liquids and how the previously introduced effects can be modeled in a numerical manner. The mathematical model and numerical implementation are of great importance for this work and are therefore discussed in detail in the Chs. 4 and 5.

2.1 Basic Equations

Most flow problems require the analysis of an arbitrary state of variable fluid motion defined by geometry, boundary conditions and the laws of mechanics. A control volume or large scale analysis is an accurate approach but is based on one dimensional properties on the boundaries. It is therefore useful for simple problems, like a straight pipe flow. For general observation of fluid flow, one must rely on differential or small scale analysis [89], which is introduced in Ch. 4. The more complex analysis results in a set of differential equations, which must be solved numerically, as shown in Ch. 5. The development of these equation can be found in numerous text books. This work is mostly based on [11, 28, 55, 89].

2.1.1 Reynolds Transport Theorem

For the analysis of a system, certain laws must be considered. First, there is the conservation of mass m over time t

$$\frac{\mathrm{d}m}{\mathrm{d}t} = 0\,. \tag{2.1}$$

Second, based on Newton's second law, the mass within a system starts to accelerate $\boldsymbol{a}$ if an external force $\boldsymbol{F}$ is acting, thus

$$\boldsymbol{F} = m\boldsymbol{a} = m\frac{\mathrm{d}\boldsymbol{v}}{\mathrm{d}t}\,. \tag{2.2}$$

Third, according to the first law of thermodynamics, any heat Q added to the system or work W done by the system changes the energy E of the system

$$\frac{\mathrm{d}Q}{\mathrm{d}t} - \frac{\mathrm{d}W}{\mathrm{d}t} = \frac{\mathrm{d}E}{\mathrm{d}t}\,. \tag{2.3}$$

Conversion of the basic laws 2.1 to 2.3 from a system analysis to a control volume (CV) analysis can be done with the Reynolds transport theorem, which is in the most general form

$$\frac{\mathrm{d}\phi_{sys}}{\mathrm{d}t} = \underbrace{\frac{\mathrm{d}}{\mathrm{d}t}\left(\int_{CV}\frac{\mathrm{d}\phi}{\mathrm{d}m}\rho\,\mathrm{d}V\right)}_{\text{change within the control volume}} + \underbrace{\int_{CS}\frac{\mathrm{d}\phi}{\mathrm{d}m}\rho\left(\boldsymbol{v}_{rel}\cdot\boldsymbol{n}\right)\mathrm{d}A}_{\text{flux terms}}\,. \tag{2.4}$$

It describes any fluid property (m, $m\boldsymbol{v}$ and E) of the system, represented by ϕ, with the change within the control volume and the flux across the surface. Since the control surface (CS) can move with $\boldsymbol{v}_{CS}$, one must define the relative velocity of the flow with respect to the moving CS, thus $\boldsymbol{v}_{rel} = \boldsymbol{v} - \boldsymbol{v}_{CS}$. The normal vector on the CS is $\boldsymbol{n}$.

2.1.2 Conservation Equations

Using the Reynolds transport theorem on eqs. 2.1 to 2.3 gives the conservation equations to characterize an arbitrary fluid flow problem. Mass conservation can be derived by using eq. 2.1 with eq. 2.4

$$\left(\frac{\mathrm{d}m}{\mathrm{d}t}\right)_{sys} = 0 = \frac{\mathrm{d}}{\mathrm{d}t}\left(\int_{CV}\rho\,\mathrm{d}V\right) + \int_{CS}\rho\left(\boldsymbol{v}_{rel}\cdot\boldsymbol{n}\right)\mathrm{d}A\,, \tag{2.5}$$

which defines the system's mass as the change of density over time within the CV and the mass entering or leaving over the CS. Replacing ϕ with the momentum $m\boldsymbol{v}$ gives the momentum conservation equation

$$\frac{\mathrm{d}}{\mathrm{d}t}\left(m\boldsymbol{v}\right)_{sys} = \sum\boldsymbol{F} = \frac{\mathrm{d}}{\mathrm{d}t}\left(\int_{CV}\boldsymbol{v}\rho\,\mathrm{d}V\right) + \int_{CS}\boldsymbol{v}\rho\left(\boldsymbol{v}_{rel}\cdot\boldsymbol{n}\right)\mathrm{d}A\,, \tag{2.6}$$

where all acting surface and body forces are represented by $\sum\boldsymbol{F}$. The energy conservation equation is derived with eq. 2.3 in eq. 2.4

$$\frac{\mathrm{d}Q}{\mathrm{d}t} - \frac{\mathrm{d}W}{\mathrm{d}t} = \left(\frac{\mathrm{d}E}{\mathrm{d}t}\right)_{sys} = \frac{\mathrm{d}}{\mathrm{d}t}\left(\int_{CV}e\rho\,\mathrm{d}V\right) + \int_{CS}e\rho\left(\boldsymbol{v}_{rel}\cdot\boldsymbol{n}\right)\mathrm{d}A\,, \tag{2.7}$$

with the intensive form of the energy $e = \dfrac{\mathrm{d}E}{\mathrm{d}m}$ which consists of the internal energy u, kinetic energy $\dfrac{1}{2}v^2$ and the potential energy gz

$$e = u + \frac{1}{2}v^2 + gz\,. \tag{2.8}$$

2.2 Multiphase Flow

The introduced equations can be used to analyze a single-phase flow problem. Once a second phase is present, such as liquid and its vapor, further equations are necessary. The conservation equations 2.5 to 2.7 must be solved for both phases. A set of equations must be developed to describe conditions at the newly formed boundary, the liquid-vapor interface. These boundary conditions will be discussed in detail in Sec. 4.5.2. In this work, the liquid-vapor interface or free surface is treated as a sharp interface with a sudden change between one phase to another. Observations of the liquid-vapor interface on a nanoscale level can be found in [15, 56]. The provided description of the free surface in presence or absence of gravity (see Sec. 2.2.3) are only valid for a right circular cylinder with an axisymmetric free surface. Changes of acceleration are considered to be abruptly, so without any transition phase.

2.2.1 Surface Tension

The liquid exposed to a second phase forms a free surface caused by the surface tension σ. Molecules at the surface are attracted to each other by van der Waals forces, so the free surface tends to minimize [15]. To increase the surface area, a certain amount of work is necessary, thus

$$\sigma = \frac{\mathrm{d}W}{\mathrm{d}A} = \frac{F\,\mathrm{d}s}{L\,\mathrm{d}s} = \frac{F}{L}\,. \tag{2.9}$$

The surface tension can also be expressed as the force applied along the free surface $\mathrm{d}s$ to increase the length L of the surface area. Temperature and pressure changes affect the surface tension. Increase in pressure or temperature results in a decreasing surface tension which converges to zero at the critical point [15].

A curved free surface causes a net pressure jump over the interface. Considering a bubble submerged in liquid, the curved interface has to be in equilibrium. The surface tension pulling on the free surface has to be balanced by a pressure difference $p^v - p^l$ between vapor (superscript v) and liquid (superscript l) [21, 56]. To compute the resulting force F_{res} we consider a point X on the free surface with the surface normal $\boldsymbol{n}$, depicted in Fig. 2.1. The normal $\boldsymbol{n}$ can be defined by two perpendicular planes. Both planes define a radius R_1 and R_2 with their origin

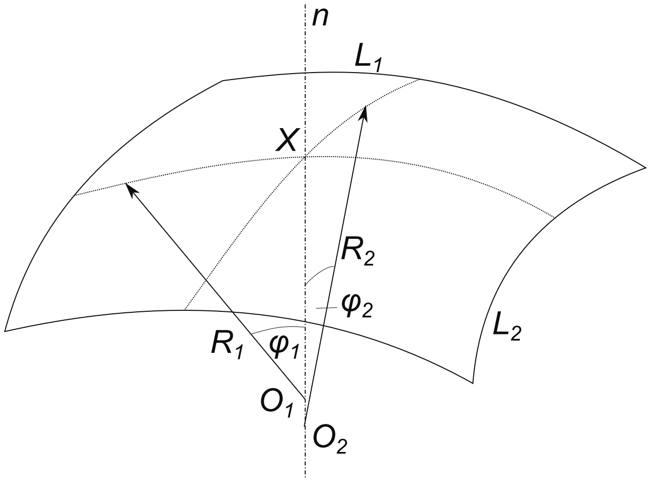

Figure 2.1: Part of a free surface with principal radii R_1 and R_2.

(O_1 and O_2) located along $\boldsymbol{n}$, which describe the curvature of the free surface. R_1 and R_2 are called principle radii. An arbitrary rectangular part of the interface $\mathrm{d}A$ has two sides L_1 and L_2 parallel to the previously defined planes. On both sides of $\mathrm{d}L_1$ tangential forces $F_1 = \sigma\,\mathrm{d}L_2$ are acting and analog for both sides of $F_2 = \sigma\,\mathrm{d}L_1$. Using the angles ϕ_1 and ϕ_2 one can write for the resulting forces normal to the surfaces:

$$F_{res,1} = 2F_1 \sin\phi_1\,, \tag{2.10}$$

$$F_{res,2} = 2F_2 \sin\phi_2\,. \tag{2.11}$$

For small angles, $\phi \ll 1$, one can write $\sin\phi \approx \phi$ and $\frac{1}{2}\,\mathrm{d}L = \phi R$, thus

$$\phi_1 = \frac{\mathrm{d}L_1}{2R_1}, \qquad \phi_2 = \frac{\mathrm{d}L_2}{2R_2}\,, \tag{2.12}$$

with eq. 2.12 in eqs. 2.10 and 2.11 gives

$$F_{res,1} = \sigma\frac{\mathrm{d}L_1\,\mathrm{d}L_2}{R_1}\,, \tag{2.13}$$

$$F_{res,2} = \sigma\frac{\mathrm{d}L_1\,\mathrm{d}L_2}{R_2}\,. \tag{2.14}$$

The resulting force $F_{res} = F_{res,1} + F_{res,2}$ is then

$$F_{res} = \sigma\left(\frac{1}{R_1} + \frac{1}{R_2}\right)\mathrm{d}L_1\,\mathrm{d}L_2\,. \tag{2.15}$$

Divided by the surface $\mathrm{d}A = \mathrm{d}L_1\,\mathrm{d}L_2$ gives the pressure jump

$$\Delta p = \sigma\left(\frac{1}{R_1} + \frac{1}{R_2}\right)\,. \tag{2.16}$$

Equation 2.16 is called the Young-Laplace equation. The higher pressure is always on the concave side of the surface.

2.2.2 Contact Angle

If the free surface is bounded by a third phase, like a wall (or immiscible fluid), a contact line (3D) or point (2D) can be found where the three phases (solid-liquid-vapor) meet. The angle between the solid-liquid interface (wall) and the tangent of the steady free surface at the contact point is called the static contact angle γ_s which evolves from the cohesion and adhesion forces [10]. The surface tensions of the three interfaces (solid-liquid, solid-vapor, liquid-vapor) must be in equilibrium [56],thus

$$\sigma^{s,l} + \sigma^{s,v} + \sigma = 0\,. \tag{2.17}$$

Young [92] performed a force balance tangential to the wall to derive the static contact angle from eq. 2.17.

$$\sigma \cos \gamma_s = \sigma^{s,v} - \sigma^{s,l} \tag{2.18}$$

For $0° < \gamma_s < 90°$ one speaks of wetting liquids and for $\gamma_s \geq 90°$ of non wetting liquids. Perfectly wetting liquids have a static contact angle of $\gamma_s = 0°$. Cryogenic liquids, such as liquid parahydrogen used for this work, have been identified to be perfectly wetting [52, 53, 73, 80, 84]. In general, the contact angle is not constant but changes with the contact line motion. An advancing contact line has a corresponding advancing contact angle and a receding contact angle for a receding contact line. The resulting hysteresis has been closely examined by Joanny and de Gennes [47] and de Gennes [20].

2.2.3 Stable Free Surface Under Varying Gravity Conditions

Concus [18] showed that a stable free surface shape is mainly influenced by gravitational acceleration g and surface tension σ, and is scaled with the Bond number

$$\mathrm{Bo} = \frac{\rho g L^2}{\sigma}\,. \tag{2.19}$$

The Bond number compares the hydrostatic pressure with the capillary pressure. For a cylindrical container with a circular free surface the tank radius R is used for the characteristic length L. For high Bond numbers ($\mathrm{Bo} \gg 1$) gravity is the dominating force which results in a flat surface as shown in Fig. 2.2 a). The free surface meets the wall under a certain static contact angle γ_s depending on the surface energies. At a certain length scale L_c, where $\mathrm{Bo} = 1$, hydrodynamic and capillary pressure are in equilibrium, thus

$$L_c = \left(\frac{\sigma}{\rho g}\right)^{1/2}\,. \tag{2.20}$$

The initial rise at a wall can be calculated with [55] as

$$z_{w,0} = L_c \left[2\left(1 - \sin \gamma_s\right)\right]^{1/2}\,. \tag{2.21}$$

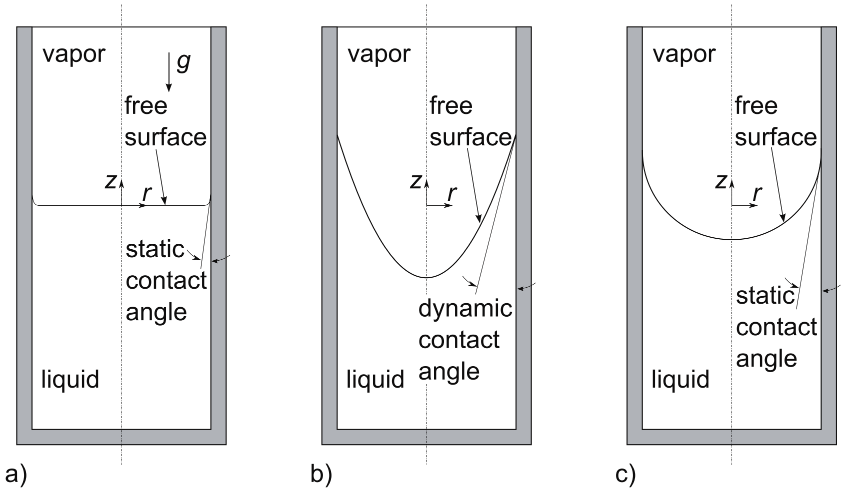

Figure 2.2: Free surface in a right circular cylinder a) in presence of gravity, b) throughout the dynamic reorientation process and c) under microgravity conditions.

Figure 2.2 b) shows the free surface in an unstable configuration throughout the reorientation process between normal gravity and microgravity. The stable free surface configuration in absence of gravity is presented in Fig. 2.2 c). In a microgravity environment low Bond numbers (Bo $\ll 1$) are achieved and the influence of hydrostatic forces can be neglected. A free surface with constant curvature (circular segment) will be formed where the radius of the curvature is only dependent on the static contact angle [18].

2.2.4 Free surface reorientation

As explained in Sec. 2.2.3, the free surface curvature is dependent on hydrostatic and capillary forces. The former vanish in a microgravity environment and the liquid vapor interface reorientates from its flat shape to a configuration with constant curvature. This reorientation process can be divided into two time regimes [22, 65]. The sudden gravity step reduction causes a low pressure within the meniscus in the vicinity of the wall. The characteristic length to determine the characteristic time $t_{pu,Lc}$ and velocity $v_{pu,Lc}$ for this regime is the capillary length L_c from eq. 2.20. Together with the liquid density ρ^l and the surface tension σ one can determine the characteristic time as

$$t_{pu,Lc} = \left(\frac{\rho^l L_c^3}{\sigma}\right)^{1/2} = \left(\frac{\sigma}{\rho^l g_0^3}\right)^{1/4} , \tag{2.22}$$

where g_0 stands for the initial gravity. The characteristic velocity $v_{pu,Lc}$ results to

$$v_{pu,Lc} = \frac{L_c}{t_{pu,Lc}} = \left(\frac{g_0 \sigma}{\rho^l}\right)^{1/4} . \tag{2.23}$$

The first initial rise is followed by a second time regime that characterizes the global reorientation process with the cylinder radius R as the characteristic length. The characteristic time t_{pu} is then

$$t_{pu} = \left(\frac{\rho^l R^3}{\sigma} \right)^{1/2} . \tag{2.24}$$

and the corresponding velocity v_{pu}

$$v_{pu} = \frac{R}{t_{pu}} . \tag{2.25}$$

2.2.5 Damping

Michaelis [65] studied the damping of an axial oscillating (first mode) free surface in a right circular cylinder. Viscous dissipation occurs in the liquid motion but is also induced in the boundary layer along the container bottom and the wall. The moving contact wall induces further dissipative terms [39] which is important in the first time regime. The damping induced by the advancing contact line occurs due to the jump of single molecules at the contact line (Blake mechanism) and due to viscous hydrodynamic losses within the advancing liquid layer (de Gennes mechanism). For the second time regime Michaelis assumed a pinned contact line where only the first two mentioned mechanisms are of importance. The damping ratio induced by the waves (liquid motion) could be estimated as $D_{wa} \propto 2\,\mathrm{Oh}$. With the Ohnesorge number given as

$$\mathrm{Oh} = \left(\frac{\rho \nu^2}{\sigma R} \right)^{1/2} . \tag{2.26}$$

The more complex influence of the boundary layer was estimated with [65] under the assumption that the influence of the container bottom can be neglected

$$D_{bl} \propto \frac{2}{3} \left[\left(\left(\frac{1}{\cos \gamma_s} + \frac{1}{3} \right)^2 - 1 \right)^{1/2} - \tan \gamma_s \right] \mathrm{Oh}^{1/2} . \tag{2.27}$$

The damping coefficient caused by liquid motion D_{wa} and the one caused by the boundary layer D_{bl} can be summed up according to [16, 81], thus

$$D = C_{wa} D_{wa} + C_{bl} D_{bl} . \tag{2.28}$$

For small Ohnesorge numbers ,which is the case for this work, damping of the free surface motion is mostly caused by the influence of the boundary layer, since $D_{wa} \propto$ Oh and $D_{wa} \propto \mathrm{Oh}^{1/2}$.

To avoid any influences from the container bottom, a sufficiently high fill level must be granted. Bauer and Eidel [9] investigated the influence of the bottom for a 90° contact angle. The container bottom has no effect for the first axial sloshing mode, if the ratio of the fill level to the cylinder radius exceeds 0.5.

2.3 Heat Transfer

Until now, only isothermal flows were considered and the temperature T did not play an active role. Introducing the temperature as a variable requires an equation to describe the relationship to the other variables. For compressible fluids the relation of temperature, pressure and density can be described with the ideal gas equation [5]

$$pV = m\Re T\,, \tag{2.29}$$

with $\Re$ as the specific gas constant. Using this assumption, one can calculate the change of the specific internal energy with the specific heat capacity at a constant volume as

$$u = \int_{T_0}^{T_1} c_v \,\mathrm{d}T\,. \tag{2.30}$$

Heat can be transferred by conduction, convection or radiation [5, 6, 11].

2.3.1 Conduction

Heat conduction is the flow of heat $\dot{Q}$ through a solid or fluid continuum. The driving gradient is the temperature gradient ∇T, whereby heat flows from areas of higher temperature to regions with lower temperature. The heat flow is further characterized by the thermal conductivity λ, a material property, which is dependent on temperature and pressure. Fourier's law describes this relation for the heat flux $\widehat{\boldsymbol{q}}$

$$\widehat{\boldsymbol{q}} = -\lambda \nabla T\,. \tag{2.31}$$

2.3.2 Convection

In a moving fluid heat is not only transferred by conduction but also by the macroscopic motion of the fluid. This mechanism, called convective heat transport, includes heat conduction and energy transport by the moving fluid. Newton's law of cooling describes the heat transfer over a solid-fluid interface with the solid temperature at the wall $T^s|_w$ and the far field fluid temperature T^f_∞. Besides the temperature difference the heat transfer coefficient α is required, which is usually unknown.

$$\widehat{q} = \alpha \left(T^s|_w - T^f_\infty\right) \tag{2.32}$$

2.3.3 Radiation

Any entity exchanges energy transmitted by electromagnetic waves to and from its environment. The maximum amount of heat flux is limited by its absolute temperature T, the temperature of the environment T_∞ and the Stefan-Boltzmann constant $\overline{\sigma}$. The surface of the object and its condition can decrease the heat flux. This fact is represented by the emissivity ϵ, which is $\epsilon = 1$ for a black body.

$$\widehat{q} = \epsilon\overline{\sigma}\left(T^4 - T_\infty^4\right) \tag{2.33}$$

2.4 Phase Change

Phase change describes the transition of molecules from one phase to another, like melting/solidification, nucleate boiling and evaporation/condensation at the free surface. For this work only the latter one is of importance and therefore discussed. Basically one can say, that if the temperature of the vapor T^v is below the saturation temperature T_{sat} condensation occurs. If it is above the saturation temperature, liquid at the surface will tend to evaporate. The saturation temperature is connected to the saturation pressure and can be described with the Clausius-Clapeyron equation [5]. Any two points (subscripts 1 and 2) on the saturation curve can be expressed by the latent heat of evaporation Δh and the specific gas constant $\Re$ of the substance with

$$\ln\frac{p_1}{p_2} = \frac{\Delta h}{\Re}\left(\frac{1}{T_2} - \frac{1}{T_1}\right) . \tag{2.34}$$

Phase change along the free surface can either exist within the micro-region, which is close to a solid wall on a micrometer scale [82, 83], or away from any solid [15, 57]. Both regions must be treated differently. The micro-region model describes the evaporation process caused by a heat flow from the hot wall to the liquid. It can be used for an accurate prediction of the contact angle in dependence of a given wall superheat or heat flux.

At a free surface in equilibrium and without radiative heat transport, the phase change can be described by the temperature gradients in the liquid and vapor in the vicinity of the free surface [15] with

$$\lambda^v\left(\frac{\partial T^v}{\partial n}\right)\bigg|_{if} - \lambda^l\left(\frac{\partial T^l}{\partial n}\right)\bigg|_{if} = \rho^l\left(v_n^l - \frac{\mathrm{d}z_{if}}{\mathrm{d}t}\right)\Delta h\,, \tag{2.35}$$

where $\frac{\mathrm{d}z_{if}}{\mathrm{d}t}$ describes the moving free surface in normal direction to compensate the mass flow across the interface. In nature and for numerical computations, the temperature gradients in the vicinity of the free surface can not be resolved properly. The Hertz-Knudsen equation, based on the kinetic theory of gases, is then usually used to calculate the net mass flux $\widehat{m}$

over a free surface with the molar mass M, universal gas constant $\overline{R}$ and the pressure and temperature on both sides of the interface

$$\widehat{m} = \frac{2\widetilde{\sigma}}{2-\widetilde{\sigma}} \left(\frac{M}{2\pi\overline{R}}\right)^{1/2} \left(\frac{p^v}{\sqrt{T^v}} - \frac{p^l}{\sqrt{T^l}}\right) . \tag{2.36}$$

This equation requires an accommodation coefficient $\widetilde{\sigma}$ as a probability factor, which is limited by $\widetilde{\sigma} \leq 1$ [15].

2.5 Numerical Implementation

The previous section gave a short overview of the physical background necessary to solve the flow problems in this work. Besides solving the conservation equations, numerical tools must be capable of modeling two-phase flow problems, conjugated heat transfer with an existing solid structure and liquid-vapor phase change in a closed system. Numerous academic and commercial codes are existent at the present time. The two flow solvers Flow-3D v.11.0.2 by *Flow Science* and Fluent v.15.0 by *Ansys* could fulfill the requirements and were available for the here presented studies.

2.6 Cryogenic Liquids

There is no defined temperature below one can speak of a cryogenic temperature regime. Scott speaks of a cryogenic environment, when the temperature drops below 150 K [76], while Jousten defines the cryogenic regime below 120 K [48]. In general, cryogenic liquids are liquids, that do exist as gases at ambient conditions [76]. Examples are liquid nitrogen, neon, methane, argon, hydrogen, oxygen and helium. Cryogenic hydrogen and oxygen are used widely in rocketry, such as the first stage of Airane 5 or the Space Shuttle, due to its high specific impulse.

Liquid parahydrogen, condensed from hydrogen vapor, was used for the drop tower experiments presented in Ch. 6. For this special case, the change from ortho (parallel) to para (anti-parallel) spin of the hydrogen molecules must be considered [14]. This conversion changes the material properties and releases heat which can be hazardous for the experimental apparatus.

Chapter 3

State of Research

This chapter provides an overview of the current state of research concerning the following fields for storable and cryogenic liquids:

- Free surface reorientation
- Influence of the contact angle on the free surface and influences on the contact angle
- Liquid-vapor phase change effects
- Effects of closed system pressurization

Research in this field started in the 1960s with the investigation of propellant tanks in accelerated and ballistic flight phases [38]. Great effort was taken to understand the surface reorientation and settling upon a gravity step reduction. The focus of current research is to predict the self and active pressurization of cryogenic tanks in microgravity. New techniques allow to simulate the complex coupled system between external heat sources (conduction, radiation), liquid, its vapor and a non condensable gas, if present. As far as applicable, all of these topics were subdivided into theoretical, experimental or numerical based research and distinguished into isothermal or non-isothermal cases.

3.1 Experimental Investigations of the Free Surface

3.1.1 Isothermal Experiments

Drop tower experiments to investigate the liquid-vapor interface behavior in a cylinder and sphere where conducted by Siegert et al. [79]. The experiment time (microgravity) was 2.25 s. Ethyl alcohol, carbon tetrachloride and a water ethyl alcohol mixture were chosen to observe the settling time, thus the time needed by the free surface to form a new stable shape. The experiments showed, that capillary and inertial forces were the driving parameters. The settling time could be scaled with the Weber number

$$\mathrm{We} = \frac{\rho L v^2}{\sigma}\,. \tag{3.1}$$

Examination of the first capillary rise of a free surface in a right cylindrical tank was done by Michaelis et al. [66]. Several silicone oils and two cylinders with differing radii were used. The experimental setup allowed static contact angles between 2° and 60°. A dependency of initial rise on the static contact angle γ_s and the Morton number Mo could be determined. With Mo as

$$\mathrm{Mo} = \left(\frac{g_0 \mu^4}{\rho \sigma^3}\right)^{1/4}\,. \tag{3.2}$$

A comprehensive scale analysis with a number of liquids, varying contact angles and cylinder diameters was performed by Weislogel et al. [87] to show the dependency of the reorientation time on contact angle and viscosity.

3.1.2 Non-Isothermal Experiments

Barsi [7] investigated the self pressurization of liquid HFE-7000 in presence of an external heat load in a normal gravity environment. The pressure rise due to self pressurization increased with the external heat but could be reduced with a higher fill level. For a correct prediction of the pressure history, the tank structure and its thermal inertia has to be considered as well as the stratification within the bulk. Ludwig and Dreyer [59] studied the active pressurization of liquid nitrogen with either its vapor or gaseous helium as non condensable gas. The observed thermal stratification in the liquid was driven by the saturation temperature at the surface. The amount of phase change mass was dependent on the pressurant gas. Throughout the relaxation phase, the pressure drop was caused mostly by the cooling of the vapor phase and not due to condensation. It was determined, that the required pressurant gas mass, to achieve a certain pressure level, was dependent on the gas temperature, phase change and tank aspect ratio. Hopfinger and Das [46] showed that the mass transfer over a free surface is furthermore influenced by capillary waves. They experimentally investigated this phenomena in circular cylinder using HFE-7000 and FC-72 as working fluids. Besides the liquid, only its vapor was present (one-species, two-phase system). The interfacial motion induced by the capillary waves enhanced the temperature gradient in proximity to the liquid-vapor interface and increased the surface area. The resulting mass flux led to a pressure decline. According to this investigation the pressure drop can increase by an order of magnitude. Ludwig et al. [60] used the same experimental setup to investigate the pressure change in a partially filled liquid nitrogen tank subjected to periodic lateral forces. Six different sloshing conditions, ranging from the first asymmetric mode to wave breaking were considered. The integrated temperature sensors allowed to resolve the temperatures in the thermal boundary layer and extend the diffusion coefficient model developed by Das and Hopfinger [19]. New findings were, that the pressure drop can be large but comes to a rapid stop. The reason for that stop is the formation of a mixing layer underneath the free surface. Furthermore, a critical sloshing Reynolds number was identified, below which sloshing does not affect the pressure drop.

The French-German research group COMPERE conducted two sounding rocket experiments, SOURCE and SOURCE-II, to investigate the free surface behavior of the test liquid HFE-7000 in presence of a superheated wall [30, 32, 31]. The first experiment was a two-species, two-phase system with HFE-7000 present in both liquid and gaseous phase and nitrogen as vapor for pressurization purposes. The presence of the non-condensable gas (nitrogen) caused thermocapillary convection, which is driven by a gradient of the surface tension. This increased the heat flow from the superheated wall towards the liquid. The increased contact angle could be scaled by the Weber-Marangoni We_M and Reynolds-Marangoni Re_M number which are

$$\mathrm{We}_M = \frac{|\sigma_T|\Theta}{\sigma}\,, \tag{3.3}$$

$$\mathrm{Re}_M = \frac{|\sigma_T|\Theta L}{\rho^l {\nu^l}^2}\,, \tag{3.4}$$

where Θ and L represent a characteristic temperature difference and a length, respectively. The experimental findings could be confirmed by the research code Navier and the commercial code Flow-3D.

The second sounding rocket experiment SOURCE-II was conducted in a similar manner as the previous one but was defined as a single-species system using only HFE-7000. With a pure HFE-7000 atmosphere Marangoni effects can be ruled out. This study could show, that pressure changes were caused by phase change effects. Condensation along the free surface was higher than evaporation in the vicinity of the superheated wall. Investigations on the apparent contact angle in dependency of the local wall superheat coincide with the prediction by the micro-region model [83].

First microgravity experiments with liquid hydrogen were performed with four Aerobee sounding rocket experiments [50, 61, 69, 72]. The experimental setup included a partially filled sphere equipped with several temperature sensors on its outside. A window allowed optical examination of the free surface. The first two flights investigated the influence of a uniform heat source whereas the third and fourth flight had a non-uniform heat source. Primary objectives were the observation of the free surface in a microgravity environment and to investigate the heat transfer between container wall and fluid. The advancing liquid along the superheated tank wall showed behavior of subcooled nucleate boiling. While the first three experiments had problems with telemetry, data recovery or microgravity quality, the fourth experiment provided 3.5 minutes of microgravity without facing problems. The liquid hydrogen volume at lift-off was 25.1 % of the container volume. The temperature sensors indicated a fully wetted inner wall within weightlessness. Due to the wall superheat, parts of the tank dried out with progression in time. Nucleate boiling and bubble formation could be detected.

First drop tower tests using cryogenic nitrogen and hydrogen were performed by Siegert et al. [80]. Glass spheres and right circular cylinders were used as experiment containers. A perfectly wetting behavior, $\gamma_s = 0°$, of the test fluids could be shown. Liquid hydrogen experiments were only carried out with the sphere. These experiments were conducted to extent the Weber number criterion for cryogenic liquids.

A full size Saturn S-IVB hydrogen tank was instrumented and used as a large scale low gravity experiment within the AS-203 flight to investigate the heat balance, self pressurization, and tank sloshing. This data was used to develop first models on cryogenic tank behavior, summarized by Bradshaw [13].

Clear images of the free surface of cryogenic nitrogen throughout the reorientation process could be achieved by Stief et al. [84]. A perfectly wetting behavior and remaining thin liquid layer could be examined.

First cryogenic drop tower experiments by Stief were continued by Kulev. Investigations of the surface reorientation in right circular cylinders with a well defined wall temperature gradient were performed by Kulev and Dreyer [53] and Kulev et al. [52]. The experimental fluids were argon and methane. A perfectly wetting behavior could be examined for these cryogenics as well. Both fluids responded in a similar manner to the superheated wall. The apparent contact angle and the center point frequency increased with the applied wall superheat. The pressure history corresponded to the contact line motion, which led to the assumption, that the pressure rise was driven by evaporation at the advancing liquid layer. Performed simulations with the research code Navier supported the experimental results.

3.2 Numerical Investigations of the Free Surface

3.2.1 Isothermal Computations

Fisher et al. [25] assessed the commercial flow solver Flow-3D with respect to sloshing motion of a partially filled container entering weightlessness. Flow-3D was capable of reproducing the experimental data gained from drop tower experiments.

Wölk et al. [90] numerically investigated the reorientation of a free surface in a right circular cylinder upon a gravity step reduction. A dynamic contact angle was imposed as a boundary condition for the liquid-vapor interface. The influence on the resonant frequency and the settling time was examined. Numerical results were in good agreement with the experimental data [87].

Gerstmann et al. [37] proposed a slip boundary condition with a model for the dynamic contact angle to numerically compute the surface reorientation. The dynamic contact angle model includes the Capillary number Ca and the contact angle hysteresis. The Capillary number is

$$\mathrm{Ca} = \frac{\mu v}{\sigma} \,. \tag{3.5}$$

The numerical results correspond well with the experiments conducted by Michaelis [66].

3.2.2 Non-Isothermal Computations

Grayson et al. [40] used Flow-3D to model a Saturn S-IVB liquid hydrogen tank. The diameter is about 7.3 m and its height is 12.3 m. It simulates the low gravity, cryogenic self pressurization test conducted in 1966. Using different meshes to rule out the influence of the cell size the pressure rise could be predicted with 4 % and the temperature within 6 % throughout more than 5000 s experimental time.

Barsi and Kassemi [8] used the commercial flow solver Fluent with their customized heat and mass transfer model to predict the self pressurization of a flightweight liquid hydrogen tank. They were able to predict the pressure rise for varying fill levels under normal gravity according to the experimental results. Deviations from the experimental data occurred for the medium fill level due to non-uniform heat distribution over the tank wall.

Simulations based on the SOURCE-II experiment presented in [31] under normal and microgravity conditions were performed by Konopka et al. [51] using the commercial flow solver Flow-3D v.10.1.1. The focus laid on the pressure change due to thermal influences from the experiment wall. They were able to predict the pressure progression with 18 % accuracy for ground experiments and within 30 % for the microgravity experiment. Deficiencies in the phase change modeling were identified as the cause for the discrepancy.

Fu et al. [29] studied the evaporation effects on the tank pressure under microgravity conditions numerically. An interfacial heat and mass transfer model was developed and implemented in Fluent. The proposed model could be validated with the normal gravity experiments by Seo and Sangkwon [77]. No experimental microgravity data was available to compare to the results computed neglecting gravity. The presented numerical results for microgravity conditions must be treated with care due to their computed free surface configuration. The computed free surface shown in Fig. 3, 6 and 7 of [29] depict a non physical behavior of the liquid advancing the wall.

Chapter 4

Mathematical Model

This chapter addresses the required equations to describe two-phase flow problems with conjugated heat transfer to and from a solid and heat and mass transfer over the free surface. The set of equations is stated in a compact form first before it is developed for Cartesian and cylindrical coordinates. All relevant boundary conditions are included in the last section of this chapter.

4.1 Coordinate Systems

To describe the fluid motion one should choose a suitable coordinate system depending on the requirements. In this section the governing equations were developed for a Cartesian (x, y, z) and a cylindrical (r, θ, z) coordinate system. A fixed (Eulerian) reference frame was applied. The following equations were defined to transform the three spatial directions from one coordinate system into the other [11, 63, 64]. Cylindrical to Cartesian coordinates are

$$x = r\cos(\theta)\,, \tag{4.1}$$

$$y = r\sin(\theta)\,, \tag{4.2}$$

$$z = z\,. \tag{4.3}$$

Cartesian to cylindrical coordinates are

$$r = \left(x^2 + y^2\right)^{1/2}\,, \tag{4.4}$$

$$\theta = \arctan\left(\frac{y}{x}\right)\,, \tag{4.5}$$

$$z = z\,. \tag{4.6}$$

Differential operators must be adjusted as well. A comprehensive summary of the differential operators in rectangular and cylindrical coordinates can be found in [11]. For Cartesian coordinates the Nabla operator is

$$\nabla = \left(\frac{\partial}{\partial x} , \frac{\partial}{\partial y} , \frac{\partial}{\partial z} \right)^{\mathsf{T}} . \tag{4.7}$$

Applied on a scalar, like the temperature T, eq. 4.7 reads

$$\nabla T = \left(\frac{\partial T}{\partial x} , \frac{\partial T}{\partial y} , \frac{\partial T}{\partial z} \right)^{\mathsf{T}} , \tag{4.8}$$

and on a vector, e.g. the velocity $\boldsymbol{v}$, it is

$$\nabla \cdot \boldsymbol{v} = \frac{\partial v_x}{\partial x} + \frac{\partial v_y}{\partial y} + \frac{\partial v_z}{\partial z} . \tag{4.9}$$

The Laplace operator ∇^2 follows as

$$\nabla^2 = \frac{\partial^2}{\partial x^2} + \frac{\partial^2}{\partial y^2} + \frac{\partial^2}{\partial z^2} . \tag{4.10}$$

Furthermore, the total differential is defined with

$$\frac{\mathrm{D}}{\mathrm{D}t} = \frac{\partial}{\partial t} + (\boldsymbol{v} \cdot \nabla) = \frac{\partial}{\partial t} + v_x \frac{\partial}{\partial x} + v_y \frac{\partial}{\partial y} + v_z \frac{\partial}{\partial z} , \tag{4.11}$$

which yields with eq. 4.8 for a scalar

$$\frac{\mathrm{D}T}{\mathrm{D}t} = \frac{\partial T}{\partial t} + (\boldsymbol{v} \cdot \nabla T) = \frac{\partial T}{\partial t} + v_x \frac{\partial T}{\partial x} + v_y \frac{\partial T}{\partial y} + v_z \frac{\partial T}{\partial z} , \tag{4.12}$$

and for a vector with eq. 4.9

$$\frac{\mathrm{D}\boldsymbol{v}}{\mathrm{D}t} = \frac{\partial \boldsymbol{v}}{\partial t} + (\boldsymbol{v} \cdot \nabla)\, \boldsymbol{v} = \begin{pmatrix} \dfrac{\partial v_x}{\partial t} & +v_x \dfrac{\partial v_x}{\partial x} & +v_y \dfrac{\partial v_x}{\partial y} & +v_z \dfrac{\partial v_x}{\partial z} \\[2ex] \dfrac{\partial v_y}{\partial t} & +v_x \dfrac{\partial v_y}{\partial x} & +v_y \dfrac{\partial v_y}{\partial y} & +v_z \dfrac{\partial v_y}{\partial z} \\[2ex] \dfrac{\partial v_z}{\partial t} & +v_x \dfrac{\partial v_z}{\partial x} & +v_y \dfrac{\partial v_z}{\partial y} & +v_z \dfrac{\partial v_z}{\partial z} \\ . & & & \end{pmatrix} . \tag{4.13}$$

The differential operators must be altered for cylindrical coordinates using eq. 4.4 to eq. 4.6 [11, 89] which gives for the Nabla operator

$$\nabla = \left(\frac{\partial}{\partial r} , \frac{1}{r} \frac{\partial}{\partial \theta} , \frac{\partial}{\partial z} \right)^{\mathsf{T}} , \tag{4.14}$$

with a scalar, such as T, it reads

$$\nabla = \left(\frac{\partial T}{\partial r} , \frac{1}{r} \frac{\partial T}{\partial \theta} , \frac{\partial T}{\partial z} \right)^{\mathsf{T}} , \tag{4.15}$$

and with a vector, like $\boldsymbol{v}$, it is

$$\nabla \cdot \boldsymbol{v} = \frac{1}{r}\frac{\partial}{\partial r}\left(r v_r\right) + \frac{1}{r}\frac{\partial v_\theta}{\partial \theta} + \frac{\partial v_z}{\partial z} \ . \tag{4.16}$$

The Laplace operator reads

$$\nabla^2 = \frac{1}{r}\frac{\partial}{\partial r}\left(r\frac{\partial}{\partial r}\right) + \frac{1}{r^2}\frac{\partial^2}{\partial \theta^2} + \frac{\partial^2}{\partial z^2} = \frac{1}{r}\frac{\partial}{\partial r} + \frac{\partial^2}{\partial r^2} + \frac{1}{r^2}\frac{\partial^2}{\partial \theta^2} + \frac{\partial^2}{\partial z^2} \ , \tag{4.17}$$

and the total differential follows with [11] for a scalar, such as T, with

$$\frac{\mathrm{D}T}{\mathrm{D}t} = \frac{\partial T}{\partial t} + \left(\boldsymbol{v}\cdot\nabla\right)T = \frac{\partial T}{\partial t} + v_r\frac{\partial T}{\partial r} + \frac{v_\theta}{r}\frac{\partial T}{\partial \theta} + v_z\frac{\partial T}{\partial z} \ , \tag{4.18}$$

and applied on a vector, like $\boldsymbol{v}$, it is

$$\frac{\mathrm{D}\boldsymbol{v}}{\mathrm{D}t} = \frac{\partial \boldsymbol{v}}{\partial t} + \left(\boldsymbol{v}\cdot\nabla\right)\boldsymbol{v} = \begin{pmatrix} \frac{\partial v_r}{\partial t} & +v_r\frac{\partial v_r}{\partial r} & +\frac{v_\theta}{r}\frac{\partial v_r}{\partial \theta} & -\frac{v_\theta^2}{r} & +v_z\frac{\partial v_r}{\partial z} \\ \frac{\partial v_\theta}{\partial t} & +v_r\frac{\partial v_\theta}{\partial r} & +\frac{v_\theta}{r}\frac{\partial v_\theta}{\partial \theta} & +\frac{v_r v_\theta}{r} & +v_z\frac{\partial v_\theta}{\partial z} \\ \frac{\partial v_z}{\partial t} & +v_r\frac{\partial v_z}{\partial r} & +\frac{v_\theta}{r}\frac{\partial v_z}{\partial \theta} & & +v_z\frac{\partial v_z}{\partial z} \end{pmatrix} . \tag{4.19}$$

4.2 Governing Equations

All governing equations are written in vector form to be independent from the used coordinate system. They are present in a general compressible and an incompressible notation. Incompressible fluids are compressible fluids which can be treated as incompressible if $\mathrm{Ma} \leq 0.3$. The spatial distribution is constant but density may change with time (added or removed mass, evaporation or condensation). With the use of eq. 4.7 to eq. 4.17 they can be evolved for the specific coordinate system, as executed in section 4.3 and section 4.4. The following equations are covered widely in literature. If not specified otherwise, all equations are based on [11, 28, 89].

4.2.1 Mass Conservation

If the mass within an infinitesimal small volume is dependent on the fluxes through its faces or density changes, one can write for the compressible mass conservation equation

$$\frac{\partial \rho}{\partial t} + \nabla\cdot\left(\rho\boldsymbol{v}\right) = 0 \, . \tag{4.20}$$

For an incompressible flow $\frac{\mathrm{D}\rho}{\mathrm{D}t} = 0$ which reduces eq. 4.20 to

$$\nabla\cdot\boldsymbol{v} = 0 \, . \tag{4.21}$$

4.2.2 Momentum Conservation

Performing a force balance on an infinitesimal small volume, one can derive the compressible momentum equation

$$\rho \frac{\mathrm{D}\boldsymbol{v}}{\mathrm{D}t} = \rho \boldsymbol{F} - \nabla p - \nabla \cdot \vec{\boldsymbol{\tau}}\,, \tag{4.22}$$

with all body forces included in $\boldsymbol{F}$ and stress tensor components included in the tensor $\vec{\boldsymbol{\tau}} = \tau_{ij}$[1].

In an incompressible flow, simplifications can be applied to eq. 4.22. The density ρ is constant and can be excluded from the derivatives. The normal terms of the stress tensor ($i = j$) simplify as shown in eq. 4.45 to eq. 4.47 (for Cartesian coordinates) and eq. 4.66 to eq. 4.68 (for cylindrical coordinates). Rearranging the remaining components gives the momentum conservation for an incompressible flow with constant viscosity μ as

$$\rho \left[\frac{\partial \boldsymbol{v}}{\partial t} + (\boldsymbol{v} \cdot \nabla)\, \boldsymbol{v} \right] = \boldsymbol{F} - \nabla p + \mu \nabla^2 \cdot \boldsymbol{v}\,. \tag{4.23}$$

4.2.3 Energy Conservation

Energy conservation can be derived from the first law of thermodynamics

$$\dot{Q} - \dot{W} = \frac{\partial}{\partial t} \int_{CV} \left(u + \frac{v^2}{2} + gz \right) \rho \; \mathrm{d}V + \int_{CS} \left(u + \frac{v^2}{2} + gz \right) \rho \, (\boldsymbol{v} \cdot \boldsymbol{n}) \, \mathrm{d}A\,, \tag{4.24}$$

with the heat transfer rate $\dot{Q}$, the rate of work $\dot{W}$, the specific internal energy u, the specific kinetic energy $\frac{v^2}{2}$ and the potential energy gz. Using Fourier's law for the heat conduction per unit area q

$$\widehat{\boldsymbol{q}} = -\lambda \nabla T\,, \tag{4.25}$$

gives for the compressible energy conservation equation

$$\rho \frac{\mathrm{D}u}{\mathrm{D}t} = -\left(\nabla \cdot \widehat{\boldsymbol{q}}\right) - p\,(\nabla \cdot \boldsymbol{v}) - \left[\nabla \cdot (\vec{\boldsymbol{\tau}} \cdot \boldsymbol{v})\right]\,, \tag{4.26}$$

where $\Phi = \left[\nabla \cdot (\vec{\boldsymbol{\tau}} \cdot \boldsymbol{v})\right]$ is the viscous dissipation function which can be found for the Cartesian and cylindrical coordinate system in eq. 4.52 or eq. 4.54 and eq. 4.73 or eq. 4.75, respectively.

Assuming, that the change of specific internal energy is only dependent on the specific heat capacity for constant volume c_v, thus $\mathrm{d}u \approx c_v \; \mathrm{d}T$ and constant values for c_v, μ, λ and ρ, eq 4.26 reduces to the incompressible form

$$\rho \frac{\mathrm{D}u}{\mathrm{D}t} = \lambda \nabla^2 T + \Phi\,. \tag{4.27}$$

---

[1] The first index i states the surface indicated by the direction of its normal vector, while the second index j defines the direction of the stress tensor component.

4.2.4 Relations for Pressure and Internal Energy

There are three differential equations derived to describe mass (eq. 4.20), momentum (eq. 4.22) and energy (eq. 4.26) conservation. Since five independent variables are present, which are $\rho, \boldsymbol{v}, p, u, T$, two more relations are necessary to solve the set of equations. For a compressible fluid these are

$$\rho = \rho\left(p, T\right) \,, \qquad u = u\left(T, p\right) \,. \tag{4.28}$$

Common and for this work used relations are the ideal gas law, which includes the specific gas constant $\Re$

$$p = \rho \Re T \,. \tag{4.29}$$

This equation is not necessary for an incompressible fluid.

The specific internal energy may be considered as a function of the specific volume $\overline{v} = \rho^{-1}$ and the temperature T, so that

$$\mathrm{d}u = \left(\frac{\partial u}{\partial \overline{v}}\right)_T \mathrm{d}\overline{v} + \left(\frac{\partial u}{\partial T}\right)_{\overline{v}} \mathrm{d}T = \left[-p + T\left(\frac{\partial p}{\partial T}\right)_{\overline{v}}\right] \mathrm{d}\overline{v} + c_v\,\mathrm{d}T \,. \tag{4.30}$$

Using eq. 4.30 on eq. 4.26 gives

$$\rho c_v \frac{\mathrm{D}T}{\mathrm{D}t} = -\left(\nabla \cdot \widehat{\boldsymbol{q}}\right) - T\left(\frac{\partial p}{\partial T}\right)_{\overline{v}} \left(\nabla \cdot \boldsymbol{v}\right) - \Phi \,. \tag{4.31}$$

For an ideal gas $\left(\frac{\partial p}{\partial T}\right)_{\overline{v}} = \frac{p}{T}$, which allows to rewrite eq. 4.31 to

$$\rho c_v \frac{\mathrm{D}T}{\mathrm{D}t} = -\left(\nabla \cdot \widehat{\boldsymbol{q}}\right) - p\left(\nabla \cdot \boldsymbol{v}\right) - \Phi \,. \tag{4.32}$$

For fluids with constant density the specific internal energy is expressed with the specific heat constant at constant pressure c_p. Using eq. 4.27 this gives

$$\rho c_p \frac{\mathrm{D}T}{\mathrm{D}t} = \lambda \nabla^2 T + \Phi \,. \tag{4.33}$$

4.3 Cartesian Coordinates

This section lists the derived conservation equations in differential form for Cartesian coordinates using eq. 4.7 to eq 4.11. They are written both in compressible and incompressible form.

4.3.1 Mass Conservation

The continuity equations for a compressible fluid in Cartesian coordinates can be written with eq. 4.7 in eq. 4.20 as

$$\frac{\partial \rho}{\partial t} + \frac{\partial}{\partial x}\left(\rho v_x\right) + \frac{\partial}{\partial y}\left(\rho v_y\right) + \frac{\partial}{\partial z}\left(\rho v_z\right) = 0\,. \tag{4.34}$$

The density is constant for incompressible flow which gives

$$\frac{\partial v_x}{\partial x} + \frac{\partial v_y}{\partial y} + \frac{\partial v_z}{\partial z} = 0\,. \tag{4.35}$$

4.3.2 Momentum Conservation

The compressible momentum equations for the three spatial directions (x, y, z) result from eq 4.22 with eq 4.11 and eq. 4.7

$$\rho\left(\frac{\partial v_x}{\partial t} + v_x\frac{\partial v_x}{\partial x} + v_y\frac{\partial v_x}{\partial y} + v_z\frac{\partial v_x}{\partial z}\right) = F_x - \frac{\partial p}{\partial x} - \frac{\partial \tau_{xx}}{\partial x} - \frac{\partial \tau_{yx}}{\partial y} - \frac{\partial \tau_{zx}}{\partial z}\,, \tag{4.36}$$

$$\rho\left(\frac{\partial v_y}{\partial t} + v_x\frac{\partial v_y}{\partial x} + v_y\frac{\partial v_y}{\partial y} + v_z\frac{\partial v_y}{\partial z}\right) = F_y - \frac{\partial p}{\partial y} - \frac{\partial \tau_{xy}}{\partial x} - \frac{\partial \tau_{yy}}{\partial y} - \frac{\partial \tau_{zy}}{\partial z}\,, \tag{4.37}$$

$$\rho\left(\frac{\partial v_z}{\partial t} + v_x\frac{\partial v_z}{\partial x} + v_y\frac{\partial v_z}{\partial y} + v_z\frac{\partial v_z}{\partial z}\right) = F_z - \frac{\partial p}{\partial z} - \frac{\partial \tau_{xz}}{\partial x} - \frac{\partial \tau_{yz}}{\partial y} - \frac{\partial \tau_{zz}}{\partial z}\,, \tag{4.38}$$

with the components of the stress tensor $\vec{\boldsymbol{\tau}}$

$$\tau_{xx} = -2\mu\frac{\partial v_x}{\partial x} + \frac{2}{3}\mu\left(\frac{\partial v_x}{\partial x} + \frac{\partial v_y}{\partial y} + \frac{\partial v_z}{\partial z}\right)\,, \tag{4.39}$$

$$\tau_{yy} = -2\mu\frac{\partial v_y}{\partial y} + \frac{2}{3}\mu\left(\frac{\partial v_x}{\partial x} + \frac{\partial v_y}{\partial y} + \frac{\partial v_z}{\partial z}\right)\,, \tag{4.40}$$

$$\tau_{zz} = -2\mu\frac{\partial v_z}{\partial z} + \frac{2}{3}\mu\left(\frac{\partial v_x}{\partial x} + \frac{\partial v_y}{\partial y} + \frac{\partial v_z}{\partial z}\right)\,, \tag{4.41}$$

$$\tau_{xy} = \tau_{yx} = -\mu\left(\frac{\partial v_x}{\partial y} + \frac{\partial v_y}{\partial x}\right)\,, \tag{4.42}$$

$$\tau_{yz} = \tau_{zy} = -\mu\left(\frac{\partial v_y}{\partial z} + \frac{\partial v_z}{\partial y}\right)\,, \tag{4.43}$$

$$\tau_{zx} = \tau_{xz} = -\mu\left(\frac{\partial v_z}{\partial x} + \frac{\partial v_x}{\partial z}\right)\,. \tag{4.44}$$

The normal components τ_{xx}, τ_{yy} and τ_{zz} reduce for an incompressible fluid to

$$\tau_{xx} = -2\mu\frac{\partial v_x}{\partial x}\,, \tag{4.45}$$

$$\tau_{yy} = -2\mu\frac{\partial v_y}{\partial y}\,, \tag{4.46}$$

$$\tau_{zz} = -2\mu\frac{\partial v_z}{\partial z}\,. \tag{4.47}$$

Using the stress tensor with the simplified normal components (eq. 4.45 to eq. 4.47) and the assumption that $\mu = \text{const}$ in eq. 4.23 gives the three components for the incompressible form

$$\rho\left(\frac{\partial v_x}{\partial t} + v_x\frac{\partial v_x}{\partial x} + v_y\frac{\partial v_x}{\partial y} + v_z\frac{\partial v_x}{\partial z}\right) = F_x - \frac{\partial p}{\partial x} + \mu\left(\frac{\partial^2 v_x}{\partial x^2} + \frac{\partial^2 v_x}{\partial y^2} + \frac{\partial^2 v_x}{\partial z^2}\right), \tag{4.48}$$

$$\rho\left(\frac{\partial v_y}{\partial t} + v_x\frac{\partial v_y}{\partial x} + v_y\frac{\partial v_y}{\partial y} + v_z\frac{\partial v_y}{\partial z}\right) = F_y - \frac{\partial p}{\partial y} + \mu\left(\frac{\partial^2 v_y}{\partial x^2} + \frac{\partial^2 v_y}{\partial y^2} + \frac{\partial^2 v_y}{\partial z^2}\right), \tag{4.49}$$

$$\rho\left(\frac{\partial v_z}{\partial t} + v_x\frac{\partial v_z}{\partial x} + v_y\frac{\partial v_z}{\partial y} + v_z\frac{\partial v_z}{\partial z}\right) = F_z - \frac{\partial p}{\partial z} + \mu\left(\frac{\partial^2 v_z}{\partial x^2} + \frac{\partial^2 v_z}{\partial y^2} + \frac{\partial^2 v_z}{\partial z^2}\right). \tag{4.50}$$

4.3.3 Energy Conservation

The compressible energy equation can be derived from eq. 4.32 with the Nabla operator and the total differential, thus

$$\begin{aligned}\rho c_v\left(\frac{\partial T}{\partial t} + v_x\frac{\partial T}{\partial x} + v_y\frac{\partial T}{\partial y} + v_z\frac{\partial T}{\partial z}\right) = \\ -\frac{\partial}{\partial x}\lambda\left(\frac{\partial T}{\partial x}\right) - \frac{\partial}{\partial y}\lambda\left(\frac{\partial T}{\partial y}\right) - \frac{\partial}{\partial z}\lambda\left(\frac{\partial T}{\partial z}\right) - p\left(\frac{\partial v_x}{\partial x} + \frac{\partial v_y}{\partial y} + \frac{\partial v_z}{\partial z}\right) - \Phi\,.\end{aligned} \tag{4.51}$$

The viscous-dissipation function Φ for the compressible fluid is

$$\begin{aligned}\Phi =& \mu\left[2\left(\frac{\partial v_x}{\partial x}\right)^2 + 2\left(\frac{\partial v_y}{\partial y}\right)^2 + 2\left(\frac{\partial v_z}{\partial z}\right)^2\right.\\ &+\left(\frac{\partial v_x}{\partial y} + \frac{\partial v_y}{\partial x}\right)^2 + \left(\frac{\partial v_y}{\partial z} + \frac{\partial v_z}{\partial y}\right)^2 + \left(\frac{\partial v_z}{\partial x} + \frac{\partial v_x}{\partial z}\right)^2\\ &\left.-\frac{2}{3}\left(\frac{\partial v_x}{\partial x} + \frac{\partial v_y}{\partial y} + \frac{\partial v_z}{\partial z}\right)^2\right].\end{aligned} \tag{4.52}$$

For incompressible flow and the assumptions made for eq. 4.33, one can write

$$\rho c_p\left(\frac{\partial T}{\partial t} + v_x\frac{\partial T}{\partial x} + v_y\frac{\partial T}{\partial y} + v_z\frac{\partial T}{\partial z}\right) = \lambda\left(\frac{\partial^2 T}{\partial x^2} + \frac{\partial^2 T}{\partial y^2} + \frac{\partial^2 T}{\partial z^2}\right) + \Phi\,. \tag{4.53}$$

For the incompressible flow the last term of eq. 4.52, which is $\frac{2}{3}(\nabla\cdot\boldsymbol{v})$, vanishes and gives

$$\begin{aligned}\Phi =& \mu\left[2\left(\frac{\partial v_x}{\partial x}\right)^2 + 2\left(\frac{\partial v_y}{\partial y}\right)^2 + 2\left(\frac{\partial v_z}{\partial z}\right)^2\right.\\ &\left.+\left(\frac{\partial v_x}{\partial y} + \frac{\partial v_y}{\partial x}\right)^2 + \left(\frac{\partial v_y}{\partial z} + \frac{\partial v_z}{\partial y}\right)^2 + \left(\frac{\partial v_z}{\partial x} + \frac{\partial v_x}{\partial z}\right)^2\right].\end{aligned} \tag{4.54}$$

4.4 Cylindrical Coordinates

This section lists the derived continuity equations in differential form for cylindrical coordinates using eq. 4.16 to eq. 4.19. They are written both in compressible and incompressible form. The formulation for incompressible flow was taken from Appendix D of [89].

4.4.1 Mass Conservation

To derive the mass conservation equation in cylindrical form for compressible fluids one can use eq. 4.14 in eq. 4.20

$$\frac{\partial\rho}{\partial t}+\frac{1}{r}\frac{\partial}{\partial r}\left(\rho r v_r\right)+\frac{1}{r}\frac{\partial}{\partial\theta}\left(\rho v_\theta\right)+\frac{\partial}{\partial z}\left(\rho v_z\right)=0\,. \tag{4.55}$$

With constant density eq. 4.55 reduces to:

$$\frac{1}{r}\frac{\partial}{\partial r}\left(r v_r\right)+\frac{1}{r}\frac{\partial v_\theta}{\partial\theta}+\frac{\partial v_z}{\partial z}=0\,. \tag{4.56}$$

4.4.2 Momentum Conservation

The compressible momentum equations for the three spatial directions $(r,\ \theta,\ z)$ result from eq 4.22 with eq. 4.16 and eq. 4.19

$$\begin{aligned}\rho\left[\frac{\partial v_r}{\partial t}+v_r\frac{\partial v_r}{\partial r}+\frac{v_\theta}{r}\frac{\partial v_r}{\partial\theta}-\frac{v_\theta^2}{r}+v_z\frac{\partial v_r}{\partial z}\right]&=F_r-\frac{\partial p}{\partial r}\\&\quad-\frac{1}{r}\frac{\partial}{\partial r}\left(r\tau_{rr}\right)-\frac{1}{r}\frac{\partial\tau_{r\theta}}{\partial\theta}+\frac{\tau_{\theta\theta}}{r}-\frac{\partial\tau_{zr}}{\partial z}\,,\end{aligned} \tag{4.57}$$

$$\begin{aligned}\rho\left[\frac{\partial v_\theta}{\partial t}+v_r\frac{\partial v_\theta}{\partial r}+\frac{v_\theta}{r}\frac{\partial v_\theta}{\partial\theta}+\frac{v_r v_\theta}{r}+v_z\frac{\partial v_\theta}{\partial z}\right]&=F_\theta-\frac{1}{r}\frac{\partial p}{\partial\theta}\\&\quad-\frac{1}{r^2}\frac{\partial}{\partial r}\left(r^2\tau_{r\theta}\right)-\frac{1}{r}\frac{\partial\tau_{\theta\theta}}{\partial\theta}-\frac{\partial\tau_{\theta z}}{\partial z}\,,\end{aligned} \tag{4.58}$$

$$\begin{aligned}\rho\left[\frac{\partial v_z}{\partial t}+v_r\frac{\partial v_z}{\partial r}+\frac{v_\theta}{r}\frac{\partial v_z}{\partial\theta}+v_z\frac{\partial v_z}{\partial z}\right]&=F_z-\frac{\partial p}{\partial z}\\&\quad-\frac{1}{r}\frac{\partial}{\partial r}\left(r\tau_{rz}\right)-\frac{1}{r}\frac{\partial\tau_{\theta z}}{\partial\theta}-\frac{\partial\tau_{zz}}{\partial z}\,,\end{aligned} \tag{4.59}$$

with the components for the stress tensor $\vec{\boldsymbol{\tau}}$

$$\tau_{rr} = -\mu \left[2\frac{\partial v_r}{\partial r} - \frac{2}{3}\left(\frac{1}{r}\frac{\partial}{\partial r}(r v_r) + \frac{1}{r}\frac{\partial v_\theta}{\partial \theta} + \frac{\partial v_z}{\partial z} \right) \right] , \tag{4.60}$$

$$\tau_{\theta\theta} = -\mu \left[2\left(\frac{1}{r}\frac{\partial v_\theta}{\partial \theta} + \frac{v_r}{r} \right) + \frac{2}{3}\left(\frac{1}{r}\frac{\partial}{\partial r}(r v_r) + \frac{1}{r}\frac{\partial v_\theta}{\partial \theta} + \frac{\partial v_z}{\partial z} \right) \right] , \tag{4.61}$$

$$\tau_{zz} = -\mu \left[2\frac{\partial v_z}{\partial z} - \frac{2}{3}\left(\frac{1}{r}\frac{\partial}{\partial r}(r v_r) + \frac{1}{r}\frac{\partial v_\theta}{\partial \theta} + \frac{\partial v_z}{\partial z} \right) \right] , \tag{4.62}$$

$$\tau_{r\theta} = \tau_{\theta r} = -\mu \left[r\frac{\partial}{\partial r}\left(\frac{v_\theta}{r} \right) + \frac{1}{r}\frac{\partial v_r}{\partial \theta} \right] , \tag{4.63}$$

$$\tau_{\theta z} = \tau_{z\theta} = -\mu \left[\frac{\partial v_\theta}{\partial z} + \frac{1}{r}\frac{\partial v_z}{\partial \theta} \right] , \tag{4.64}$$

$$\tau_{zr} = \tau_{rz} = -\mu \left[\frac{\partial v_z}{\partial r} + \frac{\partial v_r}{\partial z} \right] . \tag{4.65}$$

The normal components of the stress tensor simplify for incompressible flows to

$$\tau_{rr} = -2\mu\frac{\partial v_r}{\partial r} , \tag{4.66}$$

$$\tau_{\theta\theta} = -2\mu\left(\frac{1}{r}\frac{\partial v_\theta}{\partial \theta} + \frac{v_r}{r} \right) , \tag{4.67}$$

$$\tau_{zz} = -2\mu\frac{\partial v_z}{\partial z} . \tag{4.68}$$

The simplified stress tensor can be used with eq. 4.57 to eq. 4.59 to calculate the components for the incompressible momentum conservation equation

$$\begin{aligned} \rho\left(\frac{\partial v_r}{\partial t} + v_r\frac{\partial v_r}{\partial r} + \frac{v_\theta}{r}\frac{\partial v_r}{\partial \theta} - \frac{v_\theta^2}{r} + v_z\frac{\partial v_r}{\partial z} \right) &= \\ F_r - \frac{\partial p}{\partial r} + \mu\left[\frac{\partial}{\partial r}\left(\frac{1}{r}\frac{\partial}{\partial r}(r v_r) \right) + \frac{1}{r^2}\frac{\partial^2 v_r}{\partial \theta^2} - \frac{2}{r^2}\frac{\partial v_\theta}{\partial \theta} + \frac{\partial^2 v_r}{\partial z^2} \right] &, \end{aligned} \tag{4.69}$$

$$\begin{aligned} \rho\left(\frac{\partial v_\theta}{\partial t} + v_r\frac{\partial v_\theta}{\partial r} + \frac{v_\theta}{r}\frac{\partial v_\theta}{\partial \theta} + \frac{v_r v_\theta}{r} + v_z\frac{\partial v_\theta}{\partial z} \right) &= \\ F_\theta - \frac{1}{r}\frac{\partial p}{\partial \theta} + \mu\left[\frac{\partial}{\partial r}\left(\frac{1}{r}\frac{\partial}{\partial r}(r v_\theta) \right) + \frac{1}{r^2}\frac{\partial^2 v_\theta}{\partial \theta^2} + \frac{2}{r^2}\frac{\partial v_r}{\partial \theta} + \frac{\partial^2 v_\theta}{\partial z^2} \right] &, \end{aligned} \tag{4.70}$$

$$\begin{aligned} \rho\left(\frac{\partial v_z}{\partial t} + v_r\frac{\partial v_z}{\partial r} + \frac{v_\theta}{r}\frac{\partial v_z}{\partial \theta} + v_z\frac{\partial v_z}{\partial z} \right) &= \\ F_z - \frac{\partial p}{\partial z} + \mu\left[\frac{1}{r}\frac{\partial}{\partial r}\left(r\frac{\partial v_z}{\partial r} \right) + \frac{1}{r^2}\frac{\partial^2 v_z}{\partial \theta^2} + \frac{\partial^2 v_z}{\partial z^2} \right] &. \end{aligned} \tag{4.71}$$

4.4.3 Energy Conservation

The compressible energy equation can be derived from eq. 4.32 with the Nabla operator and the total differential

$$
\begin{aligned}
\rho c_v \left[\frac{\partial T}{\partial t} + v_r \frac{\partial T}{\partial r} + \frac{v_\theta}{r}\frac{\partial T}{\partial \theta} + v_z \frac{\partial T}{\partial z}\right] + p\left[\frac{1}{r}\frac{\partial}{\partial r}(r v_r) + \frac{1}{r}\frac{\partial v_\theta}{\partial \theta} + \frac{\partial v_z}{\partial z}\right] = \\
\frac{1}{r}\frac{\partial}{\partial r}\left(\lambda \frac{\partial}{\partial r}(rT)\right) + \frac{1}{r}\frac{\partial}{\partial \theta}\left(\lambda \frac{1}{r}\frac{\partial T}{\partial \theta}\right) + \frac{\partial}{\partial z}\left(\lambda \frac{\partial T}{\partial z}\right) + \Phi\,, \qquad (4.72)
\end{aligned}
$$

the viscous-dissipation function for compressible flow in cylindrical coordinates is

$$
\begin{aligned}
\Phi =& \mu \left[2\left(\frac{\partial v_r}{\partial r}\right)^2 + 2\left(\frac{1}{r}\frac{\partial v_\theta}{\partial \theta} + \frac{v_r}{r}\right)^2 + 2\left(\frac{\partial v_z}{\partial z}\right)^2 \right. \\
& + \left[r\frac{\partial}{\partial r}\left(\frac{v_\theta}{r}\right) + \frac{1}{r}\frac{\partial v_r}{\partial \theta}\right]^2 + \left[\frac{1}{r}\frac{\partial v_z}{\partial \theta} + \frac{\partial v_\theta}{\partial z}\right]^2 + \left[\frac{\partial v_r}{\partial z} + \frac{\partial v_z}{\partial r}\right]^2 \\
& \left. - \frac{2}{3}\left(\frac{1}{r}\frac{\partial}{\partial r}(r v_r) + \frac{1}{r}\frac{\partial v_\theta}{\partial \theta} + \frac{\partial v_z}{\partial z}\right)^2 \right]. \qquad (4.73)
\end{aligned}
$$

The incompressible form for the energy equation follows from eqs. 4.33 with the assumption of constant λ, thus

$$
\rho c_p \left(\frac{\partial T}{\partial t} + v_r \frac{\partial T}{\partial r} + \frac{v_\theta}{r}\frac{\partial T}{\partial \theta} + v_z \frac{\partial T}{\partial z}\right) = \lambda \left[\frac{1}{r}\frac{\partial T}{\partial r} + \frac{\partial^2 T}{\partial r^2} + \frac{1}{r^2}\frac{\partial^2 T}{\partial \theta^2} + \frac{\partial^2 T}{\partial z^2}\right] + \Phi\,, \qquad (4.74)
$$

with the corresponding viscous-dissipation form

$$
\begin{aligned}
\Phi =& \mu \left[2\left(\frac{\partial v_r}{\partial r}\right)^2 + 2\left(\frac{1}{r}\frac{\partial v_\theta}{\partial \theta} + \frac{v_r}{r}\right)^2 + 2\left(\frac{\partial v_z}{\partial z}\right)^2 \right. \\
& \left. + \left[r\frac{\partial}{\partial r}\left(\frac{v_\theta}{r}\right) + \frac{1}{r}\frac{\partial v_r}{\partial \theta}\right]^2 + \left[\frac{1}{r}\frac{\partial v_z}{\partial \theta} + \frac{\partial v_\theta}{\partial z}\right]^2 + \left[\frac{\partial v_r}{\partial z} + \frac{\partial v_z}{\partial r}\right]^2 \right]. \qquad (4.75)
\end{aligned}
$$

4.5 Boundary Conditions

To solve the governing equations (eqs. 4.20, 4.22, 4.26, 4.29,and 4.30) proper boundary conditions (BC) must be applied and an initial field for ρ, $\boldsymbol{v}$, p, u and T is required. Appropriate boundary conditions must be defined for all faces (3D) or edges (2D) of the computational domain and on solid-fluid interfaces. If two phases are present, boundary conditions must also be set for the liquid-vapor interface (free surface). The following sections describe the boundary conditions in a generic way. Mathematical modeling of boundary conditions for various kinds of flow are also discussed widely in literature, such as [15, 24, 89]. Descriptions of the boundary conditions as they were applied for this work can be found in [26, 3].

Two different types of boundary conditions are common (see Ch. 3 [24]). If the variable value is given, one speaks of a Dirichlet condition. Where, the boundary condition involves derivatives of the specified value it is defined as a Neumann condition.

4.5.1 Fluid-Solid Interface

The fluid velocity at the wall is usually zero with respect to the wall. This no-slip condition is defined as

$$\boldsymbol{v}^f\Big|_w = \boldsymbol{v}_w \,. \tag{4.76}$$

The temperature condition can either be defined as a Dirichlet condition with the same temperatures, thus

$$T^f\Big|_w = T_w \,, \tag{4.77}$$

or the heat flux $\widehat{q}$ over the interface is specified as a Neumann condition with

$$\widehat{q}^l\Big|_w = -\lambda^l \frac{\partial T^l}{\partial \boldsymbol{n}_w}\bigg|_w \cdot \boldsymbol{N}_w = \widehat{q}^s\big|_w = -\lambda^s \frac{\partial T^s}{\partial \boldsymbol{n}_w}\bigg|_w \cdot \boldsymbol{N}_w \,. \tag{4.78}$$

The flux within the liquid at the tank wall is described with $\widehat{q}^l\big|_w$ and vice versa $\widehat{q}^s\big|_w$. For unit conformity a vector normal to the interface with one unit length $\boldsymbol{N}$ is introduced. The corresponding surface normal is

$$\boldsymbol{N} = \frac{\boldsymbol{n}}{|\boldsymbol{n}|} \,. \tag{4.79}$$

Numerical calculations usually do not allow to resolve the gradient at the wall with enough detail. Therefore, a heat transfer coefficient $\alpha^{f,s}$ is necessary to compute the heat flux from the mean fluid temperature T^f_m and the wall temperature

$$\widehat{q}^{f,s} = \alpha^{f,s}\left(T^s - T^f_m\right) \,. \tag{4.80}$$

This expression is also known as Newtons's law of cooling (see Ch. 9 of [11]).

4.5.2 Liquid-Vapor Interface

The boundary conditions for the liquid-vapor interface (free surface) are well described in [15]. For the following equations vectors may contain components normal and tangential (two tangential directions) to the surface and are indicated by the subscripts n and t_1 or t_2, respectively. The normal direction is connected with the variable n and the tangential directions with the variable t_1 or t_2.

Mass conservation at the free surface is given by the fact, that any liquid mass which flows towards the free surface with v_n^l must be compensated by gaseous mass which exits the free surface region with v_n^v. Furthermore, any movement of the free surface normal to the interface $\frac{\partial z_{if,n}}{\partial t}$ must be considered. The resulting mass conservation is then:

$$\rho^l \left(v_n^l - \frac{\partial z_{if,n}}{\partial t} \right) = \rho^v \left(v_n^v - \frac{\partial z_{if,n}}{\partial t} \right) . \tag{4.81}$$

Momentum conservation must be considered normal and tangential to the free surface. With pressure, surface tension forces and the normal components of the stress tensor [55], the force and momentum balance normal to the surface is

$$p^l - p^v = \sigma \left(\frac{1}{R_1} + \frac{1}{R_2} \right) + \rho^v \left(v_n^v - \frac{\partial z_{if,n}}{\partial t} \right) v_n^v - \rho^l \left(v_n^l - \frac{\partial z_{if,n}}{\partial t} \right) v_n^l + \left(\vec{\boldsymbol{\tau}}^{\,l} - \vec{\boldsymbol{\tau}}^{\,v} \right) \cdot \boldsymbol{n} \cdot \boldsymbol{n} \, , \tag{4.82}$$

with R_1 and R_2 as the principal radii of the curvature of the free surface. The sign convention imposes that they are positive if measured on the liquid side of the surface. The surface curvature itself may be influenced by the three phase (liquid-vapor-solid) contact line. The contact angle γ is the angle between the free surface and the liquid-solid interface at the contact line. This angle is a result of the minimization of the three surface energies (liquid-vapor, liquid-solid, solid-vapor) [56]. If the surface motion is limited by the heat transfer to and from it, eq. 4.82 simplifies to the Young-Laplace equation

$$p^l - p^v = \sigma \left(\frac{1}{R_1} + \frac{1}{R_2} \right) . \tag{4.83}$$

The momentum equation in tangential direction is dependent on shear stresses and the variation of the surface tension, thus

$$\left(\vec{\boldsymbol{\tau}}^{\,l} - \vec{\boldsymbol{\tau}}^{\,v} \right) \cdot \boldsymbol{t}_1 \cdot \boldsymbol{t}_1 - \frac{\partial \sigma}{\partial t_1} = \rho^l \left(v_n^l - \frac{\partial z_{if,n}}{\partial t} \right) v_{t1}^l - \rho^v \left(v_n^v - \frac{\partial z_{if,n}}{\partial t} \right) v_{t1}^v \, , \tag{4.84}$$

$$\left(\vec{\boldsymbol{\tau}}^{\,l} - \vec{\boldsymbol{\tau}}^{\,v} \right) \cdot \boldsymbol{t_2} \cdot \boldsymbol{t_2} - \frac{\partial \sigma}{\partial t}_{2} = \rho^l \left(v_n^l - \frac{\partial z_{if,n}}{\partial t} \right) v_{t2}^l - \rho^v \left(v_n^v - \frac{\partial z_{if,n}}{\partial t} \right) v_{t2}^v \, . \tag{4.85}$$

If one imposes a continuous velocity over the free surface, hence a no-slip condition for the tangential velocity components $v_t^l = v_t^v$, constant surface tension $\frac{\partial \sigma}{\partial s} = 0$, eq. 4.84 and eq. 4.85 reduce to

$$\left(\vec{\boldsymbol{\tau}}^{\,l} \right) \cdot \boldsymbol{t}_1 = \left(\vec{\boldsymbol{\tau}}^{\,v} \right) \cdot \boldsymbol{t}_1 \, , \tag{4.86}$$

$$\left(\vec{\boldsymbol{\tau}}^{\,l} \right) \cdot \boldsymbol{t}_2 = \left(\vec{\boldsymbol{\tau}}^{\,v} \right) \cdot \boldsymbol{t}_2 \, . \tag{4.87}$$

Thus, the momentum equation in tangential direction reduces to the equality of the shear stresses. This can be written for Newtonian fluids as

$$\mu^l \left(\frac{\partial v_n^l}{\partial t_1} + \frac{\partial v_{t1}^l}{\partial n} \right) \Bigg|_{if} = \mu^v \left(\frac{\partial v_n^v}{\partial t_1} + \frac{\partial v_{t1}^v}{\partial n} \right) \Bigg|_{if} \, , \tag{4.88}$$

$$\mu^l \left(\frac{\partial v_n^l}{\partial t_2} + \frac{\partial v_{t2}^l}{\partial n} \right) \Bigg|_{if} = \mu^v \left(\frac{\partial v_n^v}{\partial t_2} + \frac{\partial v_{t2}^v}{\partial n} \right) \Bigg|_{if} . \tag{4.89}$$

Energy transport mechanisms at the free surface are convection, conduction and radiation, which are included in the heat flux terms $\widehat{q}^l$ and $\widehat{q}^v$. With the specific enthalpies h^l and h^v, the energy conservation requires

$$\widehat{q}^v - \widehat{q}^l = \rho_l \left(v_n^l - \frac{\mathrm{d}z_{if,n}}{\mathrm{d}t} \right) h^l - \rho_v \left(v_n^v - \frac{\mathrm{d}z_{if,n}}{\mathrm{d}t} \right) h^v . \tag{4.90}$$

Neglecting radiative heat transport and equilibrium conditions at the free surface, thus $\Delta h = h^v - h^l$, one can apply eq. 4.81 to simplify eq. 4.90 to

$$\lambda^v \left(\frac{\partial T^v}{\partial n} \right) \Bigg|_{if} - \lambda^l \left(\frac{\partial T^l}{\partial n} \right) \Bigg|_{if} = \rho^l \left(v_n^l - \frac{\mathrm{d}z_{if}}{\mathrm{d}t} \right) \Delta h . \tag{4.91}$$

This equation also implies that momentum and surface tension pressures are sufficiently small, that $p^l = p^v$ and the temperature at the free surface is at saturation conditions with

$$T_{sat} = T_{sat} \left(p^v \right) . \tag{4.92}$$

The pressure-temperature relationship at the free surface can be fulfilled with the Clausius-Clapeyron relationship for an ideal gas (see Ch. 4 of [5]). In differential form it is written as

$$\frac{1}{p} \, \mathrm{d}p = \frac{\Delta h}{\Re T^2} \, \mathrm{d}T . \tag{4.93}$$

Numerical calculations face the same problem as in eq. 4.78, that they cannot resolve the temperature gradient properly. Since a mesh size that resolves the molecular scale is not possible yet, a relationship based on the kinetic theory of gases was developed to quantify the mass flux due to condensation or evaporation [15] as previously introduced in Sec. 2.4 with eq. 2.36. The net mass flux $\widehat{m}$ is then dependent on the molecular weight M of the vapor, the universal gas constant $\overline{R}$, the pressure and temperature of the liquid and vapor

$$\widehat{m} = \frac{2\widetilde{\sigma}}{2 - \widetilde{\sigma}} \left(\frac{M}{2\pi\overline{R}} \right)^{1/2} \left(\frac{p^v}{\sqrt{T^v}} - \frac{p^l}{\sqrt{T^l}} \right) . \tag{4.94}$$

The accommodation coefficient $\widetilde{\sigma}$ is a measure for the fraction of molecules that hit the free surface and cross it (change their state). Therefore, $1 - \widetilde{\sigma}$ represents the amount of molecules that reflect on the free surface. Values for $\widetilde{\sigma}$ vary widely in literature but have an upper bound of $\widetilde{\sigma} = 1$ [15].

Chapter 5

Numerical Model

This chapter explains how the governing equations and their boundary conditions introduced in Ch. 4 were applied within the numerical codes used in this work. The flow solvers were Flow-3D v.11.0.2 and Fluent 15.0. The flow field was solved on a two-dimensional grid. The fluid was present in two phases (liquid, vapor) and thermally coupled with a solid structure. The liquid phase was treated as incompressible and the vapor phase as an ideal gas. The Boussinesq approximation (see Ch. 1.7.5 in [24]) was not applied for the fluid phase. Furthermore, heat and mass transfer over the free surface were activated and therefore require a phase change model. The way how the solver treats the set of equations is explained at the end of this chapter.

5.1 Numerical Model in Flow-3D

The general form of the equations which were necessary for the computations can be found in Ch. 7 of the manual [26]. The differential equations were solved in terms of cylindrical (r, θ, z) coordinates. The two-dimensional formulation let vanish all terms involving the θ-direction. All equations include area and volume porosity functions. This formulation is called FAVOR$^{\text{TM}}$ (Fractional Area/Volume Obstacle Representation method) and is used to define if a cell is blocked by a solid ($V_F = 0$), partially blocked ($0 < V_F < 1$) or filled with fluid or void ($V_F = 1$). The corresponding area fractions, which are open for flux of the stated variable are indicated with A [45].

5.1.1 Mass Conservation

The mass conservation of a compressible fluid is based on eq. 4.55 and solved for the gaseous phase as follows

$$V_F \frac{\partial \rho^v}{\partial t} + \frac{\partial}{\partial r}\left(\rho^v v_r^v A_r\right) + \frac{\rho^v v_r^v A_r}{r} + \frac{\partial}{\partial z}\left(\rho^v v_z^v A_z\right) = 0\,. \tag{5.1}$$

The incompressible form for the liquid phase evolves from eq. 4.56, thus

$$\frac{\partial}{\partial r}\left(v_r^l A_r\right) + \frac{v_r^l A_r}{r} + \frac{\partial}{\partial z}\left(v_z^l A_z\right) = 0\,. \tag{5.2}$$

5.1.2 Momentum Conservation

The compressible momentum equations in r- and z-direction are based on eq. 4.57 and eq. 4.59. Since none of the computations with Flow-3D in this work include body forces, F_r and F_z vanish. The compressible momentum conservation in r-direction is

$$\begin{aligned} \rho^v \left[\frac{\partial v_r^v}{\partial t} + \frac{v_r^v A_r}{V_F}\frac{\partial v_r^v}{\partial r} + \frac{v_z^v A_z}{V_F}\frac{\partial v_r^v}{\partial z}\right] &= \\ -\frac{\partial p}{\partial r} + \frac{1}{V_F}\frac{2\mu^v\left(1-A_z\right)}{A_r}\frac{\partial^2 v_r^v}{\partial r^2} - \frac{1}{V_F}\left[\frac{\partial}{\partial r}\left(A_r \tau_{rr}^v\right) + \frac{\partial}{\partial z}\left(A_z \tau_{rz}^v\right) + \frac{A_r \tau_{rr}^v}{r}\right]&\,, \end{aligned} \tag{5.3}$$

and in z-direction

$$\begin{aligned} \rho^v \left[\frac{\partial v_z^v}{\partial t} + \frac{v_r^v A_r}{V_F}\frac{\partial v_z^v}{\partial r} + \frac{v_z^v A_z}{V_F}\frac{\partial v_z^v}{\partial z}\right] &= \\ -\frac{\partial p}{\partial z} + \frac{1}{V_F}\frac{2\mu^v\left(1-A_r\right)}{A_z}\frac{\partial^2 v_z^v}{\partial z^2} - \frac{1}{V_F}\left[\frac{\partial}{\partial r}\left(A_r \tau_{rz}^v\right) + \frac{\partial}{\partial z}\left(A_z \tau_{zz}^v\right) + \frac{A_r \tau_{rz}^v}{r}\right]&\,. \end{aligned} \tag{5.4}$$

An occurring wall sheer stress, caused by a no slip condition of an obstacle, is considered in the second term of the right hand side of eqs. 5.3 and 5.4. The solid-fluid interface is represented by $1 - A_z$ and $1 - A_r$ for the r- and z- direction, respectively. The stress tensor components τ_{rr}^v, τ_{zz}^v and τ_{rz}^v are as follows

$$\tau_{rr}^v = -\mu^v \left[2\frac{\partial v_r^v}{\partial r} - \frac{2}{3}\left(\frac{\partial v_r^v}{\partial r} + \frac{\partial v_z^v}{\partial z} + \frac{v_r^v}{r}\right)\right]\,, \tag{5.5}$$

$$\tau_{zz}^v = -\mu^v \left[2\frac{\partial v_z^v}{\partial z} - \frac{2}{3}\left(\frac{\partial v_r^v}{\partial r} + \frac{\partial v_z^v}{\partial z} + \frac{v_r^v}{r}\right)\right]\,, \tag{5.6}$$

$$\tau_{rz}^v = -\mu^v \left(\frac{\partial v_r^v}{\partial z} + \frac{\partial v_z^v}{\partial r}\right)\,. \tag{5.7}$$

For the incompressible liquid phase the stresses reduce to

$$\tau_{rr}^l = -2\mu^l \frac{\partial v_r^l}{\partial r} \,, \tag{5.8}$$

$$\tau_{zz}^l = -2\mu^l \frac{\partial v_z^l}{\partial z} \,, \tag{5.9}$$

$$\tau_{rz}^l = -\mu^l \left(\frac{\partial v_r^l}{\partial z} + \frac{\partial v_z^l}{\partial r} \right) \,, \tag{5.10}$$

and the resulting momentum equations are then for the r-direction

$$\begin{aligned} \rho^l \left[\frac{\partial v_r^l}{\partial t} + \frac{v_r^l A_r}{V_F} \frac{\partial v_r^l}{\partial r} + \frac{v_z^l A_z}{V_F} \frac{\partial v_r^l}{\partial z} \right] &= \\ -\frac{\partial p}{\partial r} + \frac{1}{V_F} \frac{2\mu^l (1 - A_z)}{A_r} \frac{\partial^2 v_r^l}{\partial r^2} & \\ + \frac{1}{V_F} \left[2 \frac{\partial}{\partial r} \left(\mu^l A_r \frac{\partial v_r^l}{\partial r} \right) + \frac{\partial}{\partial z} \left(\mu^l A_z \left(\frac{\partial v_r^l}{\partial z} + \frac{\partial v_z^l}{\partial r} \right) \right) + \frac{2\mu^l A_r}{r} \frac{\partial v_r^l}{\partial r} \right] \,, & \end{aligned} \tag{5.11}$$

and for the z-direction

$$\begin{aligned} \rho^l \left[\frac{\partial v_z^l}{\partial t} + \frac{v_r^l A_r}{V_F} \frac{\partial v_z^l}{\partial r} + \frac{v_z^l A_z}{V_F} \frac{\partial v_z^l}{\partial z} \right] &= \\ -\frac{\partial p}{\partial z} + \frac{1}{V_F} \frac{2\mu^l (1 - A_r)}{A_z} \frac{\partial^2 v_z^l}{\partial z^2} & \\ + \frac{1}{V_F} \left[\frac{\partial}{\partial r} \left(\mu^l A_r \left(\frac{\partial v_r^l}{\partial z} + \frac{\partial v_z^l}{\partial r} \right) \right) + 2 \frac{\partial}{\partial z} \left(\mu^l A_z \frac{\partial v_z^l}{\partial z} \right) + \frac{\mu^l A_r}{r} \left(\frac{\partial v_r^l}{\partial z} + \frac{\partial v_z^l}{\partial r} \right) \right] \,. & \end{aligned} \tag{5.12}$$

5.1.3 Energy Conservation

For two-phase flow the specific internal fluid energy is calculated with the fill fraction F for the liquid phase, thus

$$\rho^f u^f = F \rho^l c_v^l T + (1 - F) \rho^v c_v^v T \,, \tag{5.13}$$

with $u = 0\,\mathrm{J\ kg^{-1}}$ at $T = 0\,\mathrm{K}$. With this formulation, the energy equation for the fluid evolves from eq. 4.26 neglecting the viscous dissipation term

$$\begin{aligned} V_F \frac{\partial}{\partial t} \left(\rho^f u^f \right) + \frac{\partial}{\partial r} \left(\rho^f u^f v_r^f A_r \right) + \frac{\partial}{\partial z} \left(\rho^f u^f v_z^f A_z \right) + \frac{\rho^f u^f v_r^f A_r}{r} &= \\ \frac{\partial}{\partial r} \left(\lambda^f A_r \frac{\partial T^f}{\partial r} \right) + \frac{\partial}{\partial z} \left(\lambda^f A_z \frac{\partial T^f}{\partial z} \right) + \frac{\lambda^f A_r T^f}{r} & \\ -p \left[\frac{\partial}{\partial r} \left(v_r^f A_r \right) + \frac{\partial}{\partial z} \left(u_z^f A_z \right) + \frac{v_r^f A_r}{r} \right] \,. & \end{aligned} \tag{5.14}$$

For any solid, the energy equation is

$$(1-V_F)\rho^s c^s \frac{\partial T^s}{\partial t} = \frac{\partial}{\partial r}\left[\lambda^s\left(1-A_r\right)\frac{\partial T^s}{\partial r}\right] + \frac{\partial}{\partial z}\left[\lambda^s\left(1-A_z\right)\frac{\partial T^s}{\partial z}\right]. \tag{5.15}$$

5.1.4 Relations for Pressure, Internal Energy and Multiphase Flow

Flow-3D treats the compressible fluid phase as an ideal gas and computes the specific internal energy for the fluid phase with the specific heat capacity at constant volume c_v as

$$u^f = c_v^f T\,, \tag{5.16}$$

and for the solid phase with the specific heat capacity c, thus

$$u^s = c^s T\,. \tag{5.17}$$

The Volume of Fluid (VOF) method is used to describe the dynamics of the free surface [44]. Two-fluid problems can involve two incompressible fluids or one incompressible and one compressible fluid. Fluid 1 is represented by F and the complementary region (fluid 2) with $1-F$. The fluid configuration is then defined as

$$\frac{\partial F}{\partial t} + \frac{1}{V_F}\left[\frac{\partial}{\partial r}\left(FA_r v_r\right) + \frac{\partial}{\partial z}\left(FA_z v_z\right) + \frac{FA_r v_r}{r}\right] = 0\,. \tag{5.18}$$

5.1.5 Boundary Conditions

To set appropriate boundary conditions one must understand how Flow-3D stores the variables in the mesh. Figure 5.1 shows a section of generic mesh. The edges in horizontal direction (r-direction) are labeled with the index i and those in vertical direction (z-direction) with the index k. The cell centers, indicted with a dot, are enumerated with the lower bound of the cell. Velocities are stored on the edges, thus $v_{i,k}$ is the radial velocity component on the edge between cell (i,$k-1$) and cell (i,k). All other variables which are ρ, u, T, p, F and μ are stored in the cell centers. The density of cell (i,k) is therefore $\rho_{i,k}$. The cells which discretize the computational domain are surrounded by ghost cells. These cells are necessary to define the specific conditions at the boundary itself. For a better understanding of how the boundary conditions were implemented one assumes the following boundary conditions for the generic grid in Fig. 5.1:

- $r = i$: symmetry BC
- $r = i + 1$: adiabatic wall BC
- $z = k$: velocity inlet BC

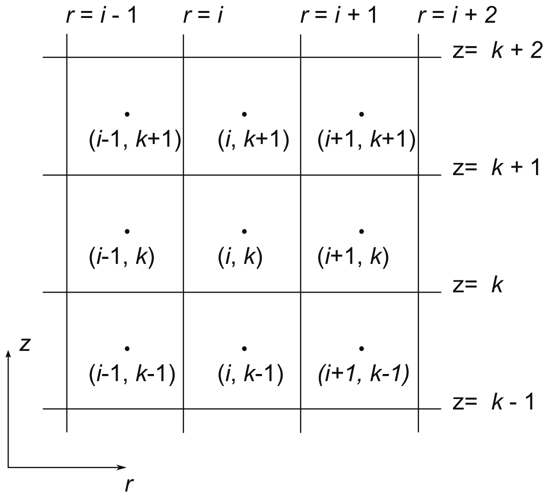

Figure 5.1: Generic mesh with nomenclature to name the cells and edges.

For all wall boundaries, conditions must be set for the fluid velocity and the heat flux across the surface. In this work all walls were treated with a no-slip velocity as introduced in eq. 4.76. Adiabatic wall conditions omit any heat flow normal to the surface, thus the temperature in either cell of the boundary must be equal. This gives the following formulation for cell (i,k)

$$v_{i+1,k+1} = 0\,\mathrm{m\,s^{-1}}\,, \tag{5.19}$$

$$T_{i,k} = T_{i+1,k}\,. \tag{5.20}$$

For thermal active solids eq. 5.14 and eq. 5.15 are coupled with each other. For a known surface temperature of the wall Newton's law of cooling (see eq. 4.80) is applied.

Symmetry boundary conditions were used to reduce the size of the computational domain. In this case all variables which are stored in the cell center (ρ, u, T, p, $\boldsymbol{F}$, μ) have the same value on both sides of the symmetry plane. Which gives

$$(\rho,\, u,\, T,\, p,\, \boldsymbol{F},\, \mu)_{i-1,k} = (\rho,\, u,\, T,\, p,\, \boldsymbol{F},\, \mu)_{i,k}\,. \tag{5.21}$$

At a velocity inlet boundary condition the specific velocity is set on the boundary itself and the other properties of the entering fluid are stored in the center of the adjacent ghost cells. For the (i,k) cell this results in

$$v_{i+1,k} = v_{bc} = 0\,\mathrm{m\,s^{-1}}\,, \tag{5.22}$$

$$(\rho,\, u,\, T,\, p,\, \boldsymbol{F},\, \mu)_{i,k-1} = (\rho,\, u,\, T,\, p,\, \boldsymbol{F},\, \mu)_{bc}\,. \tag{5.23}$$

Wall adhesion is considered as a boundary condition for the free surface and is represented by the contact angle γ. The surface tension forces are included as an equivalent surface pressure. Surface tension forces act tangent to the free surface and can be resolved into components directed along to principal tangent directions. The net surface force perpendicular to the x-axis is given in the manual [26] in Cartesian coordinates with

$$F_z = \frac{\sigma \Delta y \, \dfrac{\partial z}{\partial x}}{\left[1 + \left(\dfrac{\partial z}{\partial x}\right)^2 + \left(\dfrac{\partial z}{\partial y}\right)^2\right]^{1/2}} \, . \tag{5.24}$$

In Flow-3D the Hertz-Knudsen model (see eq. 4.94) is used to calculate the net mass flux $\widehat{m}$ over the free surface. A detailed procedure for the implementation can be found in the manual [26] and in Hirt et al. [43]. Equation 4.94 is used in the following simplified form

$$\widehat{m} = \widetilde{c} \left(\frac{M}{2\pi \overline{R} T_{if}} \right)^{1/2} \left(p^l_{sat} - p^v \right) \, . \tag{5.25}$$

The mass flux is calculated with the molecular weight M, the universal gas constant $\overline{R}$, the difference of liquid saturation pressure p^l_{sat} and vapor pressure p^v and the interface (free surface) temperature T_{if}. The accommodation coefficient is given here with $\widetilde{c}$. Note that $\widetilde{c} = \dfrac{2\widetilde{\sigma}}{2-\widetilde{\sigma}}$. To calculate the saturation conditions, the Clausius-Clapeyron equation is used in the following form

$$p_{sat} = p_{ref} \exp \left[\frac{-\left(\dfrac{1}{T_v} - \dfrac{1}{T_{ref}} \right)}{T_{vexp}} \right] \, . \tag{5.26}$$

To solve this equation another pair of values (p_{ref}, T_{ref}) that lies on the saturation curve and the exponent constant T_{vexp} must be known. The constant can be computed as the ratio of gas constant $\overline{R}$ and latent heat of evaporation Δh.

$$T_{vexp} = \frac{(\kappa - 1)\, c_{v,v}}{\Delta h} = \frac{\overline{R}}{\Delta h} \, . \tag{5.27}$$

5.2 Numerical Model in Fluent

Fluent solves the set of equations for a planar two-dimensional mesh, which means that the mesh is a surface and does not have an unity depth, as is the case for Flow-3D. Another difference to Flow-3D is, that with Fluent solid structures must be specified by the user and mesh edges must follow the solid-fluid interface. A detailed explanation of the code is given in the manual [3]. All used equations are explained in the following and stem from this source.

5.2.1 Mass Conservation

The mass conservation equation for compressible flow in cylindrical coordinates is defined as

$$\frac{\partial \rho^v}{\partial t} + \frac{\partial}{\partial r}\left(\rho^v v_r^v\right) + \frac{\rho^v v_r^v}{r} + \frac{\partial}{\partial z}\left(\rho^v v_z^v\right) = 0\,, \tag{5.28}$$

and reduces for incompressible fluids to

$$\frac{\partial v_r^l}{\partial r} + \frac{v_r^l}{r} + \frac{\partial v_z^l}{\partial z} = 0\,. \tag{5.29}$$

5.2.2 Momentum Conservation

The momentum conservation equation for compressible fluids gives for the r- and z-direction

$$\begin{aligned} \frac{\partial}{\partial t}\left(\rho^v v_r^v\right) + \frac{1}{r}\frac{\partial}{\partial r}\left(r\rho^v v_r^v v_r^v\right) + \frac{1}{r}\frac{\partial}{\partial z}\left(r\rho^v v_z^v v_r^v\right) = \\ -\frac{\partial p}{\partial r} + \frac{1}{r}\frac{\partial}{\partial r}\left[r\mu^v\left(2\frac{\partial v_r^v}{\partial r} - \frac{2}{3}\left(\frac{\partial v_r^v}{\partial r} + \frac{v_r^v}{r} + \frac{\partial v_z^v}{\partial z}\right)\right)\right] \\ -2\mu^v\frac{v_r}{r^2} + \frac{2\mu^v}{3r}\left(\frac{\partial v_r^v}{\partial r} + \frac{v_r^v}{r} + \frac{\partial v_z^v}{\partial z}\right) + \rho^v\frac{v_z^v v_z^v}{r} \\ +\frac{1}{r}\frac{\partial}{\partial z}\left[r\mu^v\left(\frac{\partial v_r^v}{\partial z} + \frac{\partial v_z^v}{\partial r}\right)\right]\,, \end{aligned} \tag{5.30}$$

$$\begin{aligned} \frac{\partial}{\partial t}\left(\rho^v v_z^v\right) + \frac{1}{r}\frac{\partial}{\partial r}\left(r\rho^v v_r^v v_z^v\right) + \frac{1}{r}\frac{\partial}{\partial z}\left(r\rho^v v_z^v v_z^v\right) = \\ -\frac{\partial p}{\partial z} + \frac{1}{r}\frac{\partial}{\partial r}\left[r\mu^v\left(\frac{\partial v_z^v}{\partial r} + \frac{\partial v_r^v}{\partial z}\right)\right] \\ +\frac{1}{r}\frac{\partial}{\partial z}\left[r\mu^v\left(2\frac{\partial v_z^v}{\partial z} - \frac{2}{3}\left(\frac{\partial v_r^v}{\partial r} + \frac{v_r^v}{r} + \frac{\partial v_z^v}{\partial z}\right)\right)\right]\,. \end{aligned} \tag{5.31}$$

These equations reduce for incompressible flow to

$$\begin{aligned} \frac{\partial}{\partial t}\left(\rho^l v_r^l\right) + \frac{1}{r}\frac{\partial}{\partial r}\left(r\rho^l v_r^l v_r^l\right) + \frac{1}{r}\frac{\partial}{\partial z}\left(r\rho^l v_z^l v_r^l\right) = \\ -\frac{\partial p}{\partial r} + \frac{1}{r}\frac{\partial}{\partial r}\left(2r\mu^l\frac{\partial v_r^l}{\partial r}\right) \\ -2\mu^l\frac{v_r^l}{r^2} + \rho^l\frac{v_z^l v_z^l}{r} \\ +\frac{1}{r}\frac{\partial}{\partial z}\left[r\mu^l\left(\frac{\partial v_r^l}{\partial z} + \frac{\partial v_z^l}{\partial r}\right)\right]\,, \end{aligned} \tag{5.32}$$

$$\begin{aligned}\frac{\partial}{\partial t}\left(\rho^l v_z^l\right)+\frac{1}{r}\frac{\partial}{\partial r}\left(r\rho^l v_r^l v_z^l\right)+\frac{1}{r}\frac{\partial}{\partial z}\left(r\rho^l v_z^l v_z^l\right) &= \\ -\frac{\partial p}{\partial z}+\frac{1}{r}\frac{\partial}{\partial r}\left[r\mu^l\left(\frac{\partial v_z^l}{\partial r}+\frac{\partial v_r^l}{\partial z}\right)\right]& \\ +\frac{1}{r}\frac{\partial}{\partial z}\left(2r\mu^l\frac{\partial v_z^l}{\partial z}\right)&\,. \end{aligned} \tag{5.33}$$

5.2.3 Energy Conservation

If both phases are present, the energy equation for a compressible fluid (index v) and an incompressible fluid (index l) is defined in Fluent as

$$\frac{\partial}{\partial t}\left(\rho^f e^f\right)+\nabla\cdot\left[\boldsymbol{v^f}\left(\rho^f e^f+p\right)\right]=\nabla\cdot\left[\lambda^f\nabla T-Fh^l\boldsymbol{J}^l-(1-F)\,h^v\boldsymbol{J}^v+\left(\vec{\boldsymbol{\tau}}^f\cdot\boldsymbol{v}^f\right)\right]\,, \tag{5.34}$$

with J indicating the diffusion flux of the corresponding species and the stress tensor $\vec{\boldsymbol{\tau}}$

$$\vec{\boldsymbol{\tau}}=\mu\left[\left(\nabla\cdot\boldsymbol{v}+\nabla\cdot\boldsymbol{v}^T\right)-\frac{2}{3}\left(\nabla\cdot\boldsymbol{v}\right)\cdot\vec{\boldsymbol{I}}\right]\,, \tag{5.35}$$

where $\vec{\boldsymbol{I}}$ represents the unity tensor. The fluid's energy e^f is calculated as

$$e^f=h^f-\frac{p}{\rho^f}+\frac{v^2}{2}\,. \tag{5.36}$$

If there is only a compressible fluid, such as vapor, eq. 5.34 transforms to

$$\begin{aligned}\frac{\partial}{\partial t}\left(\rho^v e^v\right)+\frac{\partial}{\partial r}\left(v_r^v\rho^v e^v\right)+\frac{v_r^v\rho^v e^v}{r}+\frac{\partial}{\partial z}\left(v_z^v\rho^v e^v\right)+p\left(\frac{\partial v_r^v}{\partial r}+\frac{v_r^v}{r}+\frac{\partial v_z^v}{\partial z}\right) &= \\ \frac{\partial}{\partial r}\lambda^v\left(\frac{\partial T}{\partial r}\right)+\frac{\lambda^v}{r}\left(\frac{\partial T}{\partial r}\right)+\frac{\partial}{\partial r}\left(\frac{\lambda^v T}{r}\right)+\frac{\lambda^v T}{r^2}+\frac{\partial}{\partial z}\lambda^v\left(\frac{\partial T}{\partial z}\right)& \\ -\left[\frac{\partial}{\partial r}\left(h^v J_r^v\right)+\frac{h^v J_r^v}{r}+\frac{\partial}{\partial z}\left(h^v J_z^v\right)\right]& \\ +\nabla\cdot\left(\vec{\boldsymbol{\tau}}^v\cdot\boldsymbol{v}^v\right)&\,. \end{aligned} \tag{5.37}$$

The enthalpy of the vapor h^v is calculated with the specific heat at constant pressure:

$$h^v=\int_{T_{ref}}^{T} c_p^v\,\mathrm{d}T\,. \tag{5.38}$$

In presence of only an incompressible fluid, such as the liquid phase, eq. 5.34 simplifies with $\lambda^l = \text{const}$ to

$$\begin{aligned}\frac{\partial}{\partial t}\left(\rho^l e^l\right) + p\left(\frac{\partial v_r^l}{\partial r} + \frac{v_r^l}{r} + \frac{\partial v_z^l}{\partial z}\right) = \\ \lambda^l\left[\frac{1}{r}\frac{\partial}{\partial r}\left(r\frac{\partial T}{\partial r}\right) + \frac{\partial^2 T}{\partial z^2}\right] \\ -\left[\frac{\partial}{\partial r}\left(Fh^l J_r^l\right) + \frac{Fh^l J_r^l}{r} + \frac{\partial}{\partial z}\left(Fh^l J_z^l\right)\right] \\ +\nabla\cdot\left(\vec{\boldsymbol{\tau}}^{\,l}\cdot\boldsymbol{v}^l\right)\,,\end{aligned} \tag{5.39}$$

with the enthalpy for the liquid h^l as

$$h^l = \int_{T_{ref}}^{T} c_p^l \,\mathrm{d}T + \frac{p^l}{\rho^l}\,. \tag{5.40}$$

Equation 5.39 simplifies for solid regions with $\lambda^s = \text{const}$ to

$$\frac{\partial}{\partial t}\left(\rho^s h^s\right) = \lambda^s\left[\frac{1}{r}\frac{\partial}{\partial r}\left(r\frac{\partial T}{\partial r}\right) + \frac{\partial^2 T}{\partial z^2}\right]\,, \tag{5.41}$$

and the enthalpy of the solid is computed as

$$h^s = \int_{T_{ref}}^{T} c^s \,\mathrm{d}T\,. \tag{5.42}$$

5.2.4 Relations for Pressure, Internal Energy and Multiphase Flow

All simulations with Fluent conducted for this work used the ideal gas equation (eq. 4.29) for compressible fluids. The specific energy e of a cell is defined according to eq. 5.36 with a different calculation of the specific enthalpy for compressible and incompressible flow (see eq. 5.38 and eq 5.40). Tracking of the free surface is accomplished with the VOF model by solving the continuity equation for the volume fraction for the two phases. Fluent is able to solve an infinite number of phases, which results in one equation per phase. For a liquid (incompressible) and a gaseous (compressible) phase the conservation equations have the following form

$$\frac{\partial}{\partial r}\left(Fv_r^l\right) + \frac{Fv_r^l}{r} + \frac{\partial}{\partial z}\left(Fv_z^l\right) = 0\,, \tag{5.43}$$

$$\frac{\partial}{\partial t}\left((1-F)\,\rho^v\right) + \frac{\partial}{\partial r}\left((1-F)\,\rho^v v_r^v\right) + \frac{(1-F)\,\rho^v v_r^v}{r} + \frac{\partial}{\partial z}\left((1-F)\,\rho^v v_z^v\right) = 0\,, \tag{5.44}$$

where F represents the fill fraction of liquid in a cell and $(1-F)$ the fraction of vapor. All phase change mass flows will appear on the right side of both equations. For a cell where both phases are present, the density is calculated with the volume-average of both phases, thus

$$\rho = F\rho^l + (1-F)\,\rho^v\,. \tag{5.45}$$

This is used to compute the specific energy and temperature as mass-averaged variables

$$e = \frac{F\rho^l e^l + (1-F)\,\rho^v e^v}{F\rho^l + (1-F)\,\rho^v}\,, \tag{5.46}$$

$$T = \frac{F\rho^l T^l + (1-F)\,\rho^v T^v}{F\rho^l + (1-F)\,\rho^v}\,. \tag{5.47}$$

5.2.5 Boundary Conditions

Boundary conditions at the wall (no-slip condition), inlet and symmetry boundaries are treated the same way as in Flow-3D (see 5.1.5). To model wall adhesion, Fluent [3] uses the method developed by Brackbill [12]. Instead of defining the contact angle as a boundary condition it is used to adjust the free surface normal in the cell next to the wall using the contact angle. With this dynamic boundary condition the normal and tangential free surface vector at the wall is

$$\boldsymbol{n}_{if} = \boldsymbol{n}_w \cos\gamma\,, \tag{5.48}$$

$$\boldsymbol{t}_{if} = \boldsymbol{t}_w \sin\gamma\,. \tag{5.49}$$

Fluent uses the continuum surface force (CSF) model proposed by [12] to consider surface tension forces. As seen in the Young-Laplace equation (eq. 4.83), any surface tension induces a pressure jump across the free surface. This results in a source term in the momentum equations (eqs. 5.30, 5.31, 5.32 and 5.33). The force at the surface can be used as a volume force with the surface curvature $k = \nabla \cdot \boldsymbol{n}_{if}$ in the following form

$$F = \sigma \frac{\rho k \nabla F}{\frac{1}{2}\left(\rho^l + \rho^v\right)}\,, \tag{5.50}$$

where ρ is computed from the single phases with eq. 5.45. It has to be stated, that F on the left hand side represents the resulting force, whereas F on the right hand side is the volume fraction.

The Lee model [57] in connection with the Hertz-Knudsen model [15] is implemented to compute any mass transfer caused by condensation or evaporation. This mechanism is governed by the vapor transport equation

$$\frac{\partial}{\partial t}\left((1-F)\,\rho^v\right) + \nabla \cdot \left((1-F)\,\rho^v \boldsymbol{v}^v\right) = \overline{m}_e - \overline{m}_c\,. \tag{5.51}$$

The right hand side gives the rates of mass transfer due to evaporation $\overline{m}_e$ and condensation $\overline{m}_c$ (in kg s^{-1} m^{-3}), thus $\overline{m}$ is either a source or sink of mass. These source terms can be described as

$$\overline{m}_e = \overline{f}_e F \rho^l \frac{(T^l - T_{sat})}{T_{sat}} \,, \tag{5.52}$$

$$\overline{m}_c = \overline{f}_c \left(1 - F\right) \rho^v \frac{(T_{sat} - T^v)}{T_{sat}} \,, \tag{5.53}$$

with $\overline{f}$ as the phase change frequency which includes the Hertz-Knudsen formulation. It can be interpreted as a relaxation time with the unit s^{-1}. The Hertz-Knudsen equation, eq. 4.94, with the Clausius-Clapeyron equation, eq. 2.34, gives

$$\widehat{m} = \frac{2\widetilde{\sigma}}{2 - \widetilde{\sigma}} \left(\frac{M}{2\pi \overline{R} T_{sat}}\right)^{1/2} \Delta h \left(\frac{\rho^v \rho^l}{\rho^l - \rho^v}\right) \frac{T - T_{sat}}{T_{sat}} \,. \tag{5.54}$$

To compute the mass source term, the interfacial area density l_{if} is introduced using the volume fraction F and the bubble diameter d_{bu}:

$$l_{if} = \frac{6F(1-F)}{d_{bu}} \,. \tag{5.55}$$

This gives for the mass source term:

$$\overline{m}_e = \widehat{m} l_{if} = \frac{6}{d_{bu}} \frac{2\widetilde{\sigma}}{2 - \widetilde{\sigma}} \left(\frac{M}{2\pi \overline{R} T_{sat}}\right)^{1/2} \Delta h \left(\frac{(1-F)\rho^v}{\rho^l - \rho^v}\right) \left(F \rho^l \frac{T^l - T_{sat}}{T_{sat}}\right) \,, \tag{5.56}$$

$$\overline{m}_c = \widehat{m} l_{if} = \frac{6}{d_{bu}} \frac{2\widetilde{\sigma}}{2 - \widetilde{\sigma}} \left(\frac{M}{2\pi \overline{R} T_{sat}}\right)^{1/2} \Delta h \left(\frac{F \rho^l}{\rho^l - \rho^v}\right) \left((1-F)\rho^v \frac{T_{sat} - T^v}{T_{sat}}\right) \,. \tag{5.57}$$

The resulting relaxation times result as

$$\overline{f}_e = \frac{6}{d_{bu}} \frac{2\widetilde{\sigma}}{2 - \widetilde{\sigma}} \left(\frac{M}{2\pi \overline{R} T_{sat}}\right)^{1/2} \Delta h \left(\frac{(1-F)\rho^v}{\rho^l - \rho^v}\right) \,, \tag{5.58}$$

$$\overline{f}_c = \frac{6}{d_{bu}} \frac{2\widetilde{\sigma}}{2 - \widetilde{\sigma}} \left(\frac{M}{2\pi \overline{R} T_{sat}}\right)^{1/2} \Delta h \left(\frac{F \rho^l}{\rho^l - \rho^v}\right) \,. \tag{5.59}$$

The relaxation time $\overline{c}$ includes the accommodation coefficient of the Hertz-Knudsen equation $\widetilde{\sigma}$, the latent heat of evaporation Δh, and the bubble diameter d_{bu}.

5.3 Solver Theory

For the optimum solution of a numerical problem, multiple settings are available in both codes used. An explanation of the entire theory would exceed the frame of this work. Therefore, only the used methods were considered. But a detailed description of all settings is given in the documentations [3, 26]. In the following, explicit and implicit solutions methods are introduced.

Using an explicit formulation relies on already known values of a generic variable ϕ to calculate the advanced (in space or time) value of this variable. The implicit method however, requires the advanced values of the respective cell and the neighbor cells to calculate the new value. This leads to a set of equations that needs to be solved iteratively (see Ch. 6 of [24]). Implicit methods can be considered as more computationally expensive but allow a higher step size and less iterations. The stability of the simulation depends heavily on the Courant number CFL which is defined as the ratio of time step Δt to the characteristic convection time $v/\Delta x$, the time a disturbance convected to through one cell [24], thus

$$\mathrm{CFL} = \frac{v\Delta t}{\Delta x}\,. \tag{5.60}$$

To avoid divergence of the computation any disturbance should move through one cell per time step, which results in CFL < 1.

5.3.1 Flow-3D

Flow-3D is based on a finite difference solution method. The procedure of advancing through one time step includes the following steps:

1. Using the initial conditions or the values of the previous time step with an explicit approximation of the momentum equations (eqs. 5.3, 5.4, 5.11 and 5.12) to compute a first guess of current velocities.
2. For the explicit formulation, the pressure is adjusted in each cell to satisfy the mass conservation equations (eqs. 5.1 and 5.2) and the equation of state for compressible gases.
3. In the last step, the free surface is adjusted using eq. 5.18. The density of the compressible phase is updated with eq. 5.1 and the energy with eq. 5.37 or eq 5.39.

The discretization in both space and time is first order accurate. This means, that all advective and viscous terms are evaluated using the old time level $t-\Delta t$. Wall shear stresses are evaluated implicitly. The momentum and continuity equations must be combined to solve the flow field since p^t is unknown at the beginning of the cycle (step 1). The former pressure $p^{t-\Delta t}$ is taken at the beginning. To preserve the accuracy in a non-equidistant mesh, Flow-3D uses a modified donor-cell approximation which gives for the generic advection of ϕ in x-direction

$$\widehat{\phi} = \left(\frac{A_x}{V}\right)\phi\,\frac{\partial \phi}{\partial x}\ . \tag{5.61}$$

The pressure solution algorithm differs for incompressible or compressible flows. Considering an incompressible fluid the continuity equation is an elliptic condition for the cell pressure and velocities. For compressible flows, the continuity equation is solved as a parabolic equation.

The pressure is determined by updating the cell pressure iteratively till it equals the pressure determined by the equation of state. Several methods are implemented to solve the pressure. In this work the Generalized Minimum Residual (GMRES) solver is used.

GMRES Pressure-Velocity Solver

A detailed description of this solver method can be found in [91]. The momentum and continuity equations are solved in a coupled manner. First, the momentum equations are reduced to the following form to solve the intermediate velocities indicated with the superscript $''$

$$\frac{v_{x,i,k}^{t+\Delta t} - v''_{x,i,k}}{\Delta t} = -\frac{1}{\rho}\frac{p'_{i+1,k} - p'_{i,k}}{\Delta x}\,, \tag{5.62}$$

$$\frac{v_{z,i,k}^{t+\Delta t} - v''_{z,i,k}}{\Delta t} = -\frac{1}{\rho}\frac{p'_{i,k+1} - p'_{iF,k}}{\Delta z}\,, \tag{5.63}$$

where $p' = p^{t+\Delta t} - p^t$ and represents the pressure change in each cell. To solve the above equations for each cell, they are substituted in the momentum equation to achieve

$$\nabla \cdot \boldsymbol{v}'' - \frac{\Delta t}{\rho}\nabla^2 p' = 0\,. \tag{5.64}$$

The solution process of eq. 5.64 to yield $p^{t+\Delta t}$ is explained in Appendix A of [91]. The obtained pressure is used with eqs. 5.62 and 5.63 to calculate the velocities of the next time level. In a next step all viscous terms are solved explicitly from the momentum equations.

To calculate the fluid fraction F and conserve a sharp free interface, the VOF method with a donor-acceptor flux approximation is implemented. This approximation controls the maximum amount of a species, that advects from the donor to the acceptor cell in one time step. The flux is limited by the amount the donor cell can give and the amount the acceptor cell can take.

Heat conduction and heat transfer are calculated by discretization of the energy equations implicitly, thus

$$V_F \frac{(\rho u)^{t+\Delta t} - (\rho u)^t}{\Delta t} = \sum \frac{A_f \lambda}{\Delta r_f}\left(T^t - T^t_{nb}\right) + \alpha A^s \left(T^t - T^{t,s}\right)\,. \tag{5.65}$$

This equation uses the common face area of the cell with its neighbor cell A_f, the distance between both cell centers Δr, the temperature of the neighbor cell T_{nb}, any wall surface area A_s and the temperature of the solid cell T_s to compute the cell's energy on the next time level.

5.3.2 Fluent

Using Fluent one can choose between two numerical methods, the pressure-based solver and the density-based solver. Even though both solvers are extended to operate in a wide range of flow

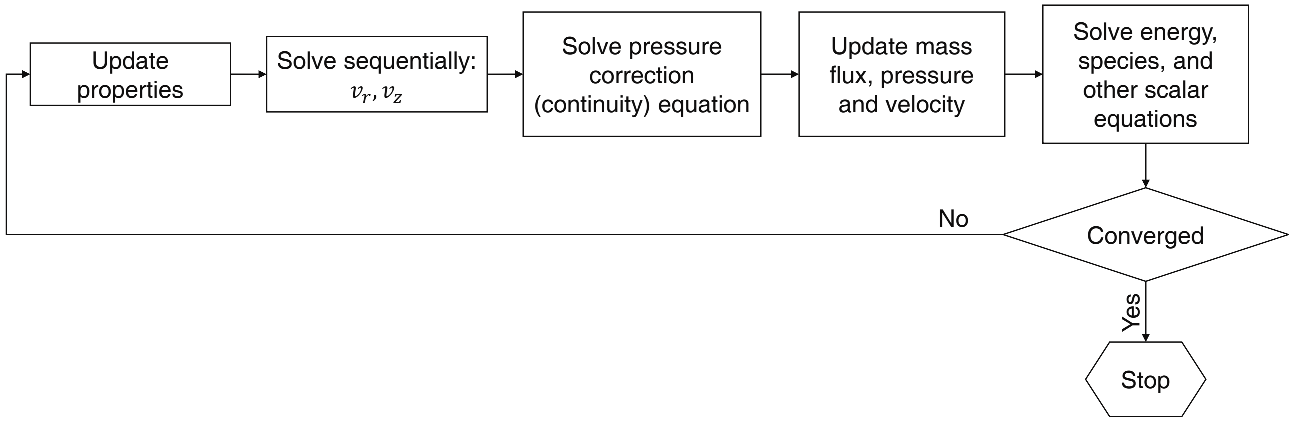

Figure 5.2: Pressure-based segregated solution algorithm used in Fluent to solve the flow field.

conditions, the pressure-based solver was chosen since it was originally designed for low speed, incompressible flows. The velocity field is obtained from the momentum equations. To solve the pressure field a pressure or pressure correction equation is used from the continuity and momentum equations. A control-volume-based technique is implemented to solve the governing equations, that consist of:

- Dividing the domain into discrete control volumes using a computational grid.
- Integration of the governing equations on the control volumes to create a set of algebraic equations for the dependent variables (velocity, pressure, temperature, viscosity, energy, phase).
- Linearization of the discretized equations and solution of the system to yield updated values of the dependent variables.

The used algorithm belongs to a class called projection method introduced by Chorin [17]. Within this method mass conservation of the continuity field is achieved by solving a pressure (or pressure correction) equation. This equation is derived in a way, that the velocity field, corrected by the pressure, satisfies continuity. Since the governing equations are nonlinear and coupled, the process involves iterations wherein the entire set of equations is solved until the solution converges. The equations are solved sequentially using the SIMPLE algorithm. This is a memory efficient way but slower than using a coupled algorithm. The steps are shown in Fig. 5.2. They are as follows:

1. Update fluid properties based on the current solution.
2. Solve momentum equations, one after another, using the updated values of pressure and face mass fluxes.
3. Solve the pressure correction equation.

4. Correct face mass fluxes, pressure and the velocity field with the correction from step 3.
5. Solve the equations for any additional scalars (energy, phase).
6. Update source arising from interaction between different phases, such as conjugated heat transfer and heat and mass transfer over the free surface.
7. Check for convergence.

To convert the general transport equations in an algebraic equation Fluent integrates over the cell. Such a generic scalar ϕ transport equation can be written with an arbitrary control volume V as

$$\int_V \frac{\partial}{\partial t}(\rho\phi)\,\mathrm{d}V + \oint \rho\phi\boldsymbol{v}\cdot\mathrm{d}\boldsymbol{A} = \oint \Gamma_\phi \nabla\phi\cdot\mathrm{d}\boldsymbol{A} + \int_A S_\phi\,\mathrm{d}V\,, \tag{5.66}$$

where $\boldsymbol{A}$ is the surface vector, Γ_ϕ is the diffusion coefficient for ϕ and S_ϕ is the volumetric source of ϕ. Discretization of eq. 5.66 gives

$$\frac{\partial}{\partial t}(\rho\phi V) + \sum_f^{N_f} \rho_f \boldsymbol{v}_f \phi_f \cdot \boldsymbol{A}_f = \sum_f^{N_f} \Gamma_\phi \nabla\phi_f \cdot \boldsymbol{A}_f + S_\phi V\,, \tag{5.67}$$

with N_f as the number of faces enclosing the cell, ϕ_f as the value of ϕ convection through face f and $\boldsymbol{A}_f$ as the area of the face. The above equation contains the unknown value of ϕ in the observed cell and its neighboring cells. This equation can be written in a linearized form as

$$C_P\phi = \sum C_{nb}\phi_{nb} + C_c\,, \tag{5.68}$$

where C_c and C_{nb} are linearized coefficients for ϕ and ϕ_{nb}. The subscript nb refers to the neighboring cell. This procedure is executed for each cell in the mesh, which results in a set of algebraic equations with a sparse coefficient matrix. It is solved by Fluent using a point implicit (Gaus-Seidel) linear equation solver.

Spatial and temporal discretization can be achieved with different schemes. In the following all used schemes are introduced.

Second-Order Upwind

This scheme provides second-order accuracy using a multidimensional linear reconstruction approach for the quantities. The face value of a scalar ϕ_f is computed with

$$\phi_f = \phi + \nabla\phi\cdot\boldsymbol{r}\,, \tag{5.69}$$

where ϕ and $\nabla\phi$ are the cell-centered value and its gradient in upstream direction. The displacement vector $\boldsymbol{r}$ is defined from the upstream cell centroid to the face centroid.

PRESTO!

The Pressure Staggering Option (PRESTO!) was implemented to discretize the pressure. It uses a discrete continuity balance for a staggered control volume to compute the staggered pressure. Therefore, it assumes new cell centers that allow to stagger the grid. In other words, it computes the velocity components in the centers of the faces whose unit vector is parallel to the component considered.

Geo-Reconstruct

The Geo-Reconstruct scheme was used to achieve a time-accurate transient behavior of the free surface. Furthermore it allows a sharp interface between the respective phases. This scheme reconstructs the interface between fluids using a piecewise-linear approach [93]. It assumes that the interface between two fluids has a linear slope within each cell. It uses this linear shape to calculate the advection of fluid through the cell faces.

First-Order Implicit

For transient simulations, the governing equations must also be discretized in time. Therefore, every term must also be integrated over the time step Δt. The time evolution of ϕ in generic form is

$$\frac{\partial \phi}{\partial t} = Y(\phi)\,. \tag{5.70}$$

All spatial discretizations are included in $Y(\phi)$ on the right hand side. With the implicit time integration one can evaluate $Y(\phi)$ on a future time level $t + \Delta t$ with

$$\frac{\phi^{t+\Delta t} - \phi^{t}}{\Delta t} = Y(\phi^{t+\Delta t})\,. \tag{5.71}$$

With this formulation the value of ϕ on a future time level can be solved with the information of $\phi^{t+\Delta t}$ of the neighboring cells, which must be done iteratively.

$$\phi^{t+\Delta t} = \phi^{t} + Y(\phi^{t+\Delta t})\Delta t\,. \tag{5.72}$$

This formulation has the advantage, that it is unconditionally stable with respect to the time step.

Least Square Cell Based

The gradient $\nabla\phi$ is used to discretize the convection and diffusion terms in the conservation equations. For this work the Least Square Cell Based method was applied to compute the gradients. The change of cell values between two adjacent cells can be written as

$$(\nabla\phi)_{0,0} \cdot \boldsymbol{r} = \left(\phi_{0,1} - \phi_{0,0}\right)\,. \tag{5.73}$$

Writing a similar equation for each surrounding cell results in the form

$$\vec{\boldsymbol{J}}\,(\nabla\phi)_{0,0} = \Delta\phi\,, \tag{5.74}$$

where $\vec{\boldsymbol{J}}$ is the coefficient matrix, which is a function of geometry. The objective is then to determine the cell gradient $\nabla\phi$ by solving the system of linear equations (eq. 5.74). The advantage of this methods is, that it still provides a good accuracy even with distorted cells. Furthermore, it is the least expensive method available in Fluent.

Chapter 6

Drop Tower Experiments

Experiments were performed to investigate the reorientation behavior and axial sloshing of liquid parahydrogen in a partially filled right circular cylinder due to a step reduction of gravity. This situation occurs at engine cutoff. Different temperature gradients along the cylinder wall in vertical direction were imposed to examine the influence of a wall superheat on the free surface. Experiments were conducted in the drop tower at the University of Bremen which provides a microgravity time of 4.7 s and a compensated gravity environment of 10^{-6} g_0 (acceleration due to gravity). The thermal preparation of the experiments allowed to create defined wall temperature gradients and a stratified or homogenous liquid temperature distribution. Several sensors along the cylinder wall and in the vapor region monitored the temperature. The pressure inside the experiment was recorded and visual access was enabled by an endoscope. Numerical simulations with the CFD solver Fluent 15.0 were carried out to supplement the experimental results.

This chapter is divided into two main parts. The first part covers a detailed description of the experimental setup and its instrumentation followed by the properties of the used materials and the experimental preparation [74]. The second part covers the numerical simulations where the used geometry, information about the spatial discretization, material properties, boundary and initial conditions are introduced. The results of the experimental and numerical investigations can be found in Sec. 8.1.

6.1 Parahydrogen Drop Tower Experiments

6.1.1 Experimental Apparatus

The experimental apparatus was designed for experiments with cryogenic fluids and first used by Kulev to investigate the reorientation behavior of liquid argon and methane [52, 53]. The experiment cylinder was enclosed in a stainless steel container under vacuum conditions (inner vacuum) and was connected with venting tubes to a tank (not shown in Fig. 6.1). This container was positioned in a second container holding a cooling bath filled with liquid helium. All this was housed in the outer cryostat. Between the outer cryostat and the cooling bath a vacuum was established to prevent heat conduction and convection (outer vacuum). Furthermore a radiation shield was inserted to avoid any radiative heat input between the environment and the cooling bath. The principal design with the several layers is illustrated in the rendering in Fig. 6.1.

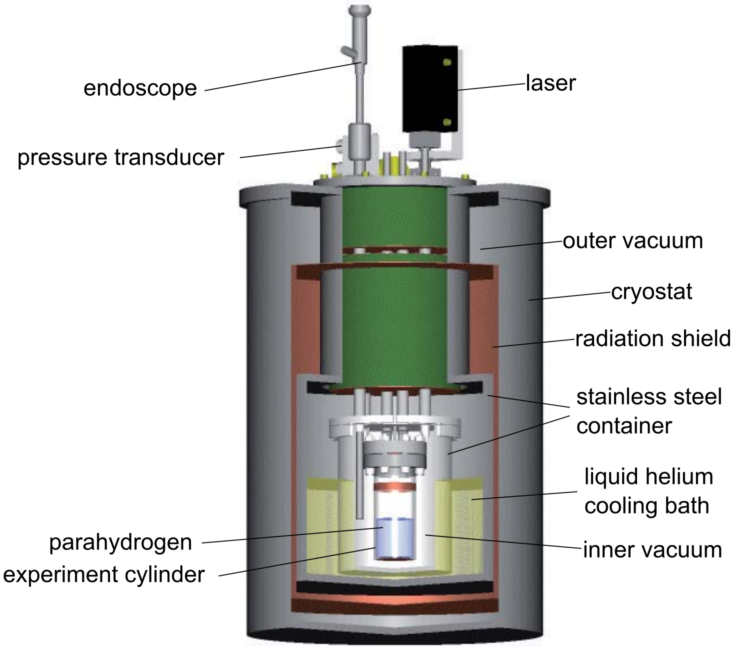

Figure 6.1: Design of the experiment with the cryostat, radiation shield, stainless steel container with cooling liquid, inner container and the glass cylinder containing the experiment liquid. Laser and pressure transducer are mounted on top of the cryostat.

The cryostat faced ambient conditions with $T_a \approx 300\,\mathrm{K}$ at $p_a \approx 101325\,\mathrm{Pa}$. Helium as coolant was kept at saturation conditions of $T_{he} \approx 4.2\,\mathrm{K}$ at $p_{he} = p_a$. These are the ambient conditions for the actual experiment. The glass cylinder contained $m^l \approx 7 \times 10^{-3}\,\mathrm{kg}$ of liquid parahydrogen in a pure parahydrogen vapor atmosphere. The space between cooling bath and experimental cylinder (the inner vacuum, usually evacuated to 0.02 Pa) could be pressurized with helium vapor to remove heat from the glass cylinder by conduction and convection. The experiment itself was sealed to the environment with a fixed volume and a fixed total amount of parahydrogen which was present as liquid and vapor.

For optical access the experimental cylinder was made of borosilicate glass fused to a stainless steel flange to connect it to the enclosing container. The glass cylinder itself has an inner diameter of $d = 52.4\,\mathrm{mm}$ ($R = 26.2$ mm) and an outer diameter of $D = 57.5\,\mathrm{mm}$ with a bottom thickness of $h_g = 5\,\mathrm{mm}$. The target fill level of liquid parahydrogen was $h_0 = 42\,\mathrm{mm}$. The coordinate system was placed on the center point location of the free surface. A drawing of the experiment cylinder with important dimensions and location of the coordinate system is given in Fig. 6.2 a). Visual detection of the free surface was enabled by an endoscope positioned next to the glass cylinder.

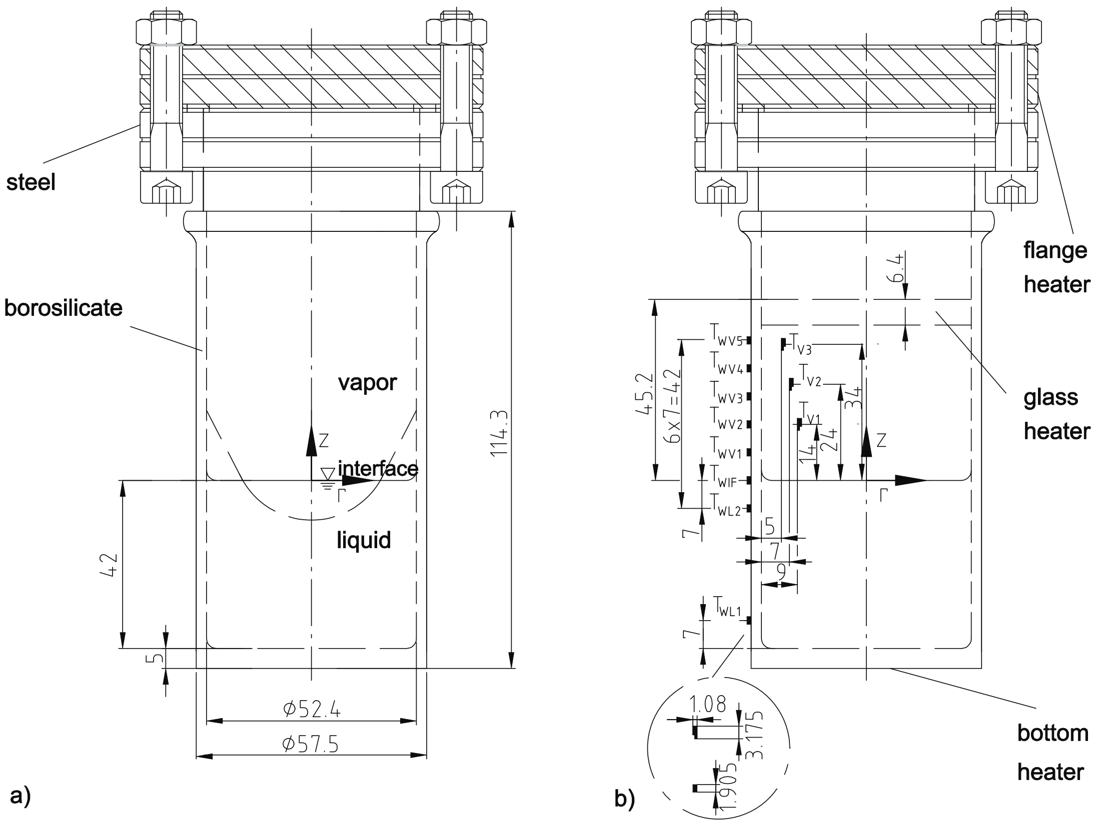

Figure 6.2: a) Experiment cylinder with dimensions and coordinate system. The free surface is shown at normal gravity (solid line) and microgravity conditions (dashed line). b) Experiment cylinder with positions and names of the temperature sensors and indicated locations of the heating elements. The dimensions of the temperature sensors are shown in the dash-dotted circle at the bottom left.

6.1.2 Temperature and Pressure Sensors

The experiment cylinder was equipped with several sensors for temperature measurement along the cylinder wall and in the vapor region. Figure 6.2 b) shows the experiment cylinder and the temperature sensor positions. The dimensions of the temperature sensors are shown in the dash-dotted circle at the bottom left of Fig. 6.2 b). DT670A-SD silicon diodes [54] manufactured by *Lake Shore* were used. They have an accuracy of $\pm 0.25\,\mathrm{K}$ and a response time to a temperature change of $100 \times 10^{-3}\,\mathrm{s}$. Their thermal dissipation is given with $10 \times 10^{-6}\,\mathrm{W}$. Two sampling rates were used. For the experiment preparation a sampling rate of 1 Hz was sufficient. The sampling rate was increased to 1000 Hz within the automated drop sequence. The sequence switched to a higher sampling rate approximately two seconds prior to the microgravity time. This higher sampling rate was kept for the entire experiment time. Eight sensors named $\mathrm{T_{wl1}}$, $\mathrm{T_{wl2}}$, $\mathrm{T_{if}}$ and $\mathrm{T_{wv1}}$ to $\mathrm{T_{wv5}}$ were glued with epoxy resin to the cylinder wall. Vapor temperature was measured with three sensors named $\mathrm{T_{v1}}$ to $\mathrm{T_{v3}}$. They were mounted on a 1.6 mm thick vertical plate made from woven fiberglass sheets. Design constraints did not allow to place sensors in the liquid phase. The vertical (z-direction) and radial (r-direction) position of the described sensors are listed in the Appendix in table A.4. The wires from the sensor were connected to a thermal anchor on the bottom of the enclosing cylinder to avoid heat exchange by conduction with the environment. The presented temperature data was averaged over $100 \times 10^{-3}\,\mathrm{s}$ (moving average) to filter out the signal noise.

The pressure inside the experiment cylinder was recorded with an ATM analog pressure transducer [85] by *TetraTec Instruments*. The range was set to $0 - 0.25 \times 10^6\,\mathrm{Pa}$ with an error of $\pm 250\,\mathrm{Pa}$. The transducer itself was located outside of the cryostat at ambient temperature conditions. The pressure data was sampled with the same rates (1 Hz for preparation, 1000 Hz for experiment) and also averaged over $100 \times 10^{-3}\,\mathrm{s}$ to filter out the signal noise.

6.1.3 Heating Elements

Thermal management was provided with three heating elements. One disk shaped heater with an effective area of $A_{BH} = 1290\,\mathrm{mm}^2$ was glued to the outside of the glass cylinder bottom. This one could be used to neutralize the stratification in the liquid. Another rectangular heat foil was glued to the cylinder wall with its top edge located 45.2 mm above the initial free surface. Its height was $h_{GH} = 6.4\,\mathrm{mm}$ with an effective area of $A_{GH} = 790\,\mathrm{mm}^2$. This one and a similar heater glued to the connecting flange at the lid were used to establish a temperature gradient along the cylinder wall. The flange heater had an effective area of $A_{FH} = 3000\,\mathrm{mm}^2$. All heating elements were produced by *MINCO* [68]. The model names are HK5544 for the bottom heater, HK5201 for the glass heater and HK5270 for the flange heater.

6.1.4 Visual Detection

Visual access was enabled through an endoscope with a CMOS camera mounted on top of the cryostat. The gray scale image resolution was 512×512 pixels with a frame rate of 60 Hz. For illumination a laser with wave length of 655 nm and 1 W power was used which was activated only when necessary to minimize heat input to the experiment. The laser was switched on three to four seconds prior to the drop. At $t = 0$ s an offset of approximately 0.3 K could be noticed between the interface temperature given by $\mathrm{T_{wif}}$ and saturation temperature calculated from the pressure data. This deviation could be noticed for every experiment. Temperature recordings without illumination showed, that the temperature T_{wif} and the saturation temperature computed with the pressure are within 0.01 K. When the laser was activated the sensors absorbed a certain amount of heat, that led to a temperature rise. All sensor recordings showed the same slope which led to the assumption that they absorbed the same amount of heat. Temperature differences between the sensors are therefore not affected by the laser.

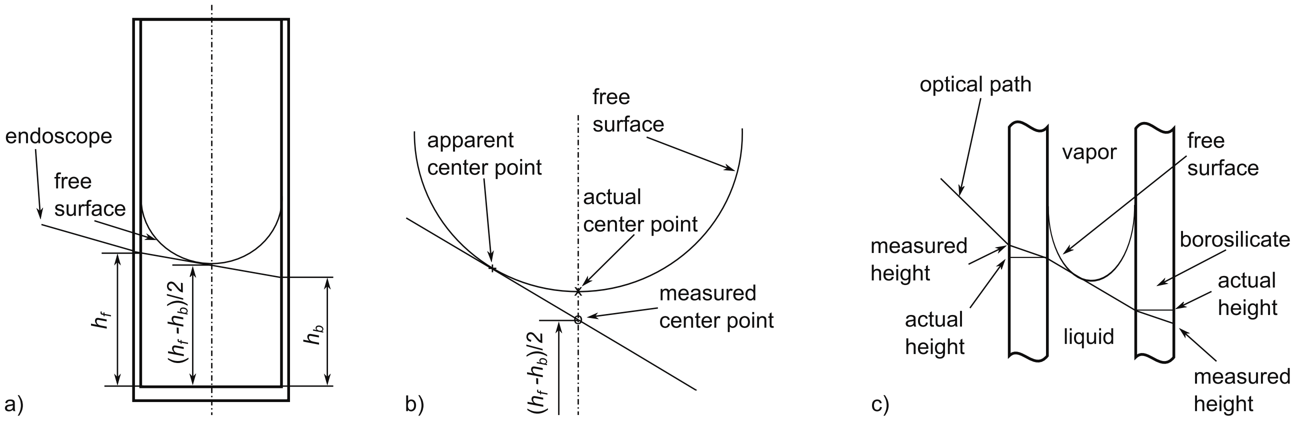

Figure 6.3: a) Scheme for indirect detection of the center point. b) Source of error for the used surface detection method. c) Optical path through the experiment.

The extraction of the surface contour requires a post-processing of the images. Several effects must be addressed to estimate the correct surface location. Certain markers were applied to the outside of the glass cylinder. The absolute position of these markers is known and was used to associate the extracted pixel value to a physical height. The position of the contact line of the free surface at the cylinder wall z_w and the center point location of the free surface z_c are of particular interest. In a first step, the corresponding pixel of the center and wall point was determined using the Canny-algorithm with Matlab. Two pixel values where extracted for each surface position, as shown in the Figs 6.3 a) and c). One corresponds to a physical height on the outside of the glass cylinder facing the endoscope, called h_f. The other one corresponds to a physical height on the outside of the glass cylinder opposite to the endoscope, called h_b. Once the pixel values for h_f and h_b were determined, they could be converted into a physical height using correction functions derived from the markers and calibration pictures. These functions were necessary since the fish eye lens of the endoscope distorted the picture in r- and z-direction. Throughout the second campaign the optical center was assigned to the geometrical center as depicted in Fig. 6.2 to minimize distortion. With this vantage point, the distortion in radial direction was not influencing the center and wall point location. So only a correction in z-direction needed to be applied. The coefficients of the polynomial correction functions are listed in the Appendix in table A.5.

The exact center point could not be detected due to the specific position of the endoscope. It was assumed, that the center point was in the middle of the free surface, so that the vertical displacement was approximated to be the arithmetic mean of the values for the front h_f and back h_b subtracted from the initial surface height h_0. With the current setting it was not possible to measure the actual center point location without knowing the free surface shape. What appears to be the center point on the recorded images is in fact only a point whose tangent points towards the camera. Hence, the derived center point deflection is generally lower than the actual center point. Figure 6.3 b) illustrates this issue. With this measurement technique, the surface position error is 0.24 mm assuming that the surface has a spherical shape (for computation see Appendix Sec. A.2.3). The error might be slightly larger for a different surface shape.

Aberration effects of the glass cylinder and the liquid parahydrogen must be considered. The refractive index of borosilicate used for the glass cylinder is well known and given by manufacturers such as *Schott* [75] with $n_{bs} = 1.5144$ for the laser wave length of $\lambda = 655\,\mathrm{nm}$. NBS-Monograph 168 [62] lists optical properties of liquid parahydrogen. At $T = 20\,\mathrm{K}$ and for the wavelength of the laser the refractive index is given with $n_{ph} = 1.1115$. The fact, that the height was measured on both sides of the glass cylinder (h_f, h_b) together with its small inner diameter d and n_{ph} close to 1 has the advantage, that the aberration effects caused by n_{bs} cancel each other out. Figure 6.3 c) depicts the optical path passing through the vacuum, cylinder wall, parahydrogen and again the cylinder wall. The endoscope position, the glass thickness and the refractive index of borosilicate caused an error between the measured height and the actual height, where h_f is estimated too high and h_b too low. We can assume, with the given values for the refractive index of parahydrogen and the cylinder radius, that the absolute difference between actual and estimated height is the same for the front and back. So both measurement errors cancel out each other.

6.1.5 Material Properties

Material properties must be treated temperature dependent in such a low temperature regime. All properties for density ρ, specific heat capacity c and heat conductivity λ for the glass cylinder and for the stainless steel flange are taken from CryoComp [23]. Properties for parahydrogen are not only dependent on temperature but also on pressure. Besides the above mentioned terms the dynamic viscosity μ is of interest for the liquid and gaseous phase. Surface tension σ is necessary to characterize the free surface motion. Saturation conditions T_{sat} and p_{sat} with the latent heat of evaporation Δh are required to calculate phase change, thus evaporation and condensation. All stated properties for parahydrogen are taken from NIST [58]. Characteristic values for parahydrogen, its vapor, borosilicate and stainless steel at the reference values $p_{ref} = 101325\,\text{Pa}$ and $T_{ref} = 20.271\,\text{K}$ are listed in table 6.1.

Table 6.1: Material properties for parahydrogen, borosilicate and stainless steel at $p = 101325\,\text{Pa}$ and $T = 20.271\,\text{K}$.

		Parahydrogen liquid	Parahydrogen gaseous	Borosilicate solid	Stainless steel solid
ρ	kg m^{-3}	70.83	1.339	2214	7900
μ	10^{-6} Pa s	13.330	1.0736	–	–
λ	10^{-3} W m^{-1} K^{-1}	103.45	17.002	147.0	1990
a	10^{-6} m^2 s^{-1}	0.150	1.056	2.34	19.4
c_p	J kg^{-1} K^{-1}	9729	12028	28.3	13.0
c_v	J kg^{-1} K^{-1}	5661	6460	–	–
Δh	10^3 J kg^{-1}	446.07	–	–	–
σ	10^{-3} N m^{-1}	1.926	–	–	–

6.1.6 Experiment Preparation

A well-defined thermal profile along the cylinder wall at the beginning of the microgravity phase was required. The experiment cavity is a closed system with a total volume of $V_E = 3.05 \times 10^{-3}\,\text{m}^3$ (experiment cylinder, venting pipes and tank), partially filled with liquid parahydrogen $V_{ph}^{l} = 90.6 \times 10^{-6}\,\text{m}^3$ and parahydrogen vapor. The experiment cylinder as presented in Fig. 6.2 has a total volume of $V_{EC} = 305.4 \times 10^{-6}\,\text{m}^3$ (up to $z = 93\,\text{mm}$ above the free surface). To avoid any external thermal influences the glass cylinder was enclosed in a container which was kept at saturation temperature conditions of helium at $T_{he} \approx 4.2\,\text{K}$. In this temperature regime heat exchange by radiation could be neglected. The open space in the housing container (inner vacuum) was evacuated to avoid heat conduction and convection. Adding some helium vapor into the evacuated space led to a heat transfer from the experiment cylinder to the cooling bath. This mechanism was used to extract heat from the experiment itself and set it to a neutral state. The experiment cylinder and the connected volumes were evacuated before each test campaign to avoid remaining fluids and to assure a filling with hydrogen gas of 99.9995 % purity [2]. The test liquid was condensed from that room temperature vapor several days prior to the experimental campaign. This ensured, that the spin of the orthohydrogen (parallel aligned spin) molecules changed to an antiparallel aligned spin and the test liquid was only parahydrogen. The heat released by the conversion was monitored indirectly by pressure changes within the experimental cylinder. Pressurization of the inner vacuum with gaseous helium (as noted) removed this heat of conversion by convection. A vacuum pump restored the pressure of the inner vacuum to the required level of 0.02 Pa.

Starting from this condition several means were used to establish the target wall temperature profile. For very low temperature gradients no stimuli were needed and the heat conducted through the connection of the two stainless steel flanges was sufficient. Even though the entire system was kept as insulated as possible this little heat flow caused rising temperatures along the cylinder wall. For a higher wall temperature gradient either the glass heater or the flange heater was used. A detailed explanation of the preparation for an isothermal and a non-isothermal experiment can be found in Sec. 6.1.7 and Sec. 6.1.8, respectively.

For some experiments a uniform temperature distribution in the liquid was required. Since it was not possible to position a sensor in the liquid phase, the three sensors along the wall T_{wl1}, T_{wl2} and T_{wif} were used. Even though they did not monitor the exact liquid temperature it was still useful for the thermal management. This method was tested in prior ground tests. The onset of nucleate boiling should be avoided since remaining vapor bubbles might disturb the reorientation process during the free fall test. For safety reasons and to avoid any interference all heating elements were turned off before the gravity step reduction.

Within two campaigns six experiments were conducted (three experiments each). Information about the experiments is listed in table 6.2. The first campaign (numbers 1 to 3) was used as a technology demonstrator. Besides an insufficient center point detection the produced data could be used for further analysis. During the first campaign the endoscope was located above the free surface focusing on the advancing contact line of the free surface along the cylinder wall. A drawback of this endoscope position was, that the center point location of the free surface could not be determined adequately. Surface detection could be improved by lowering the endoscope. Both perspectives are presented in Fig. 6.4 a) and Fig. 6.4 b). All experiments contained the same amount of liquid parahydrogen. An elevated endoscope position allowed to observe the free surface and the advancing contact line, whereas the other configuration was leveled with the initial free surface. The second perspective (numbers 4 to 6) made a sufficient center point detection possible.

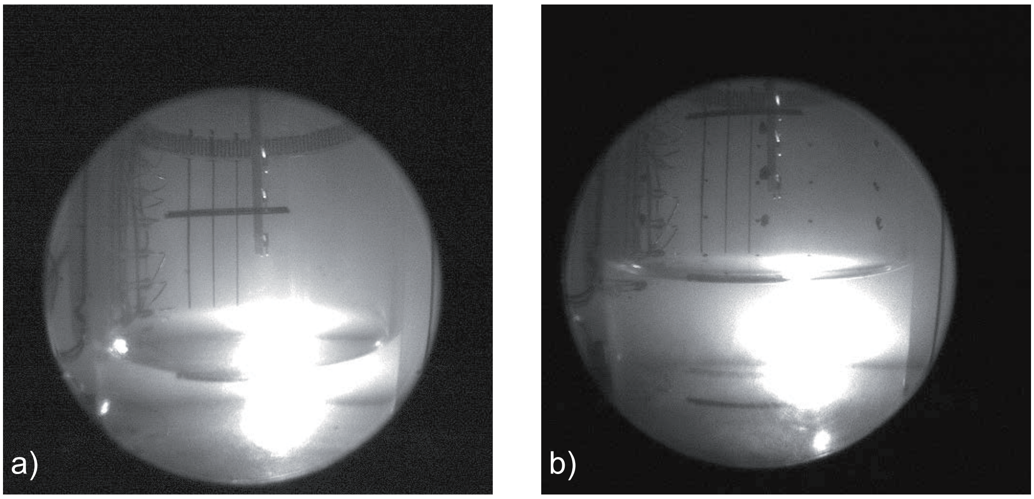

Figure 6.4: Vantage point for surface visualization for both experimental campaigns. a) Image of first experimental campaign: C1, A2, C3. Endoscope location above the initial free surface led to insufficient surface detection. b) Image of second campaign: C4, A5, B6. Endoscope position leveled with initial free surface height allowed a satisfying surface detection.

The target wall temperature gradients $\Delta T/\Delta z$ span from isothermal conditions $\Delta T/\Delta z = 0\,\mathrm{K\,mm^{-1}}$ up to $\Delta T/\Delta z = 0.7\,\mathrm{K\,mm^{-1}}$. The temperature gradient was determined from sensor $\mathrm{T_{wif}}$ upwards in positive z-direction. The experiments were separated into three groups depending on the wall superheat. The first group contains the two experiments with an isothermal wall. They are indicated with a capital A. Only one experiment is in the second group, named with a capital B. This group includes experiments with a wall temperature gradient but without nucleate boiling throughout the reorientation. The third group is identified with a capital C and consists of three experiments where the wall temperature gradient caused nucleate boiling. To distinguish the experiments the group letter is accompanied by a number which stands for the chronological order of the experiments. As an example, C3 is the third experiment conducted and had a wall temperature gradient that caused nucleate boiling.

Experiments A2 and A5 were designed as reference cases. Their initial state was achieved by short pressurization of the inner vacuum to homogenize the temperature distribution along the glass cylinder. The vacuum was re-established before the drop. The gradient for B6 and C4 was achieved with the flange heater. The wall temperature gradients for C1 and C3 were created with the glass heater. A major difference in the preparation process of both campaigns (C1, A2, C3 and C4, A5, B6) is the use of the bottom heater. The first three experiments had a stratification build up in the liquid phase. In the latter three experiments the fluid temperature was homogenized by the bottom heater.

Table 6.2: Initial wall temperature gradient with dimensions and in dimensionless form, saturation temperature, initial and final pressure, amount of subcooling, characteristic initial wall superheat, usage of heating elements, material properties used for scaling, characteristic time t_{pu} and velocity v_{pu}, Bond number in microgravity conditions and Ohnesorge number.

		A2	A5	B6	C4	C1	C3
$\Delta T/\Delta z$	K mm^{-1}	0.00	0.00	0.05	0.21	0.26	0.69
$\Delta T^*/\Delta z^*$	–	0.00	0.00	0.07	0.26	0.36	0.92
$T_{sat,0}$	K	20.52	20.06	19.20	20.60	19.32	19.70
p_0	10^3 Pa	109.15	95.01	72.74	111.54	75.66	85.22
p_1	10^3 Pa	108.98	95.02	73.21	113.85	78.20	93.84
Θ_{sub}	K	2.46	0.20	0.12	0.31	1.24	2.24
Θ_{sup}	K	0.00	0.00	0.85	4.04	5.47	14.68
Bottom heater	–	–	✓	✓	✓	–	–
Glass heater	–	–	–	–	–	✓	✓
Flange heater	–	–	–	✓	✓	–	–
σ	10^{-3} N m^{-1}	1.88	1.96	2.10	1.87	2.08	2.02
ρ	kg m^{-3}	70.54	71.07	72.01	70.45	71.88	71.47
μ	10^{-6} Pa s	13.06	13.57	14.57	12.98	14.42	13.97
t_{pu}	10^{-3} s	822	808	785	823	788	798
v_{pu}	10^{-3} m s^{-1}	31.9	32.4	33.4	31.8	33.2	32.9
Bo$_1$	10^{-4}	2.58	2.49	2.35	2.59	2.37	2.43
Oh	10^{-4}	2.22	2.25	2.31	2.21	2.30	2.27

External stimulation by the different heaters caused phase change as well as thermal expansion and compression of the vapor which influenced the pressure p_0 and therefore the saturation temperature $T_{sat,0}$. Table 6.2 summarizes the operation of heating elements, the mean gradient, subcooling of liquid, pressure and saturation temperature at the beginning of the microgravity time. The mean gradient is the average computed from the temperature difference between two adjacent wall sensors over their distance to each other

$$\frac{\Delta T}{\Delta z} = \frac{1}{5} \sum_{n=wif}^{5} \frac{T_{n+1} - T_n}{z_{n+1} - z_n} \,. \tag{6.1}$$

In the following, the cylinder radius R is chosen for the scaling of lengths. The saturation temperature $T_{sat,0}$ at the beginning of the microgravity time is chosen as a characteristic temperature since it is a material property and takes thermodynamic characteristics of the test fluid into account. A dimensionless wall temperature gradient has the following form

$$\frac{\Delta T^*}{\Delta z^*} = \frac{\Delta T}{\Delta z} \frac{R}{T_{sat,0}} \,. \tag{6.2}$$

For the characteristic time and velocity t_{pu} and v_{pu} were chosen according to the eqs. 2.24 and 2.25. The magnitude of subcooling is defined as the difference of sensor $\mathrm{T_{wif}}$ and $\mathrm{T_{wl1}}$

$$\Theta_{sub} = T_{wif} - T_{wl1} \,. \tag{6.3}$$

Furthermore, a characteristic wall superheat temperature Θ_{sup} is given. It is computed from the difference of T_{wif} and the temperature at the estimated final contact line position T_{zw1} at $z_{w,1} = 17.47\,\mathrm{mm}$. This temperature is computed by a linear interpolation between T_{wv2} and T_{wv3}, which gives for T_{sup}

$$\Theta_{sup} = T_{zw1,0} - T_{wif,0} = \big(0.496\, T_{wv2,0} + 0.504\, T_{wv3,0}\big) - T_{wif,0} \,. \tag{6.4}$$

6.1.7 Preparation of the Isothermal Experiment A5

Once the experiment was integrated into the drop tower, the preparation phase begun. Experiment A5 had isothermal boundary conditions with as little subcooling in the liquid as possible. Conditioning of the temperature distribution started $t = -784\,\mathrm{s}$ prior to the start of the experiment (capsule release). At this instant in time, an unwanted temperature gradient had build up as indicated by the black triangles in Fig. 6.5. The bottom heater was activated with $P_{BH} = 0.1\,\mathrm{W}$ to reduce the subcooling and the inner vacuum was flushed with gaseous helium to neutralize the stratification in the wall. The helium was extracted with the use of the pressure difference between inner vacuum and the vacuum conditions of the drop tower. At $t = -38\,\mathrm{s}$ a sufficient temperature profile could be established (see blue markers and line in Fig. 6.5). The bottom heater was switched off to avoid nucleate boiling in the bulk. The heat conduction and convection by the helium molecules led to a pressure decline in the experiment cylinder with a resulting drop of the saturation temperature (represented by the markers at $z = 0\,\mathrm{mm}$) from $T_{sat} = 20.43\,\mathrm{K}$ at $t = -784\,\mathrm{s}$ to $T_{sat} = 20.08\,\mathrm{K}$ at $t = -38\,\mathrm{s}$. The magenta colored marker represents the measured temperature progression at the beginning of the experiment. At this time, low pressure values of about $p = 0.02\,\mathrm{Pa}$ for the inner vacuum could be ensured. The offset between measurements at $t = -38\,\mathrm{s}$ and $t = 0\,\mathrm{s}$ are caused by the laser as explained earlier in Sec. 6.1.4.

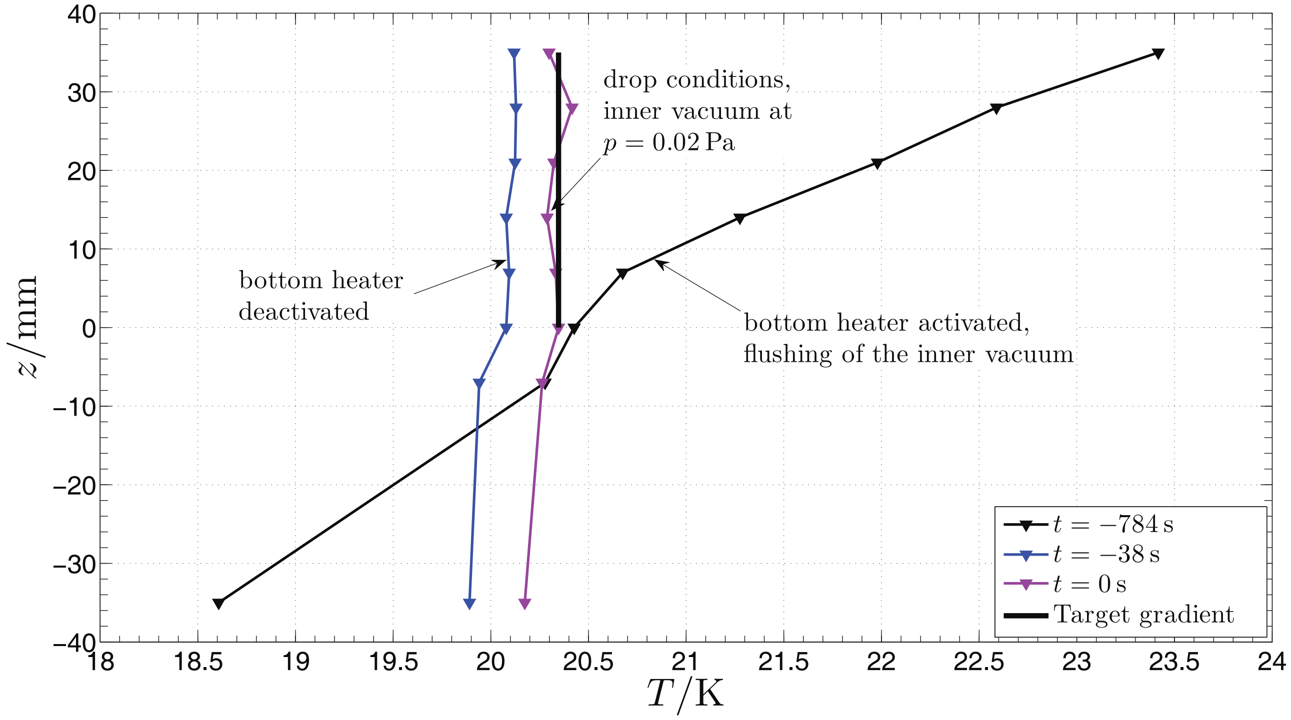

Figure 6.5: Experiment A5: Temperature progression along the wall at certain time instances. Measured temperatures are indicated by downward facing triangles. The solid lines connecting the discrete values are included for better visibility and do not represent the temperature progression between two sensors. The solid black line represents the target gradient.

6.1.8 Preparation of the Non-Isothermal Experiment B6

The preparation procedure of a non-isothermal experiment required different means to reach the target gradient. The bulk of experiment B6 was subcooled and a non-uniform and too low wall temperature gradient was established. At $t = -623\,\mathrm{s}$ a power $P_{BH} = 0.1\,\mathrm{W}$ was used to neutralize the subcooled state of the bulk (see black markers in Fig. 6.6). The temperature progression at $t = -201\,\mathrm{s}$ showed the positive effect of the bottom heater. The entire heat was absorbed by the liquid parahydrogen. Increasing temperatures above the free surface ($z < 0\,\mathrm{mm}$) resulted from the heat inflow through the connecting flange as explained in Sec. 6.1.6. To increase the wall temperature gradient, the flange heater was activated with a power of $P_{FH} = 0.5\,\mathrm{W}$ (see red marker in Fig. 6.6). Shortly after, at $t = -177\,\mathrm{s}$, the bottom heater could be deactivated. A well-defined temperature profile was reached at $t = -34\,\mathrm{s}$. At this instance in time, not only the wall temperature was increased but also the vapor temperature which caused a slight increase of the saturation temperature. This effect can be seen by comparing the surface temperatures ($z = 0\,\mathrm{mm}$) at the time of flange heater activation (red marker) and deactivation (green marker). Again, the offset of the temperatures at the beginning of the experiment (magenta markers) can be explained with the heat inflow from the laser.

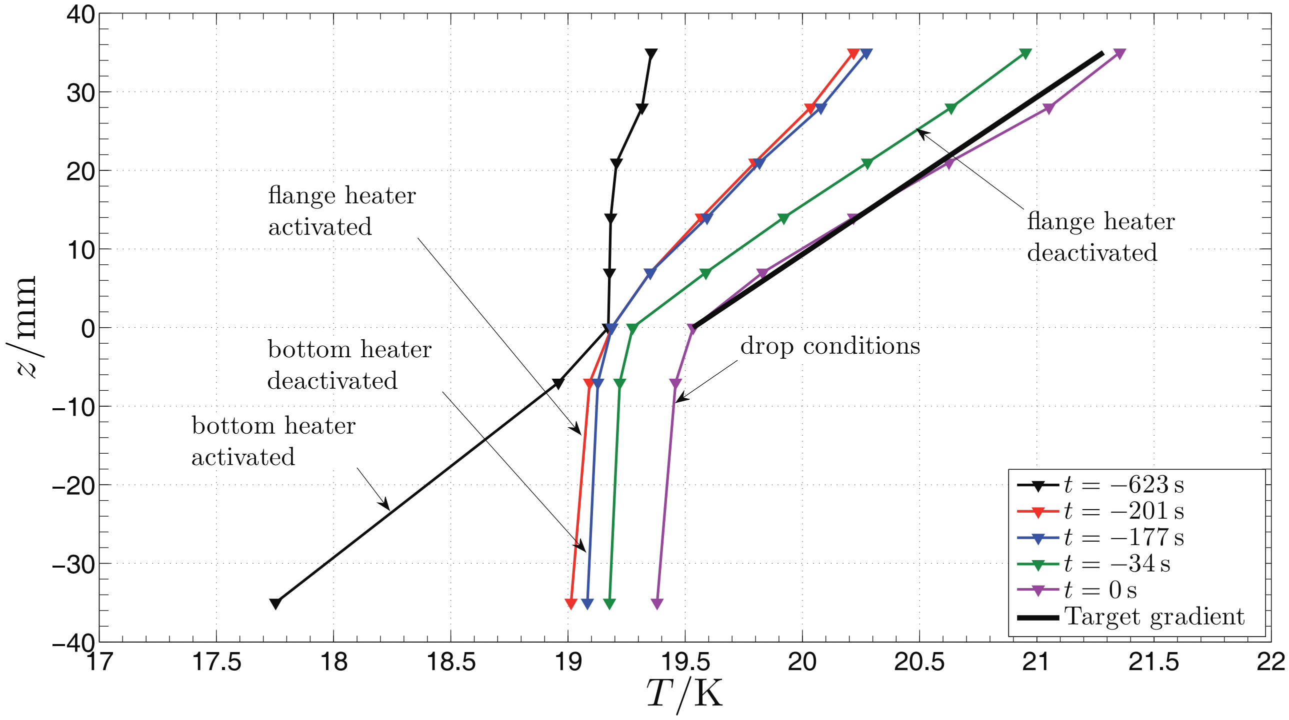

Figure 6.6: Experiment B6: Temperature progression along the wall at certain time instances. Measured temperatures are indicated by downward facing triangles. The solid lines connecting the discrete values are included for better visibility and do not represent the temperature progression between two sensors. The solid black line represents the target gradient.

6.2 Numerical Simulation of Reorientation and Axial Sloshing

The flow Solver Fluent 15.0 was used for the numerical simulations. Only experiments without nucleate boiling were of interest. Therefore, CFD simulations focused on the experiments A5 and B6. These experiments were used as reference cases to validate the numerical model. Furthermore, simulations were used to supplement the experimental data and investigate the free surface behavior in presence of other wall temperature gradients.

6.2.1 Geometry Simplifications

Not all features of the experiment geometry shown in Fig. 6.2 were necessary for the axial sloshing kinematics and the thermodynamic effects. The right circular cylinder allowed to create a two-dimensional geometry with the center line as symmetry axis. The experiment cylinder was reduced to a hollow cylinder with a bottom. Instrumentation inside the experiment cylinder (vapor sensors, mounting plate and wires) were neglected, since it would have disturbed the flow field. Only the eight wall temperature sensors were modeled physically to cover the heat diffusion. The experiment cylinder had a volume of $V_{EC} = 305.4 \times 10^{-6}\,\mathrm{m}^3$, but the total open volume was $V_E = 3.05 \times 10^{-3}\,\mathrm{m}^3$ (see Sec. 6.1.6). A cylindrical shaped volume was added on top of the cylinder geometry to consider the remaining $2.76 \times 10^{-3}\,\mathrm{m}^3$. A drawing of the simplified geometry can be found in Fig. 6.7.

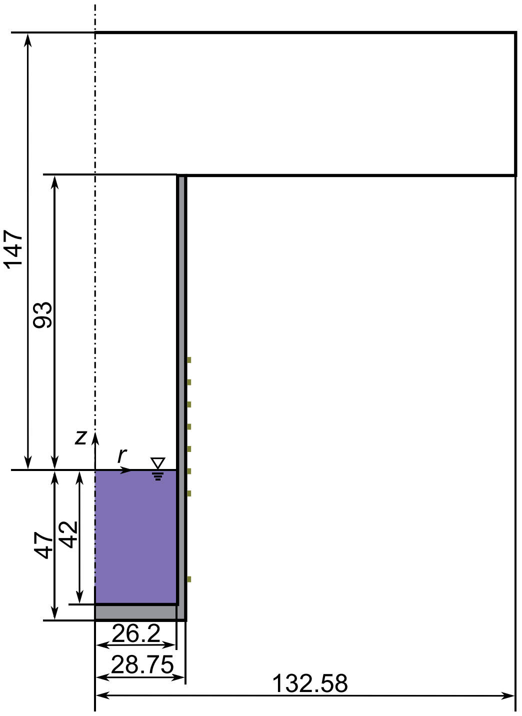

Figure 6.7: Simplified geometry used for the numerical simulations with glass cylinder (grey), liquid parahydrogen (blue) and temperature sensors in yellow. The vapor region is transparent. The volume above the glass cylinder represents the connecting pipes and the tank.

6.2.2 Mesh Generation and Boundary Conditions

As described in Sec. 6.2.1, it was possible to reduce the experimental design to a two-dimensional geometry. Fluent can use surface meshes, which have only two-dimensions extending in x- and y-direction. ICEM CFD 15.0 was used to create meshes consisting of quadrilateral elements (quads). The surface discretization is based on the blocking strategy [4]. Therefore, one initial quadrilateral block was created, which was split into smaller blocks (see Fig. 6.8 b)) that represented the discretized space (see Fig. 6.8 a)). All unnecessary blocks, which are transparent in Fig. 6.8 b), were deleted. Nodes must be set on the edges of the blocks to specify the number of cells used for the mesh. These nodes represent the corners of a cell. The cell size for either utilized mesh is too small to present the mesh as a whole. A detailed view of the mesh in the vicinity of the contact point can be found in Fig. 6.9. As a last step, regions and boundary conditions must be defined. Regions are necessary to assign the right material (parahydrogen, borosilicate or sapphire) to certain portions of the mesh. Boundary conditions specify the behavior of the corresponding edge. As shown in Fig. 6.8 b) and in the detail drawing of Fig. 6.8 c) three different zones were defined. The largest portion of the mesh was used to model parahydrogen and is colored in blue. The glass cylinder is colored in gray and had the material properties of borosilicate assigned to it. Temperature sensors along the wall are represented in red and were connected with the material sapphire. All applied boundary conditions can be found in Fig. 6.8 c). The green line represents the symmetry axis. All other outer edges were defined as adiabatic walls. Two interfaces were required to model the energy exchange between two adjacent regions. One interface defines the heat transfer between temperature sensors and glass (blue lines), whereas the other interface defines this exchange between parahydrogen and glass cylinder (orange line). Since the fluid was present in both phases, a static contact angle $\gamma_s = 0°$ was assigned to this interface and all edges bounding the fluid (blue) region.

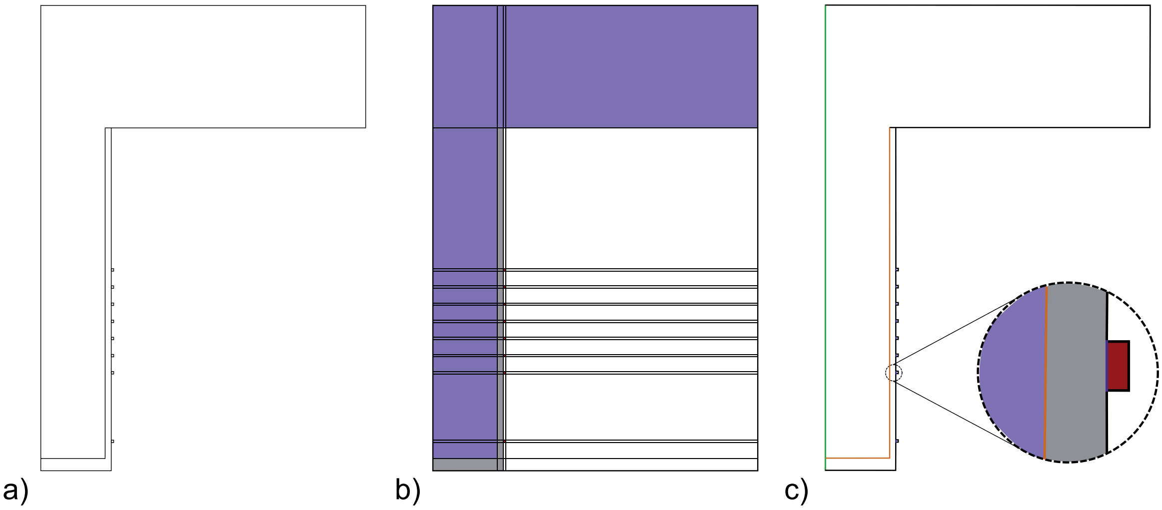

Figure 6.8: a) Simplified geometry used for the numerical simulations with glass cylinder, wall temperature sensors and surface open to the fluid. The volume above the glass cylinder represents the connecting pipes and the tank. b) Blocking strategy with marked areas that represent the different materials. Blue indicates parahydrogen, gray borosilicate for the glass cylinder and red sapphire for the wall temperature sensors. For better visibility all areas are shown in the detailed drawing in Fig. 6.7 c). The white blocks were deleted since they were not necessary for the computation. c) Boundary conditions for the used mesh. All internal edges of the used blocks are blanked out. The symmetry axis is highlighted in green. The orange edge represents the solid-fluid interface and the blue line the solid-solid interface. All adiabatic walls are colored black. The detailed drawing shows a sensor with the glass wall and fluid together with the applied boundary conditions.

Table 6.3: Characteristic values of the used grids M1, M2 and M3. Δr and Δz give the edge length of the cells within the area of interest. C_r and C_z are the factors for the exponential growth of the edge length. N gives the total number of used cells.

		M1	M2	M3
Δr, Δz	mm	0.5	0.2	0.1
C_r		1.15	1.06	1.07
C_z		1.19	1.16	1.23
N		17849	105886	408404

A mesh sensitivity study was performed to investigate the influence of the cell size on the results. Three meshes with the same blocking strategy were created only differing in the cell size. All cells were either squares or rectangles. In the area of interest which covers the inside of the glass cylinder and the cylinder itself ($0\,\mathrm{mm} \leq r \leq 28.75\,\mathrm{mm}$ and $-47\,\mathrm{mm} \leq z \leq 93\,\mathrm{mm}$) cells had the same edge length in both directions. Outside this area the cell length increased exponentially. The grids were named with increasing refinement M1, M2 and M3. Table 6.3 lists the minimum edge length of a cell (corresponding to the one in the area of interest), the exponential factor of growth in both directions and the total number of cells.

6.2.3 Material Properties

Material properties must be defined for the liquid and gaseous parahydrogen, the glass cylinder and the temperature sensors. The housing of the sensors are made from sapphire [54] which led to the assumption to model the sensors as a block of sapphire. Properties for sapphire were taken from CryoComp [23]. Fluent requires density ρ, specific heat capacity at constant pressure c_p and thermal conductivity λ for all materials. For fluids, viscosity μ, molecular weight M, specific standard state enthalpy h and the corresponding reference temperature T_{ref} must be stated additionally. To model interaction between phases or zones further properties are required. These are the static contact angle γ_s and the surface tension σ. The latent heat of evaporation is considered as the difference of the specific enthalpies of liquid and gaseous phase of the same fluid, thus $\Delta h = h^v_{sat} - h^l_{sat}$. For this work, material properties of liquid parahydrogen were treated temperature independent. The specific standard state enthalpy of the liquid was set to $h^l = 0\,\mathrm{J\,mol^{-1}}$. All required liquid properties for the pressure levels $p_{0,A5} = 95.01\,\mathrm{kPa}$ and $p_{0,B6} = 72.74\,\mathrm{kPa}$ can be found in the Appendix in table A.1.

Gaseous parahydrogen and the solid structures face temperatures up to 30 K. Table A.2 in the Appendix lists the material properties for gaseous hydrogen as n$^{\text{th}}$-order polynomial functions of the temperature. The valid temperature span lasts from saturation temperature to

31 K, which is chosen slightly higher to include all occurring temperatures. Density ρ^s, specific heat capacity c_p^s and thermal conductivity λ^s for Pyrex and Sapphire as n$^{\mathrm{th}}$-order polynomial functions of the temperature can also be found in table A.2. Static contact angle and molecular weight of parahydrogen are temperature and pressure independent. Their values are $\gamma_s = 0°$ and $M_{ph} = 2.0159\,\mathrm{kg\ kmol^{-1}}$. The saturation temperature is dependent on the pressure and given with the following equation

$$T_{sat} = 15.46\ [\mathrm{K}] + 6.00 \times 10^{-5} \left[\frac{\mathrm{K}}{\mathrm{Pa}}\right] p - 1.00 \times 10^{-10} \left[\frac{\mathrm{K}}{\mathrm{Pa}^2}\right] p^2 \,. \tag{6.5}$$

6.2.4 Initial Conditions

Two drop tower experiments were simulated to validate the numerical method and acquire more information about the occurring effects. These two experiments are A5 and B6 since they are the only experiments were a sufficient surface detection was possible and no nucleate boiling occurred. The corresponding simulations were called SA5 and SB6. Furthermore, six simulations with dimensionless wall temperature gradients between $0 < \Delta T^*/\Delta z^* < 0.07$ were conducted. Their names compose of a capital s for simulation and a number regarding to the applied dimensionless wall temperature gradient. For example, S05 stands for a simulation with $\Delta T^*/\Delta z^* = 0.05$. These simulations were used to gain data for various wall temperature gradients without nucleate boiling. All simulations had the initial surface at $z = 0\,\mathrm{mm}$. An evolved static meniscus was not considered at this point. The initial temperature distribution can be found in Fig. 6.10.

For SA5 and SB6, the initialization follows the experimental values for pressure and temperature. Data from the experiments without illumination showed that $T_{sat} = T_{wif}$. To account for this effect, the temperature sensor data was reduced by $\Theta_0 = T_{wif,0} - T_{sat,0}$. A linear interpolation between two temperature sensors was applied to initialize the temperature field where no experimental data was available. Due to the absence of sensors in the liquid parahydrogen, liquid and solid phase had the same initial temperature distribution up to $z = 0\,\mathrm{mm}$. The solid located above $\mathrm{T_{wv5}}$ was initialized by extrapolation of the progression between $\mathrm{T_{wv4}}$ and $\mathrm{T_{wv5}}$. The gaseous phase was initialized in the same way using the temperature sensors $\mathrm{T_{v1}}$ to $\mathrm{T_{v4}}$. The vapor temperature between $z = 83\,\mathrm{mm}$ ($\mathrm{T_{v4}}$) and $z = 93\,\mathrm{mm}$ was extrapolated from the progression between $\mathrm{T_{v3}}$ and $\mathrm{T_{v4}}$. Between $93\,\mathrm{mm} \le z \le 103\,\mathrm{mm}$ the ullage was strongly stratified and increased to a temperature of $T^v = 30\,\mathrm{K}$ and was held constant for $z > 103\,\mathrm{mm}$. Test simulations showed that there is no influence of the vapor temperature above $z = 103\,\mathrm{mm}$. Below $z = 0\,\mathrm{mm}$, all non-isothermal simulations had the same initial pressure and temperature distribution as experiment B6 since the preparation procedure of corresponding experiments would be the same as for B6 (see Sec. 6.1.8). Since it was not clear how the vapor would be stratified for other temperature gradients, simulations S01 to S06 had the same temperature initialization for the ullage as for the wall, thus $T_r =$ const. The wall temperature of SA5 above $\mathrm{T_{wv5}}$ was kept constant. Initial temperature values for SA5 and SB6 are plotted in Fig. 6.10 a) and Fig. 6.10 b), respectively. Figure 6.10 c) shows the progression for the other simulations. Exact values are listed in the tables A.6 and A.7 in the Appendix.

The static meniscus in the vicinity of the wall (eq. 2.21) cannot be initialized within the simulation preparation but must be calculated by Fluent. Therefore, computations were conducted with normal gravity $g_0 = 9.81\,\mathrm{m\ s^{-1}}$ acting in negative z-direction. Fluent computed the flow field for 0.2 seconds physical time to allow the meniscus to evolve. The detailed free surface shape in the vicinity of the wall is depicted for all three grids in Fig. 6.9. The mesh is visible to compare the cell size of the used grids. One can see, that the meniscus was not fully evolved and a capillary wave was moving towards the center axis. Test simulations were conducted to find a stable surface configuration. The viscosity of liquid parahydrogen was not high enough to attenuate the wave. Once the wave reached the center its amplitude amplified and caused chaotic surface perturbations. Further simulations showed, that there is no effect of the initial meniscus shape on the free surface reorientation. It has to be mentioned, that the temperature field changes from its initial conditions. The stated time for the normal gravity simulation was a reasonable compromise between the correct shape of the static meniscus and the correct temperature field at the beginning of the microgravity time. Deviations of numerically derived temperatures from experimental temperatures at t_0 are a result of the described surface initialization.

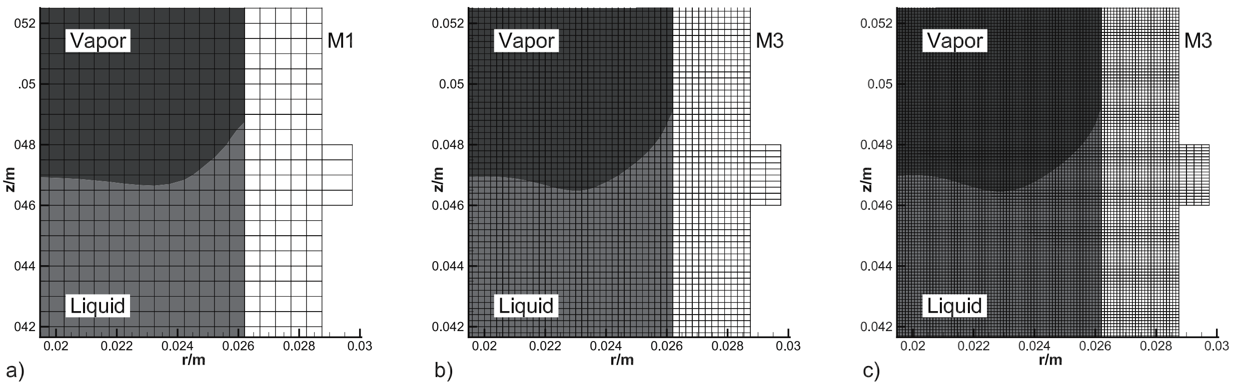

Figure 6.9: Free surface with evolved static meniscus in the vicinity of the wall after 0.2 seconds physical time. Free surface is extracted for $F = 0.5$. Mesh is visible. a) M1. b) M2. c) M3.

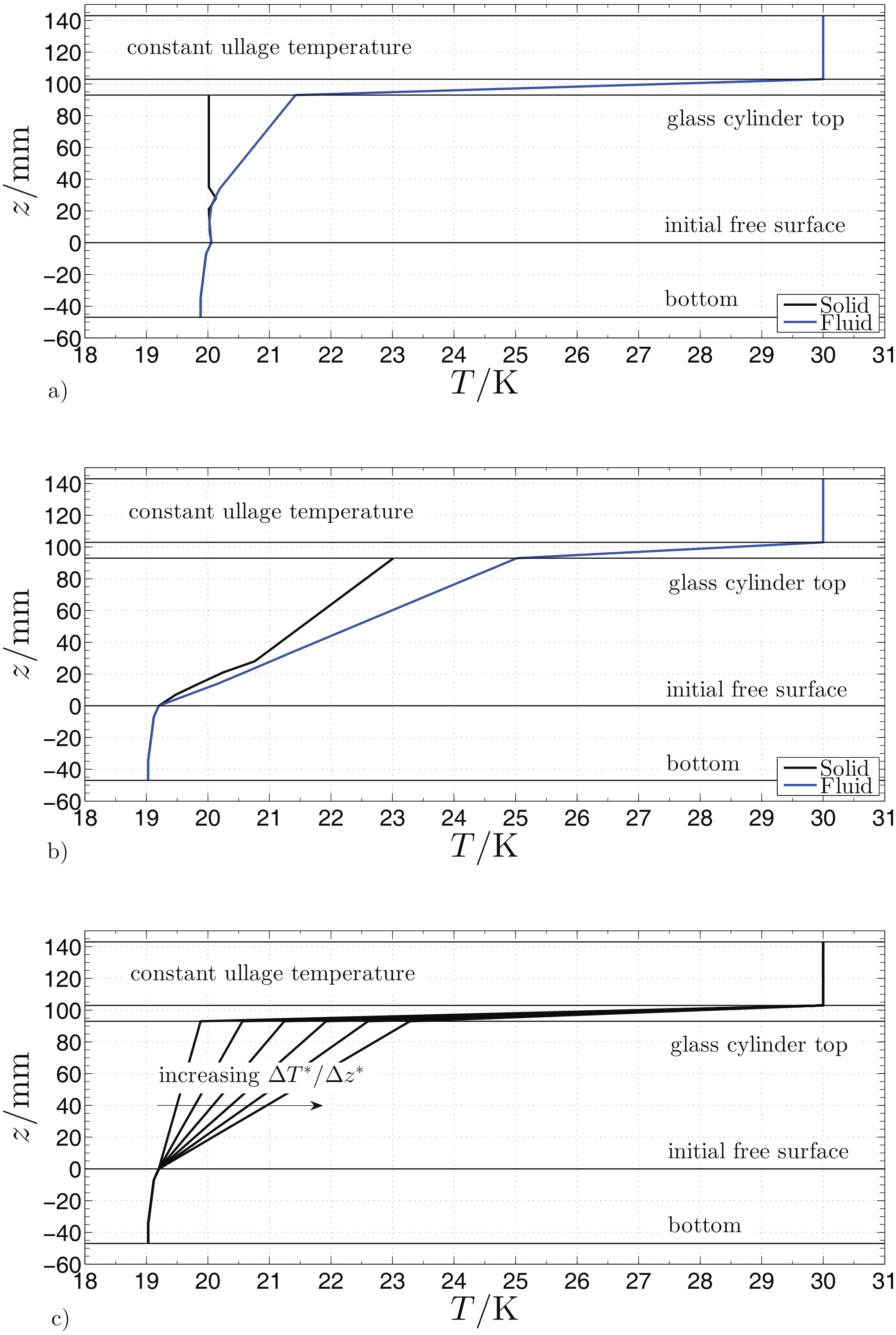

Figure 6.10: Initial temperature field for simulations. Horizontal solid lines indicate the bottom of the glass cylinder ($z = -47\,\mathrm{mm}$), the free surface ($z = 0\,\mathrm{mm}$), the top of the glass cylinder ($z = 93\,\mathrm{mm}$) and the area of constant ullage temperature ($103\,\mathrm{mm} \leq z \leq 143\,\mathrm{mm}$)). a) Isothermal simulation SA5. b) Non-isothermal simulation SB6. c) Non-isothermal simulations S01 to S06 with varying dimensionless temperature gradients $0.01 \leq \Delta T^*/\Delta z^* \leq 0.06$.

6.2.5 Numerical Settings

The intention of this section is to enable the reader to set up a simulation for the introduced experiment.

The volume of fluid (VOF) method was used to distinguish between the liquid or gaseous phase in each cell [44]. Liquid was treated as an incompressible fluid with temperature dependent material properties. The vapor phase was represented by an ideal gas model with temperature dependent material properties. A surface tension model was active with temperature dependent surface tension coefficient. To compute the phase change mass flux $\widehat{m}$ over the free surface the Lee model with the Hertz-Knudsen equation, eq. 4.94, was used [3, 57]. No feasible pressure prediction was possible with any phase change frequency $\overline{f}$ due to the VOF method as explained by van Foreest et al. [86]. However, in this work values for $\overline{f}$ in the range of $1\,\mathrm{s}^{-1} \leq \overline{f} \leq 20\,\mathrm{s}^{-1}$ were applied. To solve the set of equations presented in Sec. 5.2 the SIMPLE scheme was used for the pressure-velocity coupling on the pressure-based solver. Density, momentum and energy were discretized by the second order upwind method, the pressure with the PRESTO! algorithm and the volume fraction with the geo-reconstruct method. Gradients are least squares cell based and the transient formulation is solved using the first order implicit method. A detailed explanation of the used methods is given in Sec. 5.3.2 based on the manual [3].

Chapter 7

Sounding Rocket Experiment

The suborbital flight experiment Sounding Rocket Compere Experiment (SOURCE-II) was conducted by the French-German research group Comportement des Ergols dans les Reservoir (COMPERE) to investigate the free surface behavior of a two-phase, single-species system in presence of non-isothermal boundary conditions. This work used the experiment as a benchmark test case [35] to validate the used numerical codes. This chapter explains the experimental design and the execution procedure. For the numerical study a simplified geometry was introduced. The discretization of the used computational domain with initial and boundary conditions and material properties can be found in the following sections. The results of the numerical simulations in comparison with the experimental findings are included in Sec. 8.2.

7.1 SOURCE-II Sounding Rocket Experiment

7.1.1 Experimental Apparatus

The experiment was integrated in a sounding rocket (MASER 12) and launched in February 2012 from Esrange, Sweden. A detailed description of the experiment is given by Fuhrmann and Dreyer [31] and only an overview of the components is given here.

The experiment tank was milled into a rectangular block made of quartz glass (Suprasil®) with ground dimensions of $80\,\mathrm{mm} \times 80\,\mathrm{mm}$, height of $H = 120\,\mathrm{mm}$ and center bore radius of $R = 30\,\mathrm{mm}$. A sketch with the main components (labeled with Arabic numbers) can be found in Fig. 7.1. The test cell (1) could be filled with liquid from the bottom through two feeding lines (2) and pressurized (3) or vented (4) through the top. The diffuser (5) at the end of the vapor line was installed to prevent the free surface from distortion by the vapor entering the test cell. Two heating elements were present. One (6) was located at the bottom of the

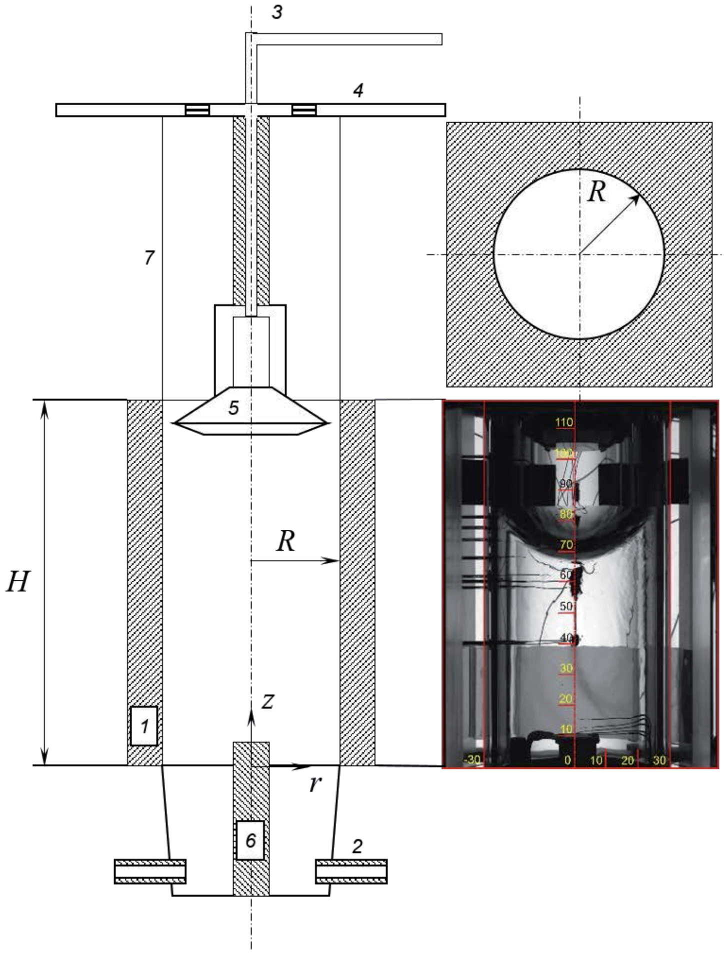

Figure 7.1: Schematic drawing of the SOURCE-II experiment with enumerated main components and an experiment image recorded by the camera.

experiment along the center line, which was not of interest for this investigation. The other (7) was placed on top of the quartz block to establish a temperature gradient along the experiment wall, as explained later. The test liquid used for both phases (liquid and gaseous) was Novec$^{\mathrm{TM}}$ 7000 (HFE-7000) by *3M*.

7.1.2 Visual Detection, Temperature and Pressure Sensors

To track the liquid-vapor interface, a camera was integrated capturing 10 bit images with a frame rate of 60 Hz. In flight transmission was limited to a frame rate of 4.4 Hz. A sample image is presented in Fig. 7.1.

A PDCR/PMP 4300 pressure transducer by *GE Sensing* was used to capture the pressure inside the experiment. The measurement accuracy is given by the provider with ±370 Pa [33].

Table 7.1: Vertical and radial location of used temperature sensors.

Sensor	z mm	r mm
TC01	115	30
TC02	90	30
TC03	84	30
TC04	78	30
TC05	5	30
TC12	60	0
TC17	40	0
TC22	11	-2

At discrete locations liquid, vapor and solid temperatures were recorded with thermocouples (type K, produced by *Thermocoax*). The measurement accuracy is given by the provider with ±1.5 K, but investigations revealed a total error of the measurement chain of ±2.5 K [31]. Thermocouples were labeled with the acronym TC and enumerated (e.g. TC12). Its temperature is given with the variable T, with the number in the subscript (e.g. T_{TC12}). Vertical and radial locations of sensors, which were necessary for this study, are listed in table 7.1. Sensor data was transmitted to the ground station with a 2 Hz rate and stored on-board with a 25 Hz rate.

7.1.3 Material Properties

The used material properties for quartz glass are given by the manufacturer [42]. Values for density ρ^s, specific heat capacity c^s and thermal conductivity λ^s for the reference conditions $T_{ref} = 298.15\,\mathrm{K}$ and $p_{ref} = 64598\,\mathrm{Pa}$ are listed in table 7.2. Material properties for liquid HFE-7000 can be found in the product information [1]. For the liquid phase the density ρ^l, specific heat capacity c_p^l, thermal conductivity λ^l and viscosity μ^l are linear dependent on temperature. HFE-7000 is a perfectly wetting liquid with a static contact angle $\gamma_s = 0°$. The pressure-temperature relationship along the saturation curve is given by the manufacturer with

$$\ln\left(P_{sat}\right) = \frac{-3548.6\,\mathrm{Pa\ K}}{T_{sat}} + 22.978\,\mathrm{Pa}\,, \tag{7.1}$$

and was validated in [31] for the experiment's temperature span. Equation 7.1 evolved from the Clausius-Clapeyron equation for ideal gases, which calculates the saturation pressure p_{sat} from the heat of evaporation Δh, the specific gas constant $\Re$ and the saturation temperature T_{sat} as follows

Table 7.2: Material properties for HFE-7000 and quartz glass at $p_{ref} = 64598\,\mathrm{Pa}$ and $T_{ref} = 298.15\,\mathrm{K}$.

		HFE7000 liquid	HFE7000 gaseous	quartz glass solid
ρ	kg m^{-3}	1400	5.96	2200
μ	10^{-6} Pa s	420	10.2	–
λ	10^{-3} W m^{-1} K^{-1}	75	7.9	1380
a	10^{-8} m^2 s^{-1}	4.12	198	81.3
c_p	J kg^{-1} K^{-1}	1300	668	772
Δh	10^3 J kg^{-1}	142	–	–
σ	10^{-3} N m^{-1}	12.4	–	–
σ_T	10^{-3} N m^{-1} K^{-1}	−0.1	–	–

$$\frac{1}{p}\mathrm{d}p = \frac{\Delta h}{\Re T^2}\mathrm{d}T\,. \tag{7.2}$$

The vapor can be treated as an ideal gas with a specific gas constant of $\Re = 41.6\,\mathrm{J\,kg^{-1}\,K^{-1}}$. The temperature dependent material properties for density ρ^v, specific heat capacity c_p^v, thermal conductivity λ^v and viscosity μ^v of the gaseous phase are listed in Barsi [7]. Surface tension σ and heat of evaporation Δh are dependent on the pressure p. The surface tension is temperature dependent. It is assumed that the free surface temperature is at saturation temperature. Material properties such as density, viscosity, heat conductivity, specific heat capacity, latent heat of evaporation, surface tension and its sensitivity coefficient at reference conditions are listed in table 7.2.

7.1.4 Experiment Procedure

At the beginning of the test ($t = 0\,\mathrm{s}$) the pressure in the experiment chamber was below 370 Pa (resolution of the sensor). Filling with liquid HFE-7000 started 65 s later with a mean volumetric flow rate of $\dot{V}_E = 12.17\,\mathrm{cm^3\,s^{-1}}$ and lasted 25 s. A second filling with a smaller flow rate of $\dot{V}_E = 5.45\,\mathrm{cm^3\,s^{-1}}$ was commanded at $t = 112.5\,\mathrm{s}$ and stopped at $t = 118\,\mathrm{s}$. Four pressurizations with superheated HFE-7000 vapor were performed throughout the campaign. The first pressurization was executed between $70\,\mathrm{s} \le t \le 80\,\mathrm{s}$ (adding 6.00×10^{-3} kg of vapor), the second between $126\,\mathrm{s} \le t \le 127\,\mathrm{s}$ (adding 0.57×10^{-3} kg of vapor), the third from $143\,\mathrm{s} \le t \le 147\,\mathrm{s}$ (adding 2.24×10^{-3} kg of vapor) and the last during $179\,\mathrm{s} \le t \le 190\,\mathrm{s}$ (adding 5.83×10^{-3} kg of vapor). Furthermore, one automated venting took place between $86\,\mathrm{s} \le t \le 91\,\mathrm{s}$ (extracting

Table 7.3: Filling times with liquid volume flow rate $\dot{V}^l_E$ and total liquid volume after each filling V^l_E. Pressurization and venting times with vapor mass flow $\dot{m}^v_E$ and added vapor mass after each event Δm^v_E [31].

t s	$\dot{V}^l_E$ 10^{-6} m^3 s^{-1}	V^l_E 10^{-6} m^3	$\dot{m}^v_E$ 10^{-3} kg s^{-1}	Δm^v_E 10^{-3} kg
$65 \leq t \leq 90$	12.17	304.25	–	–
$70 \leq t \leq 80$	–	–	0.60	6.00
$86 \leq t \leq 91$	–	–	−0.03	−0.16
$112.5 \leq t \leq 118$	5.45	29.98	–	–
$126 \leq t \leq 127$	–	–	0.57	0.57
$143 \leq t \leq 147$	–	–	0.56	2.24
$179 \leq t \leq 190$	–	–	0.53	5.83

0.16×10^{-3} kg of vapor). At $t = 210$ s the experiment was accomplished. All actions are listed in table 7.3.

7.2 Numerical Simulation of the Suborbital Flight Experiment

The SOURCE-II experiment was simulated with the numerical flow solvers Flow-3D v.11.0.2 and Fluent 15.0. The same simplified geometry was used for both codes. Each code uses its own spatial discretization method. Flow-3D uses a structured mesh which automatically detects the volume open to fluid flow and the solid phase (FAVOR$^{\text{TM}}$-method [26, 45]). Fluent uses an unstructured mesh. This results in different meshes used for the simulations. The several phases and boundary conditions must be specified by the user.

7.2.1 Geometry Simplifications

To minimize computational time a geometry with reduced complexity of the experiment was created. A drawing of the main components is shown in Fig. 7.2 a) and a detailed view of the diffuser in Fig. 7.2 b). The liquid entered the computational domain not through pipes from the side, as in the experiment, but from the bottom. The diffuser was heavily simplified but still fulfilled its purpose. Due to the design changes the total usable volume is smaller and therefore the first 5 s of the initial filling could be skipped in the simulation.

7.2.2 Mesh Generation and Boundary Conditions

According to the benchmark [35], the temperature of the inflowing liquid is $T_S^l = 299.15$ K and for the entering vapor $T_S^v = 418.15$ K.

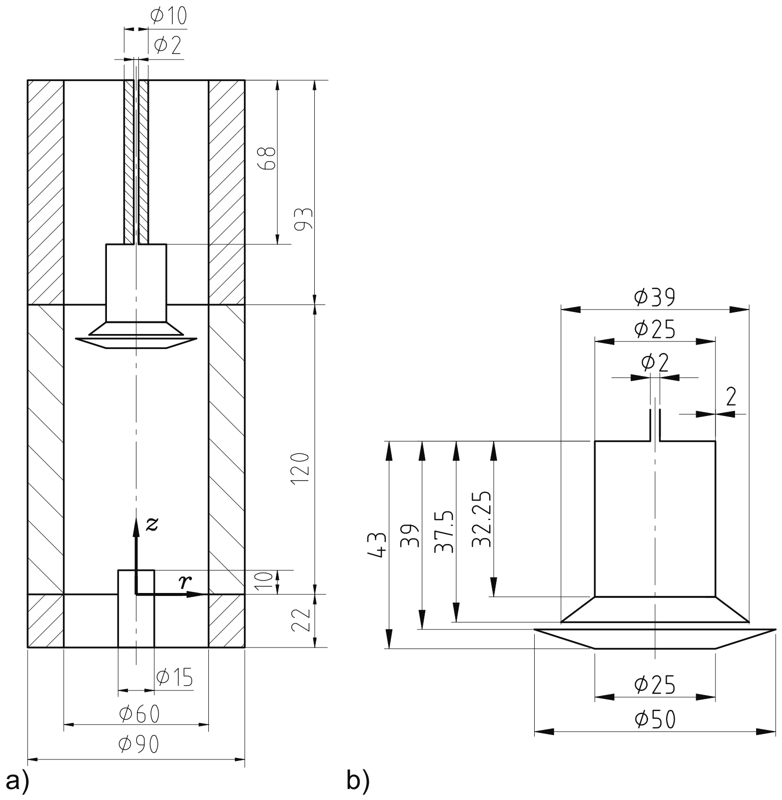

Figure 7.2: a) Drawing with dimensions of the simplified experiment tank used for the simulations. b) Drawing with dimensions of the simplified diffuser used for the simulations.

Flow-3D

Assuming, that the outer shape of the glass block (rectangular) could also be cylindrical without influencing the heat transfer between fluid and solid, the simulation could be reduced to a two-dimensional case. Cartesian and cylindrical meshes are available within Flow-3D. A cylindrical coordinate system was chosen representing the third dimension (θ-direction) with one cell covering 30° of the circumference. All solid parts, such as the feeding line, diffuser, heater and glass cylinder, were enclosed in the mesh and considered by the volume/obstacle representation of Flow-3D [45]. The mesh was mostly equidistantly spaced. However, the liquid-vapor-solid contact line was very sensitive to the mesh and therefore the mesh was refined in the vicinity of the wall. Heat conduction in the solid could be modeled with less cells. A graded mesh with increasing mesh size in r-direction was used. The space above the diffuser was needed for vol-

Table 7.4: Total amount of cells and distribution in r- and z-direction for the used meshes: Minimum and maximum values represent the smallest and longest edge length of a cell in either r-direction or z-direction.

		N	Δr		N		Δz	
			10^{-3} m				10^{-3} m	
	Total	r-direction	Min.	Max.	θ-direction	z-direction	Min.	Max.
Mesh1	29625	75	0.10	2.90	1	395	0.48	4.50
Mesh2	14893	53	0.14	4.20	1	281	0.68	6.60

ume conservation, but neither temperature nor velocity gradients were expected and recorded. Hence, larger cells were used in this area.

Two meshes were created to investigate the influence of the discretization on the numerical solution. A first mesh with an edge length of $\Delta r_{M1} = \Delta z_{M1} = 0.48\,\text{mm}$ for the quadratic cells and a refinement in r-direction to $\Delta r_{M1,w} = 0.1\,\text{mm}$ was created as a base line. Further refinement was impractical due to computational costs. The second mesh used half the cells with the same rules for refinement. Thus, the edge length was $\Delta r_{M2} = \Delta z_{M2} = \sqrt{2}\Delta r_{M1} = \sqrt{2}\Delta z_{M1} = 0.68\,\text{mm}$. The refinement to the wall changed with the same factor to $\Delta r_{M2,w} = \sqrt{2}\Delta r_{M1,w} = 0.14\,\text{mm}$. The total amount of cells and the distribution in r- and z-direction are given in table 7.4. A section of both meshes is depicted in Fig. 7.3.

The z-axis was defined as the symmetry axis with a collapsed r_{min}-plane, which is a result from the cylindrical mesh, that has a singularity at $z = 0\,\text{mm}$. A symmetry boundary condition was allocated to the resulting r_{min}-axis. The r_{max}-plane was defined as an adiabatic wall representing outer borders of the experiment. The liquid inflow took place over the z_{min}-plane and the vapor injection through the z_{max}-plane. Symmetry conditions were assigned to both planes in θ-direction. The surfaces of all obstacles had a no-slip condition assigned to it. Heat transfer between fluid and solid was activated for $0\,\text{mm} \leq z \leq 120\,\text{mm}$.

Fluent

Fluent can use surface meshes for 2D-simulations. These meshes have only two-dimensions extending in r- and z-direction. ICEM CFD 15.0 was used to create meshes consisting of quadrilateral elements (quads). Surface discretization is based on the blocking strategy [4]. The simplified geometry is shown in Fig. 7.4 a) with all external boundaries colored black and internal boundaries colored red. One internal boundary indicates the edge between the thermal active wall and the area open to fluid flow (solid-liquid boundary). The other (inside the diffuser) limits the area of the vapor source, which is explained in detail later. The block structure can be found in Fig. 7.4 b). The green color represents edges which have boundary

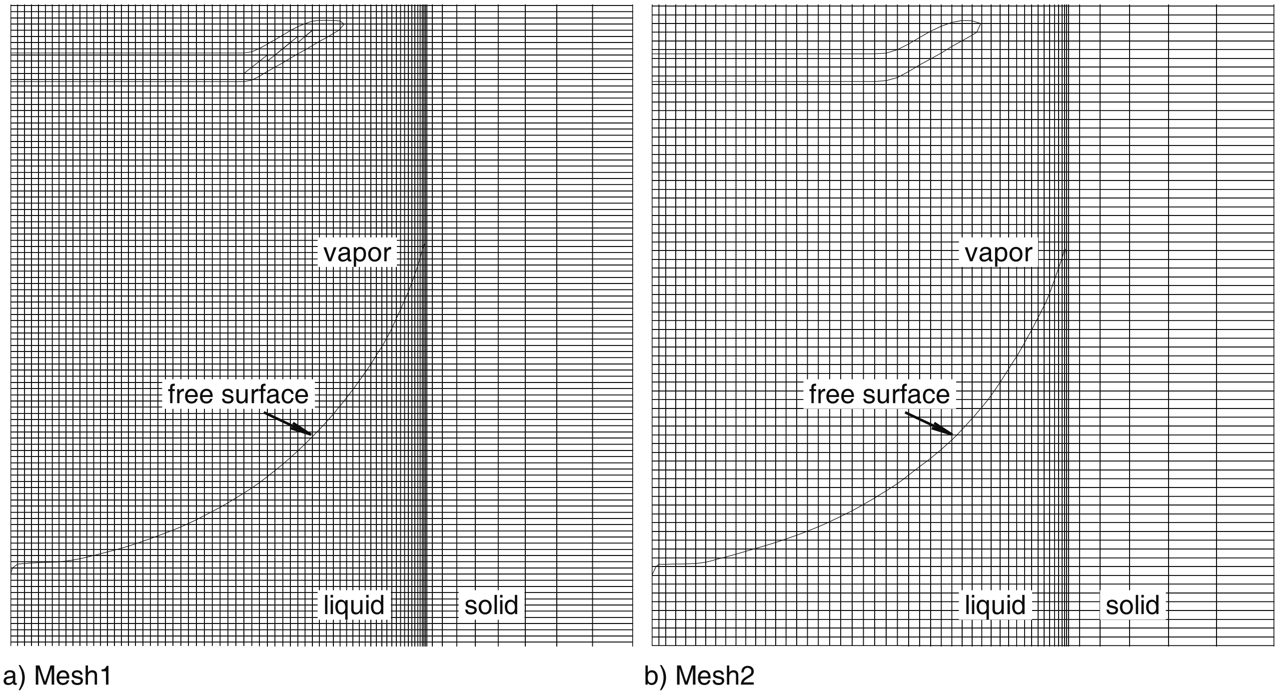

a) Mesh1 b) Mesh2

Figure 7.3: Section of the mesh created in Flow-3D with an iso-line of the free surface, diffuser and cylinder wall. a) Mesh1: 29625 cells. b) Mesh2: 14893 cells.

conditions assigned to them. Blue edges are internal edges without any boundary condition. Any mesh can be created based on this blocking strategy simply by defining the cell count on each edge. However, it has to be considered, that changing the amount of cells on one edge affects all parallel edges of the aligned blocks.

To study the influence of the cell size, two meshes were created with ICEM CFD named MeshA and MeshB. The time required to simulate the 140 seconds experimental time is much higher than for Flow-3D. To reduce the CPU-time a bigger cell size was chosen than for Mesh1 and Mesh2 from the Flow-3D computations. Best results were achieved with quadratic cells, thus an aspect ratio of 1. Another quality indicator is the $3 \times 3 \times 3$ matrix, which is the Jacobian matrix for each cell. A value of one represents a perfect square. A negative value indicates, that the cell has at least one degenerated edge which will cause solver termination. Values above 0.3 are acceptable [4]. The quality of a mesh is dependent on the blocking strategy and cannot be optimal everywhere. In this work, the focus laid on the free surface area and the solid wall. MeshA has a cell length in this are of $\Delta r_{MA} = \Delta z_{MA} = 0.5\,\text{mm}$ and MeshB of $\Delta r_{MB} = \Delta z_{MB} = 1.0\,\text{mm}$. Above $z = 120\,\text{mm}$ (the thermal active solid) the mesh size was increased to reduce the total number of cells. The total number of cells is 20605 and 6142 for MeshA and MeshB, respectively. The minimum value of the Jacobian matrix (quality) is above 0.3 for both meshes with the most distorted cells in the vicinity of the diffuser geometry. The

Table 7.5: Total amount of cells, cell length in the vicinity of the free surface and lowest value of the Jacobian matrix for MeshA and MeshB used with Fluent.

	N –	$\Delta r = \Delta z$ 10^{-3} m	Minimum cell quality –
MeshA	20605	0.50	0.3
MeshB	6142	1.00	0.3

quality in the vicinity of the free surface and the thermal active wall (gray area in Fig. 7.4 c)) is between 0.95 and 1 for both meshes. Detailed information is listed in table 7.5.

Before the mesh can be used in Fluent all cell zones and the type of the boundary conditions (BC) must be defined. Figure 7.4 c) includes this information. Three different cell zones were specified. The gray area represents the thermal active wall which is assigned to the material properties of quartz glass. The transparent area is open to the fluid HFE-7000. A special treatment for the vapor injection was necessary. The green area located in the feeding line and the diffuser was acting as a mass source emitting gaseous HFE-7000 at a temperature of $T^v = 418.15\,\mathrm{K}$. The amount of vapor was calculated in a way, that it fits the values in table 7.3. As boundary condition a mass source $\overline{m}$ was chosen. To define the right value some computations were necessary. First the volume of the mass source V_{source} is needed, which is represented by the green area in Fig. 7.4 c)

$$V_{source} = 2\pi r^2 h = 2\pi \left(1 \times 10^{-3}\,\mathrm{m}\right)^2 1.09 \times 10^{-1}\,\mathrm{m} = 6.85 \times 10^{-7}\,\mathrm{m}^3\,. \tag{7.3}$$

To get $\overline{m}^v$, one must take the values for $\dot{m}^v_E$ from table 7.3 and divide it by V_{source}. The specific values for the four pressurization phases can be found in table 7.7. This procedure was necessary since test simulations showed, that the stagnation point of the entering vapor (through a velocity BC) at the diffuser significantly decreased the time step size.

All adiabatic wall BCs are colored in red in Figure 7.4 c). The symmetry axis is marked in dark green and the mass flow inlet BC for the liquid HFE-7000 is in blue. The liquid is entering at a temperature of $T^l = 299.15\,\mathrm{K}$ and the amount is controlled to match the values in table 7.3.

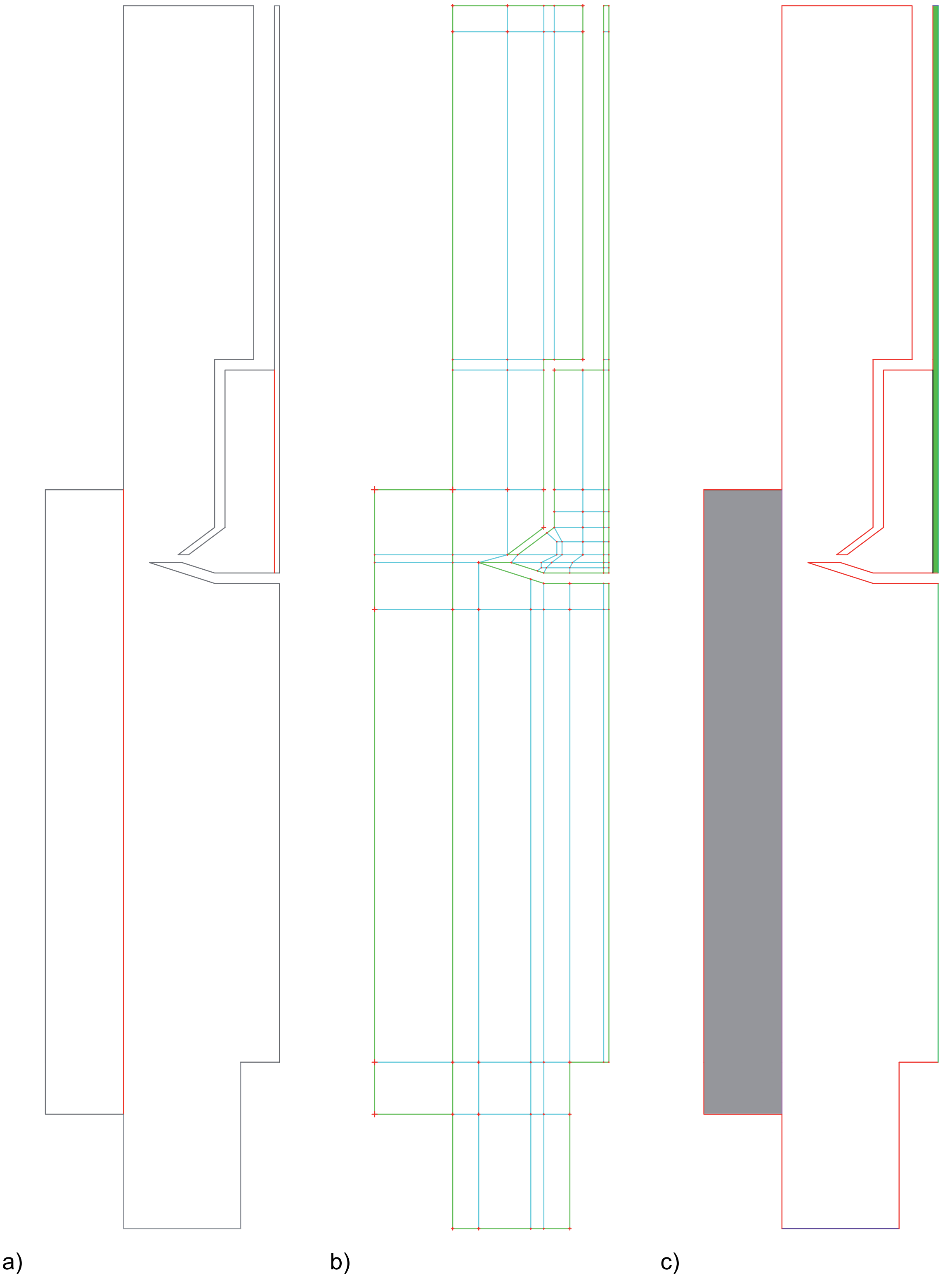

Figure 7.4: a) Simplified geometry of the SOURCE-II experiment with interfaces colored in red. b) Blocking structure. c) Cell zones and boundary condtions.

7.2.3 Material Properties

Flow-3D

For the liquid phase (liquid HFE-7000) μ^l, c_v^l and λ^l were defined as a function of the temperature within Flow-3D. Only one compressible phase is possible, thus $\rho^l = 1400\,\mathrm{kg\,m^{-3}} = \mathrm{const.}$ For the vapor (gaseous HFE-7000) ρ^v, μ^v, c_v^v and λ^v are temperature dependent. The density is calculated with the ideal gas equation (eq. 4.29) and $c_v^v = c_p^v - \Re$ [5]. For the free surface, the surface tension at $T = 299.15\,\mathrm{K}$ is $\sigma = 13.3 \times 10^{-3}\,\mathrm{N\,m^{-1}}$. Furthermore, its temperature sensitivity coefficient $\sigma_T = -0.1 \times 10^{-3}\,\mathrm{N\,m^{-1}\,K^{-1}}$ and the contact angle $\gamma_s = 0°$ is required. The latent heat of evaporation $\Delta h = 142 \times 10^3\,\mathrm{J\,kg^{-1}}$ is included for a correct approximation of phase change effects. The solid phase (Suprasil) is modeled using the $\rho^s = 2200\,\mathrm{kg\,m^{-3}}$ and the specific heat capacity $c^s = 772\,\mathrm{J\,kg^{-1}\,K^{-1}}$. The heat conductivity λ^s is dependent on the temperature. All temperature dependent properties are implemented in tabular form with the temperature and the corresponding value for the property [1, 7, 42]. The step size of the temperature is $\Delta T = 1\,\mathrm{K}$. Flow-3D uses a linear interpolation between two data points.

Fluent

For the liquid phase (liquid HFE-7000) μ^l, c_p^l and λ^l were defined as a function of the temperature within Fluent. Only one compressible phase is possible, thus $\rho^l = 1400\,\mathrm{kg\,m^{-3}} = \mathrm{const.}$ Furthermore, a specific enthalpy $h_{ref}^l = 0\,\mathrm{J\,mol^{-1}}$ at a reference temperature $T_{ref} = 298.15\,\mathrm{K}$ and the molar weight $M = 200\,\mathrm{g\,mol^{-1}}$ is needed. For the vapor (gaseous HFE-7000) ρ^v, μ^v, c_v^v and λ^v are temperature dependent. The density is calculated with the ideal gas equation (eq. 4.29). The latent heat of evaporation is included in the internal energy $u_{ref}^v = u_{ref}^l + \Delta h\, M = 28.4\,\mathrm{J\,mol^{-1}}$. The saturation temperature is approximated as a function of pressure. Surface tension and its temperature sensitivity are represented by first order polynomial function. For the solid phase (Suprasil) $\rho^s = 2200\,\mathrm{kg\,m^{-3}}$, specific heat capacity $c^s = 772\,\mathrm{J\,kg^{-1}\,K^{-1}}$ and λ^s as a function of temperature are required. All temperature dependent variables were approximated with polynomial functions, whose coefficients can be found in the Appendix in table A.3.

7.2.4 Initial Conditions

The simulation started 70 s after lift-off. Flight data at $t = 70\,\mathrm{s}$ provided pressure and temperature to initialize the computational domain. At this time the experimental volume was already filled with HFE-7000 vapor at a pressure of $p_0 = 78000\,\mathrm{Pa}$ and temperature of $T_0 = 358.15\,\mathrm{K}$. A temperature gradient was established in the glass wall between $0\,\mathrm{mm} \leq z \leq 120\,\mathrm{mm}$. Flow-3D treats the solid below $z = 0\,\mathrm{mm}$, above $z = 120\,\mathrm{mm}$, the heater and the diffuser with feeding line as lumped mass, thus they could only act as a heat source or sink to connecting solids. Fluent does not discretize these parts. The initial wall temperature distribution in z-direction was based on the temperature sensors TC1 to TC5. Figure 7.5 shows the solid temperature along the height of the glass cylinder for the experiment, Flow-3D and Fluent simulations. The downward facing triangles indicate the thermocouples, the solid and the dashed black line the initialization for simulations with Flow-3D and Fluent, respectively. Flow-3D can only use functions up to second order polynomials for initialization. Hence, the temperature distribution between $0\,\mathrm{mm} \leq z \leq 120\,\mathrm{mm}$ was interpolated with the quadratic function

$$T = C_2 z^2 + C_1 z + C_0\,, \tag{7.4}$$

with the coefficients $C_0 = 299.15\,\mathrm{K}$, $C_1 = -60.722\,\mathrm{K\,m^{-1}}$, and $C_2 = 8935.9\,\mathrm{K\,m^{-2}}$. Equation 7.4 fits well to T_1 to T_4 but has a noticeable offset to T_5. Since the area of interest was within the free surface, which was located in the vicinity of TC2 to TC4, this was still the best usable fit. Fluent allows the user defined function for the distribution of the temperature field. Best results can be obtained with

$$T = C_0 + C_1 \exp\left(\frac{z}{C_2}\right). \tag{7.5}$$

The corresponding coefficients are $C_0 = 294.43\,\mathrm{K}$, $C_1 = 285.71\,\mathrm{K}$, and $C_2 = 52.12\,\mathrm{mm}$. For all used temperature sensors the temperature values, fit, offset and offset in percentage are given in the Appendix in table A.10.

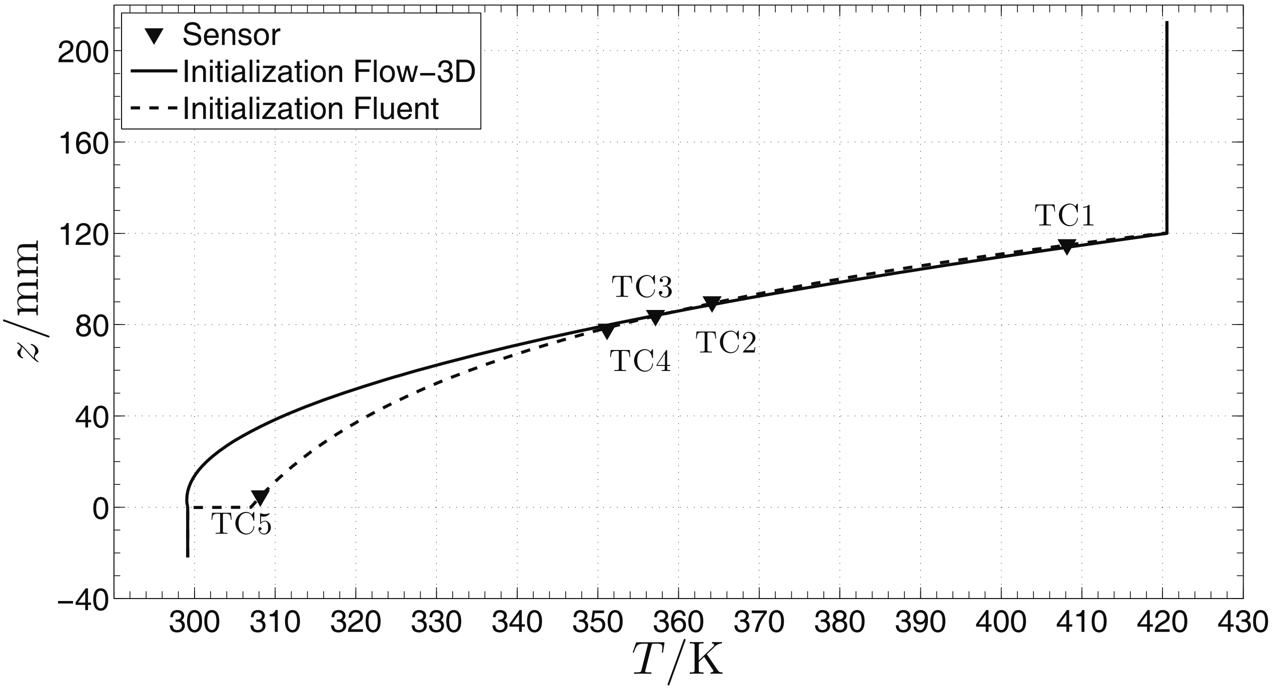

Figure 7.5: Initial temperature distribution along the wall for both numerical codes in comparison with the temperature readings of the relevant sensors at $t = 70\,\mathrm{s}$.

7.2.5 Procedure

Due to geometry simplifications the simulation could be started at $t = 70\,\mathrm{s}$. It was crucial for the computation to capture the mass flow for each filling and pressurization. The venting at $t = 86\,\mathrm{s}$, which lasted for five seconds, had no impact on the system's behavior and was therefore neglected.

Flow-3D

Best results were achieved by defining specific velocity boundary conditions for the planes were liquid and vapor entered. After the simulation was finished the total volume of liquid and total mass of vapor entering the computational domain were calculated for each phase and compared with the experiment. The geometry modifications conducted for the numerical model had to be considered as well. The free surface height is dependent on the amount of liquid added to the experiment chamber, thus dependent on the fluid velocity v_S^l and resulting volume flow rate $\dot{V}_S^l$ (see table 7.6). The derived surface height throughout and after the filling procedures is in proper accordance with the experimental values. Exact values of all four pressurization phases for vapor velocity v_S^v, added mass Δm_S^v and the mass added in the experiment Δm_E^v are presented in table 7.7. Velocities are negative because the velocity vector was facing in negative z-direction.

Table 7.6: Applied values for the liquid inflow boundary conditions and resulting flow rate for the simulations with Flow-3D and Fluent compared with the experiment.

		Flow-3D		Fluent		Experiment
Filling No.	Δt s	v_S^l 10^{-3} m s^{-1}	$\dot{V}_S^l$ 10^{-6} m^3 s^{-1}	$\dot{m}_S^l$ 10^{-3} kg s^{-1}	$\dot{V}_S^l$ 10^{-6} m^3 s^{-1}	$\dot{V}_E^l$ 10^{-6} m^3 s^{-1}
1	20	4.41	11.69	17.04	12.17	12.17
2	5	2.57	6.81	7.63	5.45	5.45

Table 7.7: Applied values for the vapor inflow boundary conditions and resulting flow rate for the simulations with Flow-3D and Fluent compared with the experiment.

		Flow-3D		Fluent		Experiment
Pressurization No.	Δt s	v_S^v m s^{-1}	Δm_S^v 10^{-3} kg	$\overline{m}_S^v$ 10^2 kg m^{-3} s^{-1}	Δm_S^v 10^{-3} kg	Δm_E^v 10^{-3} kg
1	10	−3.278	6.00	8.76	6.00	6.00
2	1	−3.118	0.57	8.32	0.57	0.57
3	4	−3.051	2.24	8.18	2.24	2.24
4	11	−2.906	5.85	7.74	5.83	5.83

Fluent

Using Fluent, a different approach was chosen. To realize the filling with liquid HFE-7000 a specific mass flow boundary condition was defined. The volume flow rate $\dot{V}_E^l$ of the experiment (see table 7.3) was multiplied with the density $\rho^l = 1400\,\mathrm{kg\,m^{-3}}$ to compute the corresponding mass flow rate $\dot{m}_S^l$. The vapor mass was emitted by the mass source zone. The interface between this zone and the fluid zone acted as a mass flux boundary condition. Liquid mass flow rates and vapor volumetric mass flow rates determined for the simulations with Fluent can be found in table 7.6 and table 7.7, respectively.

7.2.6 Numerical Settings

In this section all important settings and used models are summarized, which are recommended to utilize when setting up a simulation for the introduced experiment.

Flow-3D

The VOF method was used to distinguish between the liquid or gaseous phase in each cell [44]. Liquid was treated as an incompressible fluid with temperature dependent material properties.

The vapor phase was represented by an ideal gas model with temperature dependent material properties. The surface tension model was active with a temperature sensitive surface tension coefficient. To compute the phase change mass flux $\widehat{m}$ over the free surface a modified Hertz-Knudsen model was used [43, 15]. A feasible pressure prediction was achieved with the accommodation coefficient $\widetilde{c}_{M1} = 0.0025$ for Mesh1 and $\widetilde{c}_{M2} = 0.0018$ for Mesh2. The Navier-Stokes equations governing the fluid behavior were discretized using a finite difference scheme. For stability reasons nucleate boiling was disabled in the numerical model. The computation was first order accurate. The used equations solved by the code are written in Sec. 5.1 and the solver theory can be found in Sec. 5.3.1.

Fluent

The VOF method was used to distinguish between the liquid or gaseous phase in each cell [44]. Liquid was treated as an incompressible fluid with temperature dependent material properties. The vapor phase was represented by an ideal gas model with temperature dependent material properties. Surface tension was modeled temperature dependent. To compute the phase change mass flux $\widehat{m}$ over the free surface the Lee model with the Hertz-Knudsen equation was used [57]. Best pressure correspondence to the experiment was achieved with the phase change frequency set to $\overline{f}_{MA} = 50\,\mathrm{s}^{-1}$ for MeshA and $\overline{f}_{MB} = 5\,\mathrm{s}^{-1}$ for MeshB. To solve the set of equations presented in Section 5.2 the SIMPLE scheme was used for the pressure-velocity coupling on the Pressure-Based solver. Density, momentum and energy were discretized by the second order upwind method, the pressure with the PRESTO! algorithm and the volume fraction with the geo-reconstruct method. Gradients are least squares cell based and the transient formulation is solved using the first order implicit method. A detailed explanation of the used methods is given in Sec. 5.3.2 based on the manual [3].

Chapter 8

Results

This chapter comprises the results from experimental and numerical investigations conducted for this work. It is divided into two main sections, one for each experiment. The first section includes the experimental results of the liquid parahydrogen drop tower campaign together with the numerical results. The experimental results of the drop tower campaign were also published by Schmitt and Dreyer [74]. The second section consists of the numerical results of the SOURCE-II experiment supplemented by the experimental findings. All computations where conducted with the same workstation on an Intel® Xeon® E5-2687W processor with a clock speed of 3.1 GHz using 8 cores.

8.1 Drop Tower Experiments and Simulations

The focus on these investigation lies on the influence of a superheated wall on the free surface reorientation. Nucleate boiling was not desired but could hardly be avoided. Therefore, the results section is divided into seven parts. First, the computational performance of the simulations was assessed. The computational costs were determined and the mesh study was analyzed finding a reasonable mesh for further simulations. Second, the initial free surface in presence of gravity was compared with the theory presented in [55]. The initial capillary rise could not be captured with the used camera system. The data of the simulations for the first time regime is discussed in the third section. In the fourth and fifth part, experiments A5 and B6 were closely examined as examples for an isothermal and non-isothermal experiment, respectively. The experimental results are supplemented by numerical data. Sixth, effects of the wall temperature gradient on the free surface are analyzed using data from all experiments and the numerical study with varying gradients between A5 and B6. The last part addresses the influence of the wall superheat and stratification of the liquid on the pressure progression.

8.1.1 Computational Performance

This section focuses on the quality of the numerical results. A mesh study was performed with the settings of experiment B6 to capture all physical effects (non-isothermal, phase change, conjugated heat transfer) and how they were influenced by the cell size. The time it took for the flow solver to calculate 5 s physical time differed greatly with the used meshes. Table 8.1 shows the normalized mesh size and computational time with dimensions and in dimensionless form. The values of mesh M1 were used as the baseline. One can say, that the required computational time t_S is linear dependent on the cell size N with $t_S \propto 0.5N$. Mesh M3 is not usable for large scale numerical studies because of its computational costs.

The computed reorientation process of the free surface is a first quality indicator for the used grids. The center point progression of the simulations was compared with the experimental data. This was hardly possible for the wall point, since it could not be observed longer than 0.3 s. However, some qualitative statements about the contact line were possible. All surface positions were computed for a VOF fraction of $F = 0.5$ or as close as possible to this value, meaning the corresponding cell is half filled by liquid and vapor. The extracted center point z_c over time for the experiment and the simulations can be found in Fig. 8.1 a). It shows, that all used meshes overpredict the first minimum of the center point progression. This can be explained with the thickness of the advancing layer at the wall. Examination of the experimental data led to the assumption, that the advancing layer is quite thin (it is not possible to make a quantitative statement). The minimum layer thickness is delimited by the cell size. It seems that the cell size, even for the finest Mesh M3, was above the layer thickness. The advancing contact line influenced the reorientation as well. The limited experimental data allows only a suggestion but no solid statement. However, Fig. 8.1 b) shows a higher speed of the contact point for the simulations than for the experiments. This adds further mass to the wall region.

Table 8.1: Computational time with dimensions and in dimensionless form of the used meshes in relation to the grid size.

		M1	M2	M3
$N^* = N/N_{M1}$	–	1.00	5.93	22.88
t	dd:hh	01:12	04:17	14:23
$t_S^* = t_S/t_{S,M1}$	–	1.00	3.12	10.00

Applying mass conservation one can say that the extra mass in the vicinity of the wall is missing in the center region and led therefore to an overestimated center point displacement.

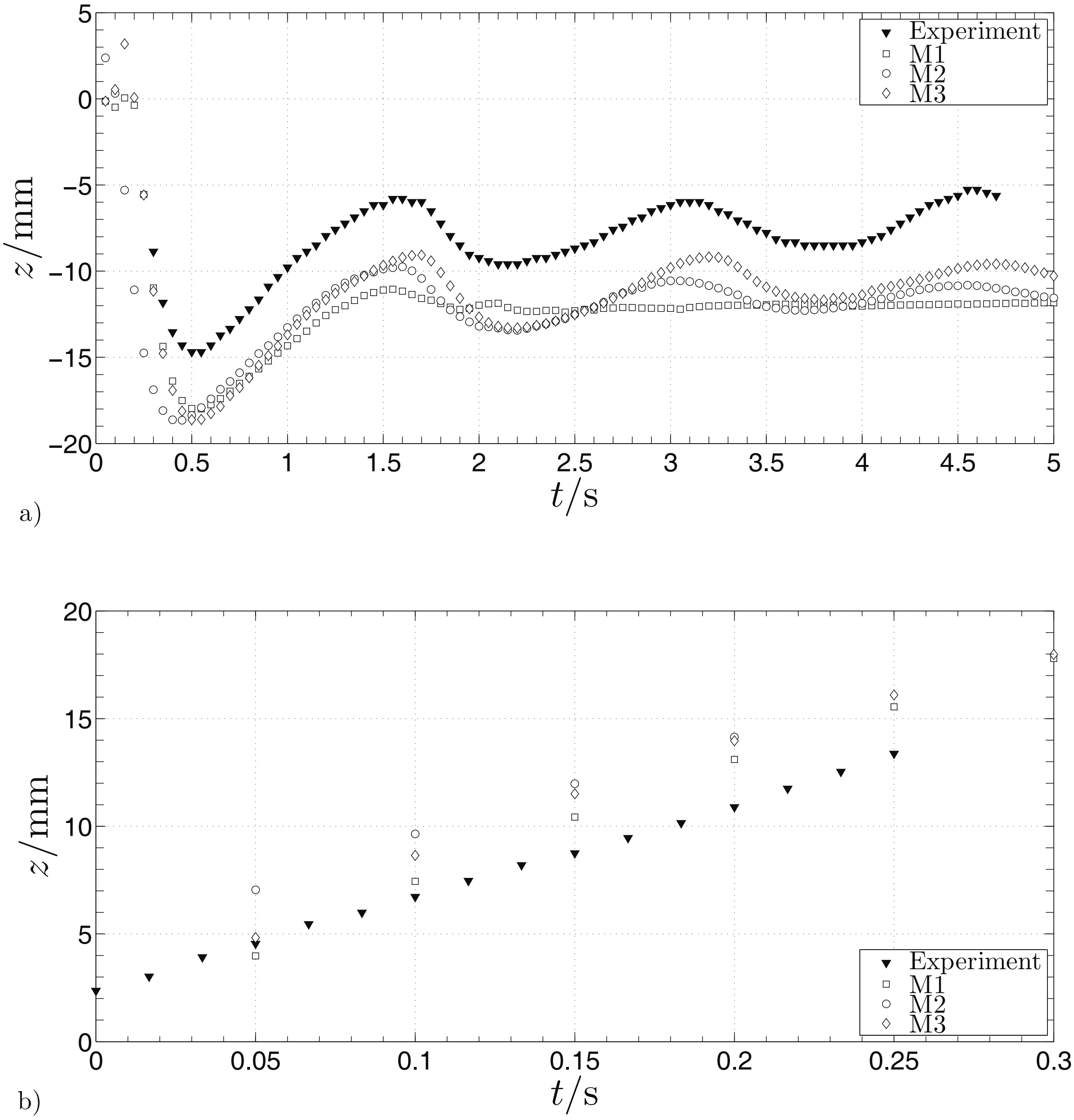

Figure 8.1: a) Center point progression of the experiment B6 ($\Delta T^*/\Delta z^* = 0.07$) and simulations using different cell sizes. b) Wall point progression of the experiment B6 ($\Delta T^*/\Delta z^* = 0.07$) and simulations using different cell sizes.

Besides the overpredicted center point displacement, M1 showed a strongly damped oscillation with a steady center point established 2.2 s after the start of the simulation. The crude discretization increased the damping of the free surface. The M2 results, with a finer spatial discretization, corresponds well with the experimental data. The mesh with the most cells, M3, is represented by diamond shaped markers. Its results are quite similar to those of M2, which is an indicator for mesh convergence. However, the oscillation frequency is not captured as well with M3 as using M2. The first two simulations showed a rupture of the free surface at the wall from the liquid layer at the wall. No rupture occurred in the simulation M3. The connection of the bulk to the liquid at the wall seemed to affect the oscillation frequency. The influence of the rupture point is also discussed in Sec. 8.1.6. Figures. 8.2 and 8.3 show the film rupture for M1 at $t = 1.7\,\mathrm{s}$ and for M2 at $t = 2.8\,\mathrm{s}$, respectively.

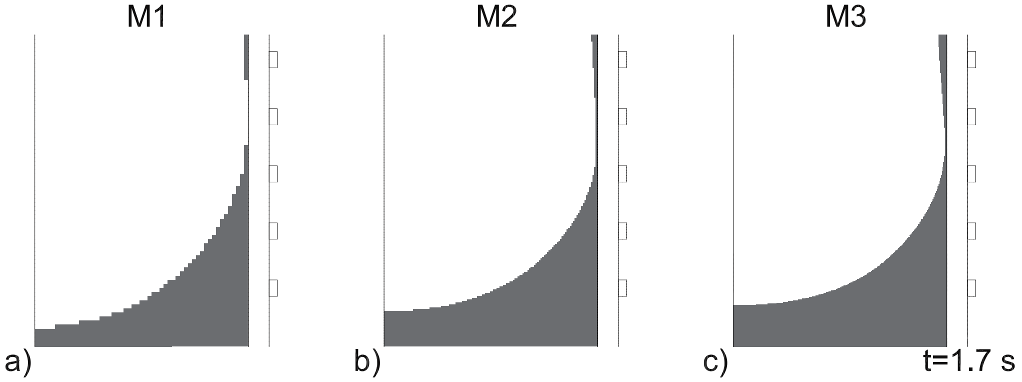

Figure 8.2: Free surface ($F = 0.5$) of the simulations at $t = 1.7\,\mathrm{s}$. a) M1 shows detachment of the liquid layer from the main free surface. b) M2 shows no detachment. c) M3 shows no detachment.

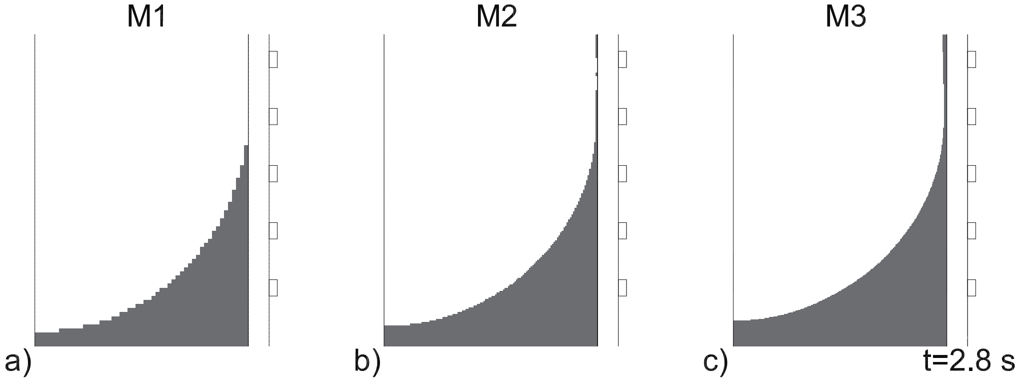

Figure 8.3: Free surface ($F = 0.5$) of the simulations at $t = 2.8\,\mathrm{s}$. M1 (a)) and M2 (b)) show detachment of the liquid layer from the main free surface. c) M3 shows no detachment.

In conclusion, it can be stated, that mesh M2 is the best choice for simulations of the drop tower experiments. Computational costs and prediction of the free surface reorientation are reasonable. One major deficiency, which is caused by the used solution algorithm, has to be noted. Only one field of variables is solved, so a mean temperature must be computed in cells where both phases are present. This is done with a density based average (explained in Sec. 5.2.4 with eq. 5.47). Van Foreest et al. [86] showed, that the averaging of the temperature

Table 8.2: Calculated capillary length $z_{w,0,T}$ in presence of gravity in comparison with the derived length $z_{w,0,E}$ from the endoscope pictures for the experiments of the second campaign.

		C4	A5	B6
$z_{w,0,T}$	mm	2.3	2.4	2.4
$z_{w,0,E}$	mm	2.4	2.5	2.4
Deviation	%	4.2	4.0	0.0

will alter the mean vapor temperature over time. Since the ideal gas equation (eq. 4.29) is used to compute the pressure, this will also affect the pressure progression. Currently, no pressure prediction can be performed for this type of experiment.

8.1.2 Initial Free Surface

The meniscus height in presence of gravity is defined with eq. 2.21. The static contact angle cannot be measured, but is assumed to be $\gamma_{s,0} = 0°$. Calculated length $z_{w,0,T}$, measured length $z_{w,0,E}$ and deviation are listed in table 8.2. Different theoretical values resulted from the corresponding material properties at different initial pressure levels. Calculated and measured lengths are in good accordance and support the image processing quality.

8.1.3 Initial Capillary Rise

The first time regime after the sudden gravity reduction described by $t_{pu,Lc}$ was to short to be captured by the used camera system. Using eq. 2.22 with the material properties given in table 6.1 yields $t_{pu,Lc} = \left(\sigma/\rho^l g_0^3\right)^{1/4} \approx 13\,\mathrm{ms}$ which is below the resolution time of the camera with 60 Hz → 17 ms. The simulations SA5 and SB6 were used to analyze this time span. Fig. 8.4 presents the plotted normalized velocity $v^*_{Lc} = v/v_{pu,Lc} = v/\left(g_0\sigma/\rho^l\right)^{1/4}$ of both simulations over the normalized time $t^*_{Lc} = t/t_{pu,Lc}$. A maximum velocity was reached after $t \approx 1.8\,t_{pu,Lc}$. The characteristic velocity was not completely met by the simulations but the order of magnitude is correct for both velocity and time. The discrepancy could be caused by the initial surface shape, which is not exact, as explained in Sec. 6.2.4.

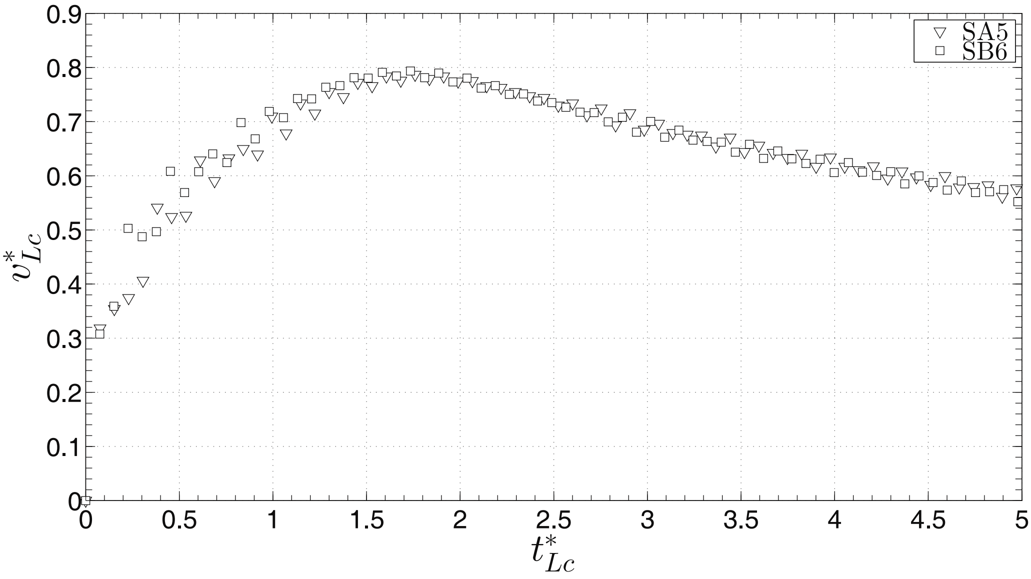

Figure 8.4: Normalized velocity $v^*_{Lc} = v/v_{pu,Lc} = v/\left(g_0\sigma/\rho^l\right)^{1/4}$ of the advancing contact line for the initial capillary rise. The time was normalized by the corresponding characteristic time, thus $t^*_{Lc} = t/t_{pu,Lc} = t/\left(\sigma/\rho^l g_0^3\right)^{1/4}$.

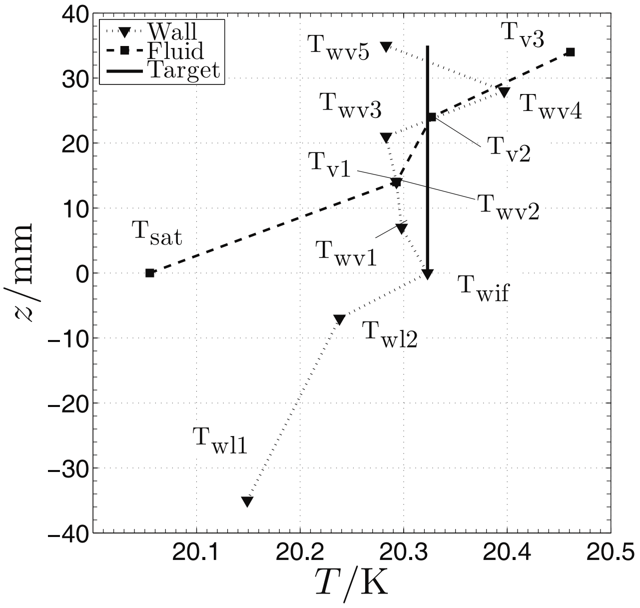

Figure 8.5: Initial temperature distribution at $t = 0\,\mathrm{s}$ for the isothermal experiment A5. Wall temperature sensors are indicated with a downward facing triangle and connected for better visibility with a dotted line which does not represent the temperature distribution between two adjacent sensors. Vapor temperatures are indicated with a square marker and connected for better visibility with a dashed line. The saturation temperature is calculated with the pressure value. The solid black line represents the target wall temperature gradient.

8.1.4 Isothermal Conditions

At the beginning of the free fall time the liquid is slightly subcooled and the recorded wall temperatures are within a range of 0.12 K which is below the accuracy of the temperature sensors. An offset of approximately 0.3 K has been noticed between the interface temperature given by $\mathrm{T_{wif}}$ and saturation temperature calculated from the pressure data (see Fig. 8.5). This deviation could be noticed for every experiment. It is caused by the laser which was switched on three to four seconds prior to the drop. Temperature recordings without illumination showed that the temperature T_{wif} and the saturation temperature computed with the pressure are within 0.01 K. When the laser was activated the sensors absorbed a certain amount of heat, which led to a temperature rise. This drift is clearly visible in Fig. 8.8. Figure 8.9 shows this trend between $-2.0\,\mathrm{s} \leq t \leq 0.3\,\mathrm{s}$ before the reorientation caused a temperature rise. All sensor recordings showed the same slope which led to the assumption that they absorbed the same amount of heat. Temperature differences between the sensors are therefore not affected by the laser. For technical reasons the recording of the temperatures was switched to a higher sampling rate at $t = -2\,\mathrm{s}$.

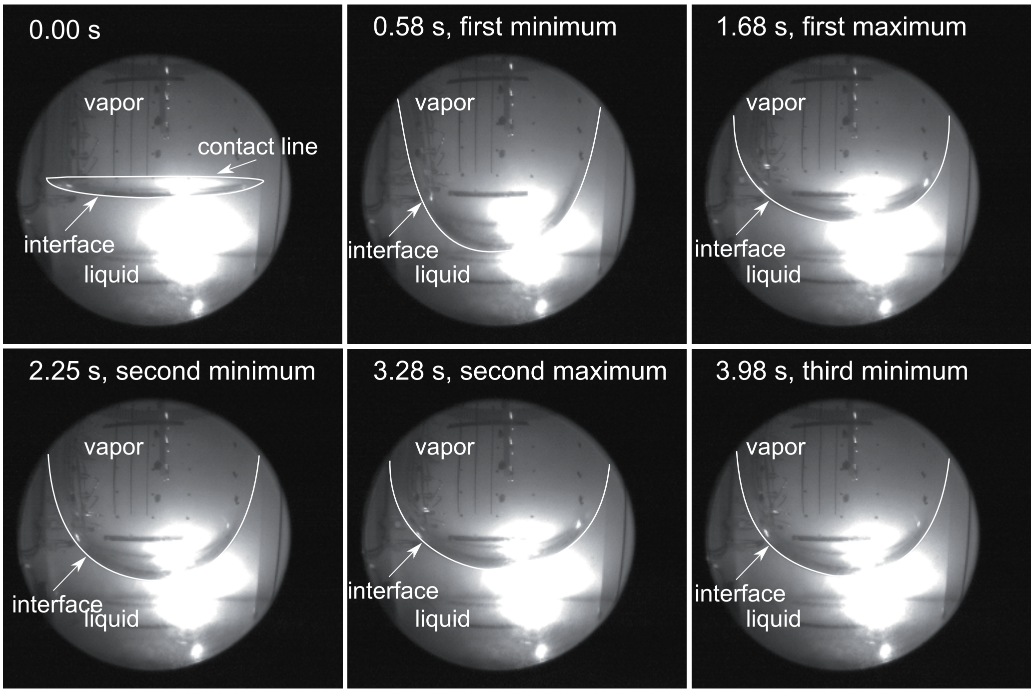

Figure 8.6: Images of the isothermal experiment A5 at certain time instances.

The gravity step reduction at $t = 0\,\mathrm{s}$ caused a reorientation of the free surface. The contact line rose along the wall and left the observable area. For isothermal experiments three local minima and two local maxima could be detected for the center point of the free surface. Figure 8.6 shows images of the free surface recorded by the CMOS camera just before the capsule release and during the microgravity phase. A quantitative evolution of the wall and center point height is presented in Fig. 8.7 and compared with results from the simulation SA5. Time t was made dimensionless with $t_{pu} = \left(\frac{\rho^l R^3}{\sigma}\right)^{1/2}$, thus $t^* = t/t_{pu}$. The dimensionless deflection z^* was calculated with the radius R as characteristic length, thus $z^* = z/R$. For the first couple of milliseconds the center point location z_c^* could not be detected due to a capillary wave traveling to the center created by the rising contact line [36]. This wave could be captured by the simulations. Throughout the reorientation, the center point oscillated around its inferred final location (indicated with the solid black line). The surface shape for Bo → 0 could not be achieved during the experiment time but was computed by the simulation. The wall point location z_w^* is also presented for better visibility in a detailed plot in Fig. 8.7. The initial offset is the capillary length as stated in table 8.2. After 0.29 s it moved out of the observable area.

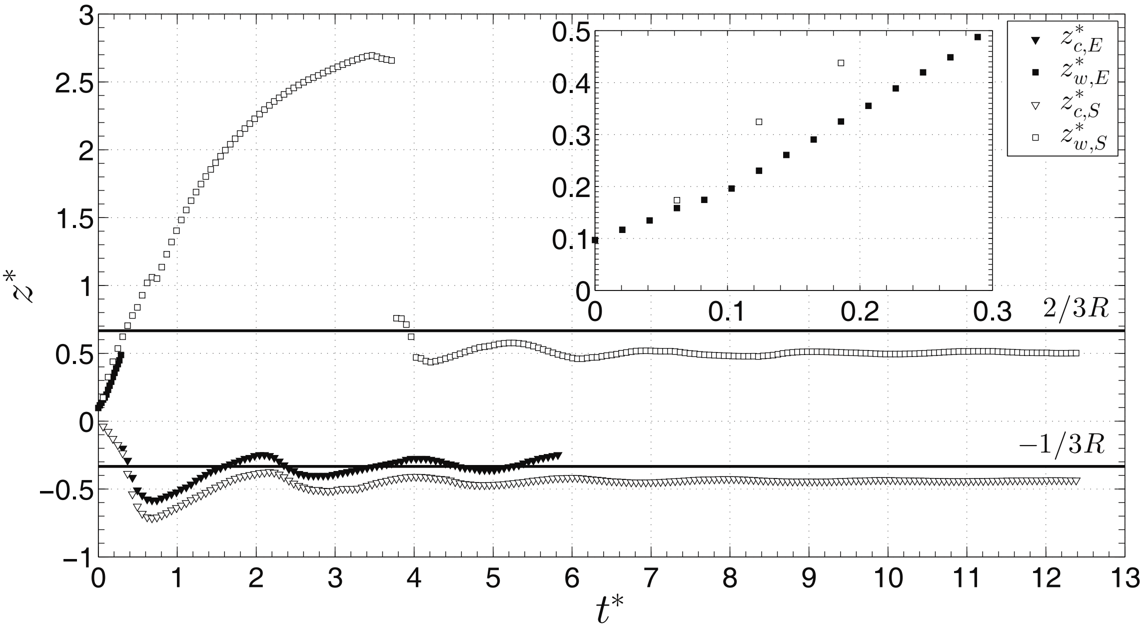

Figure 8.7: Contact line and center point motion for experiment A5 indicated with squares and downward facing triangles, respectively. Data from the simulation SA5 is indicated with corresponding hollow markers. The contact line rise is also shown in detail. The theoretical isothermal final center and wall point position at $-1/3R$ and $2/3R$ is indicated with the solid black line. All characteristic peaks are given in the tables A.8 and A.9. With $t^* = t/t_{pu} = t/\left(\rho^l R^3/\sigma\right)^{1/2}$ and $z^* = z/R$.

The numerical simulation helped to supplement the experimental data. As described in the mesh study (see Sec. 8.1.1), the simulation overpredicted the deflection of the first minimum by $\Delta z_{c,S} = 3.45\,\text{mm}$. This offset does not change for the remaining center point calculation. The computed steady state solution for the center point is $z_{c,S} = -11.39\,\text{mm}$ and the corrected position $z'_{c,S} = z_{c,S} + \Delta z_{c,S} = -7.94\,\mathrm{mm}$. This is within 9.3 % of the theoretical value $z_{c,T} = -1/3R = -8.75\,\mathrm{mm}$. The rise of the contact line along the cylinder wall was computed slightly faster than estimated from the experimental data. One can see, that the advancing motion was disturbed when the center point strode through the first minimum at $t^* = 0.74$. At $t^* = 3.72$, the liquid layer at the wall detached from the remaining free surface. The newly formed contact line reached a steady state at $z_{w,S} = 13.13\,\mathrm{mm}$ going through several oscillations. This value is 25 % below the theoretically predicted value $z_{w,S} = 2/3R = 17.51\,\mathrm{mm}$. The error was caused by the missing mass, which detached earlier in the reorientation process ($t^* = 3.72$) and remained at the wall as an isolated liquid mass.

Figure 8.8 shows the recorded wall temperatures and the calculated saturation temperature. All temperature plots in Sec. 8.1 refer to the temperature sensors depicted in Fig. 6.2. There exact locations are listed in the Appendix in table A.4. The wall temperature did not change during the reorientation but a drift could be recognized which is caused by the illumination, as explained. The slight temperature change over the free fall time indicates the good thermal insulation from the environment enabling almost isothermal conditions. For the vapor region a similar temperature progression can be noticed. Vapor temperatures are presented in Fig. 8.9. The sudden temperature increase of the vapor region at $t \approx 0.3\,\mathrm{s}$ was caused by the reorienting free surface pulling the stratified vapor downwards.

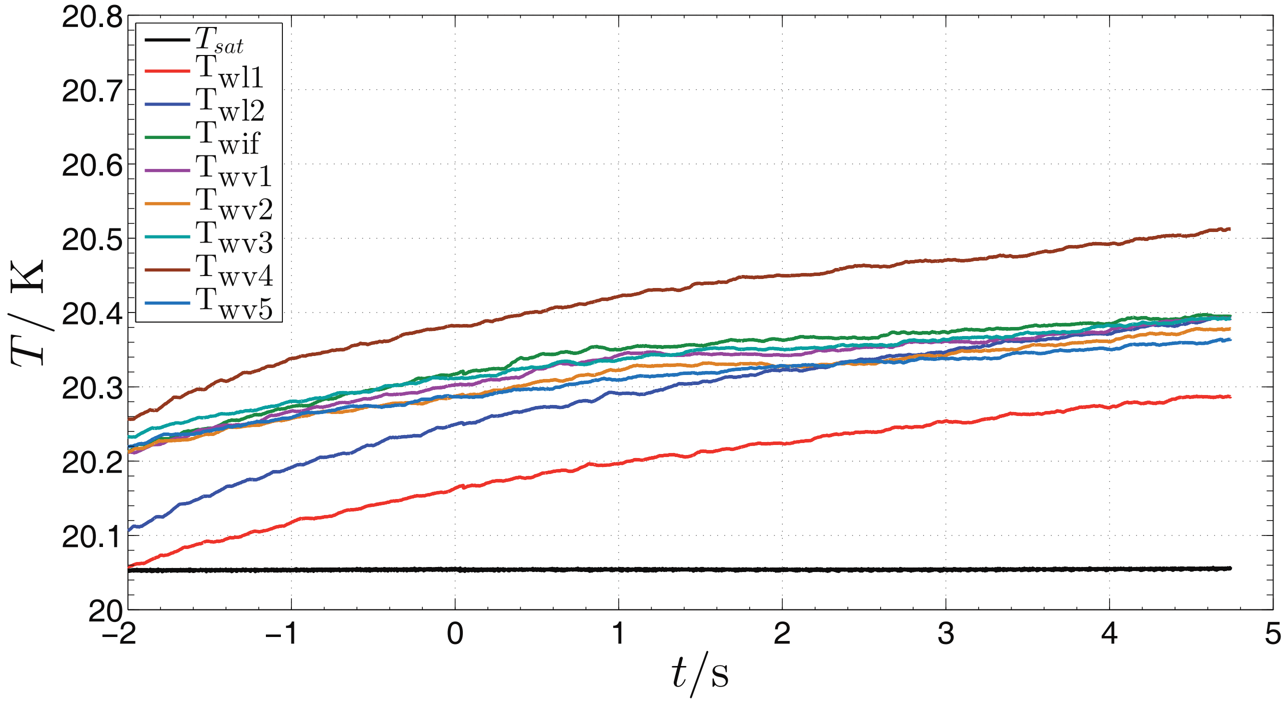

Figure 8.8: Temperature recordings of the wall sensors and computed saturation temperature for the isothermal experiment A5 starting two seconds prior to the drop.

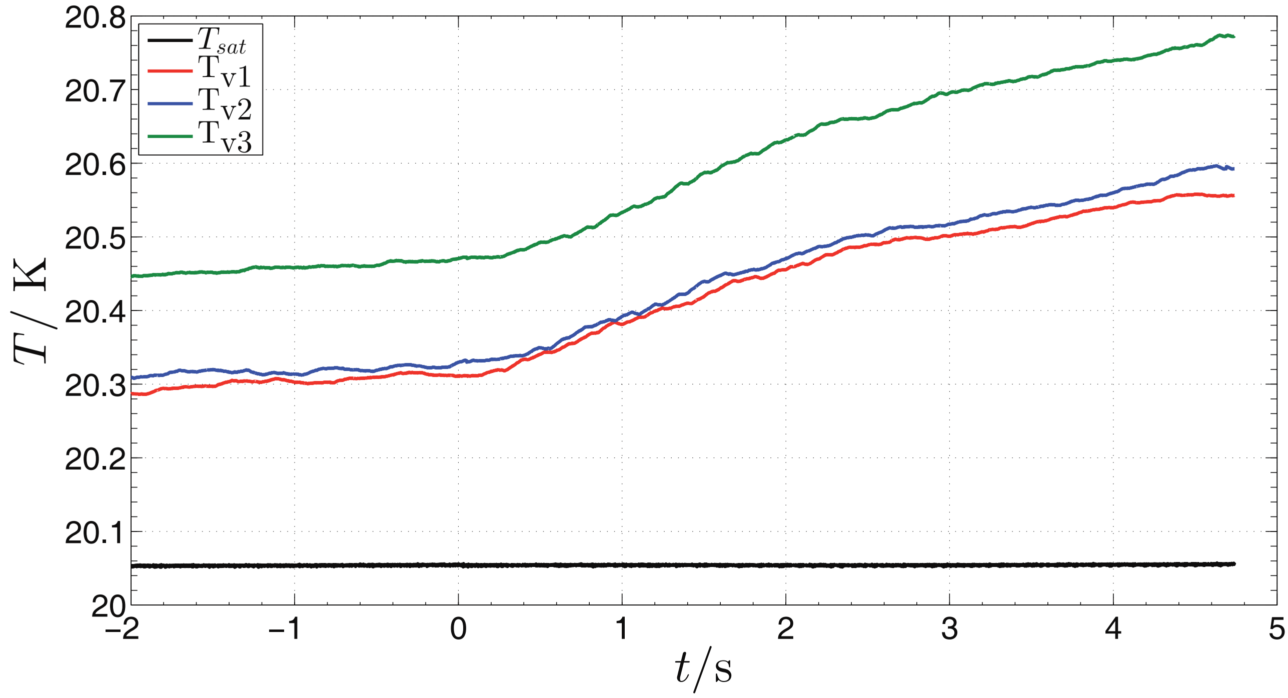

Figure 8.9: Temperature recordings of the vapor sensors and computed saturation temperature for the isothermal experiment A5 starting two seconds prior to the drop.

The simulations were initialized with $\Theta_0 = T_{wif,0} - T_{sat,0}$ reduced temperatures as explained in Sec. 6.2.4. Simulation SA5 covered 10 s of physical time. The history for wall and vapor temperatures differ from the experimental data. Wall temperatures are plotted in Fig. 8.10 and vapor temperatures in Fig. 8.11. The major difference is, that no drift of the wall temperatures as in Figs. 8.8 and 8.9 is perceptible. The non-monotonic temperature distribution along the wall (see Fig. 8.5) is equalized over the simulation. T_{wv2} to T_{wv5} converge to saturation conditions, whereas the temperature field below is slightly stratified. Vapor temperatures, however, show a certain drift. The fact that $T_{v1,0} < T_{sat,0}$ is due to the correction term Θ_0, which is not perfectly exact. The temperature in the vapor region was rapidly increased around $t \approx 0.3\,\mathrm{s}$ and returns to the initial drift after. The drift is caused by the stratification of the vapor region which was not maintained by any boundary condition and therefore started to equal out. Figure 8.12 shows temperature contour plots of the simulation SA5 at the time instances $t = 0.0\,\mathrm{s}$, $t = 0.3\,\mathrm{s}$, $t = 2.0\,\mathrm{s}$. The advancing contact line and resulting decreasing center point position caused a motion of the stratified vapor region. The downward moving free surface, indicated by the black solid line, pulled the stratified vapor with it. As a result, the vapor temperature sensors experienced a warmer environment.

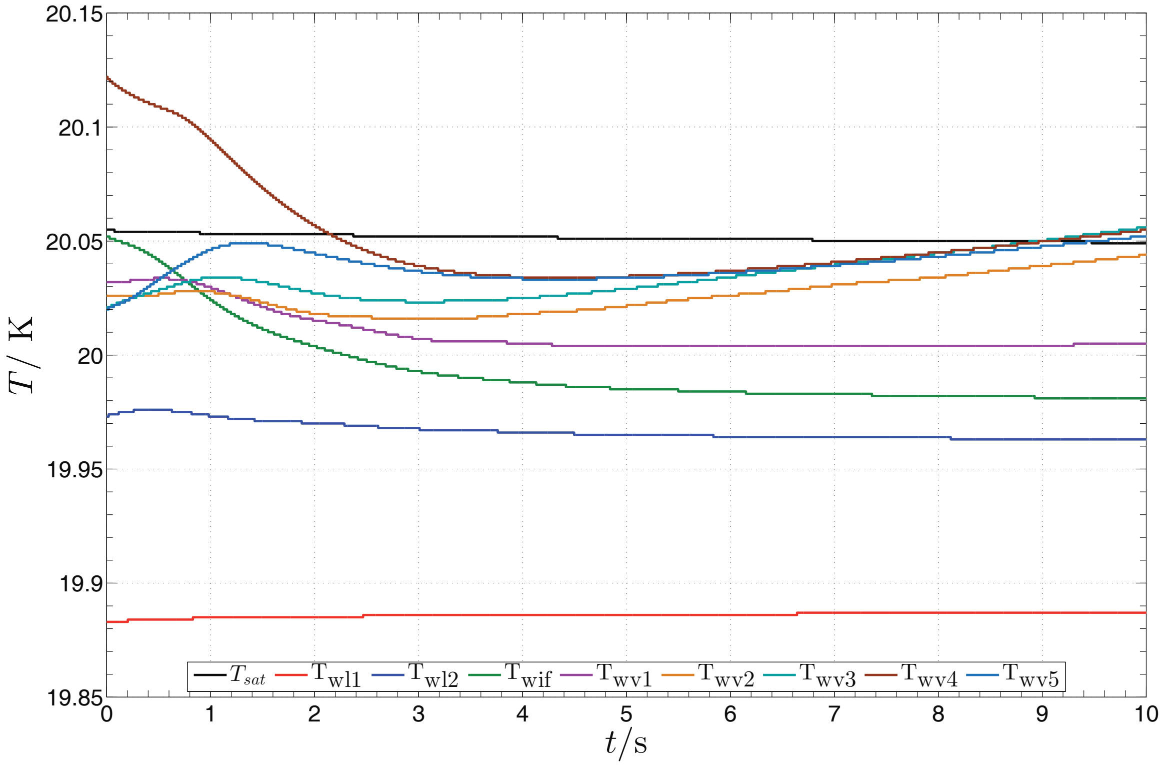

Figure 8.10: Temperature history of discrete wall points and computed saturation temperature for simulation SA5.

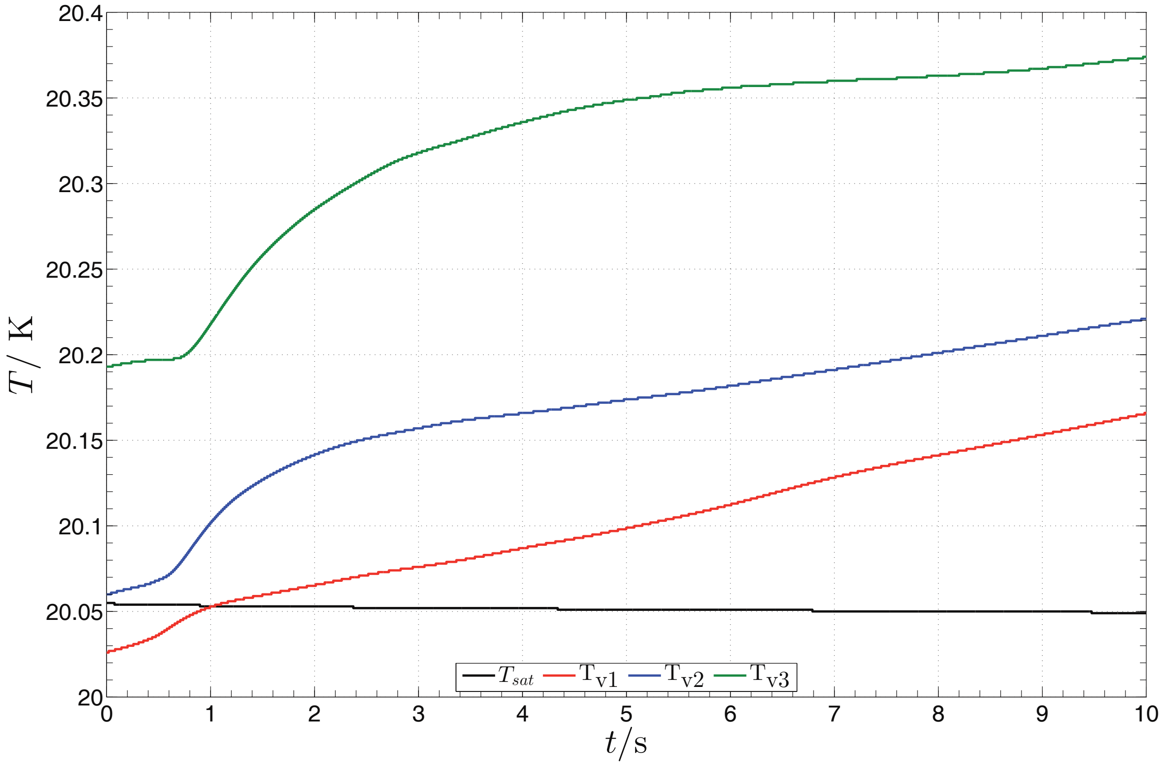

Figure 8.11: Temperature history of discrete points in the vapor region and computed saturation temperature for simulation SA5.

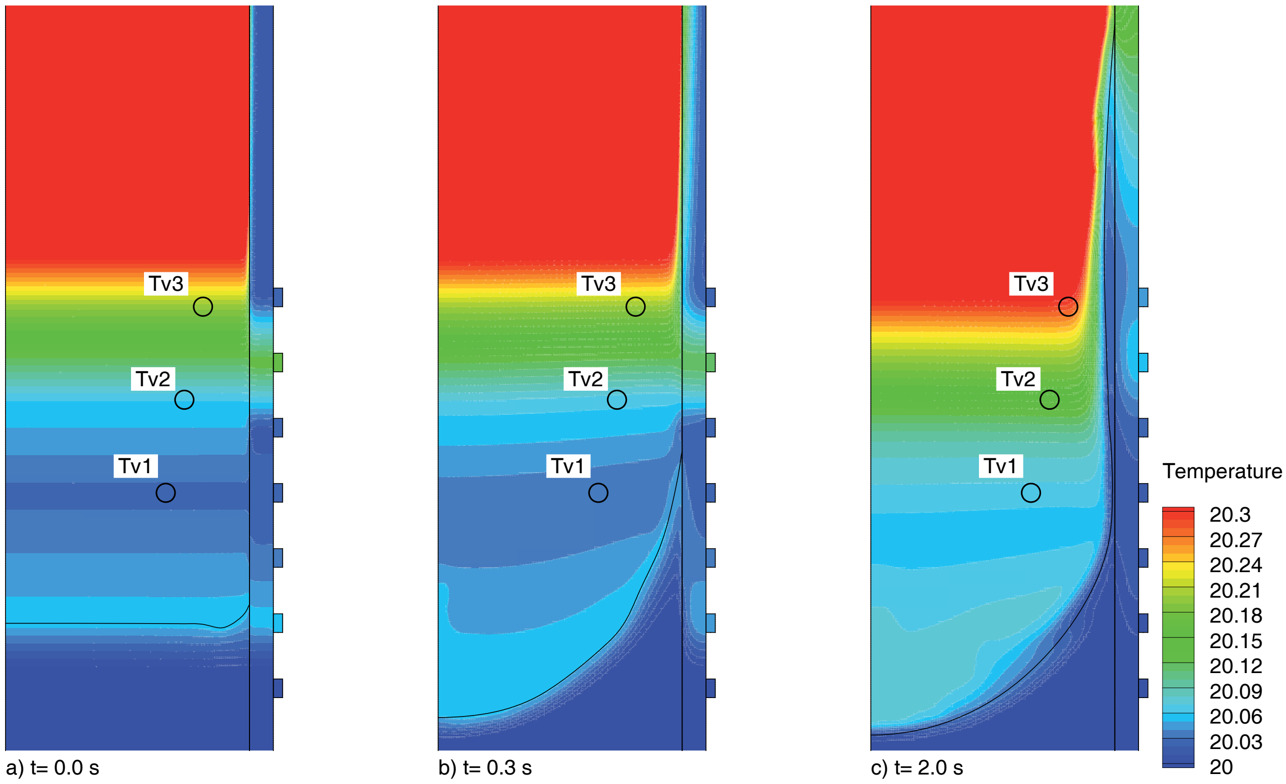

Figure 8.12: Temperature contour plots of SA5 with free surface (solid black line) at certain time instances. The temperature is given in K. Circles mark the locations of $\mathrm{T_{v1}}$, $\mathrm{T_{v2}}$ and $\mathrm{T_{v3}}$. a) $t = 0.0\,\mathrm{s}$. b) $t = 0.3\,\mathrm{s}$. c) $t = 2.0\,\mathrm{s}$.

8.1.5 Non-Isothermal Conditions without Boiling

The only experiment with a wall temperature gradient that did not cause nucleate boiling was B6. The recorded wall and vapor temperatures at $t = 0\,\mathrm{s}$ are plotted in Fig. 8.13. For a better visibility adjacent symbols are connected with each other with a dotted or dashed line. This does not necessarily represent the temperature progression between two sensors. The stratification in the liquid could be nearly neutralized and the target wall gradient (solid black line) was met. The saturation temperature and corresponding wall temperature (T_{wif}) showed the same discrepancy as for the other experiments. The vapor region was stratified alike the wall which is caused by the heating method.

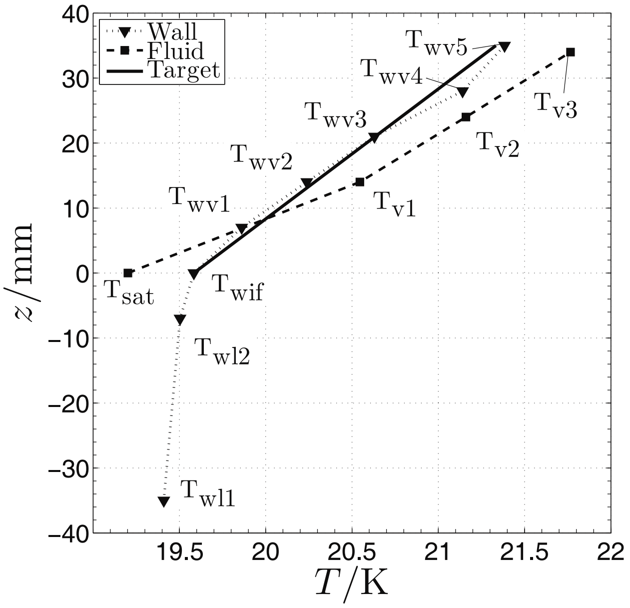

Figure 8.13: Initial temperature distribution at $t = 0\,\mathrm{s}$ for the experiment B6 ($\Delta T^*/\Delta z^* = 0.07$). Wall temperature sensors are indicated with a downward facing triangle and connected for better visibility with a dotted line, which does not represent the temperature distribution between two adjacent sensors. Vapor temperatures are indicated with a square marker and connected for better visibility with a dashed line. The saturation temperature is calculated with the pressure value. The solid black line represents the target wall temperature gradient.

The response of the free surface to the gravity step reduction is similar to the one explained in section 8.1.4. Throughout the free fall time no bubbles were visible. The contact line also moved out of the observed area shortly after the release. For this experiment three local minima and three local maxima could be detected. The corresponding pictures of the experiment are presented in Fig. 8.14. Quantitative analysis of the wall and center point progression revealed the differences from the isothermal case. Figure 8.15 depicts the wall and center point

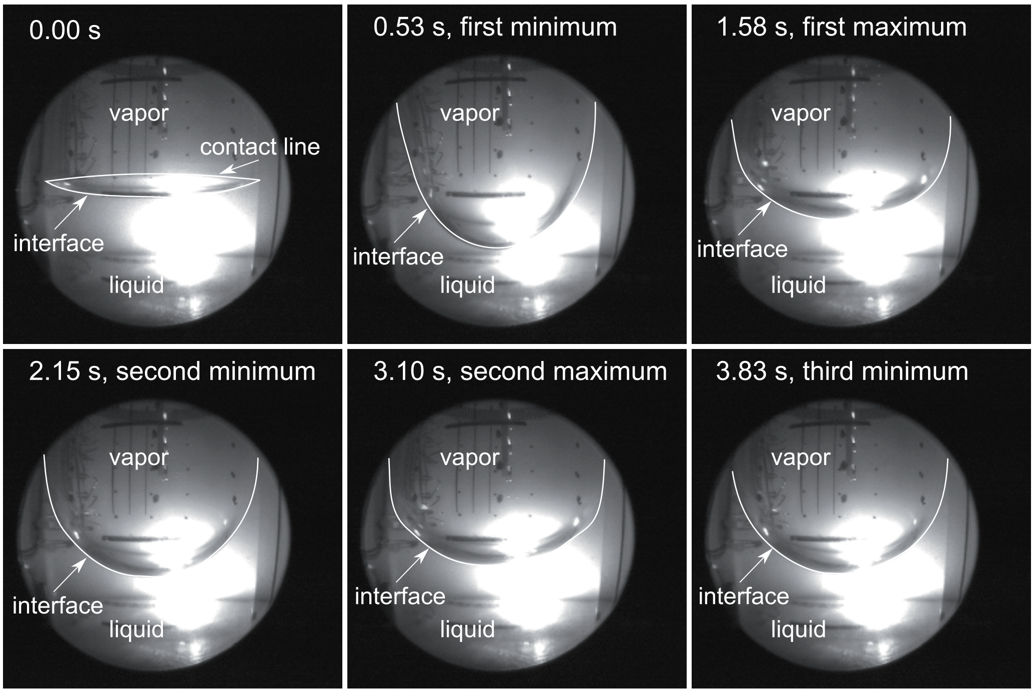

Figure 8.14: Images of experiment B6 ($\Delta T^*/\Delta z^* = 0.07$) at certain time instances.

positions throughout the test and the simulation SB6 in dimensionless form. The solid black lines indicate the expected final center point and wall point location for a zero static contact angle as in Fig. 8.7. The center point deflection was less developed than for the isothermal case. This implied a final center point position, that is above the one theoretically predicted for isothermal conditions. The advancing contact line was not affected by the superheated wall.

The simulation SB6 is in good accordance with the experiment. Again, the first center point deflection is overpredicted by $\Delta z_{c,S} = 3.95\,\mathrm{mm}$. This initial offset does not change throughout the computation. At the end of the simulation a steady center point position of $z_{c,S} = -11.32\,\mathrm{mm}$ evolves, corresponding to a corrected value of $z'_{c,S} = -7.37\,\mathrm{mm}$. The final center point position is equal to the one derived from the isothermal computation SA5 with $z_{c,S} = -11.39\,\mathrm{mm}$ and $z'_{c,S} = -7.94\,\mathrm{mm}$. Similar results were discovered for the wall point. The computed final wall point location was $z_{w,S} = 13.21\,\mathrm{mm}$ which is almost the same as in simulation SA5 with $z_{w,S} = 13.13\,\mathrm{mm}$. This point will be discussed in detail in Sec. 8.1.6. The advancing contact line motion was disturbed while the center point was at its first minimum at $t^* = 0.64$. Detachment occurred at $t^* = 3.60$. The remaining liquid from the film formed an isolated mass as for simulation SA5.

The wall temperature was influenced by the rising contact line region. Figure 8.16 shows the data from the wall temperature sensors and the calculated saturation temperature. The temperatures have a similar drift as plotted in Fig. 8.8 followed by a sudden drop when the

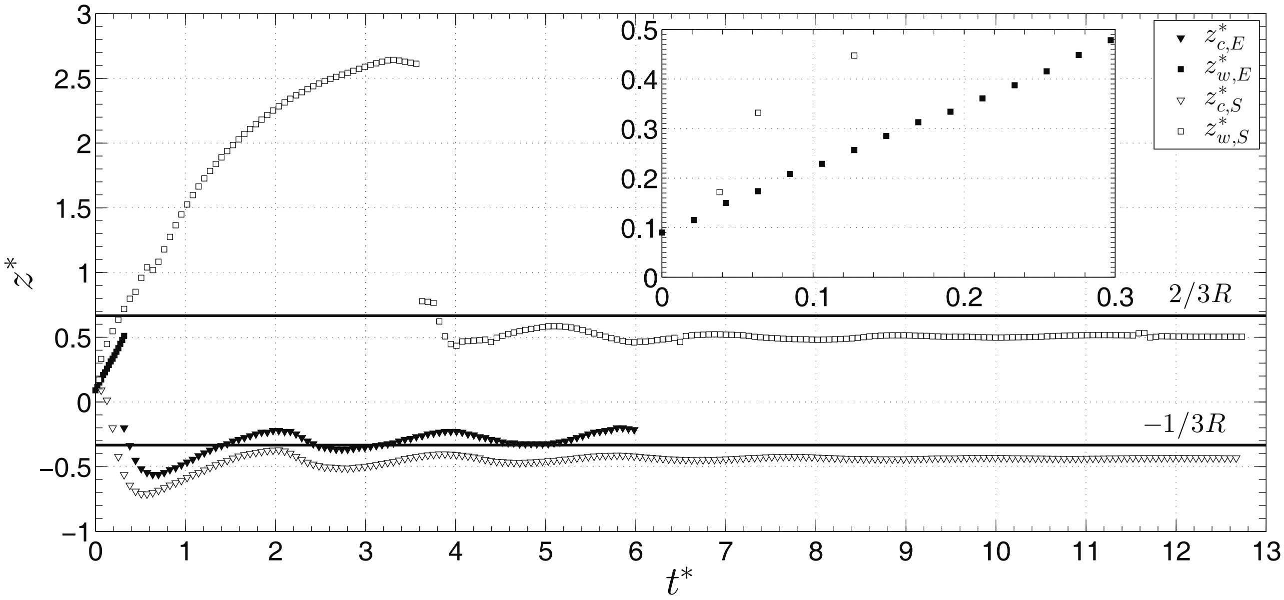

Figure 8.15: Contact line and center point motion for experiment B6 ($\Delta T^*/\Delta z^* = 0.07$) indicated with squares and downward facing triangles, respectively. Data from the simulation SB6 is indicated with corresponding hollow markers. The contact line rise is also shown in detail. The theoretical isothermal final center and wall point position at $-1/3R$ and $2/3R$ is indicated with the solid black line. All characteristic peaks are given in the tables A.8 and A.9. With $t^* = t/t_{pu} = t/\left(\rho^l R^3/\sigma\right)^{1/2}$ and $z^* = z/R$.

inside of the cylinder was wetted by the advancing contact line. The black squares mark the time when the contact line reached the height of the corresponding sensor. It is obvious, that there is a time lag between the instance of wetting and the recorded temperature drop which could be quantified to $\Delta t_E = 0.4\,\mathrm{s}$. This delay is caused by the thermal diffusivity a_{bs} of the glass cylinder and its thickness $\Delta r_{bs} = 2.55$ mm. The sensor response time of 100 ms increased the delay. After the wall was wetted, its temperature declined monotonically. The vapor temperatures presented in Fig. 8.17 showed a similar progression as for the isothermal case. $\mathrm{T_{v4}}$ recorded a temperature drop at $t = 2.8\,\mathrm{s}$ which was followed by an oscillating decrease below the recordings of $\mathrm{T_{v3}}$. It could not be confirmed that evaporation from the contact line region caused this decrease, as reported for other cryogenic liquids [52].

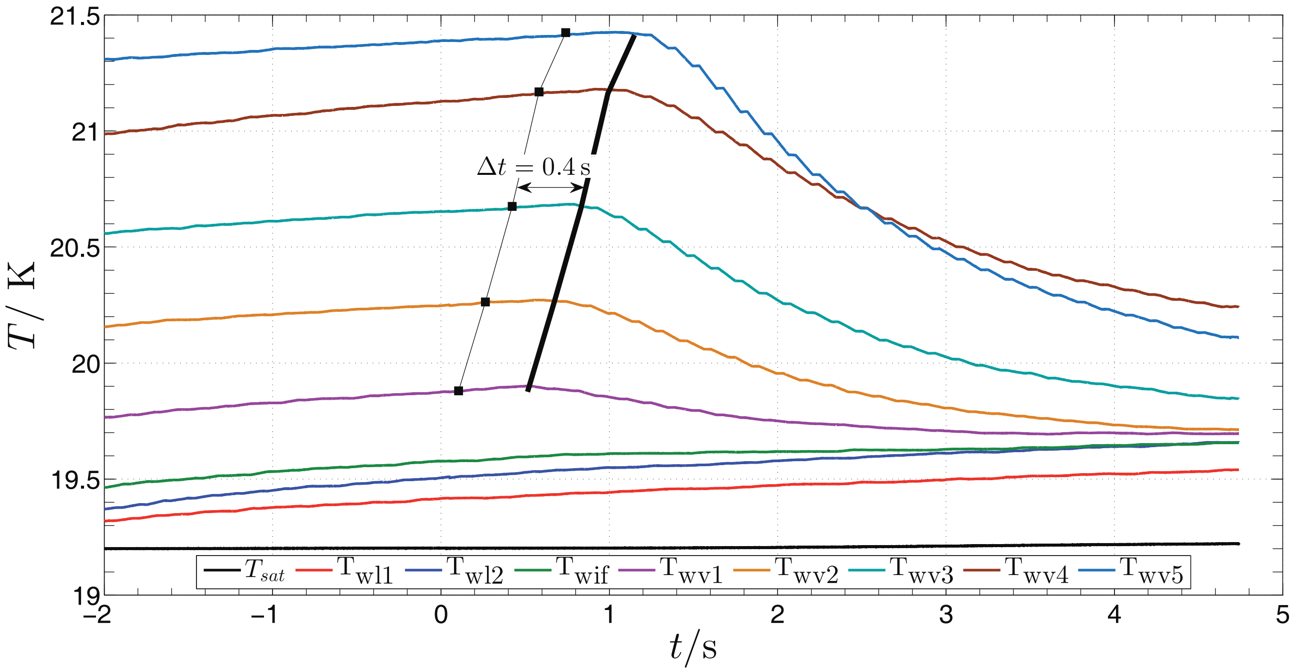

Figure 8.16: Temperature recordings of the wall sensors and computed saturation temperature for experiment B6 ($\Delta T^*/\Delta z^* = 0.07$) starting two seconds prior to the drop. Squares mark the time when the contact line reached the sensor height. The resulting temperature drop was recorded by the sensors with a delay of $\Delta t = 0.4\,\mathrm{s}$.

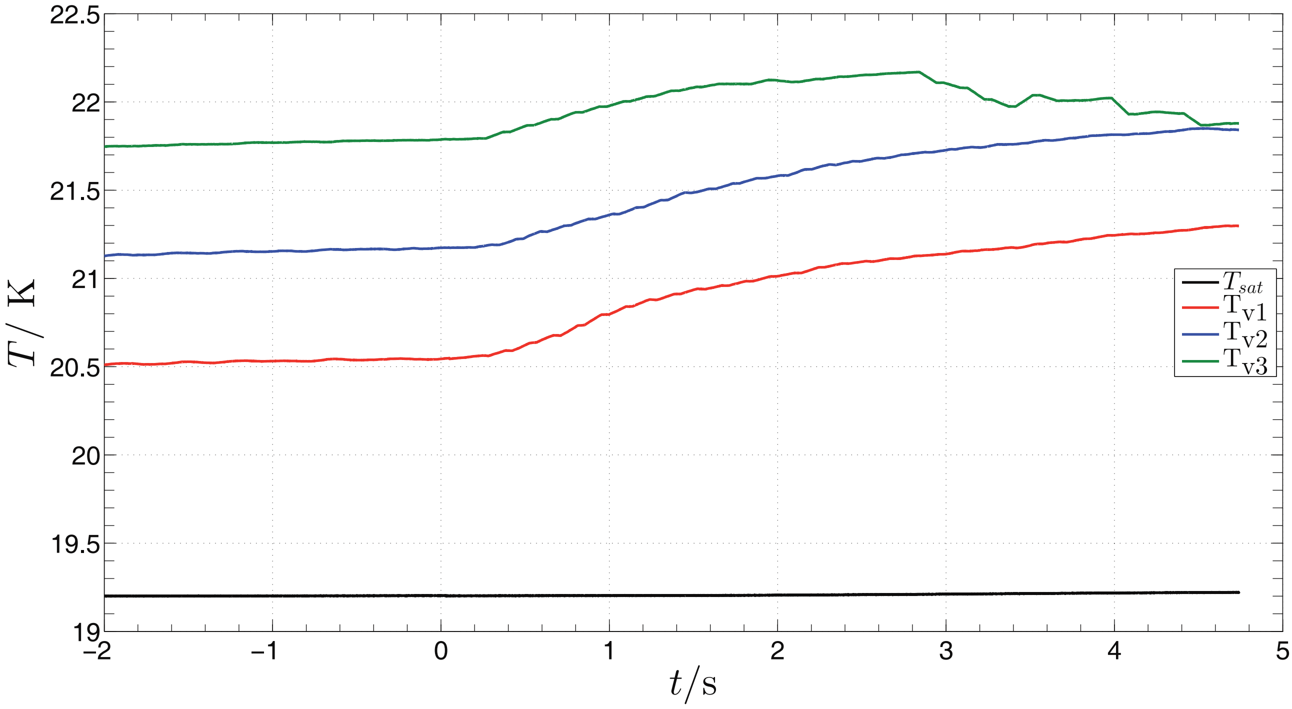

Figure 8.17: Temperature recordings of the vapor sensors and computed saturation temperature for experiment B6 ($\Delta T^*/\Delta z^* = 0.07$) starting two seconds prior to the drop.

The corresponding simulation SB6 allows to draw further conclusions about wall and vapor temperature progression. Figure 8.18 shows the wall temperature history above the free surface for the experiment (solid lines) and the simulation (dashed lines). Experimental values were corrected by $\Theta_0 = 0.38\,\mathrm{K}$ to eliminate the laser influence. The squares mark the time where the free surface in the simulation passed the sensor height. The solid black line indicates the beginning decrease of the recorded temperature. The delay between wetting and temperature regression is approximately $\Delta t_S = 0.2\,\mathrm{s}$, which is less compared to the $\Delta t_E = 0.4\,\mathrm{s}$ detected for the experiment (see Fig. 8.16). The difference can be explained by the sensor response time of 100 ms and the modeling of the sensor itself. It was modeled as a homogeneous mass neglecting the sensor's complex inner structure. The glue between sensor and cylinder wall with the resulting thermal resistance could not be determined and was not considered. Before the monitored temperature drop, the temperatures along the wall showed no drift as in the experiment. Again, this might be caused by the illumination. The temperature decrease was captured well by the simulation except for T_{wv4}. The intersection of the experimental sensor recordings of $\mathrm{T_{wv4}}$ and $\mathrm{T_{wv5}}$ at $t = 2.5\,\mathrm{s}$ cannot be explained at this point, but an external effect, which is not considered in the simulation, must have caused this behavior. At the end of the simulation, when a new stable surface configuration could be detected, the stratification in the wall was almost neutralized by the advancing liquid.

A correct initialization of the vapor region was difficult to conduct with only three available data points (T_{v1}, T_{v2} and T_{v3}). Figure 8.19 shows the corrected experimental vapor temperatures (solid lines) and the corresponding temperatures from the simulation (dashed lines). Figure 8.20 shows temperature contour plots with the free surface of the simulation at certain time instances. The stratification at the beginning is clearly visible. The initial temperature rise caused by the advancing contact line (see Sec. 8.1.4 and Figs. 8.11 and 8.12) was captured well. A rising temperature at the location for $\mathrm{T_{v3}}$ could be detected with a certain delay. Advancing in time, the simulation deviates from the experimental results. Instead of a further increase, $\mathrm{T_{v1}}$ detects a slight decrease. $\mathrm{T_{v2}}$ and $\mathrm{T_{v3}}$ experience a plateau, followed by a slight decrease. Figure 8.20 b) shows the instance in time when $\mathrm{T_{v1}}$ experiences its peak. The other two sensor locations indicate a further rise, hence an additional amount of hot gas from the ullage flowed down the cylinder. This different temperature progression might be caused by an insufficiently modeled initial temperature field of the vapor region. The drop of T_{v1} at $t = 5.5\,\mathrm{s}$ occurred after the end of the experiment. It is caused by the rising vortex carrying relatively cold vapor (saturation temperature) from the vicinity of the free surface. This ring vortex was caused by the sudden drop of the center point. Figure 8.20 c) shows the vortex arriving at the location of $\mathrm{T_{v1}}$. Figure 8.20 d) at $t = 7.5\,\mathrm{s}$ visualizes the temperature field when the vortex passed the location of $\mathrm{T_{v1}}$. This passing was detected with a temperature rise.

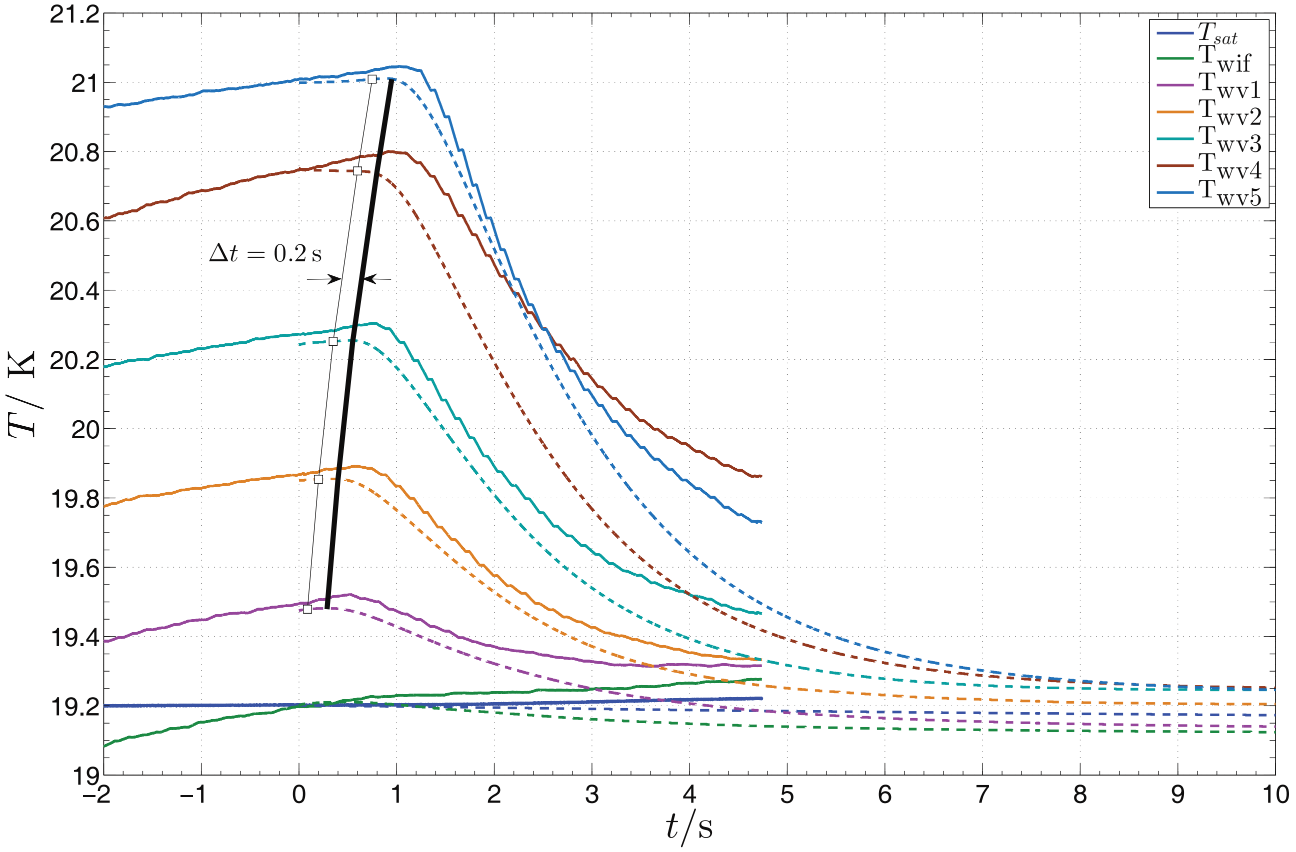

Figure 8.18: Temperature recordings of the wall sensors and computed saturation temperature for experiment B6 (solid lines) and the simulation SB6 (dashed lines). Experimental temperature history was corrected by $\Theta_0 = 0.38\,\mathrm{K}$. Squares mark the time when the simulated contact line reached the sensor height. The resulting temperature drop was recorded with a delay of $\Delta t = 0.2\,\mathrm{s}$.

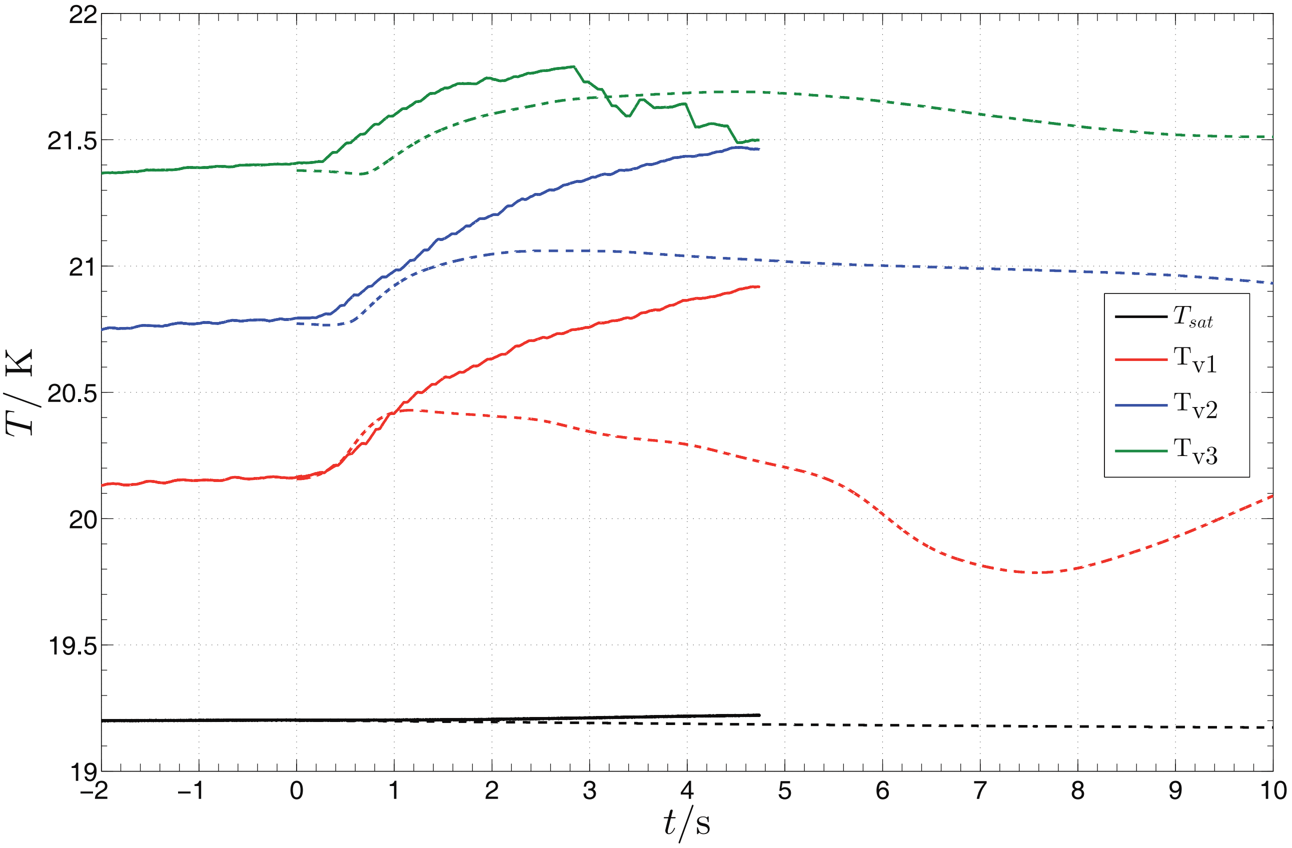

Figure 8.19: Temperature history of the vapor sensors and the saturation temperature of experiment B6 (solid lines) and the corresponding results of simulation SB6 (dashed lines). Experimental temperature history was corrected by $\Theta_0 = 0.38\,\mathrm{K}$.

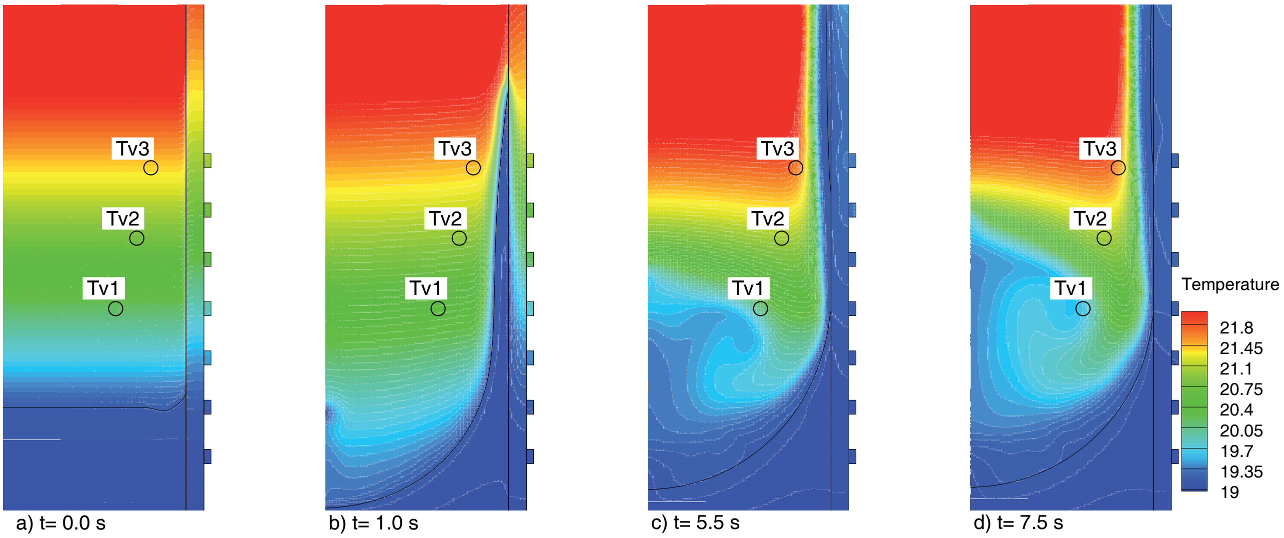

a) t= 0.0 s b) t= 1.0 s c) t= 5.5 s d) t= 7.5 s

Figure 8.20: Temperature contour plots of SB6 with free surface (solid black line) at certain time instances. Temperature is given in K. Circles mark the locations of T_{v1}, T_{v2} and T_{v3}. a) $t = 0.0\,\mathrm{s}$ b) $t = 1.0\,\mathrm{s}$ c) $t = 5.5\,\mathrm{s}$ d) $t = 7.5\,\mathrm{s}$.

8.1.6 Global Free Surface Behavior

This section covers the free surface behavior. A sufficient wall point detection was possible for all six experiments. The center point location of the free surface could only be quantified for the experiments C4, A5, and B6. It was possible to monitor the free surface motion and extract the oscillation of the center point. Experimental data is supplemented by numerical simulations of the experiment A5 and B6 and a study with gradients that lie in between the gradients of these two experiments. All simulations cover 10 s of physical time to allow the free surface to form a new stable configuration. It required about nine days to simulate the 10 s physical time.

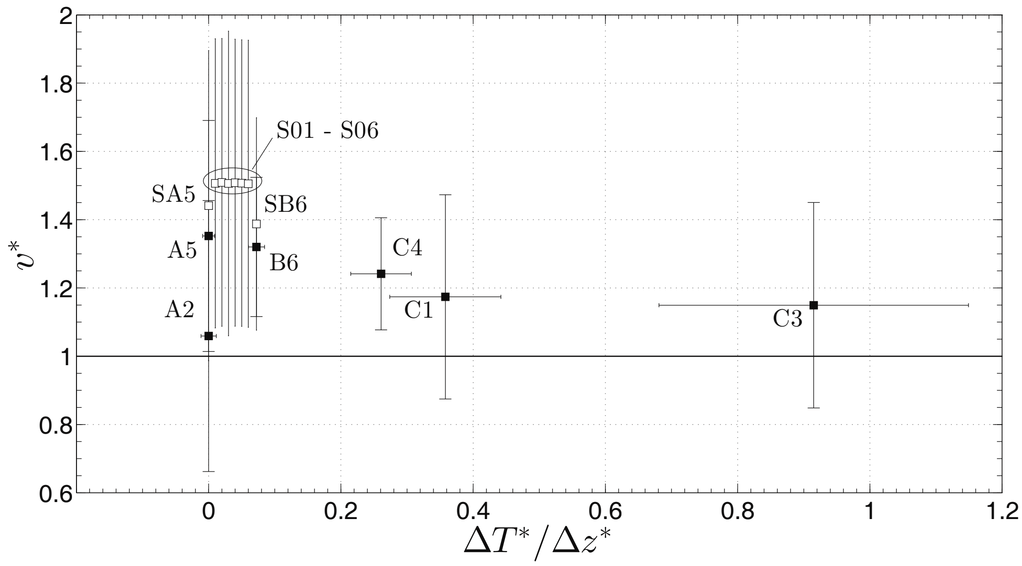

Figure 8.21: Dimensionless velocity $v^* = v/v_{pu} = v/\left(\sigma/\rho^l R\right)^{1/2}$ versus dimensionless wall temperature gradient $\Delta T^*/\Delta z^* = \left(\Delta T/\Delta z\right) / \left(T_{sat,0}/R\right)$ with standard deviation for all experiments and simulations.

To prove the scaling for the characteristic velocity v_{pu} (see eq. 2.25) a mean velocity of the rising contact line was computed from the wall point. The change of the contact line position $\Delta z_{w,n}$ was evaluated once at a time. The corresponding velocity v_n was achieved by division by the time difference between the two pictures $\Delta t = 0.017$ s. The average velocity was computed with

$$v = \frac{1}{n-1} \sum_n v_n = \frac{1}{n-1} \sum_n \frac{z_{w,n+1} - z_{w,n}}{\Delta t} \,. \tag{8.1}$$

To calculate the average velocity of the rising wall point from the simulations, eq. 8.1 was used as well for the time span between 0 s and the time of the first center point minimum. This time span excluded any influence from the center point kinematic. Figure 8.21 shows the velocity versus the applied wall temperature gradient in dimensionless form with standard deviations. The velocities are of order 1 which confirms the scaling. The characteristic velocities of the non-isothermal experiments do not show a clear trend compared to the isothermal cases. This leads to the assumption that the wall superheat does not have a significant influence on the advancing contact line. The simulations could not supplement these findings. All calculated velocities are above the experimental results but still in their standard deviations. As for the experiments, they show large standard deviations. No influence of the wall superheat could be detected.

Analyzing the experimental data shows a dependency between center point oscillation and wall superheat. For a quantitative analysis, time instances of the local minima and maxima for all experiments and simulations were extracted and are listed in the Appendix in table A.8 and table A.9, respectively. Based on this data, a mean frequency $\omega = 2\pi f$ was derived for each experiment and simulation. This was done by taking the mean of the periodic time T between two minima or maxima, thus

$$\omega = 2\,\pi\,f = 2\,\pi\left(\frac{1}{2}\left(\frac{1}{n-1}\sum_{n} T_{min,n} + \frac{1}{m-1}\sum_{m} T_{max,m}\right)\right)^{-1} . \tag{8.2}$$

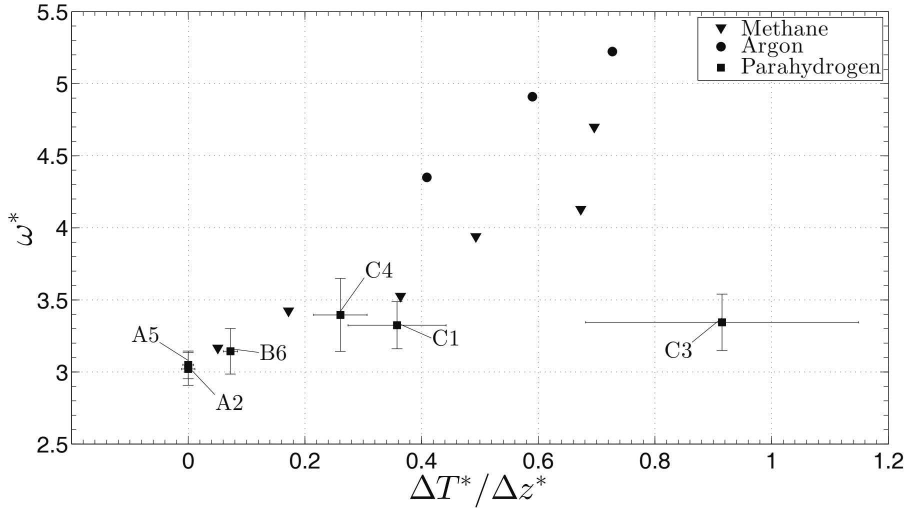

Figure 8.22: Dimensionless frequency $\omega^* = \omega\, t_{pu} = \omega\left(\rho^l R^3/\sigma\right)^{1/2}$ versus dimensionless wall temperature gradient $\Delta T^*/\Delta z^* = \left(\Delta T/\Delta z\right)/\left(T_{sat,0}/R\right)$ with standard deviation for all experiments with parahydrogen and the results for argon and methane [52].

Figure 8.22 presents the frequency (scaled with eq. 2.24) in dimensionless form together with results for argon and methane [52]. One can say, that for isothermal conditions $\omega^* \approx 3$ for all three fluids. Argon and methane show a linear dependency of the dimensionless frequency on the dimensionless wall temperature gradient. From the given data, argon shows the highest slope followed by methane. For parahydrogen an increase can be noticed for small wall temperature gradients which was followed by a constant progression of the frequency with a further increase of the wall temperature gradient. The values for the test cases with nucleate boiling at the wall must be treated with care, but are shown for completeness. Overlapping standard deviations in Fig. 8.22 resulted from the fact that the center point oscillation is not a harmonic oscillation. It is assumed, that the initial surface rise mentioned in Sec. 2.2.4 [22, 65] caused a superimposed frequency. This results in differing time intervals between two minima or maxima from which the mean frequency is computed (see tables A.8 and A.9). The standard deviation reflects the fact, that the oscillation is not linear. It is not an artifact of the evaluation of the experiments.

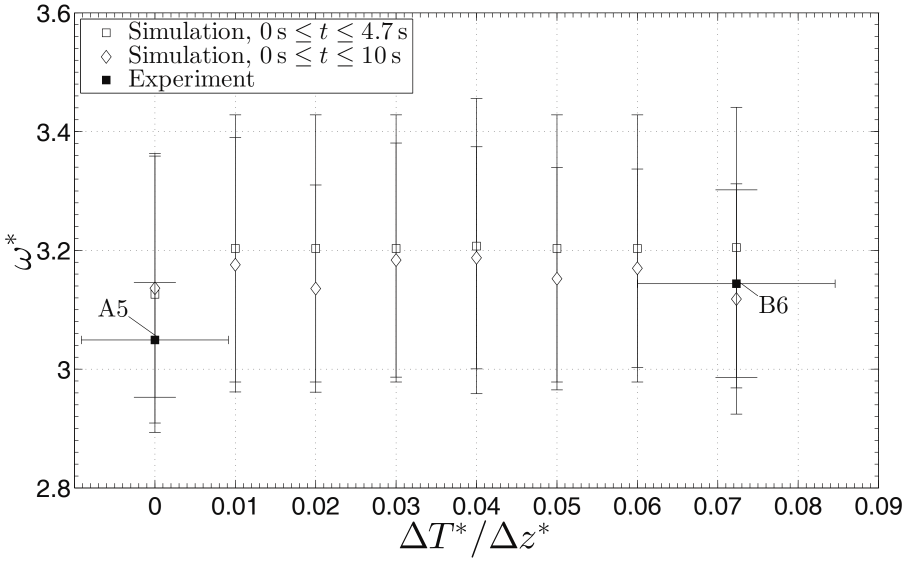

Figure 8.23: Dimensionless frequency $\omega^* = \omega\, t_{pu} = \omega\, \left(\rho^l R^3/\sigma\right)^{1/2}$ versus dimensionless wall temperature gradient $\Delta T^*/\Delta z^* = \left(\Delta T/\Delta z\right) / \left(T_{sat,0}/R\right)$ with standard deviation for experiments A5 and B6 and the simulations. Hollow square markers indicate ω^* determined from data up to $t_S \le 4.7\,\mathrm{s}$ and diamonds include all extrema ($t_S \le 10\,\mathrm{s}$).

The simulations concentrated on the wall temperature gradients between experiment A5 and B6, thus $0.00 \le \Delta T^*/\Delta z^* \le 0.07$. The motivation was to find further evidence for the influence of the wall temperature gradient on the reorientation frequency. For the evaluation of the dimensionless frequency two sets of data could be used. One includes only the extrema that occurred within the experimental time span ($t_S \le 4.7\,\mathrm{s}$), the other includes all extrema. Figure 8.23 presents the two experiments together with the numerical results for varying dimensionless wall temperature gradients. Results derived from the reduced data set are represented by hollow square markers and hollow diamonds indicate the results using the entire available data. One can see, that the standard deviation is even larger than for the experimental results and no clear trend can be detected. Square markers, show a significant jump of the dimensionless frequency between simulation without a temperature gradient (SA5) and the other simulations (S01-S06, SB6). The spread of the second data set (diamonds) is too big as that any trend could be determined. A plausible cause for this result is, that the energy from the superheated wall will be absorbed by the advancing liquid layer. Introducing Θ_{sup}

$$\Theta_{sup} = T_{2/3R} - T_{sat} \,, \tag{8.3}$$

which defines the wall superheat at $r = R = 26.26\,\mathrm{mm}$ and $z = 2/3R = 17.51\,\mathrm{mm}$ above the initial free surface. This height was chosen, since it represents the theoretically predicted isothermal final wall point [18]. This value could not be determined for the experiments, because the temperature was measured at the outer wall and not at the inside of the cylinder. Figure 8.24 shows the history of Θ_{sup} for all simulations. After approximately 1.9 s Θ_{sup} was constant, thus a steady state between wall and liquid temperature was achieved. The center point passed the first minimum and maximum at this time. The assumption is, that the wall superheat affected the center point frequency during this time ($0\,\mathrm{s} \leq t \leq 1.9\,\mathrm{s}$). This explains the difference in ω^* between A5 and B6, or SA5 and S01. However, the wall superheat was not high enough and decreased too fast to have a major impact on the free surface reorientation in comparison with argon and methane (see Fig. 8.22).

Table 8.3: Constant C and damping coefficient δ to describe the envelopes for the center point oscillation of SA5 and SB6, the mean circular frequency ω and the derived damping ratio D.

		SA5			SB6		
		Min	Max	Mean	Min	Max	Mean
C	mm	6.58	3.39	4.99	6.83	3.29	5.06
δ	s^{-1}	0.44	0.44	0.44	0.51	0.43	0.47
ω	s^{-1}	3.87	3.87	3.87	4.01	4.01	4.01
D	–	0.11	0.11	0.11	0.12	0.11	0.11

The theory of free surface oscillations and damping was discussed in detail by Gerstmann [34]. Experimental results of various non-cryogenic liquids were presented by Michaelis et al. [67] and Weislogel and Ross [88]. Due to the short experiment time, it was not possible to detect any damping characteristics of the free surface from the center point motion. Within the numerical simulations the free surface could form a new stable shape. The new stable free surface was reached after approximately 10 s and 5 periods of the center point oscillation. Here

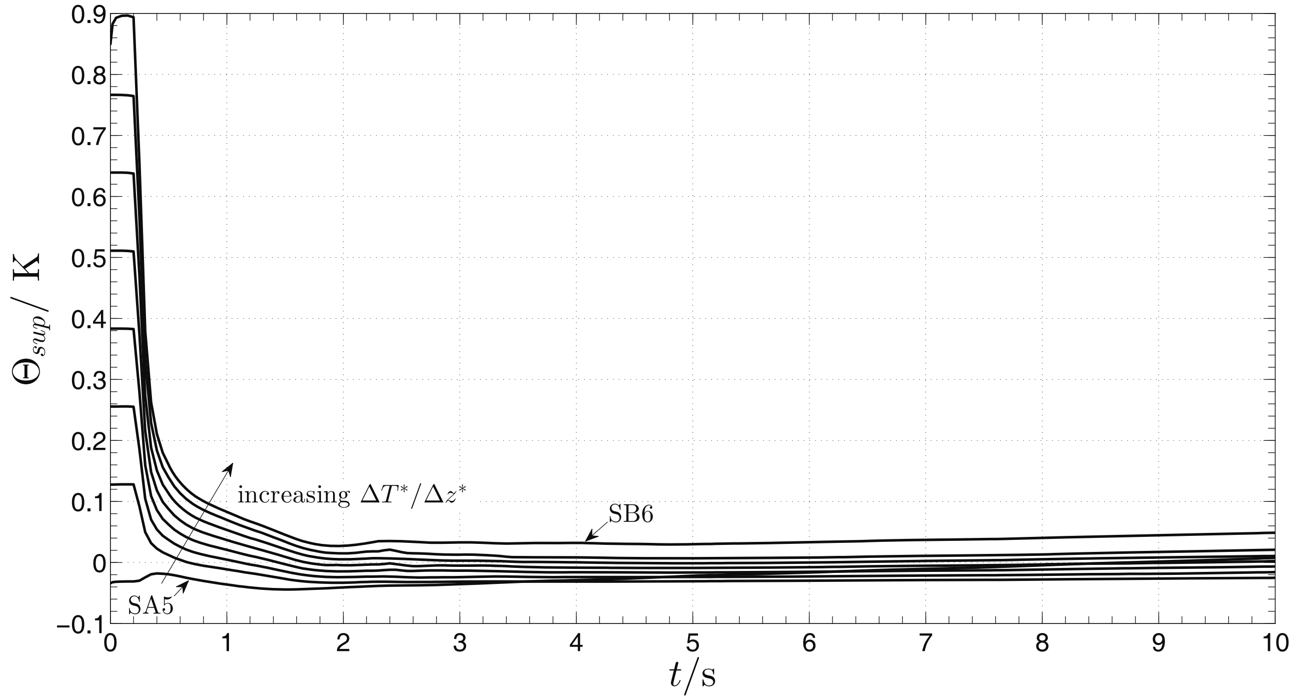

Figure 8.24: History of wall superheat $\Theta_{sup} = T_{2/3R} - T_{sat}$ for all simulations.

only the two simulations SA5 (isothermal) and SB6 (non-isothermal) were considered. The first minimum was excluded from the damping analysis since it was influenced by the advancing liquid layer along the wall. Tables A.8 and A.9 in the Appendix lists all occurring local extrema of the center point oscillation. These values were used to describe the underdamped oscillation with the envelopes [41]

$$z_{min} = -C\mathrm{e}^{-\delta_{min}t} - z_{c,1}\,, \qquad z_{max} = C\mathrm{e}^{-\delta_{max}t} - z_{c,1}\,, \tag{8.4}$$

where the minimum and maximum center point position is described by the damping coefficient δ, the time t, the constant C and the final center point location $z_{c,1}$. Figures 8.25 a) and b) plot the extracted center point progression with the envelope for simulation SA5 and SB6, respectively. The solid black triangles indicate the local extrema used for the calculation of the envelope. Using the determined damping coefficient δ with the mean circular frequency ω (calculated with eq. 8.2) gives the logarithmic decrement Λ [41]

$$\Lambda = \frac{2\pi\delta}{\omega} = \frac{\mathrm{D}}{\sqrt{1-\mathrm{D}^2}}\,. \tag{8.5}$$

This equation can also be used to calculate the damping ratio D, which is a dimensionless number to describe the decay of the oscillation. Table 8.3 summarizes C, δ, ω and D for the two simulations, where the column Min represents the terms for the envelope computed from all local minima and the column Max those computed from the local maxima. The column Mean is the arithmetic mean from the two envelopes. One can see, that the values do not differ much for the two simulations and especially the damping ratio is the same. That results in the assumption, that the wall temperature gradient does not influence the damping of the center point oscillation. Considering Fig. 8.24, the wall superheat was practically not existing anymore when the center point passed its first maximum (first considered data point for the damping analysis).

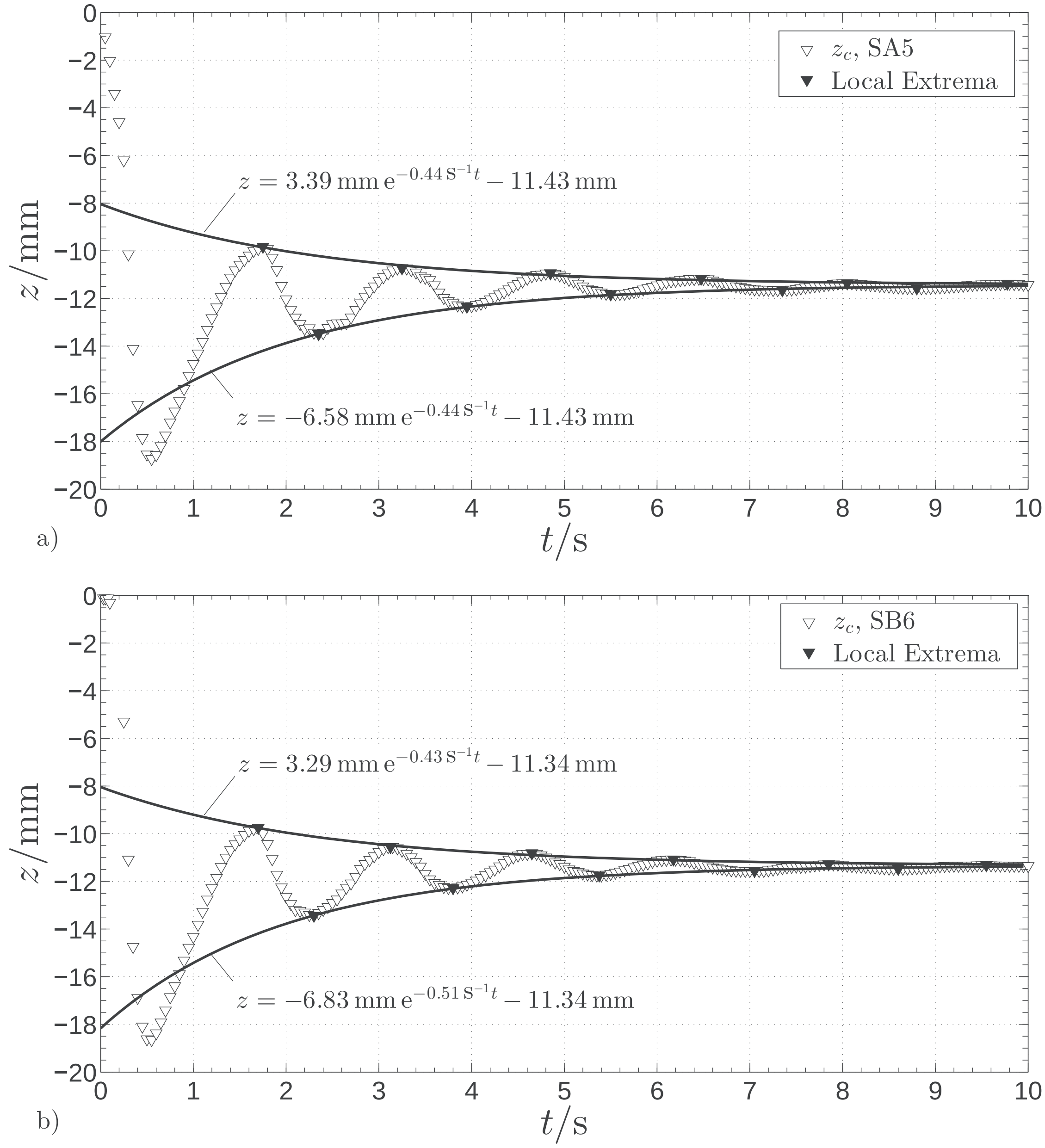

Figure 8.25: Center point displacement (hollow triangles) with envelope (solid lines) calculated from the local extrema (black triangles) for simulation SA5 a) and SB6 b).

The setting of the experiment parameters does not allow to investigate the whole decay of the oscillation versus its final equilibrium. Nevertheless, one can estimate a final center point location $z_{c,1}$. To avoid influences from the initial capillary rise, only center point locations after the second pass through the line $z_c = -1/3R$ were considered. With the assumption that the center point oscillates around its final position it could be estimated as an average of all surface positions after this second pass. The results are made dimensionless with the radius R and compared with each other in Fig 8.26. The numerical simulations reach a steady state but some jitter was visible. Therefore, the center point location was averaged over the last second and corrected by $\Delta z_{c,S}$, which is $\Delta z_{c,S} = 3.45\,\mathrm{mm}$ for SA5 and $\Delta z_{c,S} = 3.95\,\mathrm{mm}$ for SB6 and S01 to S06. The resulting standard deviation is too small to be visible in the plots. The match of the isothermal experiment A5 with the theoretical value validates the used method. The slightly lower final position might be caused by the image processing method and the errors as explained in sec. 6.1.4. With increasing wall temperature gradient, the final center point deflection decreases. The superheated wall clearly influences the final surface configuration and the transient reorientation process.

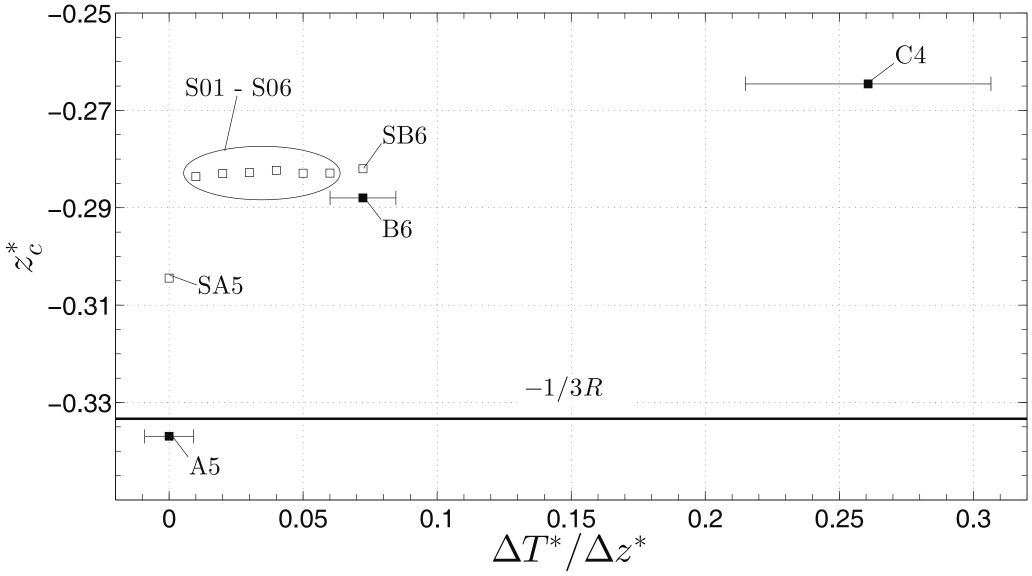

Figure 8.26: Estimated dimensionless final center point $z_c^* = z_c/R$ versus dimensionless wall temperature gradient $\Delta T^*/\Delta z^* = \left(\Delta T/\Delta z\right) / \left(T_{sat,0}/R\right)$ with standard deviation for experiments of the second campaign (solid square markers), the simulations (hollow square markers) and theoretical isothermal final center point location $-1/3R$ indicated by the solid black line.

Weislogel et al. [87] demonstrated the influence of the contact angle on the reorientation process. Raj et al. [71] showed, through experiments and numerical simulations, that the contact angle increases in the presence of a superheated wall. The micro-region model by Stephan and

Hammer [83] supports this observation. These analysis leads to the assumption that the wall superheat is causing a higher contact angle which changes the dynamics of the reorientation process. The numerical simulations show a certain difference between the isothermal and the non-isothermal cases. Hence, there is a certain influence of the wall superheat on the new stable free surface configuration. However, as explained before, the wall superheat decreased to a negligible level in the first two seconds. It means, that the thermal boundary conditions for the free surface at the end of the simulation did not differ much between the simulations. The decrease of the center point deflection in the simulations can be explained better with the height of the rupture point. The rupture point is defined as the point of the free surface at the wall where the advancing liquid layer detaches from the free surface as explained in Fig. 8.27. The height of surface break up (rupture point) seems to be influenced by the wall superheat. The final center point and wall point for all simulations are depicted in dependency of the rupture point height $z_{w,r}$ in Fig. 8.28 a) and Fig. 8.28 b), respectively. The rupture point of SA5 was significantly higher than for the non-isothermal simulations. Therefore, the isolated mass after the surface breakup differs as well (higher $z_{w,r}$ causes a smaller isolated mass). These effects could not be verified by the experiments, because the experimental setup does not aim at a close examination of the wall point. It has to be assumed, that this is a numerical effect caused by the cell size (spatial discretization) and does not represent the physics of the reorientation.

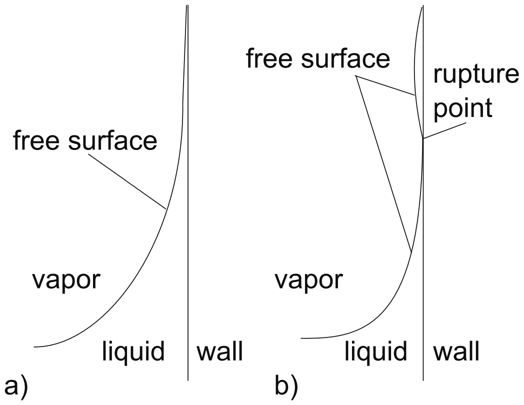

Figure 8.27: a) Free surface with advancing contact layer along the wall. b) Free surface at break up with indicated rupture point.

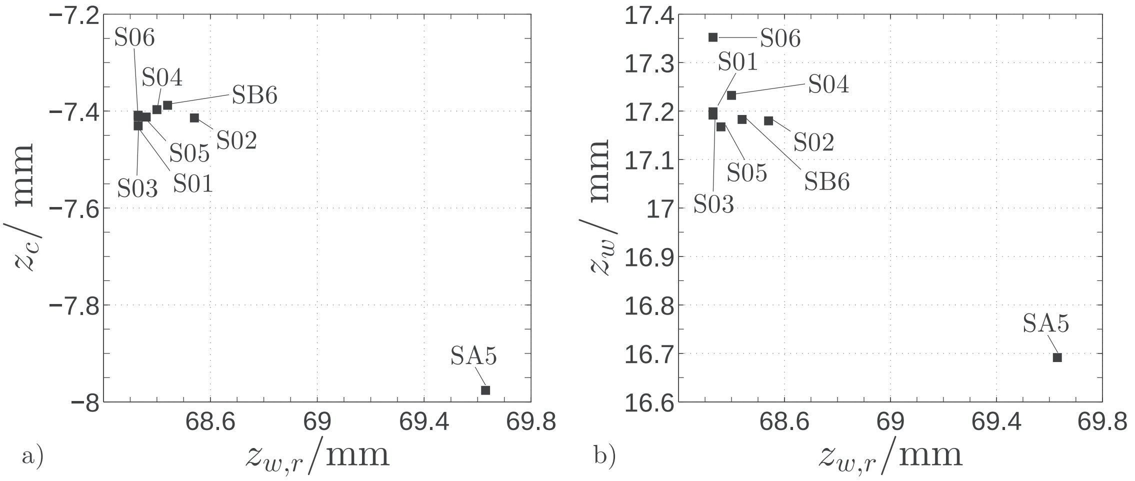

Figure 8.28: a) Final center point $z_{c,1}$ in dependency of the rupture point $z_{w,r}$. b) Final wall point $z_{w,1}$ in dependency of the rupture point $z_{w,r}$.

8.1.7 Pressure Progression

The experiment cavity is a closed system, therefore a temperature change as well as phase change may cause pressure fluctuations. Figure 8.29 compares the dimensionless pressure change $\Delta p^* = (p - p_0)/p_0$ for all experiments. The history of A2, A5 and B6 is depicted in detail for better visibility. All non-isothermal experiments show a clear pressure increase. The hypothesis is, that this is caused by evaporation of the advancing liquid layer at the superheated wall. Besides evaporation also condensation can occur if the liquid is stratified. Experiment A2 had a significant subcooling in the bulk. Throughout the reorientation the thermal boundary layer was probably disturbed. Subcooled liquid reached the free surface and caused condensation resulting in a pressure decrease of about 0.15 % of the initial pressure. Condensation effects were quickly overcome by evaporation, as shown by the history of C1 and C3, which were also stratified. To characterize the final pressure difference with respect to the wall superheat, all experiments were compared in Fig. 8.30. Pressure was averaged over the last 10 ms to suppress signal noise. The standard deviation is also indicated in Fig. 8.30, but hardly recognizable due to its low value. The values presented in Fig 8.30 show a linear dependency of the pressure change on the applied wall temperature gradient. Fluent was not able to predict the pressure progression and there is no numerical data available to supplement the experiments. Surface motion and the fact that only one temperature field exists, caused a temperature alteration in the vicinity of the free surface, which was dominant and falsified the numerical pressure calculation.

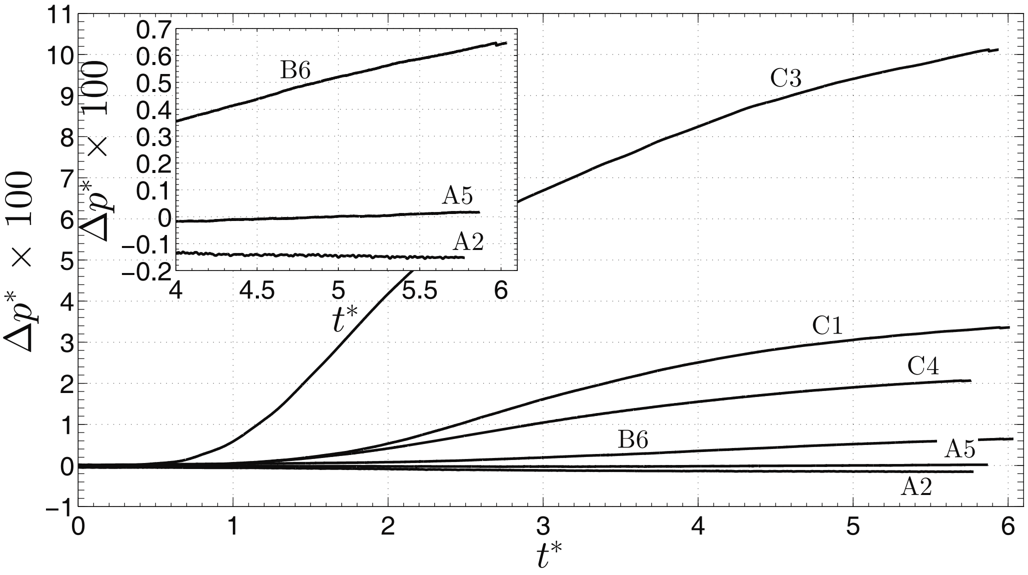

Figure 8.29: Pressure progression $\Delta p^* = \Delta p/p_0 = (p - p_0)/p_0$ throughout the microgravity phase $t^* = t/t_{pu} = t/\left(\rho^l R^3/\sigma\right)^{1/2}$ for all experiments.

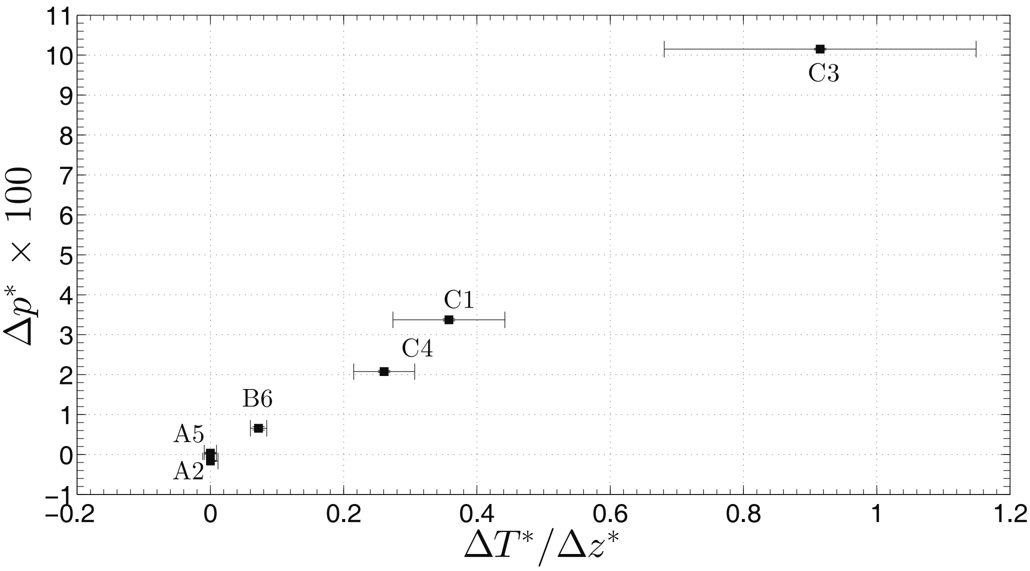

Figure 8.30: Pressure change $\Delta p^* = \Delta p/p_0 = (p - p_0)/p_0$ averaged over the last 10 ms of the microgravity phase versus the dimensionless wall temperature gradient $\Delta T^*/\Delta z^* = \left(\Delta T/\Delta z\right) / \left(T_{sat,0}/R\right)$ for all experiments.

8.2 Simulations of the SOURCE-II Experiment

The experiment was pressurized and filled several times as previously described in table 7.3. This was necessary to prepare the system as wanted which included a stable free surface and no nucleate boiling. Phase change still occurred after preparation and was indirectly monitored by pressure fluctuations. The described state was reached after the third pressurization at $t = 147\,\mathrm{s}$. The focus of the following investigations is on the time span $147\,\mathrm{s} \leq t \leq 179\,\mathrm{s}$, which is named time span of interest (TOI). It was still necessary to include the preparation phase in the simulation to achieve correct results. The simulated time was adjusted with a constant $\Delta t = 70\,\mathrm{s}$ to match the experimental time line. In the following sections, simulation time starts at $t = 70\,\mathrm{s}$ and ends with $t = 210\,\mathrm{s}$.

Within simulation Mesh1 (Flow-3D) surface perturbations occurred due to bubble formation at the wall. Data from this simulation cannot be used for the time span $163\,\mathrm{s} \leq t \leq 172\,\mathrm{s}$ and was therefore blanked out in the following plots. A new stable free surface was formed at $t = 172\,\mathrm{s}$. This effect is discussed in detail in Sec. A.3.2 of the Appendix.

First, the used meshes are assessed. The ability of a correct pressure prediction with focus on the pressurization and relaxation phases served as a quality indicator. The following section focus on the TOI. The mass flux over the free surface was quantified and its driving mechanism are discussed in the second section. The third part addresses the contact line position and resulting contact angle in presence of the superheated wall. The numerical data was always put into perspective with the experimental evaluation done by Fuhrmann and Dreyer [31].

8.2.1 Computational Performance

Predicting the pressure progression of such a system over a great amount of time is challenging and could be used to specify the quality of the solution and the solving algorithm. The calculated pressure progressions using the introduced meshes (Mesh1 and Mesh2 for Flow-3D; MeshA and MeshB for Fluent) were compared with each other to evaluate the grid influence.

Flow-3D
It took seven days and 20 hours to simulate the 140 s physical time on Mesh1. For Mesh2 the required time for the solution could be reduced to three days and two hours.

Figure 8.31 brings the experimental pressure progression and the ones from simulations into perspective. Arrows and vertical lines indicate the two filling phases (F1 and F2) and the four pressurizations (P1 to P4). The recorded pressure of the experiment was captured well by both simulations. The slope and magnitude of the pressure rise caused by vapor injection could be predicted with high accuracy. The phases between the pressurizations, dominated by phase change effects, are more difficult to model which will be investigated in Sec. 8.2.2. No explanation for the experiment's pressure peak at $t = 70.5\,\mathrm{s}$ is given and it is therefore neglected for the simulation and any following analysis.

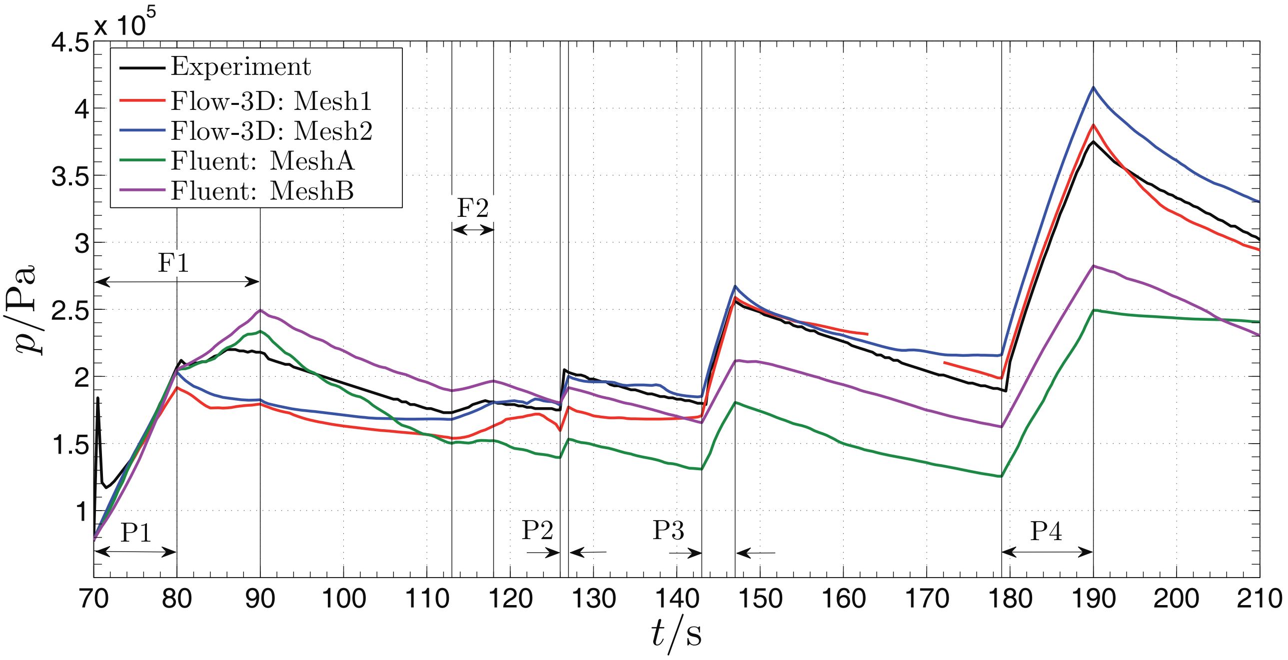

Figure 8.31: Pressure progression of the experiment 70 s after lift-off in comparison with the Flow-3D (Mesh1, Mesh2) and Fluent (MeshA, MeshB) simulations. Vertical lines indicate beginning and end of the filling and pressurization phases named with capital letters F and P, respectively.

To quantify the accuracy of the simulation, predicted pressures and experimental data were put into perspective. Therefore, the experimentally recorded pressure p_E was subtracted from the numerically predicted pressure p_S and normalized by the experimental pressure, which gives a deviation Δp^*_{M1} and Δp^*_{M2} for Mesh1 and Mesh2, respectively

$$\Delta p^* = \frac{p_S - p_E}{p_E} \,. \tag{8.6}$$

The results for Mesh1 are depicted in Fig. 8.32 a) and for Mesh2 in Fig. 8.32 b). Positive values indicate an overprediction and negative ones the opposite. Over the entire simulation the pressure progression could be captured within $-20\,\% \leq \Delta p^*_{M1} \leq 11\,\%$ using the finer mesh (Mesh1), and within $-17\,\% \leq \Delta p^*_{M2} \leq 21\,\%$ with Mesh2. Flow-3D version 10.1.1 was used in [51] to simulate the same experiment. With this older version the pressure prediction was within ±30 % of the experimental data. Hence an improvement of the numerical model was achieved with the latest version. Both simulations had a high deviation from experimental data during the first filling period. One reason for this deviation is the presence of nucleate boiling, which is not considered in the numerical model. Throughout the time span of interest (TOI), between the third and fourth pressurization, simulation Mesh1 predicted the pressure within 7 % deviation and the coarse mesh led to an overprediction of up to 14 %. To compare the influence of the cell size, the absolute difference of both pressure deviations was subtracted from each other and normalized by the experimental value. This yielded $\Delta p^*_{M1,M2}$ as a quality indicator

$$\Delta p^*_{M1,M2} = |\Delta p^*_{M1}| - |\Delta p^*_{M2}| \ . \tag{8.7}$$

The progression of $\Delta p^*_{M1,M2}$ is depicted in Fig. 8.32 c). Negative values indicate a better performance of the finer mesh and positive values a better performance for the coarse grid. None of the used mesh sizes was more accurate over the entire simulation, than the other one. The coarse grid showed better results for the first half, but deviation increased at the end of the third depressurization phase.

Fluent

It took 38 days and seven hours to simulate the 140 s physical time on MeshA. Using MeshB, the required time significantly reduced to six days and 10 hours. The reason for the extensive computational time and its change is the Courant number introduced in Sec. 5.3 with eq. 5.60. Fluent is only stable for CFL < 1, whereas Flow-3D allows higher values. This criterion directly influences the time step size which decreases significantly for the filling and pressurization phases. The computational costs allowed only one simulation using MeshA, which was unluckily conducted with a too high phase change frequency of $\overline{f}_{MA} = 50\,\mathrm{s}^{-1}$. MeshB, with a more sparse spatial discretization, could capture the pressure prediction better using $\overline{f}_{MB} = 5\,\mathrm{s}^{-1}$. The significant influence of the phase change frequency overcomes the influence of the cell size.

The pressure progression of both simulations is also included in Fig. 8.31. The first pressurization and filling period could be be captured well using either mesh. Deviation from the experimental data occurred at the end of the first filling period. The following relaxation phases were overestimated and pressurizations were computed not as pronounced as within the experiment. These errors summed up causing incorrect initial conditions for the TOI which will undergo closer examination later in this work.

A quantitative comparison of the predicted pressure with the experimental one, using the dimensionless pressure criterion computed with eq. 8.6 can be found in the Figs. 8.32 d) and e). The pressure prediction for the entire time was within $-37\,\% \leq \Delta p^*_{MA} \leq 7\,\%$ and $-25\,\% \leq \Delta p^*_{MB} \leq 15\,\%$ and below $-34\,\%$ and $-17\,\%$ for the TOI using MeshA and MeshB, respectively. The deviation at the beginning of the TOI is higher than for the Flow-3D computations, but the error increased not more than $4\,\%$ using MeshA and $2\,\%$ using MeshB.

One can say, that Fluent faced problems simulating the preparation phase, with presence of nucleate boiling, but seemed to capture the driving effects later in the experiments. However, this statement will be proven wrong in the next section. Using eq. 8.7 to compare the two meshes with each other and plot the progression in Fig. 8.32 f) shows on first glance, that with the coarser mesh the pressure could be captured better. This cannot be said, since the phase change frequency was obviously not chosen right for MeshA, which is the dominating effect. Therefore, Fig. 8.32 f) could not be used to assess effects of the cell size.

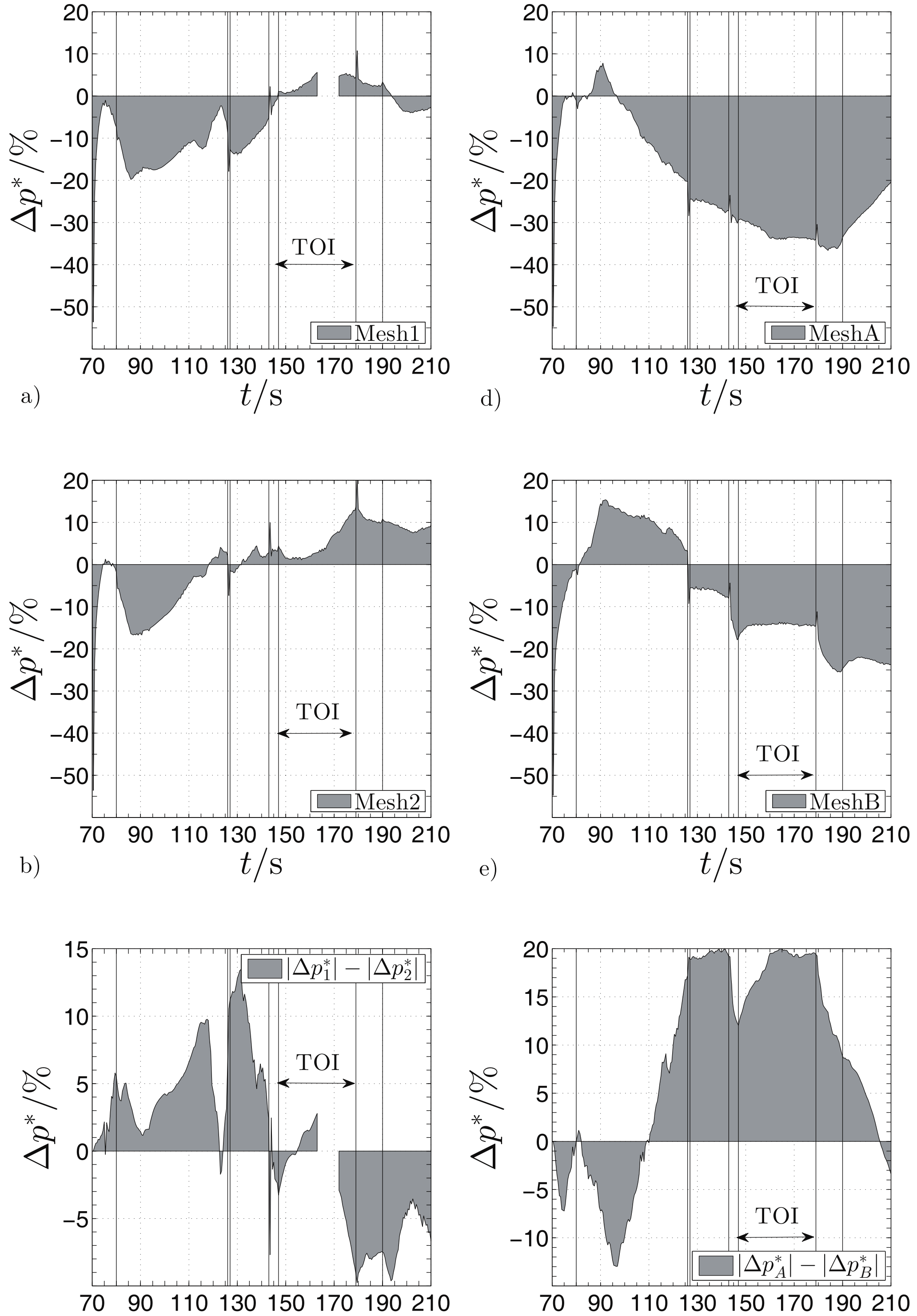

Figure 8.32: Left column uses data from Flow-3D, the right from Fluent. Pressurization phases are indicated with solid vertical lines: a) Deviation between experiment and Mesh1. b) Deviation between experiment and Mesh2. c) Difference of absolute pressure deviation between Mesh1 and Mesh2. d) Deviation between experiment and MeshA. e) Deviation between experiment and MeshB. f) Difference of absolute pressure deviation between MeshA and MeshB.

8.2.2 Mass Flux over the Free Surface

Flow-3D

The investigations by Fuhrmann and Dreyer [31] pointed out, that the pressure drop was driven by condensation at the free surface. The evaluated mass flow across the free surface $\dot{m}_{if}$ was evaluated for the time span between pressurization three and four ($147\,\mathrm{s} \leq t \leq 179\,\mathrm{s}$) and is plotted with results from both simulations in Fig. 8.33. Negative values indicate condensation and positive values evaporation. The net mass flow was negative for the entire observed time span, stating a net mass flow from the gaseous phase to the liquid which corresponds to the pressure decline. Both simulations confirm the calculated phase change mass from the experiment as depicted in Fig. 8.33. It was assumed that condensation and evaporation occurred simultaneously. The subcooled liquid in the bulk drove condensation along most of the free surface, whereas the superheated wall created an evaporation zone. Since this could not be investigated within the experiment, numerical simulations were necessary.

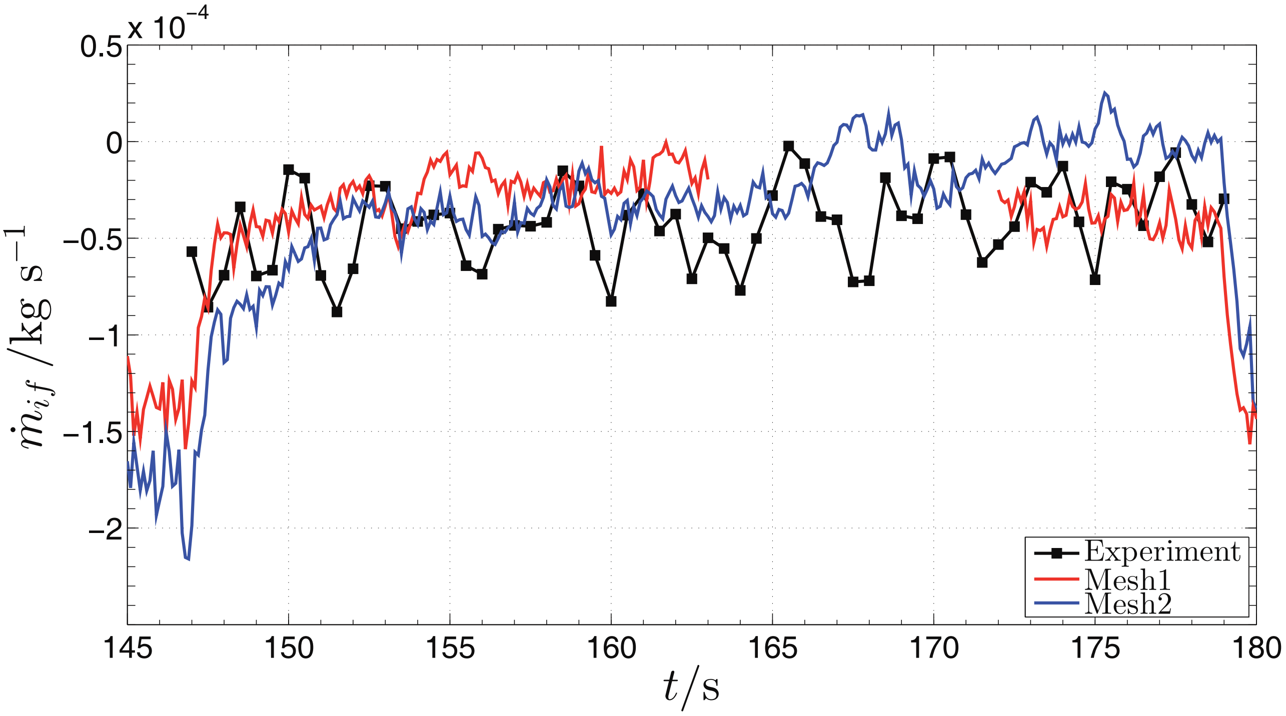

Figure 8.33: Net mass flow across the free surface. Calculated values [31] from the experiment compared with values from Flow-3D simulations. Negative values indicate condensation, positive values evaporation.

As expected, the conducted simulations showed three different zones. A major portion of the free surface is in thermal equilibrium without any net mass flux. In the vicinity of the superheated wall, a zone with a positive mass flux exists, thus evaporation occurs in the wall region. At the center line area of the free surface a negative mass flux was detected showing condensation. Figure 8.34 a) and b) shows the free surface after the third pressurization at $t = 147\,\mathrm{s}$ and before the fourth gas injection at $t = 179\,\mathrm{s}$ for both simulations, respectively. The contact point is illustrated in a detailed view with the mesh representation activated. Bluish colors in the contour plot represent a negative mass flux, thus condensation. Evaporation is represented with reddish colors and quantified by a positive mass flux. In the vicinity of the z-axis, vapor condensed on the free surface. Along the surface in radial direction, a large portion of the free surface was in thermal equilibrium with no mass transfer. The influence of the superheated wall can be seen in the detailed pictures of Fig. 8.34 where evaporation is visible in a small region close to the wall. The contour plots of both time instances do not differ much from each other which correlates with the mean mass flow in Fig. 8.33. The increasing pressure deviation of Mesh2 from the experiment before the fourth pressurization can be explained with the increasing net mass flow $\dot{m}_{if}$. This is caused by a relatively large region with a positive mass flux, which is indicated by the green patch stretching along the free surface close to the wall in Fig. 8.34 b).

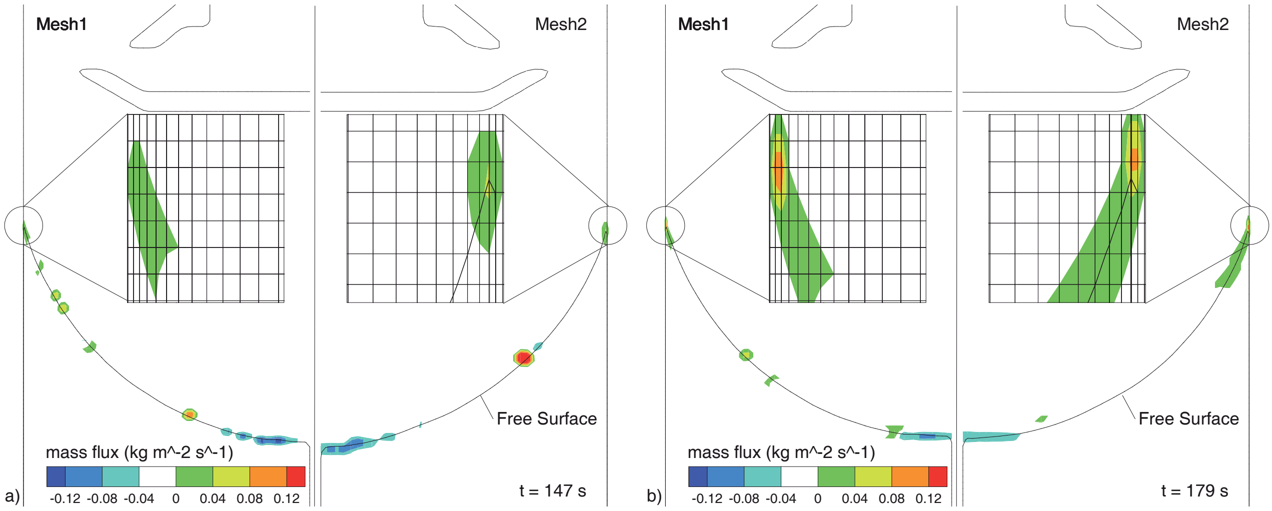

Figure 8.34: Mass flux across the free surface for Mesh1 (left half) and Mesh2 (right half) after third ($t = 147\,\mathrm{s}$) a) and before the fourth pressurization ($t = 179\,\mathrm{s}$) b). The glass cylinder is not shown. Condensation is represented by negative values and evaporation by positive values.

Evaporation was caused by the superheated wall. Due to the absence of gravity, no natural convection along the wall was present, to convey the heat into the bulk. Hence, the effect of the wall temperature on the free surface was narrowed to an area close to the wall. The resulting bulk was subcooled, causing condensation along the free surface where the wall did not heat up the liquid. Growth of two independent thermal boundary layers could be observed. One boundary layer could be located at the wall and was growing towards the center. This was caused by the thermal input from the wall. The second boundary layer increased from the free surface towards the bulk. It resulted from the latent heat, which was released by condensing vapor. For better visibility, temperature differences were introduced. The superheated state of the wall is quantified with Θ^s calculated from the solid temperature T^s and the saturation temperature T_{sat} from eq. 7.1

$$\Theta^s = T^s - T_{sat}\,. \tag{8.8}$$

A positive Θ^s indicates a superheated wall. The subcooling of the liquid is defined as

$$\Theta^l = T^l - T_{sat}\,, \tag{8.9}$$

with T^l as liquid temperature. The magnitude of subcooling is quantified with a negative Θ^l. Both temperature differences do not only consider the change of solid and liquid temperature but are also sensitive to pressure changes which influences T_{sat}. The growth of the thermal boundary layer is clearly visible comparing the two time instances in Fig. 8.35. In the wedge shaped region between free surface and wall, Θ_l was increasing to $\Theta_l = 0\,\mathrm{K}$, thus saturation conditions. Simulation Mesh2 evolved a small superheated layer at the wall in the vicinity of the free surface adjacent to a region with liquid at saturation temperature. Superheated liquid could occur, since the nucleate boiling model was deactivated and evaporation was only possible at the free surface. The small superheated area drives evaporation indicated in Fig. 8.34. Stratification stayed stable close to the center which concurs with the steady negative mass flux in this region.

Numerical surface perturbations, probably introduced by the VOF method, were detected in both simulations causing an oscillatory motion of the center point of the free surface. This pushed warmer liquid down into the bulk as indicated in Fig. 8.35 by varying contour levels along the center line. The instrumentation of the experiment allowed to measure the liquid temperature along the center axis in various heights. Recordings of the sensors TC12, TC17 and TC22 were compared with both simulations. They are plotted for the time instance between the third and fourth pressurization (TOI) for the experiment, Mesh1 and Mesh2 (from left to right) in Fig. 8.36. TC12 was placed at $z = 60\,\mathrm{mm}$ which is roughly 7 mm below the observed interface position (experimental observation). It was obviously not located in the thermal boundary layer. Its temperature was within the range of the other sensors, which were positioned even lower. The recorded temperature fluctuation was in a range of approximately 15 K and was significantly below the saturation temperature. Temperature recordings from the simulations indicate stratification along the center line with distinct periodic fluctuations. Furthermore the predicted temperature in this region was too high compared to the experimental results.

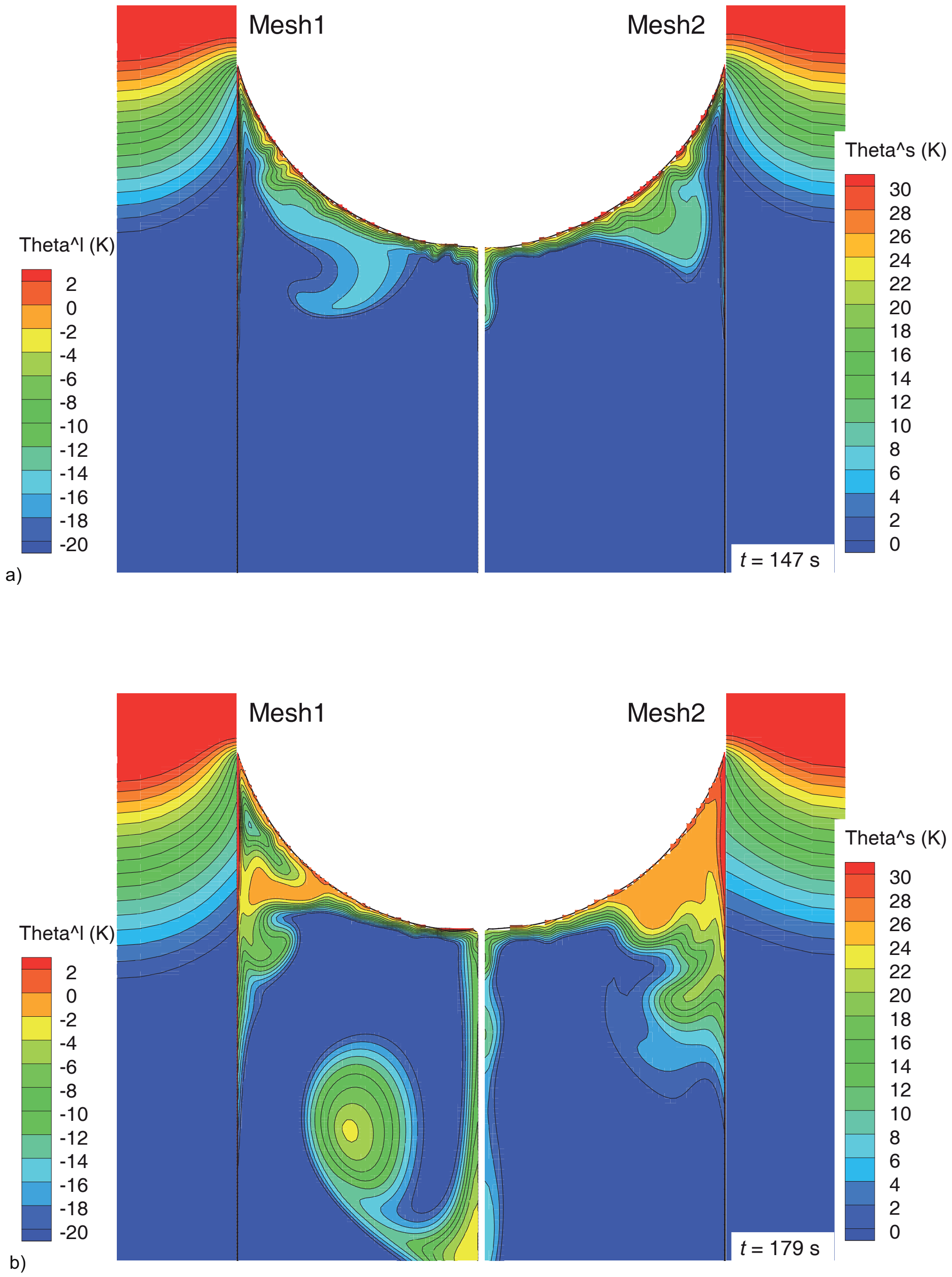

Figure 8.35: Θ^s and Θ^l contours for Mesh1 (left half) and Mesh2 (right half) after P3 ($t = 147\,\mathrm{s}$) a) and before P4 ($t = 179\,\mathrm{s}$) b). Vapor region is blanked.

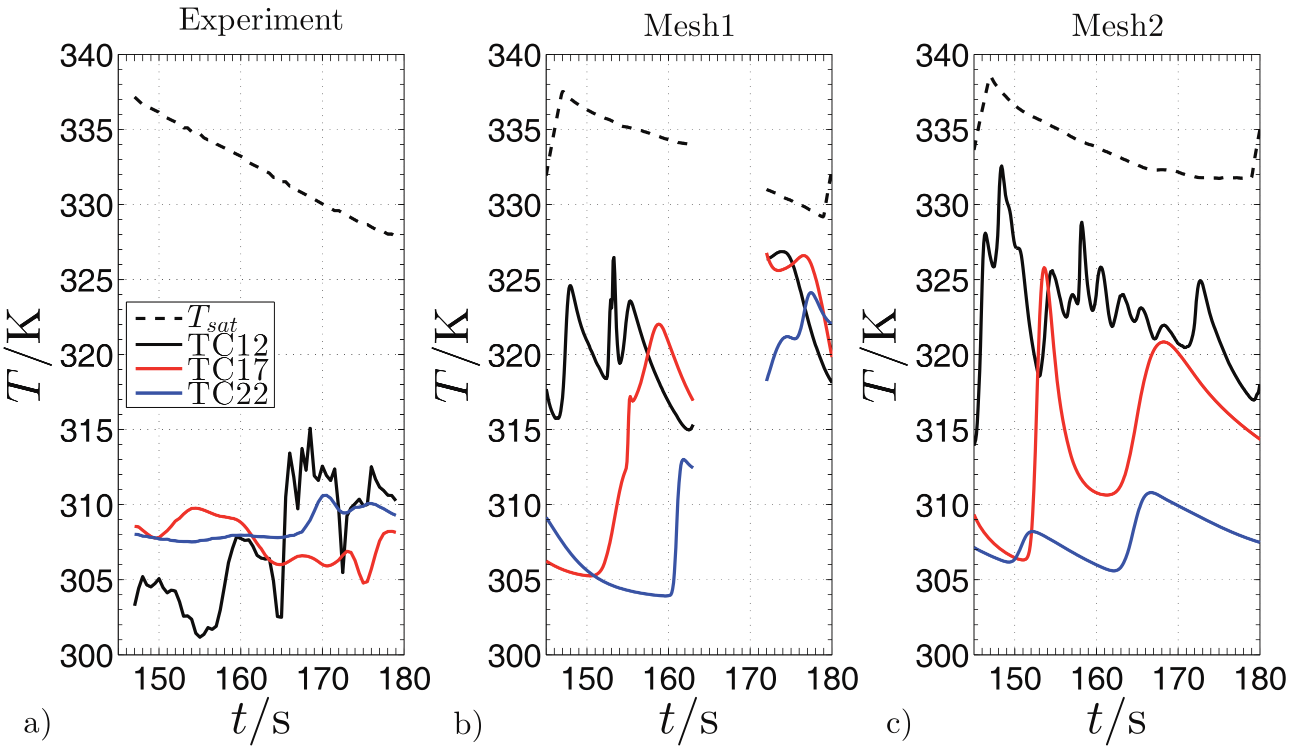

Figure 8.36: Temperature recordings along the center line in four different heights and saturation temperature. a) Experimental measurements indicate a homogenous bulk temperature. Simulation Mesh1 b) and Mesh2 c) show a stratification along the center line with fluctuating temperature levels.

Fluent

Since the initial pressure at $t = 147\,\mathrm{s}$ is significantly lower for the simulations using MeshA and MeshB, it is hardly possible to compare the mass flux calculated by Fluent with experimental data. A lower pressure results in a lower saturation temperature, thus surface temperature. Since the wall temperature is not affected by the pressure progression a higher wall superheat should cause a higher evaporation rate in the vicinity of the wall. The condensation along the free surface should increase too, since a lower surface temperature increases the temperature gradient driving condensation. The effect of the surface or saturation temperature on the phase change mechanism is of the same order, hence the pressure change with time $\frac{\mathrm{d}p}{\mathrm{d}t}$ should be independent of the initial pressure level. This assumption can be verified observing the TOI in Figs. 8.32 d) and e). The dimensionless pressure difference Δp^* only changed little throughout this time span. This is no verification, that the driving phase change effects are captured by the simulation despite the incorrect initial pressure.

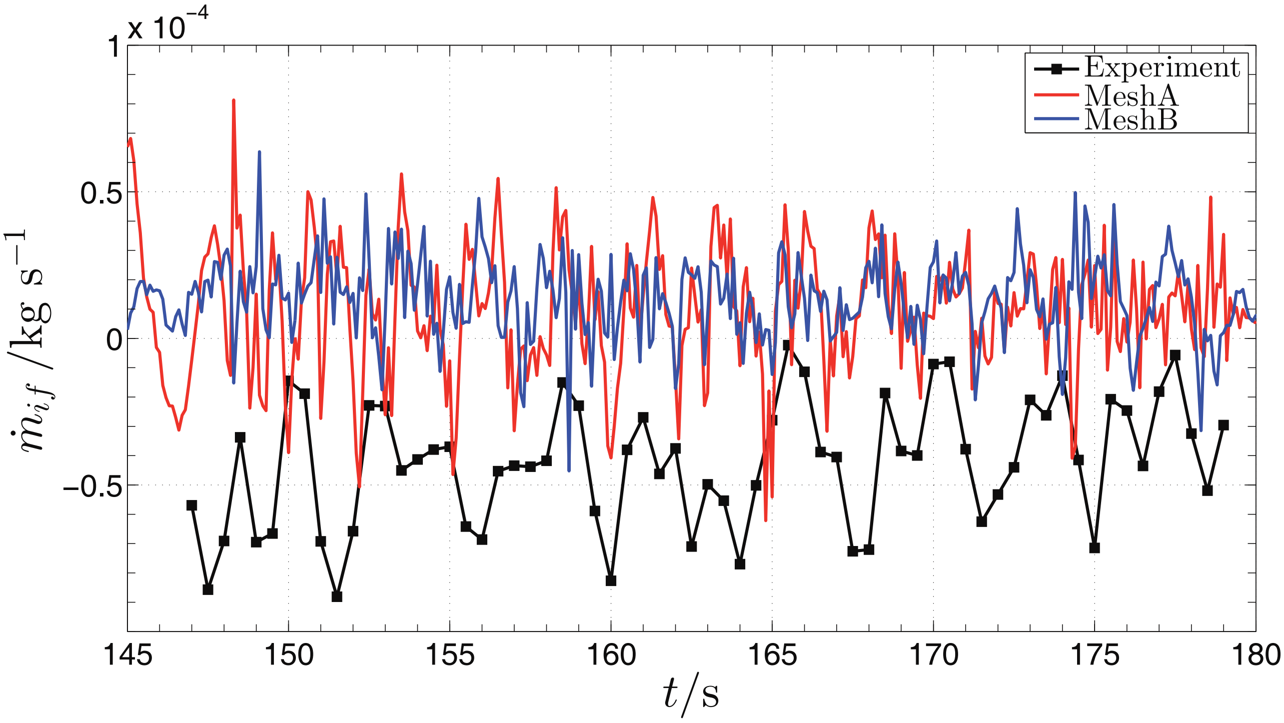

Figure 8.37: Net mass flow across the free surface. Calculated values [31] from the experiment compared with values from Fluent simulations. Negative values indicate condensation, positive values evaporation.

The mass flow over the free surface is depicted in Fig. 8.37 for both simulations (MeshA and MeshB) and the experiment. For MeshA the mass flux is significantly higher as the data derived from the experiment. The net mass transferred over the free surface between $147\,\mathrm{s} \leq t \leq 179\,\mathrm{s}$ (TOI) is $\Delta m_{MA} = 3.15 \times 10^{-4}\,\mathrm{kg}$ and $\Delta m_E = -1.36 \times 10^{-3}\,\mathrm{kg}$ for the experiment. The value

Table 8.4: Density and temperature at beginning and end of the TOI, computed pressure difference using the ideal gas equation and pressure difference from the simulation for MeshA and MeshB.

	MeshA		MeshB	
t s	147	179	147	179
T^v K	379.11	360.59	381.56	374.03
ρ^v kg m^{-3}	18.40	15.59	19.59	16.75
$\Delta p_{ig} \times 10^3$ Pa	52.36		50.32	
$\Delta p_S \times 10^3$ Pa	54.04		50.32	

for MeshB is with $\Delta m_{MB} = 4.42 \times 10^{-4}$ kg even higher. For the simulations there is obviously a net evaporation despite the net condensation for the experiment, thus the pressure should increase. Figure 8.31 shows a pressure decline, so the driving effect on the pressure history must be found elsewhere. The ideal gas equation is used to quantify the pressure difference caused by thermal contraction. The difference can be calculated with average pressure and temperature in the vapor region of the simulations at $t = 147$ s and $t = 179$ s. Density and temperature for both time instances, computed pressure difference Δp_{ig} and simulated pressure difference Δp_S can be found in table 8.4. Here, the driving parameter for the pressure change is the thermal contraction of the vapor and not the net mass flow over the free surface. The mean temperature decrease over time was caused by cooling down superheated vapor in the vicinity of the free surface.

8.2.3 Contact Angle in Presence of Local Wall Superheat

Flow-3D

Another important temperature difference characterizes the local wall superheat Θ_{sup}. The experimental value is defined as the difference of simulated[1] temperature of TC4 and saturation temperature [31]

$$\Theta_{sup,E} = T_{TC4} - T_{sat}\,. \tag{8.10}$$

Simulations made it possible to extract the wall temperature at the wall point position T_w^s and calculate the local wall superheat with

$$\Theta_{sup,if,S} = T_w^s - T_{sat}\,. \tag{8.11}$$

This has the advantage, that the wall temperature was not extracted at a fixed height but followed the contact point motion, thus $T_w^s = T(t, z_w)$. The associated height z_w of the the wall

---

[1] Due to a incorrect implementation of sensor TC4 its temperature recordings did not represent the wall temperature but the temperature of the fluid.

temperature is plotted in Fig. 8.39. The temperature progression for the several readings and the history of the wall superheat Θ_{sup} are presented in Fig. 8.38 a) and b), respectively. One can see from the Figs. 8.38 and 8.39 a), that the wall superheat Θ_{sup} extracted from experimental values was significantly higher than the local wall superheat from the simulations. $T_{TC4,E}$ had to be simulated due to a manufacturing error of the sensor positioning along the wall [31]. The sensor TC4 was located at $z_{TC4} = 78\,\mathrm{mm}$ and thus submerged approximately 7 mm into the liquid (see z_w, Experiment in Fig. 8.39). Even though, the wall superheat is still given by [31] with $7\,\mathrm{K} \leq \Theta_{sup,E} \leq 14\,\mathrm{K}$. The value computed by the simulations is significantly lower, $2\,\mathrm{K} \leq \Theta_{sup,S} \leq 4\,\mathrm{K}$, but was extracted at $z_{w,S} \approx 90\,\mathrm{mm}$, thus above z_{TC4} and in a higher initial temperature regime. Besides this obvious discrepancy, the simulations could confirm a faster decline of T_{sat} than cool down of the wall temperature resulting in an increasing Θ_{sup}.

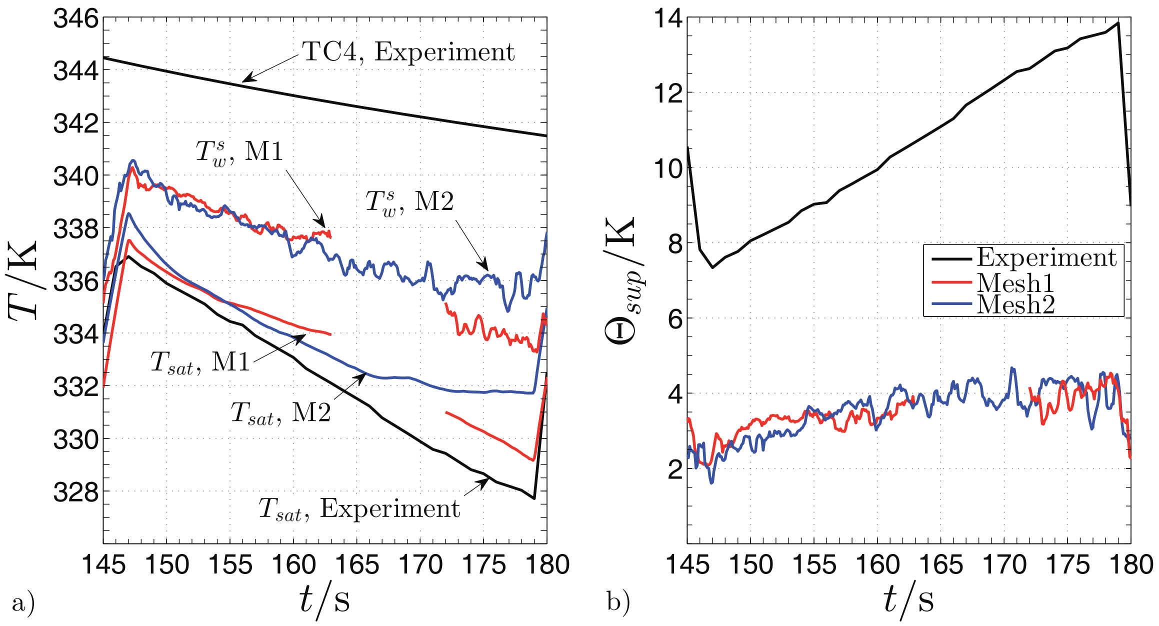

Figure 8.38: a) Saturation temperature and wall temperature at the contact point, represented by TC4 for the experiment [31]. b) Calculated wall superheat Θ_{sup} from the temperatures plotted in a).

An exact estimation of the wall superheat is important for the prediction of the contact angle with the theory of the micro-region model [82, 83]. The contact angle increases with the wall superheat. Fuhrmann and Dreyer could confirm the theory with their calculation of the temperature difference Θ_{sup} [31]. A dependency of the contact angle of the wall superheat could not be gained from the simulation since the data was interfered by too much noise. Figure 8.39 b) compares the derived contact angle from the experiment and the simulations. The contact angle was derived from the center and wall point locations using the relation

$$\gamma = \frac{\pi}{2} - 2\arctan\left(\frac{h}{R}\right), \tag{8.12}$$

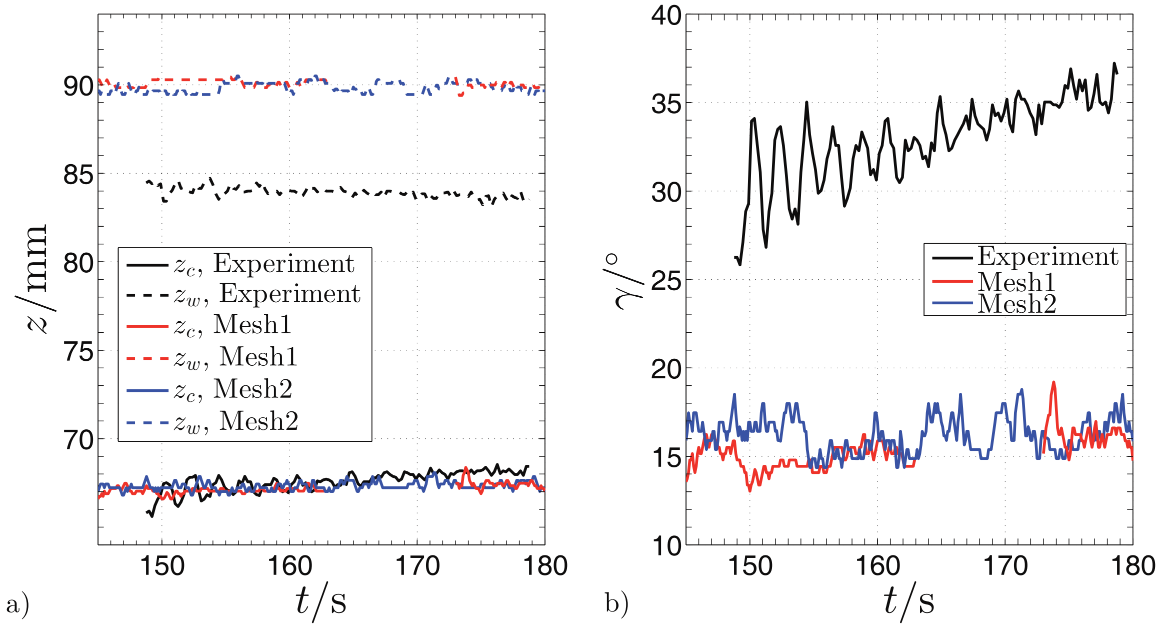

a) b)

Figure 8.39: a) Derived center z_c and wall point z_w location for experiment [31] and Flow-3D simulations. b) Derived contact angle γ for experiment [31] and simulations.

where, $h = z_w - z_c$ and R is the cylinder's inner radius. In the simulations the contact angle varied between $14° \leq \gamma \leq 19°$ but was not influenced by the rising wall superheat $\Theta_{sup,if,S}$. The micro-region model [82, 83] predicts a contact angle between $20° \leq \gamma_T \leq 26°$ for a superheat of $2\,\mathrm{K} \leq \Theta_{if,T} \leq 5\,\mathrm{K}$, as shown in the Appendix in Fig. A.4. The simulation seems to underestimate the theoretically predicted contact angle for the given wall superheat.

Fluent

Equation 8.11 is also used for the Fluent computations to extract the local wall superheat. The derived saturation temperature T_{sat} and wall temperature at the contact line T_w^s is compared with the experimental data in Fig. 8.40 a). The wall superheat Θ_{sup} is plotted in Fig. 8.40 b). One can see, that the temperature, derived from the Fluent simulations, was about 10 K higher than the data from the experiment. The saturation temperature was, corresponding to the pressure, below the experiment. This results in a significantly higher wall superheat as for the experiment. MeshA calculates $25\,\mathrm{K} \leq \Theta_{sup} \leq 35\,\mathrm{K}$ and MeshB $22\,\mathrm{K} \leq \Theta_{sup} \leq 28\,\mathrm{K}$. The difference was caused by the different pressure. The wall point was located higher than the experimentally estimated position, similar to the Flow-3D simulations. The wall and center point for both simulations and the experiment is depicted in Fig. 8.41 a). Furthermore, z_w for MeshA is about 3 mm above z_w of MeshB. The free surface of both simulations oscillates up to 4 mm and about 2 mm peak to peak amplitude of the center point for MeshA and MeshB, respectively. The peak to peak amplitude of the center point location is with 6 mm for MeshA and 5 mm for MeshB even higher. A plausible cause is the magnitude of the wall superheat. As explained before, nucleate boiling cannot be modeled in a 2D simulation. The surface seems to be excited by the superheated wall. The oscillation of the free surface is even more pronounced throughout the preparation phase where nucleate boiling was observed in the experiment. These perturbations result in an oscillating apparent contact angle, which is computed with eq. 8.12 and shown in Fig. 8.41 b). Simulation MeshA shows a varying γ within 15 to 40 degrees with increasing trend, whereas γ for MeshB seems to remain between 25 and 40 degrees. The derived apparent contact angle is below the values, which can be computed from the micro-region model presented in the Appendix in Fig. A.4.

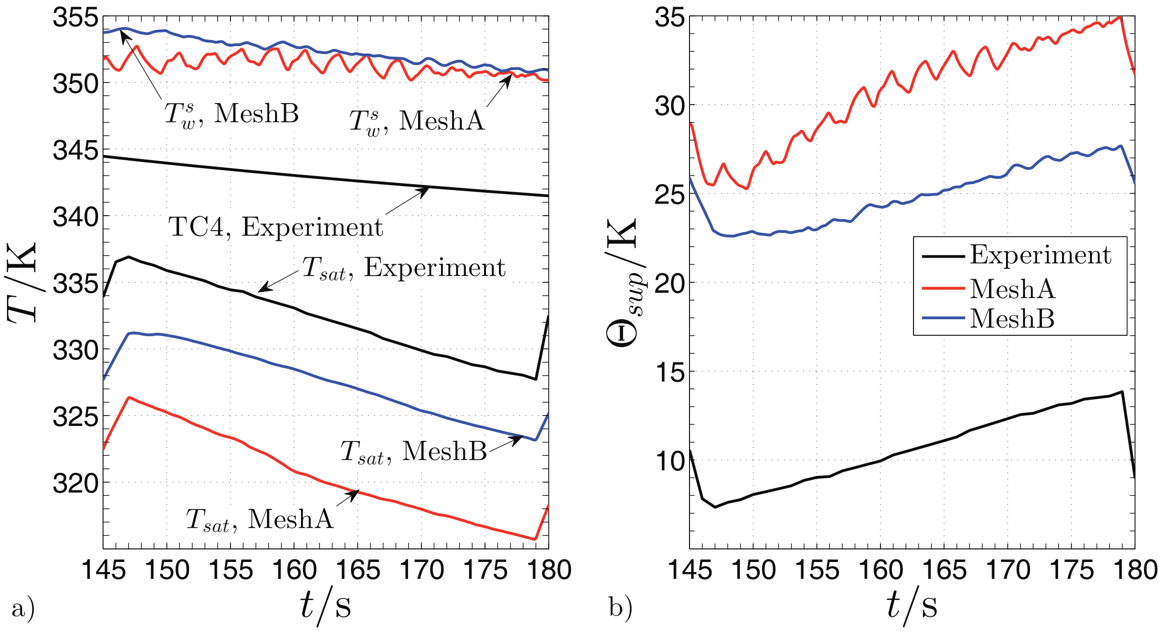

Figure 8.40: a) Saturation temperature and wall temperature at the contact point, represented by TC4 for the experiment [31]. b) Calculated wall superheat Θ_{sup} from the temperatures plotted in a).

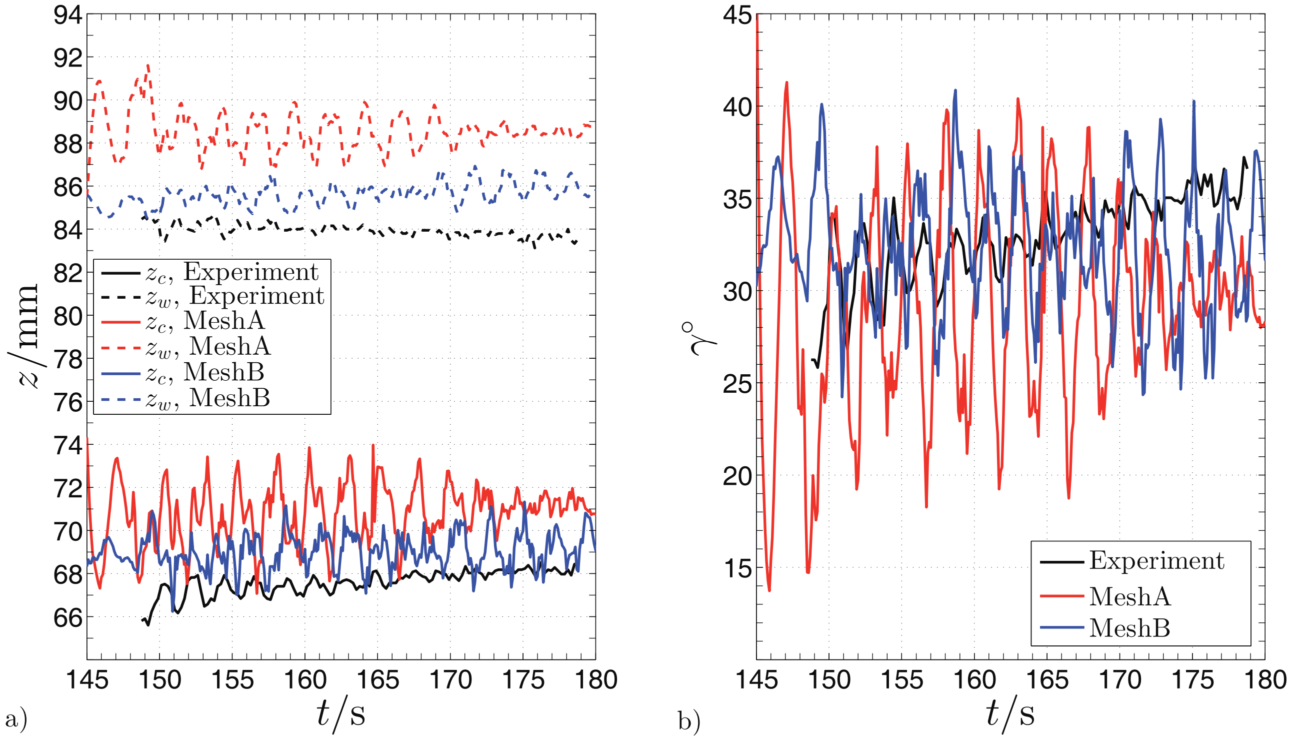

Figure 8.41: a) Derived center z_c and wall point z_w location for experiment [31] and Fluent simulations. b) Derived contact angle γ for experiment [31] and simulations.

Chapter 9

Conclusion and Outlook

9.1 Conclusion

This work focused on a two-phase, single-species system with a free surface under varying gravity levels and non-isothermal wall conditions. The motivation was to improve the knowledge about upper stage cryogenic propellant tanks. One main aspect is the free surface reorientation (axial sloshing) of the free surface upon a gravity step reduction, as it occurs after engine cutoff. The influence of the superheated wall on the reorientation frequency, final surface shape and pressure progression was analyzed. With entering the ballistic phase no further body force is acting on the fluid, which led to the second main aspect of this work. This is to understand the coupled system between two-phase flow and a superheated wall in such a low gravity environment. The stated effects were investigated with experimental and numerical means. The conducted experiment could be used to validate the flow solvers Fluent and Flow-3D. Further simulations were performed to supplement the experimental data. They helped to understand physical effects which could not be evaluated with the experimental methods alone.

9.1.1 Drop Tower Experiments

Drop tower experiments at ZARM, University of Bremen, were performed to examine the axial sloshing behavior of liquid parahydrogen in a right circular cylinder with varying temperature gradients upon a gravity step reduction. The working fluid was parahydrogen condensed from its vapor in a pure parahydrogen atmosphere. Great effort was taken to insulate the experimental cylinder from ambient conditions. Several temperature sensors along the glass cylinder wall and in the vapor region allowed to record the temperature with 1 kHz throughout the experimental time. A pressure transducer sampled the pressure inside the experiment with the same rate. Examination of the free surface was enabled with an endoscope and laser illumination. Several heaters and flushing of the enclosing vacuum (inner vacuum) allowed thermal conditioning. To investigate the influence of a superheated wall several temperature gradients were imposed. Two campaigns with three experiments each were conducted. The applied dimensionless temperature gradients varied between $0.00 \leq \Delta T^*/\Delta z^* \leq 0.92$. Three different regimes could be detected. First, isothermal conditions without a wall temperature gradient (A2 and A5) were investigated. Second, non-isothermal conditions without nucleate boiling (B6) and third, non-isothermal conditions with nucleate boiling (C1, C3 and C4) were considered. The final surface configuration could not be reached, since the settling time was larger than the experiment time. Simulations were carried out to observe the new stable surface shape. The first and second regime ($\Delta T^*/\Delta z^* \leq 0.07$) were considered and could be reproduced by numerical simulations with Fluent. To receive more data points, another six simulations with $0.00 \leq \Delta T^*/\Delta z^* \leq 0.06$ were conducted.

The presence of a superheated wall had a great influence on the entire reorientation process except for the initial rise. The experiments showed that an increasing wall temperature gradient had no significant influence on the contact line velocity. The scaling from isothermal capillary driven phenomena is valid here and the dimensionless contact line velocity is of the order of one. Wall and center point coordinates are coupled with each other due to mass conservation in the second time domain of the reorientation. The circular frequency of the center point shows an increase with increasing wall superheat. This could only be justified for the test without nucleate boiling at the wall. Larger wall superheats caused nucleate boiling but its effect on the frequency weakened. An estimation of the final center point was possible, even though it could not be reached within the experiment time. Evaporation effects on the cylinder wall may have reduced the absolute deflection of the center point.

Sensors along the glass cylinder recorded a temperature decrease when the advancing contact line wetted the inner wall. The sensors experienced a temperature drop with a certain delay caused by the glass thickness and the response time of the used temperature sensors. The vapor region was also affected by the reorientation process.

Evaporation and condensation effects dominate the pressure progression throughout the experiment time. The thermal boundary layer within the liquid was disturbed while the free surface reoriented causing condensation by subcooled liquid rising to the surface. Condensation effects are superimposed by evaporation in the vicinity of the contact line. The total pressure change significantly increased with an increasing wall temperature gradient.

Numerical simulations could verify the experimental findings. The wall superheat changed the frequency of the center point oscillation. Furthermore, it could be shown, that for $\Delta T^*/\Delta z^*$

≤ 0.07 the energy which was stored in the glass walls was transferred to the liquid within 2 s. In other words, after this time no temperature gradient was remaining along the inside wall. Any influence of the superheated wall occurred before the temperature gradient was neutralized. The simulated temperature gradients were too small to indicate any trend of the wall superheat on the reorientation. A stable free surface configuration could be achieved with the computations after 10 s physical time. The free surface oscillation was damped out after five periods. Simulations SA5 (isothermal) and SB6 (non-isothermal, no nucleate boiling) did not show any difference between the final center point location. The wall superheat was neutralized beforehand, thus the free surface in both simulations was exposed to the same thermal boundary condition (isothermal wall) after 2 s.

The temperature drop along the glass cylinder wall could be reproduced by the simulation with a shorter delay between wetting and recorded temperature drop as for the experiment, which might be caused by the sensor attachment. The thermocouples were glued to the experiment cylinder which might have introduced a further thermal resistance that could not be modeled within the simulations. The described influence of the laser causing a temperature increase of the thermocouple itself could be confirmed by the simulations.

Only one temperature field is modeled by Fluent, thus temperature is density-averaged in cells where both phases (liquid, vapor) are present. This caused a numerical cooling of the vapor phase and, using the ideal gas equation, a reduction of the pressure. Due to this effect no statement about the pressure history could be made from the simulations.

9.1.2 Sounding Rocket Experiment

The suborbital flight experiment SOURCE-II was conducted to investigate the free surface of a single-species two-phase system in microgravity and presence of a superheated wall. The driving mechanism on the pressure progression, heat and mass transfer over the free surface and the influence of the superheated wall on the static contact angle were investigated. This experiment was used as a benchmark case for numerical codes. On the other hand, numerical simulations were conducted to supplement the experimental data. In this work Flow-3D and Fluent were used with two different grids. The numerical simulations included the 140 s experimental time with two filling periods and four pressurizations. The majority of the experimental time was used for preparation and the time span of interest was between the third and fourth pressurization lasting 32 s.

Flow-3D was able to calculate the solution in a reasonable time with seven days and 20 hours for the finer mesh (Mesh1). Using the coarser mesh (Mesh2) the required time reduced to three days and two hours. All filling and pressurization phases could be captured well with an absolute deviation below 20 % for Mesh1 and 21 % for Mesh2. The relaxation phase within the time span of interest was calculated with less than 7 % and 14 % using Mesh1 and Mesh2, respectively. An unwanted bubble formation occurred with the finer mesh, partly corrupting the data. Examination of the mass flux across the free surface confirmed the experimental findings, that the pressure was decreasing due to condensation along the free surface. Evaporation occurred in a small area close to the superheated wall. The influence of thermal contraction was negligible. Some oscillation of the center point was observed, which disturbed the thermal boundary layer along the center line. This oscillation is probably caused by the VOF method and the singularity at the center line. The local wall superheat was significantly lower for both simulations than the one derived from the experimental values. One reason for this deviation might be the different wall superheat determination. Problems in the experimental design made a numerical reconstruction of the wall temperature sensors necessary. The height where the temperature was extracted was fixed to the sensor position TC4 and did not move with the wall point location. In the simulation the wall temperature was extracted directly at the wall point. Furthermore, in both simulations the wall point position was above the experimental data, whereas the center point coincided with the experiment. Therefore, a different apparent contact angle evolved, which was between 14° and 18° for both simulations. These values have been underestimated compared to the theory of the micro-region model.

Fluent was very sensitive to the Courant number and was only stable for CFL < 1. This increased the required time to 38 days and seven hours for the finer mesh, MeshA, and six days and 10 hours for the coarse mesh, MeshB. The computational costs for MeshA allowed only one simulation with this grid. The phase change frequency $\overline{f} = 50\,\mathrm{s}^{-1}$ was chosen incorrectly for this simulation. The simulation MeshB showed better results with $\overline{f} = 5\,\mathrm{s}^{-1}$. For the stated reason, MeshA could capture the pressure progression within 37 % and the time span of interest within 34 % absolute deviation. The coarser grid, MeshB, predicted the overall pressure history within 25 % and within 17 % deviation for the time span of interest. The pressure decline within these computations was caused by the thermal contraction of the vapor phase. The net mass flow was slightly positive, thus a net evaporation occurred, but had no significance on the pressure change. The overall pressure level was below the experiment, resulting in a lower saturation temperature and therefore significantly higher wall superheat. Even though nucleate boiling was not modeled the higher wall superheat disturbed the free surface resulting in an oscillatory motion. Both, center and wall point location were estimated higher than the experimental location with an superimposed oscillation caused by the wall superheat. The resulting apparent contact angle oscillated between 15° and 40° for MeshA and 25° and 40° for MeshB. The mean value of the apparent contact angle is below the theory of the micro-region model.

9.2 Outlook

This work helped to gain more knowledge of the observed physical effects but also new questions arose. This section summarizes the lessons learned and proposes some ideas how to continue with research in this specific field.

The drop tower experiment is already very advanced and precise temperature gradients can be achieved. The conducted investigations revealed, that the wall superheat is quickly neutralized for low temperature gradients ($\Delta T^*/\Delta z^* \leq 0.07$). To overcome this problem several changes could be made. One way is to increase the glass thickness to store more energy in the wall. This still does not change the fact, that the experimental time is not long enough to form a new stable surface. The settling time is dependent on the cylinder radius. A reduction of the cylinder radius will reduce the settling time and has positive effects on the thermal boundary condition (if the glass thickness is kept constant), but may decrease the optical quality. Furthermore, damping of the interface motion could be analyzed.

The scaling of the wall superheat achieved with $\Delta T^*/\Delta z^*$ shows some weaknesses. It only includes the saturation temperature of the liquid and the cylinder radius, thus liquid properties and geometry. The free surface behavior is also dependent on the boundary condition thus the wall geometry and material property. Including the Biot and Fourier number could improve the scaling

$$\mathrm{Bi} = \frac{\alpha L}{\lambda^s}\,, \tag{9.1}$$

$$\mathrm{Fo} = \frac{\lambda^s t}{c^s \rho^s L^2}\,. \tag{9.2}$$

For further numerical investigation of the temperature influence on the reorientation, one can change the wall BC to a fixed temperature condition. This excludes the effects of the glass itself. More simulations based on the proposed setup could be conducted using several fluids (e.g. methane, neon, argon) and compare the results with literature. The geometry and boundary conditions could be changed, too.

The computation of the SOURCE-II experiment showed very good results using Flow-3D. The computational costs were reasonable and the phase change model could capture the complex heat and mass transfer over the free surface. Some deficiencies remain in the contact angle model, which could be improved with respect to wall temperature influences. Nevertheless, the presented results regarding the investigated effects have not been published in this quality and detail before. The sensitivity of Fluent to the Courant number limits its use for simulations over a long physical time span, due to its excessive computational costs. The implemented phase change model seems to be not sufficient enough for the complex phase change effects that occurred within the SOURCE-II experiment.

Of the available codes only Fluent was able to simulate the free surface reorientation. Improvement of the phase change model and two energy fields, one for each phase, would enable a correct pressure prediction. Ongoing projects at ZARM and DLR Bremen aim to implement the necessary models in the open source code Open∇FOAM[1]. Keiderling et al. [49] at DLR Göttingen are working on implementing the models in the TAU code. Once other codes are capable, simulations should be conducted and compared to gain more confidence.

---

[1] Email conversation with Henning Scheufler, DLR Bremen

Appendix A

Appendix

A.1 Material Properties

Table A.1: Required material properties of liquid parahydrogen for numerical simulations with Fluent. Density ρ^l, specific heat capacity at constant pressure c_p^l, thermal conductivity λ^l, viscosity μ^l, surface tension σ and specific standard state enthalpy h^l are given at saturation conditions of the pressure levels $p_{0,B6} = 72.74\,\mathrm{kPa}$ and $p_{0,A5} = 95.01\,\mathrm{kPa}$.

p_{sat} 10^3 Pa	T_{sat} K	ρ^l kg m^{-3}	μ^l 10^{-6} Pa s	λ^l 10^{-3} W m^{-1} K^{-1}	c_p^l J kg^{-1} K^{-1}	σ^l 10^{-3} N m^{-1}
72.74	19.20	72.01	14.57	101.57	9122	2.099
95.01	20.06	71.07	13.57	103.14	9602	1.960

Table A.2: Temperature dependent material properties required to model gaseous parahydrogen at $p_{0,B6} = 72.74\,\text{kPa}$ and $p_{0,A5} = 95.01\,\text{kPa}$ and the solids Pyrex and sapphire. Specific heat capacity c, thermal conductivity λ and viscosity μ are calculated as polynomial functions of the temperature T, thus $\phi = \sum_0^n (C_n T^n)$ with ϕ as a material property. The density of gaseous parahydrogen was calculated with the ideal gas equation. Reference values can be found in table 6.1.

	Parahydrogen		Pyrex	Sapphire
	$p = 72.74$ kPa	$p = 95.01$ kPa		
T K	$19 \leq T \leq 31$	$20 \leq T \leq 31$	$18 \leq T \leq 31$	$18 \leq T \leq 31$
Material property	c_p^v	c_p^v	c^s	c^s
C_0 J kg^{-1} K^{-1}	6.92×10^{04}	9.72×10^{04}	1.37×10^{01}	-5.53×10^{-01}
C_1 J kg^{-1} K^{-2}	-8.26×10^{03}	-1.20×10^{04}	-2.78×10^{00}	8.94×10^{-02}
C_2 J kg^{-1} K^{-3}	4.43×10^{02}	6.38×10^{02}	2.26×10^{-01}	-5.10×10^{-03}
C_3 J kg^{-1} K^{-4}	-1.07×10^{01}	-1.51×10^{01}	-2.60×10^{-03}	2.00×10^{-04}
C_4 J kg^{-1} K^{-5}	9.64×10^{-02}	1.35×10^{-01}		
Material property	λ^v	λ^v	λ^s	λ^s
C_0 W m^{-1} K^{-1}	5.00×10^{-04}	1.00×10^{-03}	2.00×10^{-01}	-7.98×10^{01}
C_1 W m^{-1} K^{-2}	8.00×10^{-04}	8.00×10^{-04}	-1.11×10^{-02}	-3.88×10^{01}
C_2 W m^{-1} K^{-3}			5.00×10^{-04}	1.69×10^{01}
C_3 W m^{-1} K^{-4}			-6.00×10^{-06}	-3.10×10^{-01}
C_4 W m^{-1} K^{-5}				
Material property	μ^v	μ^v		
C_0 Pa s	4.00×10^{-08}	5.00×10^{-08}		
C_1 Pa s K^{-1}	5.00×10^{-08}	5.00×10^{-08}		

Table A.3: Temperature dependent material properties for HFE-7000 [1, 7] at $T_{ref} = 298.15\,\mathrm{K}$, $\rho^l_{ref} = 1400\,\mathrm{kg\ m^{-3}}$ and $p_{ref} = 64598\,\mathrm{Pa}$ and quartz glass [42] required for Fluent computations. Specific heat capacity c, thermal conductivity λ, viscosity μ and surface tension σ are temperature dependent. The polynomial function is defined as $\phi = \sum_0^n (C_n T^n)$ with ϕ as a material property. The saturation temperature T_{sat} is given as a function of pressure, thus $T_{sat} = \sum_0^n (C_n p^n)$. The density of gaseous HFE-7000 was calculated with the ideal gas equation. Reference values can be found in table 7.2.

	HFE-7000		quartz glass
	liquid	vapor	solid
T K	$290 \leq T \leq 350$	$290 \leq T \leq 370$	$290 \leq T \leq 480$
Material Property	c_p^l	c_p^v	–
C_0 J kg^{-1} K^{-1}	3.82×10^{02}	3.14×10^{02}	–
C_1 J kg^{-1} K^{-2}	3.08×10^{00}	5.73×10^{-01}	–
Material Property	λ^l	λ^v	λ^s
C_0 W m^{-1} K^{-1}	1.35×10^{-01}	3.49×10^{-05}	1.15×10^{00}
C_1 W m^{-1} K^{-2}	-2.00×10^{-04}	2.64×10^{-05}	9.00×10^{-04}
Material property	μ^l	μ^v	–
C_0 Pa s	3.68×10^{-03}	-1.36 $\times 10^{-07}$	–
C_1 Pa s K^{-1}	-1.83×10^{-05}	3.47×10^{-08}	–
C_2 Pa s K^{-2}	2.46×10^{-08}	–	–
Material property	σ	–	–
C_0 N m^{-1}	4.24×10^{-02}	–	–
C_1 N m^{-1} K^{-1}	-1.00×10^{-04}	–	–
		–	–
p $\times 10^{03}$ Pa	$50 \leq p \leq 400$	–	–
Material property	T_{sat}	–	–
C_0 K	2.80×10^{02}	–	–
C_1 K Pa^{-1}	3.00×10^{-04}	–	–
C_2 K Pa^{-2}	-4.00×10^{-10}	–	–

A.2 Drop Tower Experiments

A.2.1 Temperature Sensor Locations

Table A.4: Vertical and radial locations of the temperature sensors.

Sensor	z mm	r mm
$\mathrm{T_{wl1}}$	-35	28.75
$\mathrm{T_{wl2}}$	-7	28.75
$\mathrm{T_{wif}}$	0	28.75
$\mathrm{T_{wv1}}$	7	28.75
$\mathrm{T_{wv2}}$	14	28.75
$\mathrm{T_{wv3}}$	21	28.75
$\mathrm{T_{wv4}}$	28	28.75
$\mathrm{T_{wv5}}$	35	28.75
$\mathrm{T_{v1}}$	14	17.20
$\mathrm{T_{v2}}$	24	19.20
$\mathrm{T_{v3}}$	34	21.20

A.2.2 Correction Functions for Surface Extraction

These functions were used to transform the pixel value of the extracted center and wall point location into a physical height.

Table A.5: Correction functions to convert the pixel value of h_f and h_b into a physical height. The polynomial function is defined as $z = 0.5\left(\sum_0^n \left(C_n h_f^n\right) + \sum_0^n \left(C_n h_b^n\right)\right)$ with h as the pixel value.

		to compute h_f	to compute h_b
C_0	$\times 10^{1}$ mm	3.766	0.000
C_1	$\times 10^{-1}$ mm Pixel^{-1}	-2.449	2.414
C_2	$\times 10^{-4}$ mm Pixel^{-2}	6.790	–
C_3	$\times 10^{-7}$ mm Pixel^{-3}	-9.839	–

A.2.3 Error Estimation for Center Point Detection of Spherical Surfaces

Figure A.1 shows a sketch of the glass cylinder, optical path and free surface together with all important points. The coordinate system has its origin in the center of the free surface curvature for simplification of the following calculations.

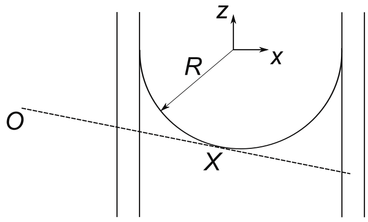

Figure A.1: Sketch to illustrate the surface detection error estimation.

Considering the free surface as a section of a circle with the radius R gives the equation

$$z = \sqrt{R^2 - x^2} \tag{A.1}$$

and the optical path from the endoscope to the (yet unknown) tangential point of the free surface $X(X_x,\, X_z)$ can be approximated (neglecting the refraction from the borosilicate) with the linear equation

$$z = kx + z_0\,. \tag{A.2}$$

The relative location of the endoscope is known as $O(O_x,\, O_z)$, thus

$$O_z = kO_x + z_0\,. \tag{A.3}$$

With the requirement that eq. A.2 is tangential to eq. A.1 the slope can be computed as

$$k = -\frac{X_x}{X_z}\,. \tag{A.4}$$

Inserting X in eq. A.2, combining with eq. A.3 and eq. A.4 gives

$$X_z = -\frac{X_x}{X_z}\,(X_x - O_x) + O_z\,, \tag{A.5}$$

and multiplied by X_z

$$X_z^2 = -X_x^2 + X_xO_x + X_zO_z\,. \tag{A.6}$$

Equation A.1 with the tangential point X inserted in eq. A.6 results in

$$R^2 - X_x^2 = -X_x^2 + X_xO_x + \sqrt{R^2 - X_x^2}O_z\,. \tag{A.7}$$

Solving for X_x

$$X_x = \frac{O_x R^2 \pm \sqrt{O_z^4 R^2 + O_x^2 O_z^2 R^2 - O_z^2 R^4}}{O_x^2 + O_z^2}\,. \tag{A.8}$$

With $O(-67.08\,\mathrm{mm}, -\frac{2}{3}R = -17.57\,\mathrm{mm})$ and $R = 26.26\,\mathrm{mm}$ two solutions for X can be computed, which are

$$X_1\,(-15.763\,\mathrm{mm},\ -21.000\,\mathrm{mm})\,, \tag{A.9}$$

$$X_2\,(-3.486\,\mathrm{mm},\ -26.027\,\mathrm{mm})\,. \tag{A.10}$$

The wanted tangential center point is X_2 which is used to calculate the slope with $k = -0.134$ and the y-intercept with $z_0 = -26.500\,\mathrm{mm}$. Since the x-coordinate of the center point is $z_{c,x} = 0\,\mathrm{mm}$ and the z-coordinate in this coordinate system is is $z_{c,z} = -R = -26.26\,\mathrm{mm}$, the resulting error with this measurement technique is $|z_0 - z_{c,z}| = 0.24\,\mathrm{mm}$.

A.2.4 Initial Wall and Vapor Temperature Distribution for the Simulations

Table A.6: Initial wall temperature values at discrete locations. The temperature progression between two adjacent locations was interpolated with a linear function. The initial temperature in r-direction was constant for a single region.

	SA5	SB6	S01	S02	S03	S04	S05	S06
$p_0 \times 10^3$ Pa	95.01				72.74			
z mm	T_w K							
-45.00	19.88	19.03	19.03	19.03	19.03	19.03	19.03	19.03
-35.00	19.88	19.03	19.03	19.03	19.03	19.03	19.03	19.03
-7.00	19.97	19.12	19.12	19.12	19.12	19.12	19.12	19.12
0.00	20.06	19.20	19.20	19.20	19.20	19.20	19.20	19.20
7.00	20.03	19.48	19.25	19.30	19.36	19.41	19.46	19.51
14.00	20.03	19.86	19.30	19.41	19.51	19.61	19.71	19.82
21.00	20.02	20.25	19.36	19.51	19.66	19.82	19.97	20.12
28.00	20.13	20.76	19.41	19.61	19.82	20.02	20.23	20.43
35.00	20.02	21.00	19.46	19.71	19.97	20.23	20.48	20.74
93.00	20.02	23.02	19.88	20.56	21.24	21.92	22.60	23.28
103.00	30.00	30.00	30.00	30.00	30.00	30.00	30.00	30.00
143.00	30.00	30.00	30.00	30.00	30.00	30.00	30.00	30.00

Table A.7: Initial vapor temperature values at discrete locations. The temperature progression between two adjacent locations was interpolated with a linear function. The initial temperature in r-direction was constant for a single region. Simulations S01 to S06 have same temperatures for the solid and liquid region.

	SA5	SB6	S01	S02	S03	S04	S05	S06
$p_0 \times 10^3$ Pa	95.01	72.74						
z mm	T_v K							
-45.00	19.88	19.03	–	–	–	–	–	–
-35.00	19.88	19.03	–	–	–	–	–	–
-7.00	19.97	19.12	–	–	–	–	–	–
0.00	20.06	19.20	–	–	–	–	–	–
14.00	20.03	20.16	–	–	–	–	–	–
24.00	20.06	20.78	–	–	–	–	–	–
34.00	20.19	21.38	–	–	–	–	–	–
84.00	21.24	24.47	–	–	–	–	–	–
93.00	21.42	25.02	–	–	–	–	–	–

A.2.5 Local Minima and Maxima of the Center Point

Table A.8: Time and center point displacement for the local extrema of all experiments.

		Experiments					
		C1	A2	C3	C4	A5	B6
$t_{min.1}$	s	0.53	0.59	0.53	0.50	0.58	0.53
$z_{c.min.1}$	mm	–	–	–	-14.10	-15.2	-14.70
$t_{max.1}$	s	1.56	1.67	1.63	1.70	1.68	1.58
$z_{c.max.1}$	mm	–	–	–	-4.20	-7.00	-5.80
$t_{min.2}$	s	2.10	2.27	2.14	2.20	2.25	2.15
$z_{c.min.2}$	mm	-	–	–	-8.70	-10.5	-9.60
$t_{max.2}$	s	2.94	3.32	3.01	3.08	3.28	3.10
$z_{c.max.2}$	mm	–	–	–	-4.90	-7.2	-6.00
$t_{min.3}$	s	3.65	4.07	3.63	3.73	3.98	3.83
$z_{c.min.3}$	mm	–	–	–	-7.70	-9.4	-8.50
$t_{max.3}$	s	4.42	–	4.55	4.60	–	4.58
$z_{c.max.3}$	mm	–	–	–	-4.90	-	-5.20

Table A.9: Time and center point displacement for the local extrema of all simulations.

		Simulations							
		SA5	S01	S02	S03	S04	S05	S06	SB6
$t_{min.1}$	s	0.55	0.55	0.55	0.50	0.55	0.55	0.55	0.55
$z_{c.min.1}$	mm	-18.73	-18.66	-18.66	-18.67	-18.65	-18.66	-18.66	-18.65
$t_{max.1}$	s	1.75	1.70	1.70	1.65	1.70	1.70	1.70	1.7
$z_{c.max.1}$	mm	-9.82	-9.78	-9.82	-9.84	-9.80	-9.83	-9.83	-9.75
$t_{min.2}$	s	2.35	2.30	2.3	2.25	2.33	2.30	2.30	2.30
$z_{c.min.2}$	mm	-13.49	-13.43	-13.45	-13.41	-13.40	-13.44	13.47	-13.44
$t_{max.2}$	s	3.25	3.15	3.15	3.15	3.15	3.15	3.15	3.13
$z_{c.max.2}$	mm	-10.73	-10.58	-10.69	-10.65	-10.68	-10.65	-10.60	-10.56
$t_{min.3}$	s	3.95	3.80	3.8	3.75	3.80	3.80	3.80	3.80
$z_{c.min.3}$	mm	-12.34	-12.32	-12.32	-21.3	-12.30	-12.26	-12.26	-12.28
$t_{max.3}$	s	4.85	4.65	4.65	4.60	4.65	4.65	4.65	4.65
$z_{c.max.3}$	mm	-10.94	-10.85	-10.90	-10.88	-10.87	-10.88	-10.88	-10.82
$t_{min.4}$	s	5.50	5.33	5.35	5.30	5.35	5.35	5.38	5.38
$z_{c.min.4}$	mm	-11.82	-11.75	-11.78	-11.73	-11.77	-11.76	-11.75	-11.75
$t_{max.4}$	s	6.48	6.15	6.20	6.15	6.10	6.18	6.20	6.18
$z_{c.max.4}$	mm	-11.17	-11.08	-11.10	-11.11	-11.07	-11.10	-11.10	-11.08
$t_{min.5}$	s	7.35	7.08	7.00	7.03	6.95	7.00	6.95	7.05
$z_{c.min.5}$	mm	-11.65	-11.61	-11.60	-11.60	-11.58	-11.58	-11.58	-11.56
$t_{max.5}$	s	8.05	7.78	7.75	7.70	7.68	7.75	7.80	7.85
$z_{c.max.5}$	mm	-11.36	-11.32	-11.30	-11.31	-11.27	-11.30	-11.28	-11.28
$t_{min.6}$	s	8.80	8.50	8.60	8.45	8.48	8.50	8.43	8.60
$z_{c.min.6}$	mm	-11.57	-11.51	-11.50	-11.48	-11.49	-11.49	-11.47	-11.47
$t_{max.6}$	s	9.78	9.38	9.45	9.28	9.33	9.48	9.45	9.55
$z_{c.max.6}$	mm	-11.38	-11.35	-11.35	-11.33	-11.31	-11.34	-11.35	-11.32

A.3 Simulations of the SOURCE-II Experiment

A.3.1 Initial Temperature Distribution for the Simulations

Table A.10: Temperature readings of TC1 to TC5 at $t = 70\,\text{s}$ in comparison with the used fits for Flow-3D and Fluent.

	Experiment	Flow-3D			Fluent		
Position	T K	T K	Offset K	Offset %	T K	Offset K	Offset %
TC5	308.15	299.07	-9.08	-2.95	308.3	0.15	0.05
TC4	351.15	348.78	-2.37	-0.67	350.5	0.65	0.19
TC3	357.15	357.10	-0.05	-0.01	357.4	0.25	0.07
TC2	364.15	366.07	1.92	0.53	365.0	0.85	0.23
TC1	408.15	410.34	2.19	0.54	408.5	0.35	0.09

A.3.2 Instability in Simulation Mesh1 with Flow-3D

The simulation Mesh1 showed a strong surface fluctuation between $163\,\text{s} \leq t \leq 172\,\text{s}$. Volume of fluid contour plots taken every second from $t = 163\,\text{s}$ to $t = 170\,\text{s}$ presented in Fig. A.2 show the fluctuation and attenuation. This perturbation was caused by a suddenly appearing bubble on the wall. Figure A.3 depicts a detailed VOF contour plot of the free surface in the vicinity of the wall. In Fig. A.3 a) the vapor pocket can be seen at $t = 163.7\,\text{s}$ still attached to the wall and rapidly growing. Figure. A.3 b) shows it detaching from the wall and breaking through the free surface. A second bubble formed from the remaining vapor pocket, which is already distorted by the moving fluid layer at the wall (Figure A.3 c)). The remaining vapor detached from the wall and vanished to the vapor region. The free surface motion attenuated and formed a stable shape.

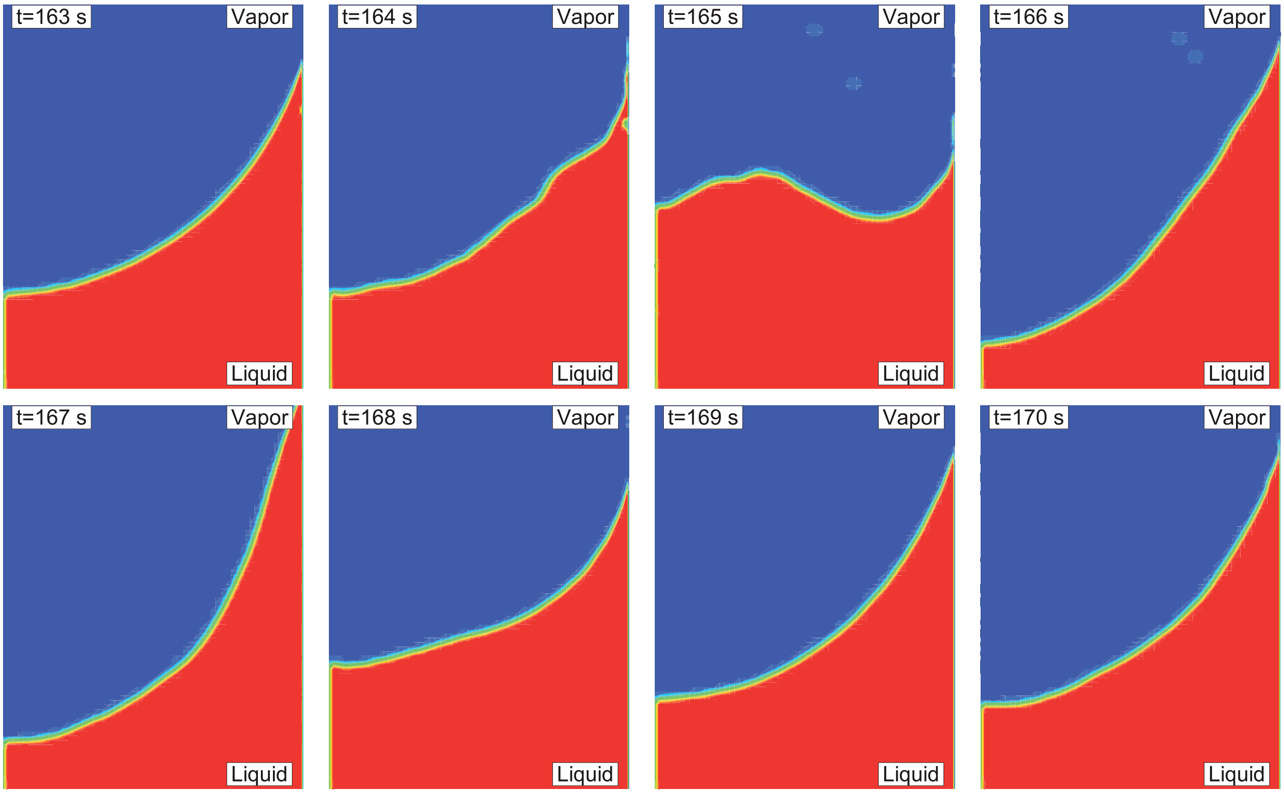

Figure A.2: Volume of fluid contour plot of the simulation Mesh1 between $163\,\mathrm{s} \leq t \leq 170\,\mathrm{s}$ to visualize the surface perturbation and attenuation.

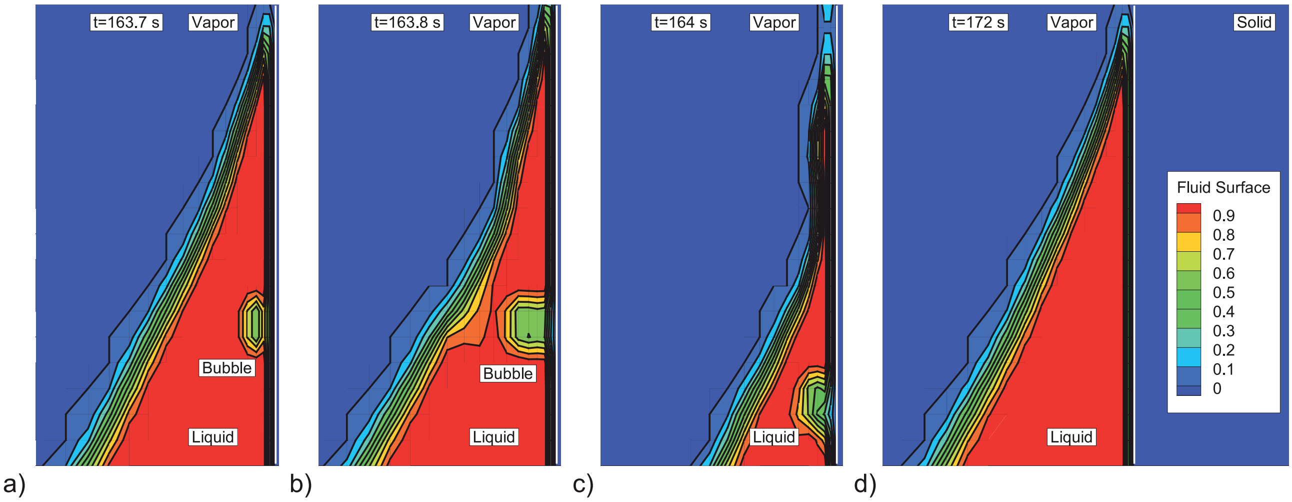

Figure A.3: Detailed view of the free surface in the vicinity of the wall with a volume of fluid contour plot of the simulation Mesh1 at certain time instances. The contour plots illustrate the influence of the bubble on the free surface stability: a) Bubble before detachment. b) Bubble at detachment. c) Remaining vapor pocket and distorted liquid layer. d) Stable free surface without remaining vapor at the wall.

A.3.3 Apparent Contact Angle with Respect to the Wall Superheat

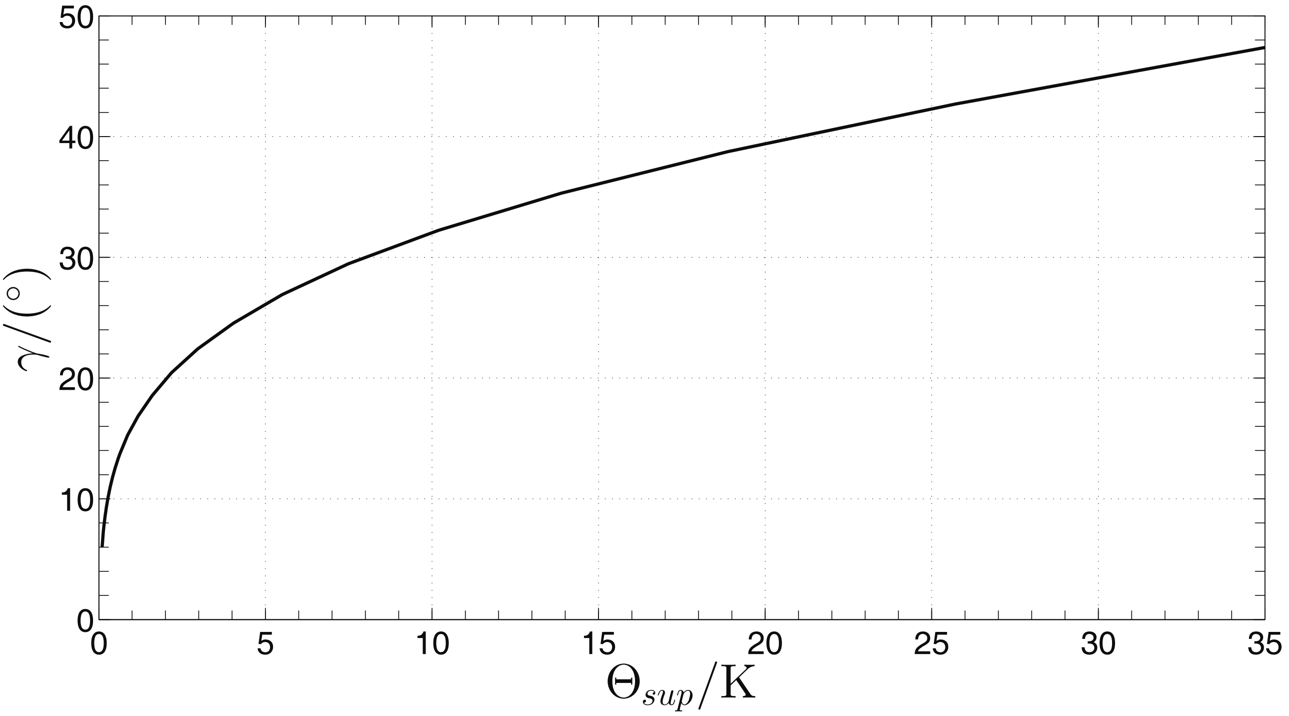

Figure A.4: Derived apparent contact angle for HFE7000 with respect to the local wall superheat using the micro-region model [82, 83].

List of Figures

List of Tables

Bibliography

[1] 3M Electronics. 3M Novec 7000 Engineered Fluid. Building 21-1W-10, 900 Bush Avenue, St. Paul, MN 55106, USA, 2005.

[2] Air Liquide. ALPHAGAZ Specifications. 75 quai d'Orsay, 75007 Paris, France, 2014.

[3] ANSYS, Inc. ANSYS Fluent Theory Guide Release 15.0. 275 Technology Drive, Canonsburg, PA 15317, USA, 2013.

[4] ANSYS, Inc. ANSYS ICEM CFD User's Manual. 275 Technology Drive, Canonsburg, PA 15317, USA, 2013.

[5] Baehr, H. D., and Kabelac, S. Thermodynamik, 15 ed. Springer Vieweg, Berlin, Heidelberg, Germany, 2012.

[6] Baehr, H. D., and Stephan, K. Wärme- und Stoffübertragung, 7 ed. Springer Vieweg, Berlin, Heidelberg, Germany, 2010.

[7] Barsi, S. Ventless Pressure Control of Cryogenic Storage Tanks. PhD thesis, Case Western Reserve University, January 2011.

[8] Barsi, S., and Kassemi, M. Numerical and experimental comparisons of the self-pressurization behavior of an LH2 tank in normal gravity. Cryogenics 48, 3-4 (2008), 122–129.

[9] Bauer, H. F., and Eidel, W. Linear liquid oscillations in cylindrical container under zero-gravity. Appl. Microgravity Tech. 4 (1990), 212–220.

[10] Bikerman, J. J. Surface Chemistry Theory and Applications, 2 ed. Academic Press, New York, New York, USA, 1958.

[11] Bird, R. B., Stewart, W. E., and Lightfoot, E. N. Transport Phenomena, 1 ed. Wiley international Edition, New York, New York, USA, 1960.

[12] Brackbill, J. U., Kothe, D. B., and Zemach, C. A continuum method for modeling surface tension. J. Comput. Phys. 100, 2 (June 1992), 335–354.

[13] Bradshaw, R. S. Evaluation and application of data from low-gravity orbital experiment, phase 1 final report. Tech. Rep. NASA-CR-109847, General Dynamics Convair Division, 1970.

[14] Buntkowsky, G., Walaszek, B., Adamczyk, A., Xu, Y., H.-H., L., and Chaudret, B. Mechanism of nuclear spin initiated para-h_2 to ortho-h_2 conversion. Physical Chemistry Chemical Physics 8, 1 (2006), 1929–1935.

[15] Carey, V. P. Liquid-Vapor Phase-Change Phenomena, 2 ed. CRC Press, 270 Madison Avenue, New York, NY,10016, USA, 2008, ch. 4., pp. 107–143.

[16] Case, K. M., and Parkinson, W. C. Damping of surface waves in an incompressible liquid. J. Fluid Mech. 2, 2 (March 1957), 172–184.

[17] Chorin, A. J. Numerical solutions of the Navier-Stokes equations. Mathematics of Computation 22, 104 (1968), 745–762.

[18] Concus, P. Static menisci in a vertical right circular cylinder. Journal of Fluid Mechanics 34, 3 (May 1968), 481–495.

[19] Das, S. P., and Hopfinger, E. J. Mass transfer enhancement by gravity waves at a liquid-vapour interface. Int. J. Heat Mass Tran. 52, 5-6 (February 2009), 1400–1411.

[20] de Gennes, P. G. Wetting: Statics and dynamics. Rev. Mod. Phys. 57, 3 (July 1985), 827–863.

[21] Dodge, F. T. The new Dynamic Behavior of Liquids in Moving Containers. Southwest Research Institute, San Antonio, Texas, USA, 2000.

[22] Dreyer, M. E., Gerstmann, J., Stange, M., Rosendahl, U., Woelk, G., and Rath, H. J. Capillary effects under low gravity, part 1: Surface settling, capillary rise and critical velocities. Space Forum 3 (1998), 87–136.

[23] Eckels, P. Cryocomp. Software, September 2009. CryoComp Version 5.0.

[24] Ferziger, J. H., and Perić, M. Computational Methods for Fluid Dynamics, 3 ed. Springer Vieweg, Berlin, Heidelberg, Germany, 2002.

[25] Fisher, M. F., Schmidt, G. R., and Martin, J. J. Analysis of cryogenic propellant behaviour in microgravity and low thrust environments. Cryogenics 32, 2 (1992), 230–235.

[26] Flow Science, Inc. Flow-3D Documentation Release 11.0.0. 683 Harkle Road, Santa Fe, NM 87505, USA, 2014.

[27] Fortescue, P., Swinderd, G., and Stark, J. Spacecraft Systems Engineering, 4 ed. John Wiley & Sons, The Atrium, Southern Gate, Chichester, West Sussex, PO19 8SQ, United Kingdom, 2011, ch. 6, pp. 177–219.

[28] Fox, R. W., Pritchard, P. J., and McDonald, A. T. Introduction to Fluid Mechanics, 7 ed. John Wiley & Sons, Inc., 111 River Street, Hoboken, NY, 07030, USA, 2009, ch. 5., pp. 161–196.

[29] Fu, J., Sunden, B., Chen, X., and Huang, Y. Influence of phase change on self-pressurization in cryogenic tanks under microgravity. Appl. Therm. Eng. 87 (August 2015), 225–233.

[30] Fuhrmann, E., and Dreyer, M. Description of the sounding rocket experiment-SOURCE. Microgravity Sci. Technol. 20, 3-4 (2008), 205–212.

[31] Fuhrmann, E., and Dreyer, M. Heat and mass transfer at a free surface with diabatic boundaries in a single-species system under microgravity conditions. Exp. Fluids 55, 1760 (June 2014), 1–18.

[32] Fuhrmann, E., Dreyer, M., Basting, S., and Baensch, E. Free surface deformation and heat transfer by thermocapillary convection. Heat Mass Transfer DOI 10.1007/s00231-015-1600-9 (2015).

[33] GE Measurment & Control. PDCR/PMP 4300 Series, Druck Motorsport/Automotive Pressure Transducers. 1100 Technology Park Dr, Billerica, MA 01821, USA, 2007.

[34] Gerstmann, J. Numerische Untersuchungen zur Schwingung freier Flüssigkeitsoberflächen. PhD thesis, University of Bremen, Duesseldorf, 2004.

[35] Gerstmann, J. COMPERE SOURCE-II numerical benchmark definition. Unpublished Internal Documentation, January 2014.

[36] Gerstmann, J., and Dreyer, M. E. Experiments on reorientation under non-isothermal conditions. Technical report, ZARM, University of Bremen, 2003.

[37] Gerstmann, J., Michaelis, M., Dreyer, M. E., and Rath, H. J. An applicable boundary condition at the moving contact line in case of a free surface reorientation after step reduction in gravity. Proc. Appl. Math. Mech. 2 (2003), 316–317.

[38] Glover, D. NASA cryogenic fluid management space experiment efforts, 1960-1990. In Conference on Advanced Space Exploration Initiative Technologies (September 1991), AIAA, Ed.

[39] Golestanian, R., and Raphael, E. Dissipation in dynamics of a moving contact line. Phys. Rev. E 64, 031601 (August 2001), 1–7.

[40] Grayson, G., Lopez, A., and Chandler, F. Cryogenic tank modeling for the saturn AS-203 experiment. In 42nd AIAA/ASME/SAE/ASEE Joint Propulsion Conference and Exhibit (July 2006), AIAA, Ed.

[41] Gross, D., Hauger, W., Schröder, J., and Wall, W. A. Technische Mechanik 3, 9 ed. Springer Vieweg, Berlin, Heidelberg, 2006, ch. 5., pp. 2015–270.

[42] Heraeus Quarzglas GmbH & Co. KG. Quartz Glass for Optics - Data and Properties. Quarzstr. 8, 63450 Hanau, Germany, 2014.

[43] Hirt, C. W., Milano, D., and Barkhudarov, M. R. Modeling phase change and homogeneous bubbles. Tech. rep., Flow Science, Inc., 683 Harkle Road, Santa Fe, NM 87505, USA, 2013.

[44] Hirt, C. W., and Nichols, B. D. Volume of fluid (VOF) method for the dynamics of free boundaries. J. Comput. Phys. 39, 1 (January 1981), 201–225.

[45] Hirt, C. W., and Sicilian, J. M. A porosity technique for the definition of obstacles in rectangular cell meshes. Tech. rep., Flow Science, Inc., 683 Harkle Road, Santa Fe, NM 87505, USA, 1985.

[46] Hopfinger, E. J., and Das, S. P. Mass transfer enhancement by capillary waves at a liquid-vapour interface. Exp. Fluids 46, 4 (2009), 597–605.

[47] Joanny, J. F., and de Gennes, P. G. A model for contact angle hysteresis. J. Chem. Phys. 81, 1 (July 1984), 552–562.

[48] Jousten, K. Wutz Handbuch Vakuumtechnik, 10 ed. Vieweg+Teubner, Wiesbaden, Germany, 2010, ch. 12, p. 456.

[49] Keiderling, D., Hannemann, K., Gauer, M., and Hurst, J. Numerical modelling of cryogenic two-phase flow in the DLR TAU code. In Space Propulsion 2014 (May 2014).

[50] Knoll, R. H., Smolak, G. R., and Nunamaker, R. R. Weightlessness experiments with liquid hydrogen in aerobee sounding rockets: Uniform radiant heat addition - flight 1. Tech. Rep. X-484, NASA, June 1962.

[51] Konopka, M., Behruzi, P., Schmitt, S., and Dreyer, M. E. Phase change in cryogenic upper stage tanks. In 50th AIAA/ASME/SAE/ASEE Joint Propulsion Conference in Cleveland (July 2014), AIAA, Ed.

[52] Kulev, N., Basting, S., Baensch, E., and Dreyer, M. E. Interface reorientation of cryogenic liquids under non-isothermal boundary conditions. Cryogenics 62 (July /August 2014), 48–59.

[53] Kulev, N., and Dreyer, M. E. Drop tower experiments on non-isothermal reorientation of cryogenic liquids. Microgravity Sci. Technol. 22, 4 (2010), 463–474.

[54] Lake Shore Cryotonics, Inc. Temperature Measurement and Control Catalog, Cryogenic Sensors, Instruments, and Accessories. 575 McCorkle Blvd, Westerville, OH 43082, USA, 2005.

[55] Landau, L. D., and Lifschitz, E. M. Course of Theoretical Physics, vol. 6. Pergamon Press, Oxford, Great Brittain, 1987, ch. 2, pp. 238–244.

[56] Langbein, D. Capillary Surfaces, Shape - Stability - Dynamics, in Particular Under Weightlessness, 1 ed., vol. 178. Springer Tracts in Modern Physics, Berlin, Heidelberg, Germany, 2002, ch. 2, pp. 30–35.

[57] Lee, W. H. A pressure iteration scheme for two-phase flow modeling. Tech. rep., Energy Division, Los Alamos Scientific Laboratory, University of California, Los Alamos, NM 87545, USA, 1985.

[58] Lemmon, E. W., Peskin, A. P., McLinden, M. O., and Friend, D. NIST thermodynamic and transport properties of pure fluids - NIST pure fluids. Software, September 2010. NIST Standard Reference Database 23, Version 9.0.

[59] Ludwig, C., and Dreyer, M. E. Investigations on thermodynamic phenomena of the active-pressurization process of a cryogenic propellant tank. Cryogenics 63 (September /October 2014), 1–16.

[60] Ludwig, C., Dreyer, M. E., and Hopfinger, E. J. Pressure variations in a cryogenic liquid storage tank subjected to periodic excitations. Int. J. Heat Mass Tran. 66 (November 2013), 223–234.

[61] McArdle, J. G., Dillon, R. C., and Altmos, D. A. Weightlessness experiments with liquid hydrogen in aerobee sounding rockets: Uniform radiant heat addition - flight 2. Tech. Rep. X-718, NASA, December 1962.

[62] McCarty, R. D., Hord, J., and Roder, H. M. Selected properties of hydrogen (engineering design data). No. 168 in NBS Monograph Series. U.S. Department of Commerce. National Bureau of Standards, Boulder, CO, 80303, USA, 1981, ch. 1.2.21., pp. 131–132.

[63] Merziger, G., Mühlbach, G., Wille, D., and Wirth, T. Formeln + Hilfen zur Höheren Mathematik. Binomi Verlag, Am Bergfelde 28, 31832 Springe, 2004, ch. 12., pp. 143–148.

[64] Merziger, G., and Wirth, T. Repetitorium der Höheren Mathematik. Binomi Verlag, Am Bergfelde 28, 31832 Springe, 2006, ch. 15., p. 384.

[65] Michaelis, M. Kapillarinduzierte Schwingungen freier Flüssigkeitsoberflächen. PhD thesis, University of Bremen, Düsseldorf, 2003.

[66] Michaelis, M., Dreyer, M. E., and Rath, H. J. Experimental investigation of the liquid interface reorientation upon step reduction in gravity. Ann. NY Acad. Sci. 974 (2002), 246–260.

[67] Michaelis, M., Gerstmann, J., Dreyer, M. E., and Rath, H. J. Damping behaviour of the free liquid interface oscillation upon step reduction in gravity. Proc. Appl. Math. Mech. 2 (2003), 320–321.

[68] Minco, Inc. Flexible Heaters Design Guide. 7300 Commerce Lane, Minneapolis, Mn 55432, USA, 2007.

[69] Nunamaker, R. R., Corpas, E. L., and McArdle, J. G. Weightlessness experiments with liquid hydrogen in aerobee sounding rockets: Uniform radiant heat addition - flight 3. Tech. Rep. X-872, NASA, December 1963.

[70] Partridge, J. K. Fractional consumption of liquid hydrogen and liquid oxygen during the space shuttle program. Tech. Rep. NASA KSC-2011-132, NASA Kennedy Space Center, 2012.

[71] Raj, R., Kunkelmann, C., P. Stephan, P., Plawsky, J., and Kim, J. Contact line behavior for a highly wetting fluid under superheated conditions. Int. J. Heat Mass Tran. 55, 9-10 (April 2012), 2664–2675.

[72] Regetz Jr., J. D., Conroy, M. J., and Jackson, R. G. Weightlessness experiments with liquid hydrogen in aerobee sounding rockets, nonuniform radiant heat addition-flight 4. Tech. Rep. NASA-TM-X-873, NASA Glenn Research Center, 1964.

[73] Ross, D., Taborek, P., and Rutledge, J. E. Wetting behavior of H2 on cesium. Phys. Rev. B 58 (Aug 1998), R4274–R4276.

[74] Schmitt, S., and Dreyer, M. E. Free surface oscillations of liquid hydrogen in microgravity conditions. Cryogenics 72, 1 (December 2015), 22–35.

[75] Schott North America, Inc. Optical Glass Data Sheets. 400 York Avenue, Duryea, PA 18642, USA, 2010.

[76] Scott, R. B. Cryogenic Engineering, 1 ed. D. Van Nostrand Company, Inc., Princton, New Jersey, USA, 1959.

[77] Seo, M., and Jeong, S. Analysis of self-pressurization phenomenon of cryogenic fluid storage tank with thermal diffusion model. Cryogenics 50, 9 (September 2010), 549–555.

[78] Shivers, H. The space launch system- the biggest, most capable rocket ever built, for entirely new human exploration missions beyond earth's orbit. Tech. Rep. NASA M11-1118, NASA Marshall Space Flight Center, 2012.

[79] Siegert, C. E., Petrash, D. A., and Otto, E. W. Time response of liquid-vapor interface after entering weightlessness. Tech. Rep. NASA TN D-2458, Lewis Research Center, Cleveland, Ohio, 1964.

[80] Siegert, C. E., Petrash, D. A., and Otto, E. W. Behavior of liquid-vapor interface of cryogenic liquids during weightlessness. National Aeronautics and Space Administration, 1965.

[81] Snyder, H. A. Sloshing in microgravity. Cryogenics 39, 12 (December 1999), 1047–1055.

[82] Stephan, P. Wärmedurchgang bei Verdampfung aus Kapillarrillen in Wärmerohren. PhD thesis, University of Stuttgart, 1992.

[83] Stephan, P., and Hammer, J. A new model for nucleate boiling heat transfer. Heat and Mass Transfer 30, 2 (1994), 119–125.

[84] Stief, M., Gerstmann, J., and Dreyer, M. E. Reorientation of cryogenic fluids upon step reduction of gravity. PAMM 5, 1 (2005), 553–554.

[85] TetraTec Instruments GmbH. Manual ATM Analog Pressure Transducer. Gewerbestr. 8, 71144 Steinenbronn, Germany, 2005.

[86] van Foreest, A., Dreyer, M. E., and Arndt, T. Moving two-fluid systems using the volume-of-fluid method and single-temperature approximation. AIAA J. 49, 12 (December 2011), 2805–2813.

[87] Weislogel, M. M., and Ross, H. D. Surface reorientation and settling in cylinders upon step reduction in gravity. Microgravity Sci. Technol. 3, 1 (1990), 24–32.

[88] Weislogel, M. M., and Ross, H. D. Surface settling in partially filled containers upon step reduction in gravity. Tech. Rep. NASA TM 103641, NASA Lewis Research Center, 1990.

[89] White, F. M. Fluid Mechanics, 7 ed. McGraw-Hill Companies, Inc., 1221 Avenue of the Americas, New York, NY, 10020, USA, 2011, ch. 4., pp. 235–258.

[90] Woelk, G., Dreyer, M. E., Rath, H. J., and Weislogel, M. M. Damped oscillations of a liquid/gas surface upon step reduction in gravity. J. Spacecraft Rockets 34, 1 (1997), 110–117.

[91] Yao, G. F. Development of new pressure-velocity solvers in Flow-3D. Tech. rep., Flow Science, Inc, 683 Harkle Road, Santa Fe, NM 87505, USA, 2004.

[92] Young, T. An essay on the cohesion of fluids. Philos. T. R. Soc. 95 (1805), 65–87.

[93] Youngs, D. L. Time-dependent multi-material flow with large fluid distortion. Tech. rep., Atomic Weapons Research Establishment, Aldermaston, Berkshire, Great Britain, 1982.